ΠΑΝΕΠΙΣΤΗΜΙΟ ΘΕΣΣΑΛΙΑΣ
ΠΟΛΥΤΕΧΝΙΚΗ ΣΧΟΛΗ
ΤΜΗΜΑ ΜΗΧΑΝΟΛΟΓΩΝ ΜΗΧΑΝΙΚΩΝ

Εργαστήριο Δυναμικής Συστημάτων

ΜΕΘΟΔΟΙ ΑΝΑΓΝΩΡΙΣΗΣ ΜΟΝΤΕΛΩΝ ΣΥΝΘΕΤΩΝ ΚΑΤΑΣΚΕΥΩΝ ΜΕ ΑΞΙΟΠΟΙΗΣΗ ΠΛΗΡΟΦΟΡΙΩΝ ΑΠΟ ΜΕΤΡΗΣΕΙΣ ΤΗΣ ΤΑΛΑΝΤΩΤΙΚΗΣ ΤΟΥΣ ΑΠΟΚΡΙΣΗΣ

Διδακτορική Διατριβή

υπό

ΝΤΟΤΣΙΟΥ ΕΥΑΓΓΕΛΟΥ

Διπλωματούχου Μηχανολόγου Μηχανικού, Π.Θ., 2005
Μ.Δ.Ε. Μηχανολόγου Μηχανικού, Π.Θ., 2009

Υπεβλήθη για την εκπλήρωση μέρους των
απαιτήσεων για την απόκτηση του
Διδακτορικού Διπλώματος

2009

UNIVERSITY OF THESSALY

SCHOOL OF ENGINEERING

DEPARTMENT OF MECHANICAL ENGINEERING

System Dynamics Laboratory

METHODS FOR IDENTIFYING MODELS OF COMPLEX STRUCTURES USING INFORMATION FROM MEASURED VIBRATIONS

Thesis by

EVANGELOS NTOTSIOS

Diploma in Mechanical Engineering, University of Thessaly, 2005
M.Sc. in Mechanical Engineering, University of Thessaly, 2009

In partial fulfillment of the requirements
for the degree of
Doctor of Philosophy

2009

Η παρούσα διδακτορική διατριβή συγχρηματοδοτήθηκε κατά:

- 75% της Δημόσιας Δαπάνης από την Ευρωπαϊκή Ένωση - Ευρωπαϊκό Κοινωνικό Ταμείο
- 25% της Δημόσιας Δαπάνης από το Ελληνικό Δημόσιο

  Υπουργείο Ανάπτυξης - Γενική Γραμματεία Έρευνας και Τεχνολογίας
- και από τον Ιδιωτικό Τομέα

στο πλαίσιο του Μέτρου 8.3 του Ε.Π. Ανταγωνιστικότητα - Γ' Κοινοτικό Πλαίσιο Στήριξης.



This research is part of the 03-ED-524 project, implemented within the framework of the "Reinforcement Programme of Human Research Manpower" (PENED) and co-financed 25% from the Greek Ministry of Development (General Secretariat of Research and Technology), 75% from E.U. (European Social Fund) and the private sector, in the context of measure 8.3 of the Operational Program Competitiveness (3rd Community Support Framework Program).

Ντότσιος Ευάγγελος

Μέθοδοι αναγνώρισης μοντέλων σύνθετων κατασκευών

με αξιοποίηση πληροφοριών από μετρήσεις

της ταλαντωτικής τους απόκρισης

Ημερομηνία προφορικής εξέτασης: 16 Δεκεμβρίου 2009

Διδακτορική Διατριβή

Υποβλήθηκε στο Τμήμα Μηχανολόγων Μηχανικών
Τομέας Μηχανικής, Υλικών & Κατεργασιών
Εργαστήριο Δυναμικής Συστημάτων

Εξεταστική Επιτροπή:

Καθηγητής Κ. Παπαδημητρίου, Επιβλέπων, μέλος τριμελούς Συμβουλευτικής Επιτροπής
Καθηγητής Σ. Νατσιάβας, Μέλος τριμελούς Συμβουλευτικής Επιτροπής
Αν. Καθηγητής Σ. Καραμάνος, Μέλος τριμελούς Συμβουλευτικής Επιτροπής

Καθηγητής Ν. Αράβας, Εξεταστής
Αν. Καθηγητής Ι. Αντωνιάδης, Εξεταστής
Αν. Καθηγητής Π. Τσόπελας, Εξεταστής
Επ. Καθηγητής Α. Σταμάτης, Εξεταστής

Ntotsios Evangelos

Methods for identifying models of complex

structures using information from

measured vibrations

Defended December 16, 2009

Ph.D. Thesis

Submitted to the Department of Mechanical Engineering
Division of Mechanics, Materials & Manufacturing Processes
System Dynamics Laboratory

Evaluation Committee :

Professor C. Papadimitriou, Supervisor
Professor S. Natsiavas, member
Associate Professor S. Karamanos, member

Professor N. Aravas, member
Associate Professor I. Antoniadis, member
Associate Professor P. Tsopelas, member
Assistant Professor A. Stamatis, member

Μέθοδοι αναγνώρισης μοντέλων σύνθετων κατασκευών με αξιοποίηση πληροφοριών από μετρήσεις της ταλαντωτικής τους απόκρισης

ISBN

Η έγκριση της παρούσας Διδακτορικής Διατριβής από το Τμήμα Μηχανολόγων Μηχανικών της Πολυτεχνικής Σχολής του Πανεπιστημίου Θεσσαλίας δεν υποδηλώνει αποδοχή των απόψεων του συγγραφέα (Ν. 5343/32 αρ. 202 παρ. 2).

Ευχαριστίες

Η παρούσα διδακτορική διατριβή εκπονήθηκε στο Εργαστήριο Δυναμικής Συστημάτων του τμήματος Μηχανολόγων Μηχανικών στο Πανεπιστήμιο Θεσσαλίας.

Φτάνοντας στο τέλος αυτής της προσπάθειας, πρώτα απ' όλα, θα ήθελα να ευχαριστήσω τον επιβλέποντα της διδακτορικής εργασίας μου, Καθηγητή κ. Κώστα Παπαδημητρίου, για την ενθάρρυνση, πολύτιμη βοήθεια και καθοδήγησή του κατά όλη τη διάρκεια της συνεργασίας μας, αλλά και για τη διαρκή του προσπάθεια να με μυήσει στις αρχές και αξίες που επικρατούν στην διεθνή επιστημονική κοινότητα. Επίσης, ευχαριστώ τα υπόλοιπα μέλη της τριμελούς συμβουλευτικής επιτροπής της διδακτορικής διατριβής μου, Καθηγητές κκ. Νατσιάβα Σωτήρη και Καραμάνο Σπύρο, καθώς και τα υπόλοιπα μέλη της επταμελούς επιτροπής για την προσεκτική ανάγνωση της εργασίας μου και για τις πολύτιμες υποδείξεις τους. Ευχαριστίες οφείλω σε όλους τους μεταπτυχιακούς και προπτυχιακούς φίλους και φοιτητές του Εργαστηρίου Δυναμικής Συστημάτων για την άριστη συνεργασία που είχαμε κατά τη διάρκεια της εκπόνησης της παρούσας διδακτορικής διατριβής. Ευχαριστώ όλους τους φίλους και φίλες μου και κυρίως τους Γρηγόρη, Διονύση και Μαρία για την ανοχή τους, την υποστήριξή τους και για τις ωραίες στιγμές που περάσαμε όλα αυτά τα χρόνια.

Πάνω απ' όλα, είμαι ευγνώμων στους γονείς μου, Γιώργο και Παρασκευή για την ολόψυχη αγάπη και υπομονή τους όλα αυτά τα χρόνια καθώς και για τη υποστήριξη που μου έδωσαν να συνεχίσω τις σπουδές μου. Σε αυτούς και αφιερώνω την εργασία αυτή.

Ντότσιος Βαγγέλης,
Δεκέμβρης 2009, Βόλος.

Στους γονείς μου,

Γιώργο και Παρασκευή

Περίληψη

Στόχος της εργασίας είναι η ανάπτυξη και πιστοποίηση μεθοδολογιών για την αναγνώριση δυναμικών μοντέλων σύνθετων κατασκευών καθώς και για την πρόβλεψη της συσσώρευσης βλαβών λόγω κόπωσης, με αξιοποίηση πληροφοριών από μετρήσεις της ταλαντωτικής απόκρισης των κατασκευών. Τα αναγνωρισμένα μοντέλα αναφέρονται σε μαθηματικά ιδιομορφικά μοντέλα καθώς και σε μηχανικά μοντέλα πεπερασμένων στοιχείων. Οι προτεινόμενες μεθοδολογίες καλύπτουν εφαρμογές κυρίως σε κατασκευές οχημάτων εδάφους/αέρος αλλά και κατασκευές πολιτικού μηχανικού. Η εργασία είναι χωρισμένη σε τρία συσχετιζόμενα μέρη.

Μέρος Α: Παρουσιάζονται μεθοδολογίες βελτιστοποίησης ελαχίστων τετραγώνων για την αναγνώριση ιδιομορφικών μοντέλων μη κλασικής απόσβεσης κατασκευών χρησιμοποιώντας (1) μετρήσεις απόκρισης και μετρήσεις διέγερσης στις πολλαπλές βάσεις της κατασκευής, και (2) μετρήσεις μόνο της απόκρισης της κατασκευής σε διέγερση από άγνωστα λειτουργικά φορτία Για την πρώτη περίπτωση, αξιοποιήθηκε η ενιαία δομή των εξισώσεων στο πεδία χρόνου και συχνοτήτων για την ανάπτυξη αλγορίθμου και λογισμικού αναγνώρισης κοινό για τις δύο διατυπώσεις. Η μεθοδολογία αναγνώρισης βασίζεται στην ελαχιστοποίηση του μέτρου της διαφοράς μεταξύ των μετρούμενων και των προβλεπόμενων από το ιδιομορφικό μοντέλο χρονοϊστοριών απόκρισης για το πεδίο χρόνου καθώς και του μέτρου της διαφοράς μεταξύ του μετασχηματισμού Fourier των μετρούμενων και των προβλεπόμενων από το ιδιομορφικό μοντέλο χρονοϊστοριών απόκρισης για το πεδίο συχνοτήτων. Για τη δεύτερη περίπτωση, η μεθοδολογία βασίζεται στην ελαχιστοποίηση του μέτρου της διαφορας μεταξύ των μετρούμενων και των προβλεπόμενων από το ιδιομορφικό μοντέλο συναρτήσεων διαφασματικής πυκνότητας. Αξιοποιήθηκε η δομή των εξισώσεων για την ανάπτυξη υπολογιστικά αποδοτικών αλγορίθμων δυο και τριών βημάτων για την επίλυση του έντονα μη-κυρτού, μη γραμμικού, προβλήματος βελτιστοποίησης που προκύπτει για τον προσδιορισμό των ιδιομορφικών χαρακτηριστικών, όπως ο αριθμός των ιδιομορφών, οι ιδιοσυχνότητες, οι συντελεστές απόσβεσης, οι ιδιομορφικές συνιστώσες και οι ιδιομορφικοί συντελεστές συνεισφοράς. Εφαρμόζοντας τον αλγόριθμο δύο βημάτων τα ιδιομορφικά χαρακτηριστικά υπολογίζονται γρήγορα και με ακρίβεια επιλύοντας δύο αλγεβρικά γραμμικά συστήματα και εφαρμόζοντας ανάλυση SVD. Το τρίτο βήμα του αλγόριθμου επιλύει το αρχικό μη γραμμικό πρόβλημα βελτιστοποίησης χρησιμοποιώντας ως αρχικές εκτιμήσεις των ιδιομορφικών χαρακτηριστικών τις τιμές που προκύπτουν από τα δύο πρώτα βήματα, επιταχύνοντας αισθητά τη σύγκλιση των διαθέσιμων τεχνικών ελαχιστοποίησης βαθμίδας. Η εφαρμογή του τρίτου βήματος του αλγορίθμου κρίνεται απαραίτητη για τον υπολογισμό κυρίως των κοντινών και επικαλυπτόμενων ιδιομορφών. Η προτεινόμενη μεθοδολογία αυτοματοποιεί την εκτίμηση των ιδιομορφικών χαρακτηριστικών χωρίς την, η με ελάχιστη, επέμβαση του χρήστη και επομένως είναι εφαρμόσιμη στη διαρκή, real-time παρακολούθηση της δομικής ακεραιότητας κατασκευών.

Μέρος Β: Παρουσιάζονται καινοτόμες μέθοδοι αναθεώρησης μοντέλων πεπερασμένων στοιχείων και πρόβλεψης της απόκρισης κατασκευών βάσει των ιδιομορφικών χαρακτηριστικών. Εξετάζεται και αναδεικνύεται η αντιστοιχία μεταξύ των μεθόδων πολυκριτηριακής αναγνώρισης, συμβατικής

μονοκριτηριακής αναγνώρισης σταθμισμένων υπολοίπων, και Bayesian στατιστικής αναγνώρισης μοντέλων κατασκευών. Οι μέθοδοι καταλήγουν στη αναγνώριση πολλαπλών Pareto βέλτιστων μοντέλων πεπερασμένων στοιχείων με σημαντική μεταβλητότητα, ενώ επίσης προτείνεται μέθοδος επιλογής του προτιμητέου Pareto μοντέλου. Η μεταβλητότητα των υπολογιζόμενων Pareto μοντέλων οφείλεται σε σφάλματα μοντελοποίησης και σφάλματα μετρήσεων και επηρεάζουν τη μεταβλητότητα μεγεθών απόκρισης που προβλέπονται από τα Pareto μοντέλα. Συγκεκριμένα, η Bayesian στατιστική μέθοδος αναγνώρισης προσφέρει το πλεονέκτημα της ποσοτικοποίησης της αβεβαιότητας στα Pareto βέλτιστα μοντέλα και επί τη βάσει αυτής πρόβλεψη της αβεβαιότητας σε μεγέθη απόκρισης. Εξετάζονται θεωρητικά και υπολογιστικά θέματα που προκύπτουν κατά την εφαρμογή των μεθοδολογιών αναθεώρησης, συμπεριλαμβανομένων θεμάτων που αφορούν την ύπαρξη ολικών-τοπικών βέλτιστων λύσεων, τη σύγκλιση των προτεινόμενων αλγορίθμων, και προβλήματα μη αναγνωρισιμότητας. Προτείνονται υβριδικοί αλγόριθμοι βελτιστοποίησης για τον υπολογισμό των ολικών βέλτιστων και υιοθετείται πολυκριτηριακός αλγόριθμος βελτιστοποίησης NBI για τον υπολογιστικά αποδοτικότερο υπολογισμό του μετώπου Pareto και των βέλτιστων Pareto μοντέλων. Αναπτύσσονται επίσης υπολογιστικά αποδοτικοί αλγόριθμοι για τον αναλυτικό υπολογισμό των πρώτων και δευτέρων παραγώγων των αντικειμενικών συναρτήσεων απαραίτητων για την επιτάχυνση της σύγκλισης κατά την πολυκριτηριακή και μονοκριτηριακή βελτιστοποίηση. Οι αλγόριθμοι βασίζονται στη μέθοδο του Nelson για τον υπολογισμό των παραγώγων των ιδιομορφικών παραμέτρων. Αποδεικνύεται ότι ο υπολογιστικός χρόνος που απαιτείται για τον υπολογισμό των Pareto βέλτιστων μοντέλων είναι ανεξάρτητος από τον αριθμό των παραμέτρων του μοντέλου. Ο αναλυτικός υπολογισμός των δευτέρων παραγώγων των αντικειμενικών συναρτήσεων είναι επίσης απαραίτητος και στην εφαρμογή των Bayesian ασυμπτωτικών σχέσεων που ποσοτικοποιούν την αβεβαιότητα των Pareto βέλτιστων μοντέλων. Ιδιαίτερη έμφαση δίδεται επίσης για τη γενίκευση του ορισμού των αντικειμενικών συναρτήσεων που εμπλέκονται στις μεθοδολογίες αναθεώρησης μοντέλων έτσι ώστε να αντιμετωπιστούν σοβαρά προβλήματα αντιστοιχίας μεταξύ μετρούμενων και υπολογιζόμενων από το μοντέλο ιδιομορφών που παρουσιάζονται στις περιπτώσεις εμφάνισης κοντινών ιδιομορφών. Αξιόλογα θεωρητικά και υπολογιστικά θέματα καταδεικνύονται με εφαρμογές σε μια μικρής κλίμακας μεταλλική κατασκευή και σε ένα μεταλλικό σκελετό εργαστηριακού μοντέλου οχήματος χρησιμοποιώντας μετρήσεις ταλάντωσης. Επιτυγχάνεται η πιστοποίηση των μεθοδολογιών και εξακριβώνονται τα πλεονεκτήματα των προτεινόμενων πολυκριτηριακών μεθόδων αναθεώρησης. Τέλος, μελετάται η επίδραση των σφαλμάτων μοντελοποίησης και μετρήσεων στην μεταβλητότητα των Pareto βέλτιστων μοντέλων και στις προβλέψεις μεγεθών απόκρισης από τα μοντέλα αυτά.

Μέρος Γ: Παρουσιάζεται μία καινοτόμος μεθοδολογία για την πρόβλεψη της συσσώρευσης βλαβών λόγω κόπωσης σε ολόκληρο το φορέα μεταλλικών κατασκευών με αξιοποίηση πληροφοριών από μετρήσεις της ταλαντωτικής τους απόκρισης σε περιορισμένο αριθμό θέσεων στην κατασκευή. Εφαρμόζονται διαθέσιμες στατιστικές μεθοδολογίες εκτίμησης της κόπωσης που βασίζονται στον κανόνα Palmgren-Miner, στις S-N καμπύλες κόπωσης για απλά δομικά στοιχεία που υπόκεινται σε σταθερού εύρους κυκλικές φορτίσεις, και στην κατανομή πιθανότητας του εύρους των τάσεων κατά Dirlik χρησιμοποιώντας τις συναρτήσεις διαφασματικής πυκνότητας των μετρούμενων τάσεων στην κατασκευή. Οι συναρτήσεις διαφασματικής πυκνότητας των τάσεων

σε όλο τον φορέα της κατασκευής προβλέπονται από τις μετρούμενες αποκρίσεις χρησιμοποιώντας το Kalman filter και ένα δυναμικό μοντέλο της κατασκευής. Η ακρίβεια των προβλέψεων του Kalman filter μπορούν να βελτιωθούν εισάγοντας τις μεθοδολογίες αναθεώρησης που αναπτύχθηκαν στο Β Μέρος. Η απόδοση και ακρίβεια της προτεινόμενης μεθοδολογίας παρουσιάζεται με ένα απλοϊκό μοντέλο μερικών βαθμών ελευθερίας για την περίπτωση μονοαξονικής κατάστασης των τάσεων.

Summary

This thesis concentrates on the development and validation of methods for identifying dynamic models of complex structures as well as predicting fatigue damage accumulation by exploiting measured vibration information. The identified models refer to mathematical modal models as well as linear finite element models of structures, while the applications cover mainly ground/air vehicles and civil structures. The thesis is divided into three interrelated parts.

Part A: Least-squares optimization methods are introduced for identifying non-classically damped modal models of complex structures using (1) output response measurements obtained from measured excitations at multiple support, and (2) output-only ambient vibration measurements. In the first case, a common structure of the time and frequency formulations is revealed and exploited to develop an identification software common for both formulations. The measure of fit represents the difference between the measured response time histories (or their Fourier transform) and the response time histories (or their Fourier transforms) predicted by a modal model when subjected to multiple support measured excitations. In the second case, the measure of fit represents the difference between measured and modal model predicted cross power spectral density functions. Computationally efficient two-step and three-step algorithms are developed to solve the resulting highly non-convex nonlinear optimization problems and identify the modal characteristics such as number of contributing models, modal frequencies, modal damping ratios, modeshapes and modal participation factors or operational reference vectors. The two-step approach is a very fast and accurate non-iterative algorithm, involving solution of two linear systems and singular value decomposition operations for estimating the modal characteristics. The third step solves the original nonlinear optimization problem using the estimates from the two-step approach to notably accelerate convergence of gradient based optimization algorithms. It is demonstrated that the third step is required only for closely spaced and overlapping modes to improve the estimates of the modal characteristics. The proposed methodology automates the estimation of the modal characteristics without, or with minimal, user interference and thus is especially applicable to continuous, real-time, structural health monitoring purposes.

Part B: The problem of finite element structural model updating and response prediction variability based on measured modal characteristics is revisited. The correspondence between the recently proposed multi-objective identification, the conventional single-objective weighted residuals identification and the Bayesian statistical identification is established. These methods result in multiple Pareto optimal finite element models. An optimally weighted modal residuals method is also proposed for selecting the most preferred Pareto optimal model. The variability of these optimal models depends on the model and measurement error and affects the variability in the response predictions. In particular, Bayesian statistical identification offers the advantage of quantifying the uncertainty in the Pareto optimal models and the response predictions. Theoretical and computational issues arising in multi-objective and single-objective identification are addressed, including issues related to estimation of global optima, convergence of the

proposed algorithms, and identifiability. Hybrid methods are proposed to identify global optima and the normal boundary intersection method is adopted to efficiently estimate the Pareto front and the Pareto optimal models. Finally, computational efficient algorithms are developed for estimating the gradients and the Hessians of the single and multiple objectives based on Nelson's method for finding the sensitivity of eigenproperties to model parameters. It is shown that the computation time for estimating the Pareto optimal models is independent of the number of model parameters involved. The simplified computation of the Hessians of the objectives is useful in the Bayesian asymptotic formulas quantifying the uncertainty in the Pareto optimal models. Particular emphasis is also given in generalizing the definition of objectives in model updating methods to face the severe problems of corresponding measured and model predicted modes encountered for closely spaced modes. Theoretical and computational issues are illustrated by applying the model updating methodologies to small-scale three-story laboratory steel building structure and small-scale vehicle structure using experimentally obtained modal data. Validation studies are performed to show the applicability of the methodologies, the advantages of the multi-objective identification, and the performance of the most preferred Pareto optimal model. The effect of model error uncertainty on model updating and model response prediction variability is assessed.

Part C: A novel methodology is presented for estimating damage accumulation due to fatigue in the entire body of a metallic structure using output-only vibration measurements from a sensor network installed at a limited number of structural locations. Available frequency domain stochastic fatigue methods based on Palmgren-Miner damage rule, S-N fatigue curves on simple specimens subjected to constant amplitude loads, and Dirlik's probability distribution of the stress range are used to predict the expected fatigue damage accumulation of the structure in terms of the power spectral density (PSD) of the stress processes. The PSD of stresses at unmeasured locations covering the entire body of the structure are estimated from the response time history measurements available at the limited measured locations using Kalman filter and a dynamic model of the structure. The accuracy of the Kalman filter predictions can be improved by integrating the model updating techniques developed in Part B. The effectiveness and accuracy of the proposed formulation is demonstrated using a multi-degree-of-freedom spring-mass chain model arising from structures that consist of members with uniaxial stress states.

Contents

List of Figures

List of Tables

Chapter 1

Introduction

1.1 Research context

Mathematical or physics-based models (e.g. modal models or finite element models) are widely used to represent the dynamic behaviour of a structure. However, it is always observed that the initial model developed is often a poor reflection of the observed structural behavior, particularly in the field of structural dynamics. This is due to uncertainties that arise from the simplified assumptions and idealizations used for developing models for simulating the behaviour of engineering structures, as well as models for simulating the loads (mechanical, thermal, etc) that are applied on the structures. These uncertainties include:

Modelling uncertainties: arising in modelling the constitute behaviour of materials, the damage mechanisms (e.g. due to fatigue, corrosion), the support conditions of structures and their interaction with their environment, the connection between structural members (fixity conditions, friction mechanisms, impact phenomena), the geometric variability due to manufacturing processes.

Loading uncertainties: arising from the lack of detailed knowledge of the spatial and temporal variation of the forces (mechanical, thermal, etc) applied to engineering structures. Examples include spatial variability of road roughness affecting the dynamics of vehicles, spatial and temporal variability of earthquake-induced excitations on civil engineering structures, turbulent wind loads affecting the design of aircrafts, variability of thermal loads affecting the design of a large class of mechanical and aerospace structures.

Numerical uncertainties: stemming from PDE spatial discretization using finite element methods, temporal discretization used in numerical time integration schemes, rounding-off errors in numerical solutions due to computer inaccuracies.

The uncertainties may affect considerably the prediction of performance and safety of the analyzed systems. Modeling tools and techniques are needed to identify accurate mechanical models taking into account all uncertain factors, properly quantify uncertainties for the purpose of integrating them with the mechanical models, as well as analyze through model simulation the effect of uncertainties on the performance of engineering structures.

Structural identification, in particular, is an inverse problem according to which a model of a structure, usually a modal model for linear structures or a finite element model for linear and nonlinear structures, is adjusted so that either the time histories, frequency response functions, or modal characteristics, simulated from the model, best match the corresponding quantities measured or identified from vibration data recorded during various states of structural operation. This inverse process aims at providing updated models and their corresponding uncertainties in these models based on the available measured data. These updated models are expected to give more accurate response predictions to future loadings, as well as allow for an estimation of the uncertainties associated with such response predictions.

Recently, it has been recognized that the development of reliable algorithms and software that exploit measured data for the updating and validation of mathematical/mechanical models as well as the quantification and propagation of uncertainties in simulations, constitutes one of challenging issues for the advancement of engineering sciences (Oden et al., 2006). In most cases, the model updating/validation is based on simulated data that do not correspond to realistic situations encountered in practical applications. However, even simple models and simulated data present theoretical and computational challenges related to their identification/updating. Greater challenges are expected using real measurements for the updating and validation of complex models that involve a very large number of DOFs.

The objective of this thesis is to confront these challenges and provide solutions to a number of important issues encountered in the identification of models of structures and their use for response/damage predictions, exploiting the information contained in vibration measurements. Novel contributions of this thesis constitute the use of vibration measurements for the improvement of the fidelity of mathematical/mechanical models and estimating the confidence in the response/reliability predictions from these models. Such predictions are important in evaluating the performance and safety of structures and making informed decisions for cost-effective maintenance of these structures.

1.2 Organization of this Thesis

The research work presented in the thesis contributes to three interrelated research areas of model identification and prediction using vibration measurements:

(1) Development of methods for identifying non-classically damped modal models of linear structures, presented in Chapters 2 and 3,

(2) Development of identification methods for finite element model updating and response prediction variability, presented in Chapters 4 and 6, and

(3) Development of methods for predicting the fatigue damage accumulation in the entire body of metallic structures exploiting vibration measurements from a limited number of sensors, presented in Chapter 5.

The analyzed structures are assumed to behave linearly and the identification of finite element models in the second research area is based for convenience on modal properties (modal frequencies and modeshapes) identified from the measured excitation/response time history. Modal identification methods required to give accurate estimates of these modal characteristics are thus developed in the first research area. New contributions in this direction are provided for the case of input-output vibration measurements as well as the case of output-only vibration measurements. Emphasis is also given in the integration of the information contained in vibration measurements for making informed response predictions using the identified mechanical models. In the third research area, a problem that is formulated and solved for the first time is related to

the estimation of fatigue damage accumulation in the entire body of a metallic structure using ambient vibration measurements collected from a limited number of sensors placed on the structure. The application areas of this research are mainly related to ground/air vehicle and civil structures. Emphasis though is given to applications on ground vehicles.

A more detailed overview of the contents of this thesis is given in the following.

In Chapter 2, time and frequency domain least squares methods for the identification of non-classically-damped modal models of linear structures using multiple-support excitations and multiple responses are proposed. The methods are extension of the Beck (1978) and McVerry (1980) algorithms developed for classically-damped modal models. The identification involves the estimation of the number of contributing modes, the modal frequencies, the modal damping ratios, the modeshapes, the modal participation factors, the pseudo-response matrix, and the initial conditions of the contributing modes. A common structure of the response in the time and frequency domains is revealed and exploited to develop an identification method common for both time and frequency domain formulations. Novel computationally efficient algorithms for solving the resulting highly non-convex nonlinear optimization problems proposed that result in automatically estimating the number of contributing modes, as well as the modal frequencies, modal damping ratios, modeshapes and modal participation factors of the physical modes without or minimal user intervention. Specifically, a three-step approach is proposed to carry out efficiently the optimization. The proposed algorithms for identifying non-classically damped models are applicable to the cases where the damping is not proportionally distributed through out a structure. The computational efficiency and the accuracy of the modal identification methods developed are illustrated using input-output acceleration measurements from a bridge structure subjected to multi-support earthquake excitations.

The methodologies and computational algorithms presented in Chapter 2 are extended in Chapter 3 to develop frequency domain least squares methods for the identification of non-classically damped modal models of linear structures using ambient vibration measurements. The identification is based on minimizing the square difference between the measured CPSD matrix estimated from the available output only measurements and the CPSD matrix predicted by a non-classically damped modal model. The identification involves the estimation of the number of contributing modes, the modal frequencies, the modal damping ratios and the complex modeshapes of the contributing modes. Computational efficient algorithms for solving the resulting, highly non-convex, nonlinear optimization problem is proposed that result in automatically estimating the number of contributing modes, as well as the modal frequencies, the damping ratios and the modeshapes of the physical modes without or minimal user intervention. A three-step approach was proposed to carry out efficiently the optimization. The effectiveness, computational efficiency and accuracy of the develoepd algorithms are illustrated using simulated ambient vibration data from simple structural models subjected to unknown white noise excitations and real measured data from a full scale bridge structure subjected to ambient wind excitations.

In Chapter 4, the problem of finite element model updating using vibration measurements is addressed. The updating is based on the modal characteristics obtained from vibration

measurements using the modal identification methodologies presented in Chapters 2 and 3. Thus, the model updating methodologies are concentrated on structures that behave linearly. Modal grouping schemes are introduced along with modal residuals norms measuring the fit between the measured and model predicted modal properties. The structural model updating problem is first formulated as a multi-objective optimization problem and then as a single-objective optimization with the objective formed as a weighted average of the multiple objectives using weighting factors. The multi-objective identification method characterizes and computes all Pareto optimal models from a model class, consistent with the measured data and the residuals used to measure the fit between the measured and model predicted modal properties. The similarities with and differences from the conventional weighted modal residuals method is established. The problem of rationally estimating the optimal values of the weights or, equivalently, selecting the most probable structural model among the Pareto optimal models utilising the available measured data is addressed. A rational approach for chossing an optimal weight value for carrying out the model updating is proposed based on the measured modal data. Thus, the selection of the optimal structural model is based on weight values that are estimated based on the data, avoiding an arbitrary a priori selection of these weight values. This optimal weight value is shown to arise from the application of a Bayesian statistical framework for model selection. The Bayesian framework also quantifies the uncertainty in the Pareto optimal models by updating the probability distribution of the weights using the modal data. Emphasis is also given in addressing theoretical and computational issues associated with solving the resulting multi-objective and single-objective optimization problems, including important issues related to estimation of global optima, convergence of the proposed algorithms, and identifiability. Novel computationally efficient algorithms are also proposed for estimating the gradients and the Hessians of the objective functions using the Nelson's method (Nelson, 1976) for finding the sensitivities of the eigenproperties to model parameters. Theoretical and computational issues are demonstrated by updating simple and higher fidelity model classes using experimental data from two configurations of a scaled three-story steel structure.

In chapter 5 addresses the problem of estimating the expected damage accumulation or remaining lifetime due to fatigue in the entire body of a metallic structure using output-only vibration measurements obtained from a sensor network installed at a limited number of structural locations. Available frequency domain stochastic fatigue methods based on Palmgren-Miner damage rule, S-N fatigue curves on simple specimens subjected to constant amplitude loads, and Dirlik's probability distribution of the stress range are used to predict the expected fatigue damage accumulation of the structure in terms of the power spectral density (PSD) of the stress processes. The PSD of stresses at unmeasured locations are estimated from the response time history measurements available at the limited measured locations using Kalman filter and a dynamic finite element model of the structure. The effectiveness and accuracy of the proposed formulation is demonstrated using a multi-degree-of-freedom spring-mass chain model arising from structures that consist of members with uniaxial stress states.

In Chapter 6 vibration experiments from a scaled vehicle model carried out in the Machine Dynamics Laboratory of the Department of Mechanical Engineering in Aristotle University were used to explore and compare the applicability and effectiveness of the proposed methods for

system identification and structural model updating and to develop high fidelity finite element models of the experimental vehicle using acceleration measurements. The identification of modal characteristics of the vehicle is based on acceleration time histories obtained from impulse hammer tests. Modal identification methodologies are used to obtain the modal characteristics from the analysis of the various sets of vibration measurements. The modal characteristics are then used to update an increasingly complex set of finite element models of the vehicle. A detailed finite element model of the vehicle developed using shell elements. The multi-objective structural identification method developed in Chapter 4 is used for estimating the optimal finite element structural models based on minimizing the modal residuals. Varius parameterization schemes are introduced and their affect on the updating results, the fidelity of the optimal finite element models, as well as the variability and uncertainty in response predictions from these finite element models are explored. The sources of these variabilities in the finite element model and thei response prediction are identified.

Finally, Chapter 7 summarizes the conclusions and the novel contributions of this work. Also it presents suggestions for future research on issues related to this thesis.

Chapter 2

Least squares identification of non-classically damped modal models of structures subjected to multiple support excitations

2.1 Introduction

The evaluation of the actual dynamic characteristics of engineering structures through measurements of their dynamic response has been attracting an increasing research effort worldwide. Measured response data of civil engineering structures (e.g. bridges, buildings, dams, towers and offshore structures) from earthquake-induced vibrations, and vehicles from vibrations induced by road roughness, offer an opportunity to study quantitatively and qualitatively their dynamic behaviour within the resulting vibration levels. These vibration measurements can be processed for the estimation of the modal characteristics of these structures, as well for the calibration of corresponding (finite element) models used to simulate their behaviour. The information for the identified modal models and the updated finite element models is useful for validating the assumptions used in model development or for improving modelling, analysis and design procedures. Also, such information is useful for structural health monitoring purposes.

This chapter is concerned with the development methods for identifying the modal characteristics of vehicle and civil engineering structures based on vibration measurements that are caused by multiple support excitations. The evaluation of the actual dynamic characteristics of engineering structures through measurements of their dynamic response has been attracting an increasing research effort worldwide (Wilson, 1986; Werner et al., 1987; Safak, 1995; Lus et al., 1999; Chaudhary et al., 2000; Chaudhary et al., 2002; Smyth et al., 2003; Arici and Mosalam, 2003; Lin et al., 2005; Liu et al., 2005; Siringoringo and Fujino, 2007). For earthquake-induced vibrations on civil structures and for road roughness induced vibrations on vehicles, the modal characteristics are estimated from the measured acceleration excitations occurred at the multiple supports of the structure and the measured vibration responses. It has been observed from response measurements of these structures that their dynamic properties are markedly different during response to strong motion than in small amplitude ambient and forced vibration tests. Hence, it is of considerable interest and importance to extract information about structural behaviour from strong motion data.

Modal identification algorithms provide estimates of the modal frequencies, modal damping ratios, modeshapes at the measured DOFs and modal participation factors using classically-damped or non-classically damped modal models. For the case of earthquake-induced vibrations, modal identification methods have been developed in time domain (Beck, 1978; Beck and Jennings, 1980) and in frequency domain (McVerry, 1980), based on a minimization of the measure of fit between the time history or its Fourier transform of the acceleration responses estimated from the measurements and the corresponding ones predicted from a classically-damped modal model of the structure. Beck (1978) and Beck and Jennings (1980), had presented an output-error approach for the identification of linear, time-invariant models from strong motion records, through the minimization of a measure of fit including displacement, velocity and acceleration records.

McVerry (1980), has applied an output-error approach in the frequency domain, using the Fast Fourier Transform of the acceleration response time histories to estimate the modal properties through least-squares matching. These methods have been applied to identify the modal characteristics of bridges (Werner et al., 1987; Chaudhary, 2002) and buildings (Papageorgiou and Lin, 1989) by processing input-output earthquake recordings. Werner et al. (1987) formulated a methodology in the time domain for the case of measured input excitation, such as earthquake excitation, for an elastic system with classical normal modes and with motion measurements from any number of input and system response degrees of freedom. Their procedure was an extension of the least-squares-output-error method which was used by Beck (1978).

Extensions for identifying non classically-damped modal models in the frequency domain have also been developed by Chaudhary et al. (2000). Tan and Cheng (1993) proposed an iterative identification algorithm, which was based on the modal sweep concept and the band-pass filtering process, to identify the modal parameters of a non-classically damped linear structure from its recorded earthquake response. Mahmoudabadi et al. (2006) developed a method for parametric system identification in frequency domain for classically and non-classically damped linear systems subjected up to six components of earthquake ground motions, which is able to work in multi-input/multi-output (MIMO) case.

Most of the aforementioned methods, although they have developed for earthquake engineering applications, they are also in principle applicable to aerospace and vehicle engineering to identify modal models from input-output vibration measurements of various structural components induced by multiple support excitations. A particular example is the modal identification of the vehicle body using multi-support input acceleration measurements at the connections of the vehicle body with the suspensions and output acceleration measurements at various locations of the vehicle body.

The methods developed by McVerry (1980) in the frequency domain and Beck and Jennings (1980) in the time domain, are extended in this work to treat non-classically damped modal models, since damping may not be proportionally distributed in various structural components. For the special case of bridges, non - proportionally damping appears due to the energy dissipation mechanism provided locally by the elastomeric bearings and the foundation soil. For base isolated buildings, non proportional damping may appear due to the energy dissipation mechanism provided locally by the isolation system. For vehicles, non-proportional damping may result from the damping mechanisms provided locally by the front and rear suspension systems. Least-squares output-error methods are used in which the optimal values of the modal parameters are obtained by minimizing the discrepancy between measured responses and the predicted responses of the system. Time domain output error methods process the response time histories measured from a network of sensors (e.g. accelerometers), while frequency domain output error methods process the Fourier transforms of the measured response time histories.

A novel aspect of this study is the use of a three step approach to solve the resulting highly non-convex nonlinear optimization problem. The first step provides estimates of the modal frequencies and modal damping ratios by solving a system of linear algebraic equations. Stabilization diagrams are used to identify the number of contributing modes by distinguishing

between physical and mathematical modes. The second step provides estimates of the modeshapes and the participation factors by solving a system of linear algebraic equations for the modal residue matrices of the contributing modes and using singular value decomposition to estimate the complex modeshapes and modal participation factors. The first two steps usually give accurate estimates of the modal characteristics. A third step is added to improve the estimates of the modal characteristics by efficiently solving the full nonlinear optimization problem with initial estimates of the modal parameters those obtained from the first and second steps. The gradients of the objective function with respect to the parameters are obtained analytically in order to significantly accelerate the convergence of the optimization in the third step. The effectiveness of the proposed methodology is illustrated applied to earthquake recordings available from a full-scale reinforced concrete bridge.

This Chapter is organised as follows. The state space formulation of the equation of motion of structures subjected to multi-support excitations is presented in Section 2.2. The formulation of the response in terms of the modal characteristics of the non-classically damped modal model is presented in Sections 2.3. A common structure of the response in time and frequency domain is revealed that is useful in the unification of the identification algorithms for the time and frequency domain formulations. Section 2.4 formulates the identification of the modal characteristics as a least squares optimization problem, while Section 2.5 presents efficient optimization algorithms for estimating the modal characteristics. The effectiveness of the proposed methodology in terms of the accuracy and computational efficiency is demonstrated in the application Section 2.6. The conclusions of this work are summarized in Section 2.7.

2.2 State space formulation of equations of motion

Consider a structure that is subjected to multiple support (base) excitations. The equations of motion for the structure, assumed to behave within the linear range, can be derived using a spatial discretization method, such as finite element analysis. Let $M \in \mathbb{R}^{n\times n}$, $C_0 \in \mathbb{R}^{n\times n}$ and $K \in \mathbb{R}^{n\times n}$ be the fixed-support mass, damping and stiffness matrices, respectively, of a finite element model of the structure, $\underline{y}_s(t) \in \mathbb{R}^n$ be the response at the DOFs of the mathematical model of the structure and $\ddot{\underline{z}}(t) \in \mathbb{R}^{N_{in}}$ be the displacement of the supports DOFs, where n is the number of model DOFs and N_{in} is the number of excitation DOFs at the supports (bases). The response $\underline{y}_s(t)$ of the finite element model of the structure is given by (Clough and Penzien, 1993; Werner et al., 1987)

$$\underline{y}_s(t) = \underline{s}(t) + \underline{q}(t) \tag{2.1}$$

where $\underline{s}(t)$ is the pseudostatic component and $\underline{q}(t)$ is the dynamic component of the response. The pseudostatic component of the response represents the ‘static’ contributions of the individual support motions to the system response and it is given by

$$\underline{s}(t) = D\,\underline{z}(t) \tag{2.2}$$

where $D = -K^{-1} K_{sb}$ is the pseudostatic matrix, which expresses the responses in all degrees of freedom due to unit support motions, where K_{sb} is the stiffness matrix that couples the system and base degrees of freedom (DOFs).

The dynamic component $\underline{q}(t)$ in (2.1) accounts for the contributions of the system's fixed-base modal vibrations about its pseudostatic reference position. The equation of motion for the dynamic response component (part) of the response is given by

$$M\,\ddot{\underline{q}}(t) + C_0\,\dot{\underline{q}}(t) + K\,\underline{q}(t) = L\ddot{\underline{z}}(t) \tag{2.3}$$

where $L = -(M\,D + M_{sg})$, and M_{sg} is the mass matrix that couple the system and base degrees of freedom (DOFs). Throughout the analysis, it is assumed that the system matrices M, C_0 and K are symmetric.

In the general case of a non-classically damped structure, the set of equations (2.3) must be converted to a set of first order state space formulation. This is accomplished by introducing the state vector $\underline{x} = [\underline{q}^T \quad \dot{\underline{q}}^T]^T$. Equations (2.3) along with the complementary equation $M\,\dot{\underline{q}}(t) = M\,\dot{\underline{q}}(t)$ can be written in the state space form

$$P\dot{\underline{x}} + Q\underline{x} = \begin{bmatrix} L \\ 0 \end{bmatrix} \ddot{\underline{z}}(t) \tag{2.4}$$

where the matrices P and Q are given by

$$P = \begin{bmatrix} C_0 & M \\ M & 0 \end{bmatrix}, \quad \mathrm{Q} = \begin{bmatrix} K & 0 \\ 0 & -M \end{bmatrix} \tag{2.5}$$

Let $\underline{y}(t) \in \mathbb{R}^{N_{out}}$ be the observation vector containing the measured output acceleration responses, given in general by

$$\underline{y}(t) = C_\alpha \ddot{\underline{y}}_s(t) = C_c\,\underline{x} + D_c\,\ddot{\underline{z}}(t) \tag{2.6}$$

where $C_\alpha \in \mathbb{R}^{N_{out} \times n}$ is a matrix indicating which DOFs are measured (considered in the output measurements). Using (2.1), (2.2), (2.3) and the fact that $L = -(M\,D + M_{sg})$, the matrices C_c and D_c are given by $C_c = -C_\alpha M^{-1}[K \quad C_0] \in \mathbb{R}^{N_{out} \times 2n}$ and $D_c = C_\alpha (M^{-1}L + D) = -C_\alpha M^{-1} M_{sb} \in \mathbb{R}^{N_{out} \times N_{in}}$

2.3 Non-classically damped modal models

Modal analysis is used to describe the response at the measured (observable) degrees of freedom of the structure in terms of the complex eigenproperties (eigenvalues and eigenvectors) and the excitation. The analysis is used in subsequent Sections for solving the inverse problem of identifying the eigenproperties given input-output measurements.

2.3.1 Time domain formulation

Let $\underline{\psi}_r \in \mathbb{C}^{2n}$ be the complex eigenvector and λ_r the corresponding compex eigenvalue satisfying the eigenproblem associated with the system (2.4), i.e.

$$(P\lambda + Q)\underline{\psi} = \underline{0} \tag{2.7}$$

Introducing the eigenmatrix $\Psi = \left[\underline{\psi}_1 \quad \cdots \quad \underline{\psi}_n \, \underline{\psi}_1^* \quad \cdots \quad \underline{\psi}_n^*\right] \in \mathbb{C}^{2n\times 2n}$, where the superscript <*> denotes complex conjugate, it can easily be shown (Natsiavas, 1999) that the eigenmatrix Ψ is partitioned in the form

$$\Psi = \begin{bmatrix} \Phi & \Phi^* \\ \Phi\Lambda & \Phi^*\Lambda^* \end{bmatrix} \in \mathbb{C}^{2n\times 2n} \tag{2.8}$$

where $\Phi \in \mathbb{C}^{n\times n}$ is the eigenmatrix associated with the displacement DOFs $\underline{q}(t)$ of the state vector $\underline{x}(t)$. The complex eigenvectors satisfy the orthogonality condition $\Psi^T P \Psi = diag\left[\alpha_r\right]$ and $\Psi^T P \Psi = diag\left[\beta_r\right]$. The matrix $\Lambda = diag(\lambda_r) \in \mathbb{C}^{n\times n}$ is a diagonal matrix with diagonal elements the complex eigenvalues $\lambda_r = -\beta_r / \alpha_r$ represented in the form

$$\lambda_r = -\zeta_r\omega_r \pm j\omega_r\sqrt{1-\zeta_r^2} = -a_r \pm jb_r, \qquad r = 1,\ldots,m \tag{2.9}$$

with the modal frequency ω_r and the modal damping ratio ζ_r satisfying $\omega_r = \left|\lambda_r\right|$ and $\zeta_r = -\mathrm{Re}\left\{\lambda_r\right\} / \omega_r$. The parameters $\alpha_r = \zeta_r\omega_r$ and $b_r = \omega_r\sqrt{1-\zeta_r^2}$ are expressed in terms of the modal frequency ω_r and the modal damping ratio ζ_r. Given α_r and b_r in (2.9), the modal frequency ω_r and the damping ratio ζ_r are obtained from the following relationships $\omega_r = \sqrt{a_r^2 + b_r^2}$ and $\zeta_r = a_r / \sqrt{a_r^2 + b_r^2}$.

For the realization of modal analysis method the following transformation is introduced

$$\underline{x}(t) = \Psi \begin{Bmatrix} \underline{\xi}(t) \\ \underline{\xi}^*(t) \end{Bmatrix} \tag{2.10}$$

where $\underline{\xi} = [\xi_1(t), \cdots, \xi_m(t)]^T \in \mathbb{C}^m$ is the vector of the main modal coordinates. Using conventional modal analysis, the vector $\underline{y}(t;\underline{\theta})$ in (2.6) of the acceleration responses at the N_{out} measured degrees of freedom, based on the non-classically damped modal models, can be written in the form

$$\underline{\ddot{y}}(t) = U\underline{\xi}(t) + U^*\underline{\xi}^*(t) + D_c\underline{\ddot{z}}(t) = \sum_{r=1}^{m}[\underline{u}_r\xi_r(t) + \underline{u}_r^*\xi_r^*(t)] + D_c\underline{\ddot{z}}(t) \tag{2.11}$$

where the complex-valued modal coordinates $\xi_r(t)$, $r = 1, \cdots, m$, satisfy the complex modal state space equations

$$\dot{\xi}_r(t) = \lambda_r\xi_r(t) + \underline{l}_r^T\underline{\ddot{z}}(t) \tag{2.12}$$

$D_c = -C_\alpha M^{-1}M_{sb} \in \mathbb{R}^{N_{out}\times N_{in}}$ is a real matrix,

$$U \equiv [\underline{u}_1, \cdots, \underline{u}_m] = C_c\begin{bmatrix}\Phi \\ \Phi\Lambda\end{bmatrix} = C_\alpha\Phi\Lambda^2 \in \mathbb{C}^{N_{out}\times m} \tag{2.13}$$

is the matrix of the complex eigenvectors $\underline{u}_r = \lambda_r^2 C_\alpha\underline{\phi}_r \in \mathbb{C}^{N_{out}}$, $r = 1, \cdots, m$, at N_{out} DOFs, and $\underline{l}_r^T = (1/\alpha_r)\underline{\phi}_r^T L \in \mathbb{C}^{1\times N_{in}}$ is the complex vector of the modal participation factors relating the N_{in} inputs to the r mode of the system. The modal response $\xi_r(t)$ can be obtained by solving (2.12) using the complex-valued initial condition $\xi_r(0)$. From the modal formulation, it is evident that the parameter set $\underline{\theta} = \left\{\lambda_r, \underline{u}_r, \underline{l}_r^T, \xi_r^0, r = 1, ..., m, D_c\right\}$ completely defines the acceleration response at the measured DOFs using m complex modes.

Alternatively, the acceleration response can be conveniently written in the form

$$\underline{y}(t) = \sum_{r=1}^{m}[\underline{u}_r\underline{l}_r^T\underline{\eta}_r(t) + \underline{u}_r^*\underline{l}_r^{*T}\underline{\eta}_r^*(t)] + D_c\underline{\ddot{z}}(t) \tag{2.14}$$

where the modal vector $\underline{\eta}_r(t)$ satisfies the modal vector equation

$$\dot{\underline{\eta}}_r(t) = \lambda_r\underline{\eta}_r(t) + \underline{\ddot{z}}(t) \tag{2.15}$$

which is solved using the non-zero initial conditions $\underline{\eta}_r(0)$ with $\xi_r(0) = \underline{l}_r^T\underline{\eta}_r(0)$.

Alternatively, the acceleration response can be conveniently written in the form

$$\underline{y}(t) = \sum_{r=1}^{m}[\underline{u}_r\underline{l}_r^T\underline{\eta}_r(t) + \underline{u}_r^*\underline{l}_r^{*T}\underline{\eta}_r^*(t)] + D_c\underline{\ddot{z}}(t) + \sum_{r=1}^{m}[\underline{u}_r\xi_r(0)e^{\lambda_r t} + \underline{u}_r^*\xi_r^*(0)e^{\lambda_r^* t}] \tag{2.16}$$

where the modal vector $\underline{\eta}_r(t)$ satisfies the modal vector equation (2.15) which is solved using zero initial conditions $\underline{\eta}_r(0) = \underline{0}$.

2.3.2 Frequency domain formulation

The finite Fourier transform (FT) $\hat{f}(\omega)$ of a function $f(t)$ over a time segment T is defined by

$$\hat{f}(\omega) = \int_0^T f(t) e^{-j\omega t} dt \tag{2.17}$$

Using the fact that the finite FT $\hat{\dot{\xi}}_r(\omega)$ of the derivative $\dot{\xi}_r(t)$ of a function $\xi_r(t)$ is related to the FT $\hat{\xi}_r(\omega)$ of the function $\xi_r(t)$ as

$$\hat{\dot{\xi}}_r(\omega) = \int_0^T \dot{\xi}_r(t) e^{-j\omega t} dt = e^{-j\omega T} \xi_r(\mathrm{T}) - \xi_r(0) + j\omega \hat{\xi}_r(\omega) \tag{2.18}$$

and applying FT to both sides of (2.11) and (2.12), one has that the FT $\hat{\underline{y}}(\omega)$ of the response $\underline{y}(t)$ is related to the FT $\hat{\underline{\ddot{z}}}(\omega)$ of the excitation by

$$\begin{aligned} \hat{\underline{y}}(\omega) = & \left[\sum_{r=1}^{m} \left(\frac{\underline{u}_r \underline{l}_r^T}{j\omega - \lambda_r} + \frac{\underline{u}_r^* \underline{l}_r^{*T}}{j\omega - \lambda_r^*} \right) + D_c \right] \hat{\underline{\ddot{z}}}(\omega) - \sum_{r=1}^{m} \left[\frac{\underline{u}_r \xi_r(0)}{j\omega - \lambda_r} + \frac{\underline{u}_r^* \xi_r^*(0)}{j\omega - \lambda_r^*} \right] + \\ & e^{-j\omega T} \sum_{r=1}^{m} \left[\frac{\underline{u}_r \xi_r(\mathrm{T})}{j\omega - \lambda_r} + \frac{\underline{u}_r^* \xi_r^*(\mathrm{T})}{j\omega - \lambda_r^*} \right] \end{aligned} \tag{2.19}$$

2.3.3 Common structure of response in time and frequency domain

Comparing the structure of equations (2.16) and (2.19), it should be noted that for either the time or the frequency domain formulation the acceleration response vector $\underline{y}(t)$ at time $t = k\Delta t$ or its Fourier tranform $\hat{\underline{y}}(\omega)$ at frequency component $\omega = k\Delta\omega$, where Δt is the discretization step (sampling time interval), $\Delta\omega$ is the sampling frequency interval and k is a time or frequency index set, can be written in the common form

$$\begin{aligned} \underline{y}_k(\underline{\theta}) = & \sum_{r=1}^{m} [\underline{u}_r \underline{l}_r^T \underline{\eta}_k(\lambda_r) + \underline{u}_r^* \underline{l}_r^{*T} \underline{\eta}_k(\lambda_r^*)] + D_c \underline{\ddot{z}}_k \\ & + \sum_{r=1}^{m} [(\underline{\alpha}_r + \underline{b}_r e^{-jk\Delta\omega T}) A_k(\lambda_r) + (\underline{\alpha}_r^* + \underline{b}_r^* e^{-jk\Delta\omega T}) A_k(\lambda_r^*)] \end{aligned} \tag{2.20}$$

where for the time domain formulation, $\underline{y}_k(\underline{\theta})$ represents the acceleration response $\underline{y}(k\Delta t)$, $\underline{\eta}_k(\lambda_r)$ is given by the solution of the modal equation (2.15) with zero initial conditions, $\underline{\alpha}_r = \underline{u}_r \xi_r(0) \in \mathbb{C}^{N_{out}\times 1}$, $\underline{b}_r = \underline{0} \in \mathbb{C}^{N_{out}\times 1}$,

$$A_k(\lambda_r) = e^{\lambda_r k\Delta t} \qquad \text{and} \qquad \underline{\ddot{z}}_k = \underline{\ddot{z}}(k\Delta t) \tag{2.21}$$

while for the frequency domain formulation, $\underline{y}_k(\underline{\theta})$ represents the Fourier transform $\underline{\hat{y}}(k\Delta\omega)$ of the acceleration response $\underline{y}(t)$, $\underline{\alpha}_r = \underline{u}_r \xi_r(0) \in \mathbb{C}^{N_{out}\times 1}$, $\underline{b}_r = -\underline{u}_r \xi_r(T) \in \mathbb{C}^{N_{out}\times 1}$,

$$\underline{\eta}_k(\lambda_r) = \frac{\underline{\hat{\ddot{z}}}(k\Delta\omega)}{jk\Delta\omega - \lambda_r}, \qquad A_k(\lambda_r) = -\frac{1}{jk\Delta\omega - \lambda_r} \qquad \text{and} \qquad \underline{\ddot{z}}_k = \underline{\hat{\ddot{z}}}(k\Delta\omega) \tag{2.22}$$

It should be noted that for the time domain formulation, the following expressions hold true: $A_k(\lambda_r^*) = A_k^*(\lambda_r)$ and $\underline{\eta}_k(\lambda_r^*) = \underline{\eta}_k^*(\lambda_r)$.

Note that the parameter set $\underline{\theta}$ has been introduced in (2.20) to include all the necessary modal and other variables that completely define the response vector $\underline{y}_k$. From the structure of the response function in (2.20), the parameter set $\underline{\theta}$ includes the modeshapes $\underline{u}_r$, the participation vectors $\underline{l}_r^T$, the eigenvalues λ_r, the elements of the real matric D_c, and the initial conditions $\underline{\alpha}_r$ and $\underline{b}_r$.

Note that consistent estimates of $\underline{\alpha}_r$ and $\underline{b}_r$ should give $\underline{u}_r = \underline{\alpha}_r / \xi_r(0) = -\underline{b}_r / \xi_r(T)$ or equivalently $\underline{\alpha}_r = -[\xi_r(0)/\xi_r(T)]\underline{b}_r$, something that will be violated in practical applications due to model error and measurement noise.
Also, introducing the functions

$$g_k(\underline{\theta}_r^a) = \underline{l}_r^T \underline{\eta}_k(\lambda_r) + [\xi_r(0) - \xi_r(T)e^{-jk\Delta\omega T}]A_k(\lambda_r) \tag{2.23}$$

$$h_k(\underline{\theta}_r^a) = \underline{l}_r^{*T} \underline{\eta}_k(\lambda_r^*) + [\xi_r^*(0) - \xi_r^*(T)e^{-jk\Delta\omega T}]A_k(\lambda_r^*) \tag{2.24}$$

equation (2.20) can also be written in an alternative convenient form

$$\underline{y}_k = \sum_{r=1}^{m} [\underline{u}_r g_k(\underline{\theta}_r^a) + \underline{u}_r^* h_k(\underline{\theta}_r^a)] + D_c \underline{\ddot{z}}_k \tag{2.25}$$

where the parameter set $\underline{\theta}_r^a$ is defined by

$$\underline{\theta}_r^a = (\underline{l}_r, \lambda_r, \xi_r(0), \xi_r(T)) \tag{2.26}$$

The importance of the alternative form (2.25) will be made clear in the next section

2.4 Least-squares identification of structural modes

A modal model output least-squares error identification approach seeks the optimal values of the parameter set $\underline{\theta}$ that minimize a measure of fit between the modal model predictions $\underline{y}_k\left(\underline{\theta}\right)$, $k=1,\cdots,N$ and the corresponding response $\underline{\hat{y}}_k$ estimated from the measured data. That is, the modal model identification is formulated as a minimization problem of finding the values of $\underline{\theta}$ that minimizes the weighted measure of fit

$$J\left(\underline{\theta}\right)=\frac{1}{V}\sum_{k=0}^{N}\left[\underline{\varepsilon}_k^{NL}\right]^T W\left[\underline{\varepsilon}_k^{NL}\right]=\frac{1}{V}\sum_{k=0}^{N}\left\|\underline{\varepsilon}_k^{NL}\right\|^2 \tag{2.27}$$

where the error $\underline{\varepsilon}_k^{NL}\left(\underline{\theta}\right)$ between the measured and modal model predicted responses

$$\underline{\varepsilon}_k^{NL}\left(\underline{\theta}\right)=\underline{y}_k\left(\underline{\theta}\right)-\underline{\hat{y}}_k \tag{2.28}$$

is a nonlinear fucntion of the parameter set $\underline{\theta}$, N is the number of sample data over the analysed time period T, and $V=\sum_{k=0}^{N}\left\|\underline{\hat{y}}_k\right\|^2$ is the normalization factor, and $\left\|\underline{y}\right\|^2=\underline{y}^T W\underline{y}$ with $W\in\mathbb{R}^{N_{out}\times N_{out}}$ being a user selected weighting matrix. Herein, it is selected to be the identity matrix, $W=I$.

2.5 Optimization algorithm

A three step approach is used to estimate the modal properties by solving the least-squares optimization problem. The first step provides estimates of the modal frequencies and modal damping ratios by re-formulating the objective (error) function in a convenient way so that these modal properties can be obtained by solving a system of linear algebraic equations using the common denominator model (Heylen et al., 1997). Stabilization diagrams are also used as part of the approach to distinguish between physical and mathematical modes and automatically estimate the number of contributing modes. This first step is an extension of the PolyMAX or polyreference least-squares complex frequency domain method, developed by Peeters et al. (2004). It is employed herein to treat non-classically damped modal models describing the system's response characteristics based on earthquake-induced vibration data. The second step provides estimates of the modeshapes and the participation factors given the estimates of the modal frequencies and modal damping ratios obtained in the first step, by solving a system of linear algebraic equations. It should be noted that two different approaches have been developed for the computation of the modeshapes and participation factors in this second step. The first approach is based on the form (2.20) for the response predictions $\underline{y}_k\left(\underline{\theta}\right)$ with unknown parameters to be the residues $R_r=\underline{u}_r\underline{l}_r^T\in\mathbb{C}^{N_{out}\times N_{in}}$, the real matrix D_c and the vectors $\underline{\alpha}_r$ and $\underline{b}_r$. Noting that the objective function is quadratic in these parameters, one can apply the stationarity conditions to estimates these residue terms by solving a system of linear algebraic

equations. Then noting that residue terms admit the representation $R_r = \underline{u}_r \underline{l}_r^T$, the modeshapes and the participation factors are derived directly by the Singular Value Decomposition (SVD) for the resulting numerator matrix R_r. The second approach is based on the form (2.25) for the response predictions $\underline{y}_k(\underline{\theta})$. Advantage is taken of the fact that the error function is quadratic with respect to the modeshapes $\underline{u}_k$ and the real matrix D_c. The modeshapes are computed by taking stationary conditions that lead to a linear system of equations from which the modeshapes $\underline{u}_k$ and the elements of the matrix D_c are readily derived with respect to the system parameters in $\underline{\theta}^a = (\underline{\theta}_1^a, \cdots, \underline{\theta}_m^a)$, where $\underline{\theta}_r^a$ is defined in (2.26). An optimization with respect to the parameter set $\underline{\theta}^a$ is required in this step. The first two steps usually give accurate estimates of the modal characteristics. However, a third step is often recommended to improve these estimates, especially for closely spaced and overlapping modes, by efficiently solving the full nonlinear optimization problem with initial estimates of the modal parameters those obtained from the first and second steps.

These steps are described in more details in the sub-sections that follow.

2.5.1 Step 1: Identification of contributing modes, modal Frequencies and damping ratios

Consider the frequency domain formulation of the response. Assuming zero initial and final conditions of the response, the FT of the responses in (2.19) can also be written in the form

$$\underline{\hat{y}}(\omega) = \left[\sum_{r=1}^{m} \left(\frac{\underline{u}_r \underline{l}_r^T}{j\omega - \lambda_r} + \frac{\underline{u}_r^* \underline{l}_r^{*T}}{j\omega - \lambda_r^*} \right) + D_c \right] \underline{\hat{z}}(\omega) = H(j\omega) \underline{\hat{z}}(\omega) \tag{2.29}$$

where the frequency response function

$$H(j\omega) = \sum_{r=1}^{m} \left[\left(\frac{\underline{u}_r \underline{l}_r^T}{j\omega - \lambda_r} + \frac{\underline{u}_r^* \underline{l}_r^{*T}}{j\omega - \lambda_r^*} \right) + D_c \right] = \frac{B(s(j\omega))}{A(s(j\omega))} \tag{2.30}$$

is a rational fraction of two polynomials in $s = s(j\omega)$ of order $p = 2m$, of which the denominator polynomial $A(s) \in \mathbb{C}$ given by

$$A(s) = \sum_{r=0}^{p} s^r a_r \tag{2.31}$$

is common for all output quantities, and the numerator polynomial matrix $B(j\omega) \in \mathbb{C}^{N_{out} \times N_{in}}$ is given by

$$B(s) = \sum_{r=0}^{p} s^r \beta_r \tag{2.32}$$

with $s = s(j\omega) = j\omega$ is the polynomial basis in the continuous time formulation and $s = s(j\omega) = \exp(j\omega\Delta t)$ in a discrete time formulation of the system dynamics, while $\underline{\alpha} = (a_0, a_1, \cdots, a_p)^T \in \mathbb{R}^{p+1}$ and $\beta_r \in \mathbb{R}^{N_{out} \times N_{in}}$, $r = 0, \cdots, p$, are the coefficients of the denominator and numerator polynomials, respectively.

Using the relation (2.30), it is clear that the poles of the structure are given by the roots of the denominator $A(s)$. Given the values of the coefficients $\underline{\alpha}$ of the denominator polynomial, these roots are readily obtained by the solution of the eigenvalue problem for the companion matrix (Kailath, 1980; Haylen et al., 1997). So the problem of finding the poles is reduced to the problem of finding the coefficients of the denominator polynomial $A(s) \in \mathbb{C}$. This can be readily done by using the formulation for the FRF in (2.29) and substituting in the error function (2.28) to obtain

$$\underline{\varepsilon}_k^{NL}(\underline{\theta}) = \frac{B(j\omega_k, \beta)}{A(j\omega_k; \underline{\alpha})} \underline{\hat{z}}(\omega_k) - \underline{\hat{y}}_k \tag{2.33}$$

where the parameter set $\underline{\theta}$ consists of the coefficients $\underline{\alpha}$ and β_r, $r = 0, \cdots, p$, of the polynomials. It should be noted that the error function (2.33) is a nonlinear function of $\underline{\alpha}$ and a linear function of β_r, $r = 0, \cdots, p$. Instead of using the nonlinear error function (2.33), one can redefine the error function

$$\underline{\varepsilon}_k^{L}(\underline{\theta}) = A(j\omega; \underline{\alpha}) \underline{\varepsilon}_k^{NL}(\underline{\theta}) = B(j\omega, \beta) \underline{\hat{z}}(\omega) - \underline{\hat{y}}_k A(j\omega; \underline{\alpha}) \tag{2.34}$$

which is a linear function of the parameters $\underline{\alpha}$ and β_r, $r = 0, \cdots, p$. So the optimization problem can be readily solved analytical and obtain the coefficients $\underline{\alpha}$ and β_r, $r = 0, \cdots, p$ from the solution of a linear system of equations. Specifically, replacing $\underline{\varepsilon}_k^{NL}(\underline{\theta})$ in (2.27) by $\underline{\varepsilon}_k^{L}(\underline{\theta})$, carrying out the optimization of (2.27) analytically using the stationarity conditions, and finally eliminating the variables β_r, $r = 0, \cdots, p$ in the resulting linear system, one readily obtains the following reduced system of normal equations for estimating the coefficients $\underline{\alpha}$

$$\left\{ \sum_{o=1}^{N_{out}} \left(\mathrm{T}_o - \mathrm{S}_o^{\mathrm{T}} \mathrm{R}^{-1} \mathrm{S}_o \right) \right\} \underline{\alpha} = 0 \tag{2.35}$$

where R, S_o and T_o, $o = 1, \cdots, N_{out}$, are real matrices defined by

$$R = \mathrm{Re}(Z^{*T} Z) \in \mathbb{R}^{N_{in}(p+1) \times N_{in}(p+1)} \tag{2.36}$$

$$S_o = \mathrm{Re}(Z^{*T} Y_o) \in \mathbb{R}^{N_{in}(p+1) \times (p+1)} \tag{2.37}$$

$$T_o = \mathrm{Re}(Y_o^{*T} Y_o) \in \mathbb{R}^{(p+1) \times (p+1)} \tag{2.38}$$

and Z and Y_o, $o = 1, \cdots, N_{out}$, are complex matrices given by

$$Z = \begin{bmatrix} \hat{\underline{z}}_k^{\,T}(\omega_1) \otimes \left[s_1(j\omega_1) \cdots s_p(j\omega_1) \right] \\ \vdots \\ \hat{\underline{z}}_k^{\,T}(\omega_N) \otimes \left[s_1(j\omega_N) \cdots s_p(j\omega_N) \right] \end{bmatrix} \in \mathbb{C}^{N \times (N_{in}(p+1))} \tag{2.39}$$

$$Y_o = \begin{bmatrix} -\left[s_1(j\omega_1) \cdots s_p(j\omega_1) \right] \otimes \hat{y}_o(\omega_1) \\ \vdots \\ -\left[s_1(j\omega_N) \cdots s_p(j\omega_N) \right] \otimes \hat{y}_o(\omega_N) \end{bmatrix} \in \mathbb{C}^{N \times (p+1)} \tag{2.40}$$

In the above equations, ω_k, $k = 1, 2, \ldots, N$, are the discrete frequencies at which the FRF are evaluated and $\otimes$ denotes the Kronecker product. This equation can be solved for the denominator polynomial $\underline{\alpha}$ in a least-squares sense. To avoid finding the trivial solution $\underline{\alpha} = \underline{0}$, a constraint is imposed on the parameters. Such a constraint also removes the parameter redundancy that exists in the common denominator model (multiplying numerator and denominator with the same matrix yields different numerator and denominator polynomials, but the same transfer function matrix). Specifically, to remove the parameter redundancy the value of the coefficient α_0 is selected to be $\alpha_0 = 1$.

Once these coefficients $\underline{\alpha}$ are obtained, the poles μ_r of the polynomial $A(s)$ are readily obtained by solving an eigenvalue problem of order $p = 2m$ of the companion matrix of the polynomial $A(s)$ (Heylen et al., 1997). The eigenvalues λ_r are then obtained from μ_r using the relation $\lambda_r = \ln(\mu_r)/\Delta t$.

Stabilization diagrams (Haylen et al., 1997) can be used to distinguish between the mathematical and the physical modes and eventually keep only the physical modes of the system. When trying to estimate the modal parameters from real data, it is generally a good idea to over-specify the model order considerably, i.e. to try to fit high order models that contain much more modes than present in the measured data. In particular, the poles corresponding to a certain model order are compared to the poles of a one order lower model. If their differences are within pre-set limits, the poles are considered as stable one. The spurious mathematical poles will not stabilize at all during this process and can be sorted out of the estimated modal parameter data set more easily. Thus the previous methodology not only provide estimates of the modal frequencies and modal damping ratios but also gives the number of contributing modes through the appropriate-conventional use of stabilization diagrams. Examples of stabilization diagrams will be shown in the application Section 2.6.

2.5.2 Step 2: Identification of modeshapes and participation factors

In the second step, the number of contributing modes m and the estimated values of the poles λ_r are considered to be known and are used with (2.20) or (2.25) in order to obtain estimates of the remaining unknown modal parameters, the modeshapes $\underline{u}_r$, the participation factors $\underline{l}_r$, the

real matrix D_c, and the vectors $\underline{a}_r$ and $\underline{\beta}_r$ or the initial conditions $\xi_r(0)$ and $\xi_r(T)$. Two different approaches have been developed for the computation of these quantities in the second step.

2.5.2.1 First approach

In the first approach, given the number of contributing modes m and the estimated values of the poles λ_r, estimates of the residue matrices $R_r = \underline{u}_r \underline{l}_r^T$, the real matrix D_c, and the vectors $\underline{a}_r$ and $\underline{\beta}_r$ are obtained by minimizing (2.27) with $\underline{\varepsilon}_k^{NL}(\underline{\theta})$ given by (2.28) and $\underline{y}_k(\underline{\theta})$ given by (2.20) with $\underline{u}_r \underline{l}_r^T$ replaced by R_r. It is evident from the structure of the problem that the objective function is quadratic in the elements R_r, D_c, $\underline{a}_r$ and $\underline{\beta}_r$. So, using the stationarity conditions, one can develop a system of linear equations for the elements R_r, D_c, $\underline{a}_r$ and $\underline{\beta}_r$. For completeness, this system of equations is given next as a function of the measurements $\underline{\hat{z}}$, $\underline{\hat{y}}_k$ and the values of the system poles λ_r estimated in the first step. Defining the matrix of unknown quantities partitioned as follows:

$$X^T = \Big[\mathrm{Re}(R_1 \cdots R_m) \quad \mathrm{Im}(R_1 \cdots R_m) \quad | \quad D_c \quad | \quad \mathrm{Re}(\underline{a}_1 \cdots \underline{a}_m) \quad \mathrm{Im}(\underline{a}_1 \cdots \underline{a}_m) \quad | \quad -\mathrm{Re}(\underline{\beta}_1 \cdots \underline{\beta}_m) \quad -\mathrm{Im}(\underline{\beta}_1 \cdots \underline{\beta}_m) \Big] \in \mathbb{R}^{N_{out} \times (2N_{in}m + N_{in} + 2m + 2m)} \tag{2.41}$$

it can be readily shown that the stationarity conditions yield the following system of equations for X:

$$\mathrm{Re}\left[\sum_{k=1}^{N} \underline{\sigma}_k^*(\underline{\lambda}) \underline{\sigma}_k^T(\underline{\lambda}) \right] X = \mathrm{Re}\left[\sum_{k=1}^{N} \underline{\sigma}_k^*(\underline{\lambda}) \underline{\hat{e}}_k^* \right] \tag{2.42}$$

where

$$\underline{\sigma}_k^T(\underline{\lambda}) = \Big[\underline{\upsilon}_k^T(\underline{\lambda}) \quad \underline{\ddot{z}}_k^T \quad \underline{\mu}^T(\underline{\lambda}) e^{-j\omega_k T} \quad \underline{\mu}^T(\underline{\lambda}) \Big] \in \mathbb{C}^{2m(2+N_{in})+N_{in}} \tag{2.43}$$

and $\underline{\mu} = \underline{\mu}(j\omega)$ is a complex valued vector given by

$$\underline{\mu} = \begin{Bmatrix} \underline{\mu}^+ \\ \underline{\mu}^- \end{Bmatrix} \in \mathbb{C}^{2m} \tag{2.44}$$

with

$$\underline{\mu}^{+} = \begin{Bmatrix} \dfrac{1}{(j\omega)-\lambda_1} + \dfrac{1}{(j\omega)-\lambda_1^*} \\ \vdots \\ \dfrac{1}{(j\omega)-\lambda_m} + \dfrac{1}{(j\omega)-\lambda_m^*} \end{Bmatrix} \in \mathbb{C}^m \tag{2.45}$$

$$\underline{\mu}^{-} = j\begin{Bmatrix} \dfrac{1}{(j\omega)-\lambda_1} - \dfrac{1}{(j\omega)-\lambda_1^*} \\ \vdots \\ \dfrac{1}{(j\omega)-\lambda_m} - \dfrac{1}{(j\omega)-\lambda_m^*} \end{Bmatrix} \in \mathbb{C}^m \tag{2.46}$$

$$\underline{\upsilon}_k\left(\underline{\lambda}\right) = \begin{Bmatrix} \underline{\eta}_k(\lambda_1) + \underline{\eta}_k(\lambda_1^*) \\ \vdots \\ \underline{\eta}_k(\lambda_m) + \underline{\eta}_k(\lambda_m^*) \\ j\underline{\eta}_k(\lambda_1) - j\underline{\eta}_k(\lambda_1^*) \\ \vdots \\ j\underline{\eta}_k(\lambda_m) - j\underline{\eta}_k(\lambda_m^*) \end{Bmatrix} \in \mathbb{C}^{2mN_{in}} \tag{2.47}$$

and

$$\underline{\hat{e}}_k = \underline{\hat{y}}_k \tag{2.48}$$

For the frequency domain formulation, $\underline{\upsilon}_k\left(\underline{\lambda}\right)$ simplifies to

$$\underline{\upsilon}_k\left(\underline{\lambda}\right) = \underline{\mu}\left(\underline{\lambda}\right) \otimes \ddot{\underline{z}}_k \tag{2.49}$$

The solution of the system of equations in (2.42) provide estimates of the residue matrices R_r, the real matrix D_c and the vectors $\underline{a}_r$ and $\underline{\beta}_r$. Given the residue matrix R_r and noting that it admits the representation $R_r = \underline{u}_r \underline{l}_r^T$, i.e. is expected to be of rank one, the modeshapes $\underline{u}_r$ and the modal participation factors $\underline{l}_r$ are derived directly by the Singular Value Decomposition (SVD) for the resulting numerator matrices R_r using the left-hand and right-hand singular vectors corresponding to the highest singular value. For closely spaced and overlapping modes this approach may fail to give accurate enough estimates of the modal characteristics for the closely spaced modes.

2.5.2.2 Second approach

The second approach is based on the form (2.25) for the response predictions $\underline{y}_k(\underline{\theta})$. In this case the parameters to be identified are $\underline{u}_r$, $\underline{l}_r$, $\xi_r(0)$, $\xi_r(T)$, $r=1,\cdots,m$, and the real matrix D_c. The total number of parameters is $2m(1+N_{out}+N_{in})+N_{out}N_{in}$ for non-classically damped modal models. The total number of parameters can be reduced to $2m(1+N_{in})$, containing the parameters $\underline{l}_r$, $\xi_r(0)$ and $\xi_r(T)$ for each mode by recognizing that the objective function in (2.27) is quadratic with respect to the complex modeshape $\underline{u}_r$ and the real matrix D_c. Applying the optimality conditions in (2.27) with respect to the components of $\underline{u}_r$ and D_c, a linear system of equations results for obtaining $\underline{u}_r$ and D_c with respect to the parameters $\underline{l}_r$, $\xi_r(0)$ and $\xi_r(T)$. This system of equations is given in Nikolaou (2008). The resulting nonlinear optimization problem with respect to the remaining $2m(1+N_{in})$ parameters $\underline{l}_r$, $\xi_r(0)$ and $\xi_r(T)$, $r=1,\cdots,m$, is solved in Matlab using available gradient-based optimization algorithms

2.5.3 Step 3: Modal identification by full nonlinear optimization

The two-step approach gives results that are very close to the optimal estimates. However, for closely spaced and overlapping modes, the two step approach may not be adequate. In this case it is recommended to solve the full nonlinear optimization problem for the identification of all modal parameters simultaneously. Specifically, the modal parameters in the set $\underline{\theta}$ are identified by minimizing the objective function (2.27) with $\varepsilon_k^{NL}(\underline{\theta})$ given by (2.28). The number of contributing modes m are obtained using the stabilization diagrams in the first step of the algorithm. The initial estimates for the parameters involved in the optimization problem can be obtained by the first and second steps of the algorithm, assisting the convergence of the optimization algorithm and reducing the computational cost. Two approaches are next introduced depending on the form of the response function $\underline{y}_k(\underline{\theta})$ and the type of the modal parameters involved.

2.5.3.1 First approach

In the first approach the response vector $\underline{y}_k(\underline{\theta})$ is given by (2.20) with $\underline{u}_r\underline{l}_r^T$ replaced by R_r. The modal parameter set $\underline{\theta}$ to be identified contains the parameters ω_r, ζ_r, R_r, $\underline{a}_r$, $\underline{\beta}_r$, $r=1,\cdots,m$, and D_c that completely define the response vector in (2.20). The total number of parameters is $2m(1+N_{out}N_{in})+N_{out}N_{in}+4N_{out}$ for non-classically damped modal models.

The minimization of the objective function (2.27) can be carried out efficiently, significantly reducing the computational cost, by recognizing that the error function in (2.27) is quadratic with respect to the complex matrices R_r, the real matrix D_c, and the elements in the vectors $\underline{a}_r$ and $\underline{\beta}_r$. This observation is used to develop explicit expressions that relate the parameters R_r, $\underline{a}_r$,

$\underline{\beta}_r$ and D_c to the modal frequencies ω_r and the damping ratios ζ_r, so that the number of parameters involved in the optimization is reduced to $2m$. This reduction is considerable for a relatively large number of measurement points. Applying the optimality conditions with respect to the components of R_r, $\underline{a}_r$, $\underline{\beta}_r$ and D_c, a linear system of equations result for obtaining R_r, $\underline{a}_r$, $\underline{\beta}_r$ and D_c with respect to ω_r and ζ_r, $r=1,\cdots,m$. This linear system is given in (2.42). The resulting nonlinear optimization problem with respect to the remaining variables ω_r and ζ_r, $r=1,\cdots,m$, is solved in Matlab using available gradient-based optimisation algorithms. The starting values of the parameters required in the optimization are obtained from the estimates provided by the first and second steps of the algorithm. These starting values are usually very close to the optimal values for most of the modes and thus the optimization algorithm converges in a relatively few iterations.

Once the modal frequencies ω_r and the damping ratios ζ_r are estimated by the optimization problem, the solution of the system of equations in (2.42) provide estimates of the residue matrices R_r, the real matrix D_c and the vectors $\underline{a}_r$ and $\underline{\beta}_r$. Given the residue matrix R_r and noting that it admits the representation $R_r = \underline{u}_r \underline{l}_r^T$, i.e. is expected to be of rank one, the modeshapes $\underline{u}_r$ and the modal participation factors $\underline{l}_r$ are derived directly by the Singular Value Decomposition (SVD) for the resulting numerator matrices R_r using the left-hand and right-hand singular vectors corresponding to the highest singular value. For closely spaced and overlapping modes this approach may fail to give accurate enough estimates of the modal characteristics for the closely spaced modes.

2.5.3.2 Second approach

In the second approach the response vector is given by (2.25). The modal parameter set $\underline{\theta}$ to be identified contains the parameters ω_r, ζ_r, $\underline{u}_r$, $\underline{l}_r$, $\xi_r(0)$, $\xi_r(T)$, $r=1,\cdots,m$, and the real matrix D_c that completely define the response vector in (2.25). The total number of parameters is $2m(2+N_{out}+N_{in})+N_{out}N_{in}$ for non-classically damped modal models.

The minimization of the objective function (2.27) can be carried out efficiently, significantly reducing the computational cost, by recognizing that the error function in (2.27) is quadratic with respect to the complex modeshapes $\underline{u}_r$ and the elements in the matrix D_c. This observation is used to develop explicit expressions that relate the parameters $\underline{u}_r$ and D_c to the vectors $\underline{l}_r$, the modal frequencies ω_r, the damping ratios ζ_r, and the initial conditions $\xi_r(0)$, $\xi_r(T)$ so that the number of parameters involved in the optimization is reduced to $2m(N_{in}+2)$. This reduction is considerable for a relatively large number of measurement points. Applying the optimality conditions with respect to the components of $\underline{u}_r$ and D_c, a linear system of equations results for obtaining $\underline{u}_r$ and D_c with respect to the ω_r, ζ_r, $\underline{l}_r$, $\xi_r(0)$ and $\xi_r(T)$, $r=1,\cdots,m$. This linear system is given in Nikolaou (2008). The resulting nonlinear optimization problem with respect to

the remaining variables $\underline{l}_r$, ω_r, ζ_r, $\xi_r(0)$ and $\xi_r(T)$, $r=1,\cdots,m$, is solved in Matlab using available gradient-based optimisation algorithms. The starting values of the parameters required in the optimization are obtained from the estimates provided by the first and second steps of the algorithm. These starting values are usually very close to the optimal values for most of the modes and thus the optimization algorithm converges in a relatively few iterations. The derivatives of the objective function with respect to the modal parameters are evaluated analytically, accelerating the convergence of the algorithm. Modal sweep approaches (Werner et al. 1987) could also be implemented to improve the effectiveness of the proposed algorithm.

2.6 Application

This section applies the developed modal identification methodologies for estimating the dynamic modal characteristics of a representative bridge on the Egnatia Odos motorway, using earthquake induced vibration measurements. Egnatia Motorway is a new, 670 km long highway, that transverses Northern Greece in an E-W direction. The R/C bridge of Polymylos that were instrumented with special accelerometer arrays are the 9th Ravine Bridge on the Veroia - Polymylos section (Figure 2.1). The bridge has two, almost identical, statically independent branches, one for each traffic direction, one of which was instrumented. Modal identification results (modal frequencies modal damping ratios and modeshape components) for the Polymylos bridge are estimated for the low level, magnitude $M_L = 4.6$, earthquake event that occurred on 21/2/2007 (2:04:38 GMT) at a distance 35km Northeast of the bridge.

The T-shaped 9th Polymylos bridge is curved in plan and has a total length of 170m. The deck cross section is a box girder of height varying parabolically from 9m at the central pier to 4m at the two abutments. It is supported monolithically by a central pier (M1), of 35m height, which is founded on a massive rectangular R/C rock socket at its basement and continues with two transverse flanges for the rest of its height. Each of the two 85m-long cantilever parts of the deck girder rests on each abutment through special elastomeric bearings that allow free sliding in the longitudinal direction (to accommodate thermal expansions/contractions), while functioning as normal elastomeric pads in the transverse (radial) direction.

Figure 2.1: View of Polymylos bridge

Two 12-channel Kinemetrics K2 ® recording units were installed on the northern branch of the 9th Polymylos bridge (on deck level at the middle of the total bridge deck), each supporting 12 uniaxial Kinemetrics Episensor ® accelerometers (± 2g full scale) installed on both sides of the bridge deck. The recording units have a 19-bit resolution, a sampling rate capacity of up to 200sps and a dynamic range of 108 dB @ 200 sps. Fifteen sensors were installed on the deck, three on the basement of the central pier and three on each of the two abutments (at the support level of the elastomeric bearings), as shown in Figure 2.2. Thus, the nine sensors monitor the earthquake-induced excitations at the two abutments and the basement of the pier. The particular layout of the instrumentation permits the analysis of earthquake-induced response of the bridge. The 3 to 4-letter sensor labels follow the following convention: The last letter denotes the orientation of the uniaxial sensor (L: longitudinal, T: transverse, V: vertical). The previous one denotes the side of the bridge deck on which the sensor lies (R: right, L : left). Finally, the first one or two letters denote the bridge section that the sensor lies on (first letters U1 and U3 refer here to the abutment level where the elastomeric bearings are seated, U2 refers to the base of the central pier and all other letters refer to positions on the level of the bridge deck). The numbers next to each sensor label denotes the length of the cable used to connect the sensor to each recording unit. Among the 15 accelerometers located on the bridge deck, 8 record in the vertical, 1 in the longitudinal and the rest 6 in the transverse direction.

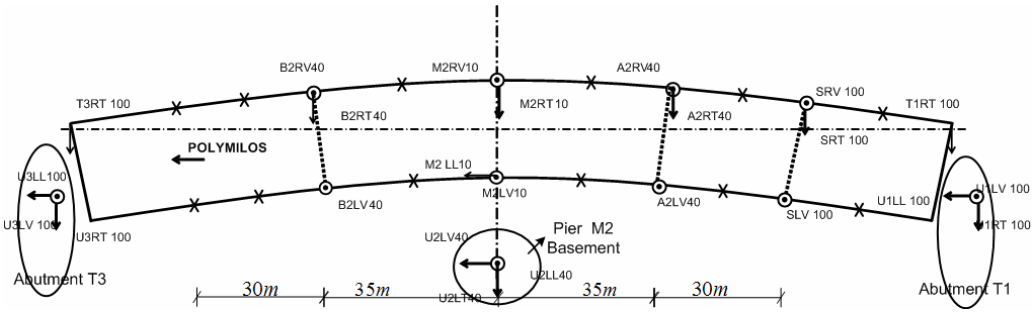

Figure 2.2: Instrumentation layout of Polymylos bridge

The modal identification carried out in the time domain and in the frequency domain using the measurements of the 24 accelerometers which were installed on the northern branch of the 9th Polymylos bridge. In particular, in the time domain the modal identification carried out using both non-classically damped and classically damped modal models. From the 15 accelerometers located on the bridge deck, accelerometers A2LV, A2RV and M2RV were excluded because they were damaged during the earthquake event. The accelerometer U1LV which monitors the earthquake-induced excitations at the right abutment of the bridge was also excluded for the same reason.

Using all the eight available input sensors which monitor the earthquake-induced excitations at the two abutments and the basement of the pier and all twelve available output sensors, the values of the modal frequencies and modal damping ratios resulted from Stabilization Diagrams are presented in Figure 2.3 for: (a) the Fourier Transform of the accelerations of all vertical sensors, and (b) the Fourier Transform of the accelerations of all transverse sensors. After distinguishing the physical from the mathematical poles the values of the modal frequencies and modal damping ratios are presented in Table 2.1. Eight values of modal frequencies and modal damping ratios were identified. These values for the modal frequencies and the damping ratios were used for applying the next two steps described in Chapters 3 and 4 and estimating the modeshape components and participation factors on the measured locations of the bridge.

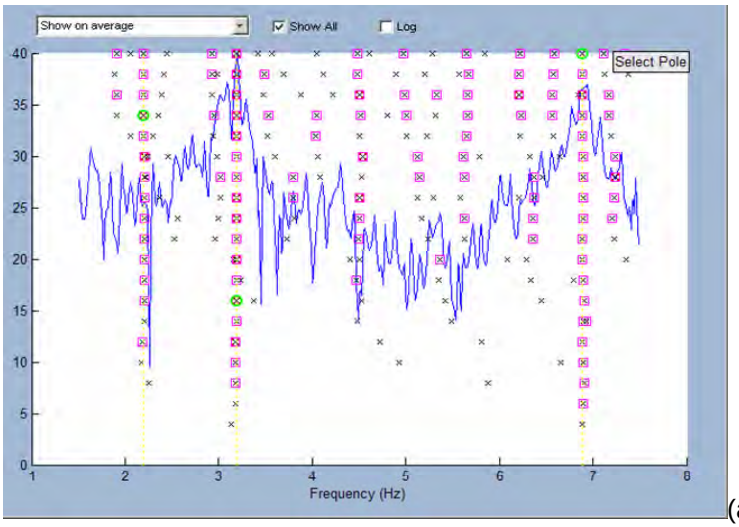

(a)

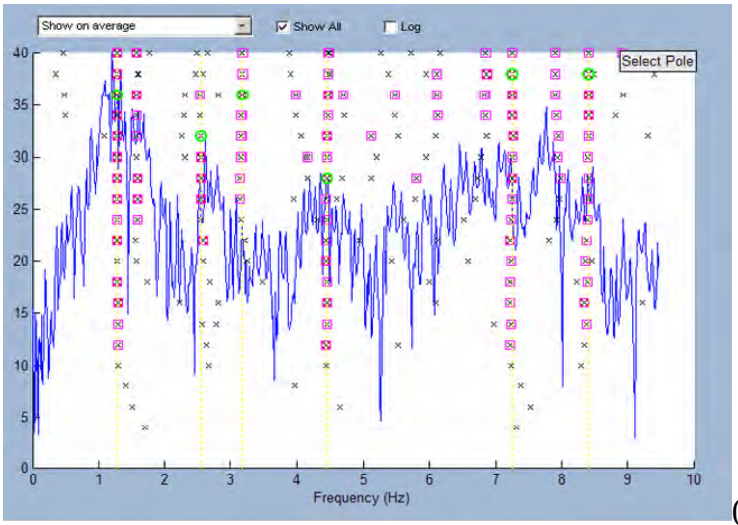

(b)

Figure 2.3: Stabilization Diagram for the Polymylos bridge: (a) vertical Sensors, (b) transverse sensors.

Table 2.1: Identified modal frequencies ω and damping ratios ζ of the Polymylos Bridge, obtained by the Stabilization Diagram for Earthquake Vibrations.

Mode	Polymylos Bridge Stabilization Diagram	
	ω Hz	ζ (%)
1st Transverse	1,28	2.07
1st Bending (deck)	2.19	0.42
2nd Transverse	2.56	4.39
2nd Bending (deck)	3.19	0.66
3rd Transverse	4.46	1.46
3rd Bending (deck)	6.89	0.66
4th Transverse	7.25	1.20
1st Torsional	8.40	0.58

In Table 2.1 the values for the modal frequencies and damping ratios resulted from the identification algorithms for non-classically and classically damped modal models in time and frequency domain are presented and compared with the values identified using ambient vibration measured data presented in the work by Ntotsios et al. (2008) based on the system identification theory presented in Chapter 3 of this thesis.

Comparing the modal frequencies and damping ratios resulted from the Stabilization Diagrams and the modal identification algorithm for time and frequency domain it is observed that there are no major discrepancies. This validates that the values of the modal frequencies and the modal damping ratios which result from the Stabilization Diagrams constitute a very good approach of the optimal values that result from the modal identification algorithm.

Table 2.2: Identified and design FE model predicted modal frequencies ω and damping ratios ζ of the Polymylos bridge for Earthquake Vibrations.

Mode	Earthquake Vibrations						Ambient Vibrations (Ntotsios et. al, 2008)
	Frequency Domain (non-classically damped)		*Time Domain (non-classically damped)*		*Time Domain (classically damped)*		
	ω Hz	ζ (%)	ω Hz	ζ (%)	ω Hz	ζ (%)	ω Hz
1st Transverse	1.26	2.07	1.29	1.8	1.29	1.8	1.13
1st Bending (deck)	2.19	0.47	2.19	0.4	2.20	0.6	2.13
2nd Transverse	2.61	3.86	2.57	4.12	2.56	3.5	2.22
2nd Bending (deck)	3.19	0.61	3.19	0.66	3.20	0.7	3.07
3rd Transverse	4.45	1.55	4.30	2.49	4.23	3.2	4.10
3rd Bending (deck)	6.88	0.58	6.89	0.44	6.89	0.6	6.66
4th Transverse	7.17	1.38	7.24	1.2	7.24	1.2	6.78
1st Torsional	8.41	0.73	8,39	2,1			-

From the earthquake vibration data, it is noted that eight modes were successfully and reliably identified for the Polymylos bridge: four transverse modes, three bending modes and one torsional. In Table 2.2, comparing the modal damping ratios, resulted from time domain and frequency domain, it is observed that the bending modes have significantly lower values of damping, of the order of 0.4% to 0.7%, than the damping values of the lower transverse modes which are of the order of 1.2% to 4.12%. The higher damping values observed for the lower transverse modes can be attributed to the energy dissipation arising from the higher modal deformation levels of the elastomeric bearings at the ends of the bridges which dominate the motion of these modes. Also, soil damping could also have contributed to the higher damping values observed for these modes.

Comparing the modal frequencies resulted from non-classically damped case and classically damped case for the time domain it is observed that there are no major discrepancies. For the modal damping ratios of bending modes, it is observed that the resulted values from non-

classically damped case have lower values of the order of 0.4%-0.6% than the values resulted from classically damped case which are of the order of 0.6%-0.7%. For the transverse modes it is observed that the resulted damping ratios from non-classically and classically damped case of 1st and 4th mode have the same values, while the resulted damping ratios of the rest two modes have different values.

Comparing the results from time domain and frequency domain using non-classically damped modal models it is observed that the modal frequency of the 3rd transverse mode resulted from the time domain has lower value of the order of 4.23 Hz than the value resulted from the frequency domain which are of the order of 4.30 Hz. For the rest modes there are no major discrepancies between the values of the modal frequencies. Differences are also observed for the modal damping ratios for the transverse modes of the order of 0.26% - 0,94% and of the order of 0.05% - 0.14% for the bending modes.

From the results in Table 2.2, it is observed that the modal frequencies due to earthquake vibrations are 4% to 15% higher than the modal frequencies identified in Ntotsios et. al (2008) from the ambient vibrations. No conclusive explanation can be given for these differences without making assumptions about the bridge behavior within the measured vibration levels. These differences could be attributed to the nonlinear softening hysteretic behavior of the structural components, especially the elastomeric bearings. The results in Ntotsios et. al (2008) reveal that the peak acceleration responses for the earthquake induced vibrations are 1.4 to 3.8 times lower than the peak acceleration responses of the ambient vibrations (Table 2.3). Accepting that the estimation of the equivalent modal frequencies is dominated by the peak vibration levels, this could justify a higher secant stiffness of the elastomeric bearings for the lower earthquake peak vibration levels which results in stiffer structures and thus justifies the increase in the equivalent values of the modal frequencies observed in Table 2.2 for earthquake induced vibrations. However, this explanation cannot be used to justify the higher modal frequency values observed for the modes associated with bending of the deck since these modes are not affected by the bearing stiffness. It is unlikely that similar softening nonlinear effects will arise by the deformation of the pier and deck elements in these low vibration levels.

In Ntotsios et. al (2008) the values of the modal frequencies were also identified using much shorter duration segments of the ambient vibrations recordings shown in Figure 2.4, selected so that the peak acceleration levels are the same as or smaller that the peak acceleration of the earthquake recordings. The estimated values of the modal frequencies obtained by analyzing these short duration segments were found to be almost identical to the values of the modal frequencies that were estimated using the whole, approximate 30 minutes, segment of the records shown in Figure 2.4. This verifies that at the low vibration levels considered, the aforementioned differences in the peak acceleration levels between the ambient and the earthquake induced vibrations cannot justify the large differences in the modal frequencies observed in Table 2.2.

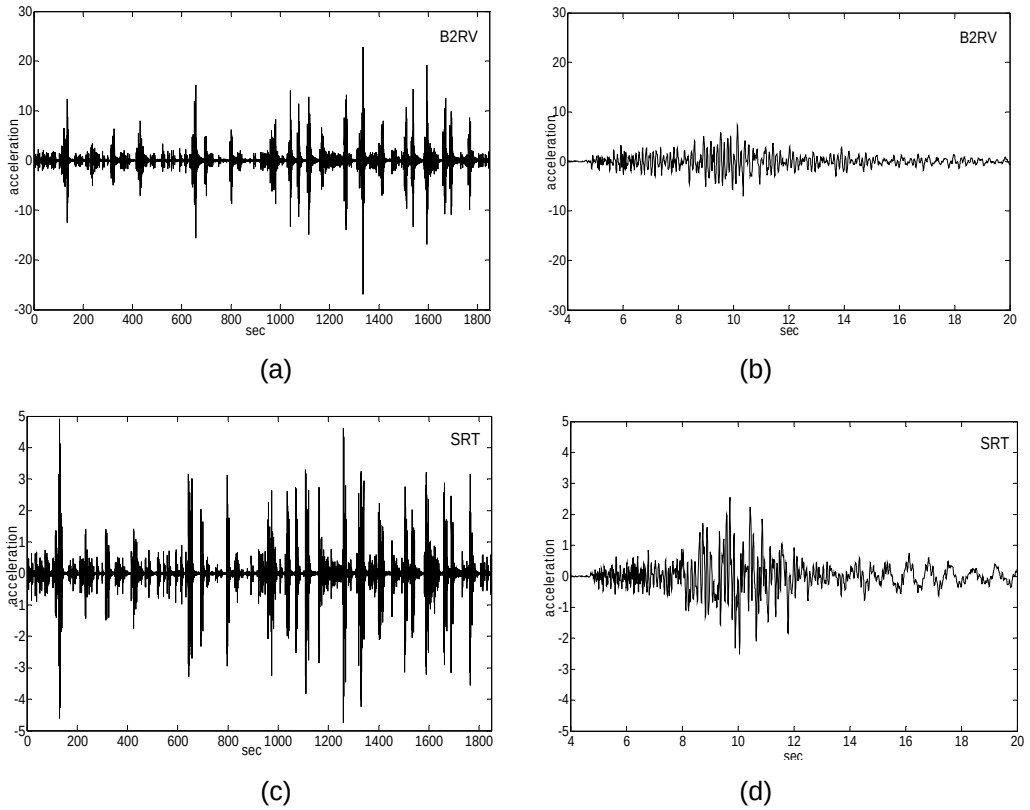

Figure 2.4: Accelerations time history measurements from ambient (Ntotsios et. al, 2008) and earthquake vibrations at sensors B2RV and SRT, (a,c) ambient, (b,d) earthquake

Table 2.3: Comparison of Peak and RMS response acceleration obtained from Ambient (AV) and Earthquake (EV) induced Vibrations (Ntotsios et. al, 2008).

	Peak response (cm/sec^2)			RMS (cm/sec^2)		
Channel	AV	EV	AV/EV	AV	EV	AV/EV
B2LV	23.2470	7.1062	3.2714	0.9181	1.9397	0.4733
M2LL	2.1767	1.0009	2.1747	0.0922	0.2407	0.3830
M2LV	11.2310	2.9575	3.7975	0.6044	0.7350	0.8223
SLV	15.9950	6.6148	2.4181	0.8847	2.0163	0.4388
T3RT	5.9160	3.3652	1.7580	0.1825	0.7129	0.2561
B2RV	26.9220	7.3206	3.6776	0.9704	1.7120	0.5668
B2RT	7.7054	2.3919	3.2215	0.2928	0.6667	0.4392
M2RT	4.3362	2.5179	1.7221	0.2582	0.6141	0.4204
A2RT	5.5674	2.5210	2.2084	0.2559	0.5911	0.4329
SRV	17.4100	12.3900	1.4052	0.9418	2.5206	0.3737
SRT	4.9252	2.5542	1.9283	0.2783	0.5786	0.4810
T1RT	1.2481	2.3865	0.5230	0.0401	0.6104	0.0657

In contrast to the peak vibration levels, the levels of the RMS response in Table 2.3 of the approximately 30 minutes ambient acceleration measurements are 0.25 to 0.82 times the corresponding root mean square earthquake response levels. Accepting that the estimation of the

equivalent modal frequencies in Table 2.2 is dominated by the RMS vibration levels, the modal frequencies due to higher RMS earthquake vibration levels are expected to decrease if softening of the elastomeric bearings take place, which is not consistent with the opposite increasing trend observed in Table 2.2.

A more reasonable explanation that can account for the differences in the identified values of the modal frequencies in Table 2.2 is soil structure interaction effects (Safak 1995). In this work (earthquake vibration case), the modal properties of the system were identified using as input acceleration the eight recordings at the two abutments and the base of the central pier and as output accelerations the twelve available recordings along the bridge deck. Thus, ignoring the rigid body rotation of the central pier foundation at the low vibration levels measured, the modal frequencies identified by the input-output earthquake vibration measurements are those of the fixed base bridge, excluding the effects of soil-structure interaction since the base motion of the abutment and the pier foundation were used as input accelerations in the modal identification process. In contrast, in Ntotsios et. al (2008) for the ambient vibration case, the modal properties of the system, obtained from the ambient measurements due to excitations from the traffic and wind loads, were identified using only the twelve output accelerations recorded along the bridge deck. Thus, the modal frequencies due to ambient vibrations correspond to the dynamic characteristics of the combined system consisting of the bridge and accounting for soil structure interaction effects. This interaction effect is due to the additional soil flexibility provided at the base supports of the bridge. The presence of this effect is also supported from the non-zero vibration levels recorded at the base of the pier and the top of the side abutments during ambient measurements. Thus, soil-structure interaction effects cause the combined soil-foundation-superstructure system to appear as less stiff than the superstructure (fixed-based bridge) itself, resulting in lower values of the modal frequencies which is consistent with the results observed in Table 2.2.

The modeshape components at the measured locations for the eight identified modes are shown in Figure 2.5 for the Polymylos Bridge obtained by the time domain identification algorithm using non-classically damped modal models. The identified modeshapes are in general complex valued. Figure 2.6 represents in polar plots the modeshapes based on earthquake-induced vibrations. These plots have the advantage to show directly the extent of non-classically damping characteristics of a modeshape. If all components of a modeshape vector are collinear (in phase or 180 degrees out of phase) then this mode is said to be classically (or proportionally) damped. On the contrary, the more these modeshape components are scattered in the complex plane, the more the mode is non-classically (or non-proportionally). For example, in Figure 2.6 it is observed that the 1st transverse mode (1.29 Hz) is nearly classically damped. In Figure 2.7 the earthquake-induced accelerations and the accelerations predicted by the optimal modal model for selected sensors are compared. In Figure 2.8 the Fourier transform (FT) of the earthquake-induced accelerations and the FT of the accelerations predicted by the optimal modal model for selected sensors are compared. A very good fit is observed, validating the effectiveness of the proposed modal identification software based on earthquake recordings.

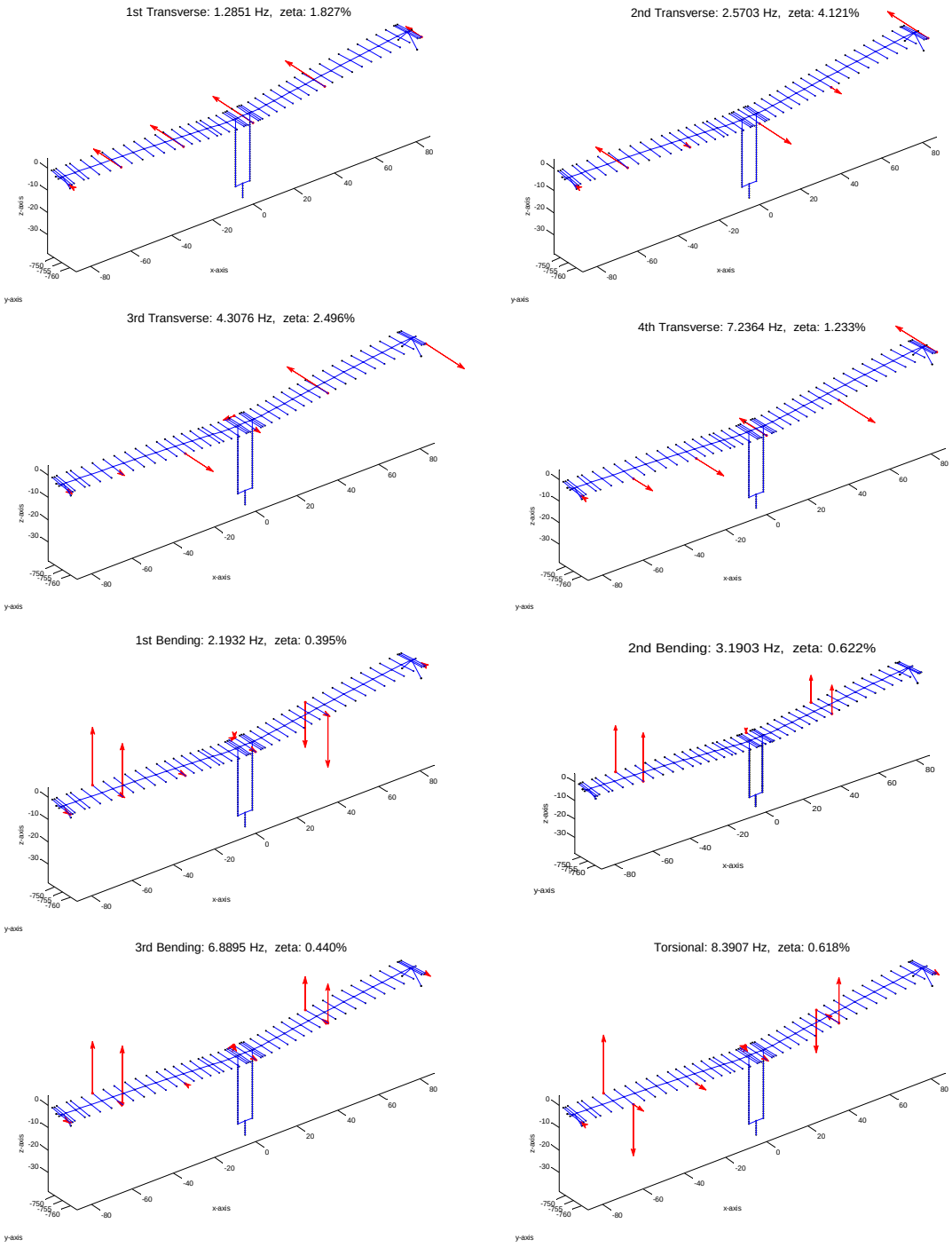

Figure 2.5: The eight identified modeshapes of the Polymylos bridge.

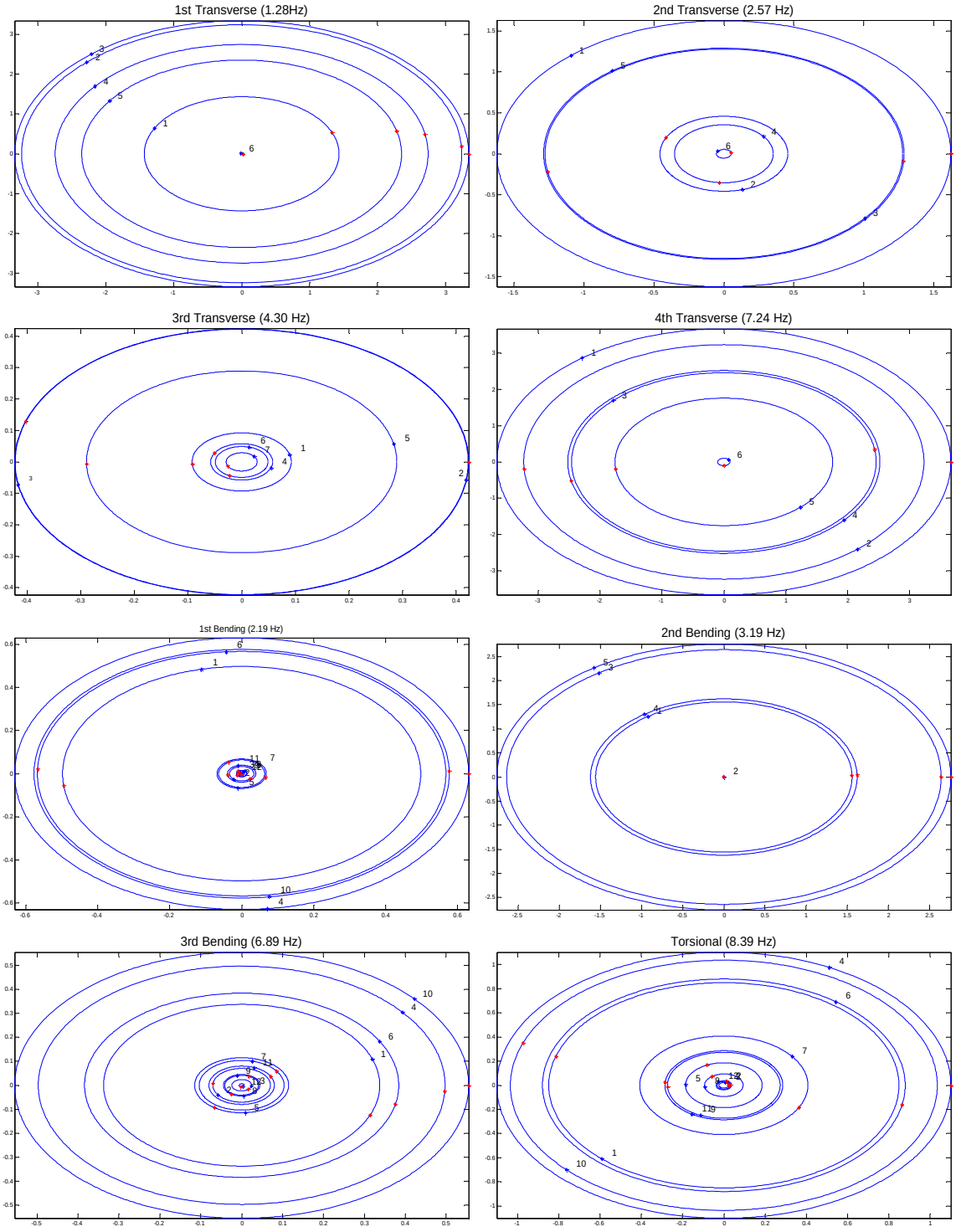

Figure 2.6: Polar plots representation of the eight identified modeshapes of the Polymylos Bridge.

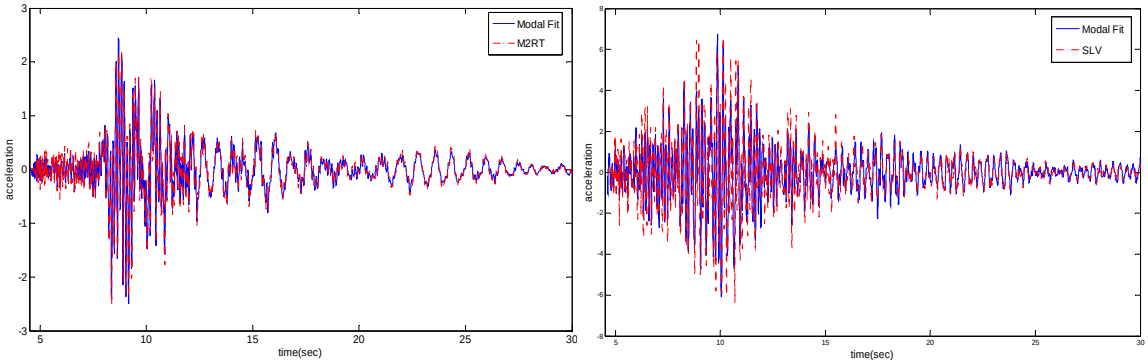

Figure 2.7: Comparison between measured and optimal modal model predicted accelerations recordings for selected sensors of the Polymylos Bridge

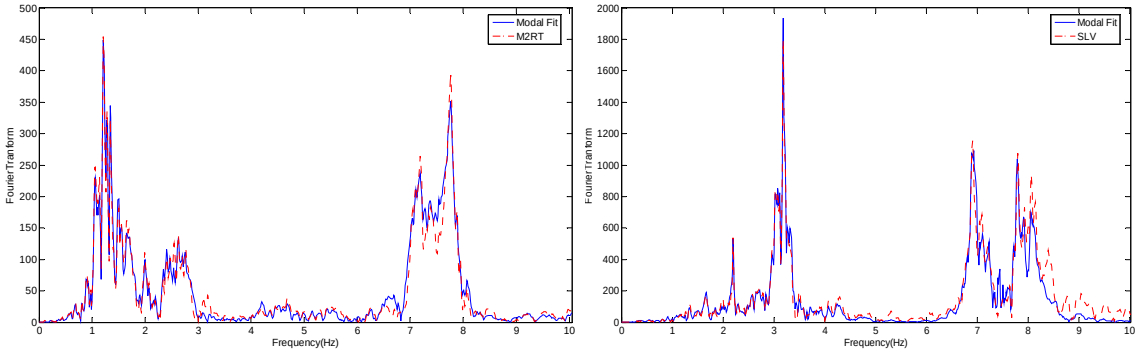

Figure 2.8: Comparison between measured and optimal modal model predicted Fourier Transforms of accelerations recordings for selected sensors of the Polymylos Bridge

2.7 Conclusions

Time and frequency domain least squares methods for the identification of non-classically-damped modal models of linear structures from multiple-support excitations and multiple responses were developed. The methods are extension of the Beck (1978) and McVerry (1980) algorithms developed for classically-damped modal models. The identification involves the estimation of the number of contributing modes, the modal frequencies, the modal damping ratios, the complex modeshapes, the pseudo-response matrix, and the initial conditions of the contributing modes. The common structure of the time and frequency domain formulation is revealed and exploited to develop an identification formulation common for both time and frequency domains. Computational efficient algorithms for solving the resulting highly non-convex nonlinear optimization problems were proposed, including features of automatically estimating the number of contributing modes, as well as the modal frequencies and the damping ratios of the physical modes without or minimal user intervention. Specifically, a three-step approach was proposed to carry out efficiently the optimization. In the first step, non-iterative conventional least squares complex frequency domain algorithms along with stabilization diagrams are used to automatically estimate the modal frequencies and the damping ratios of the modal model and to

distinguish between the physical and mathematical modes. In the second step, two alternative approaches were introduced to estimate the modeshapes and the participation factors. The first approach is non-iterative and estimates the modal residue matrices by solving a linear system of equations given the values of the modal frequencies and damping ratios estimated in the first step. Singular value decomposition on the residue matrices provides the complex modeshape components and the participation factors. The second approach is a least squares optimization approach that takes advantage of the quadratic dependence of the objective function on the modeshapes and other matrices to reduce the number of parameters involved to the smallest possible number, consisting of the participation factors and the modal initial conditions. The estimates provided from the first two steps are in most cases close to the optimal estimates. In order to improve the estimates, the full non-convex nonlinear optimization problem has to be solved in the third step by using the initial estimates of the parameters obtained in the first two steps to accelerate convergence of the optimization algorithm. An efficient solution method was proposed. It is demonstrated that the third step improves significantly the accuracy of the modal characteristics for closely-spaced and overlapping modes.

The proposed non-classically damped modal identification algorithms are applicable to the cases where the damping is not proportionally distributed through out a structure. Such cases arise in base isolated building and bridges using local dissipation mechanics such as elastomeric bearings and viscous dampers. Also it arises in the analysis of the combined vehicle-suspension structural systems. The computational efficiency and the accuracy of the modal identification methods developed were illustrated using input-output acceleration measurements from a bridge structure subjected to multi-support earthquake excitations.

Chapter 3

Least squares identification of non-classically damped modal models based on ambient vibrations

3.1 Introduction

Experimental modal analysis (EMA) identifies a modal model from the measured forces applied to the test structure and the measured vibration responses. Classically, one applies an artificial, measurable input to the system and one measures the output. From these measurements, the experimental model can be obtained by a variety of parameter estimation methods. During an EMA, the structure is often removed from its operating environment and tested in laboratory conditions. The latter experimental situation can differ significantly from the real-life operating conditions. Also, cases exist where it is rather difficult to apply an artificial force on a structure, especially for massive civil structures for which large exciters have to be used to excite the structure.

Vibration measurements during various operational conditions of the structure are easily obtained using a monitoring system. Such measurements in most cases contain only responses of the structure at various locations. The excitation forces caused by wind, turbulence, waves, traffic and other excitation sources on civil structures, ground and air vehicles, are difficult to measure and they are not available. System identification techniques have been developed to identify the modal model from the structure under its operational conditions from vibration responses only. These techniques, referred to as operational modal analysis (OMA) or output-only modal identification techniques, take advantage of the ambient excitation which is generated from wind and traffic on civil infrastructure (e.g. bridges, buildings), road roughness on ground vehicles, wind and waves on offshore structures and turbulence on aircrafts. The main assumption for these modal identification methods is that the excitations are broadband processes so that can be modeled by white noise.

There are certain advantages for using output only measurements for identifying the structural modes. In operational modal analysis there is no need to use artificial devises for exciting the structure (Farrar et al. 1994). Instead, the modes are identified from the vibrations obtained during the operation of the structure. This has certain advantages for massive civil structures for which large exciters have to be used to excite the structure. The use of exciters is not only very costly but it is also time-consuming and impractical (Peeters and De Roeck, 1999) for structural health monitoring applications. Ambient vibration measurement can directly be used for continuously monitoring the civil engineering structures (Peeters, 2000; Peeters and De Roeck, 2001). Such ambient vibration measurements have also been recently used in identifying the modal characteristics of ground and air vehicles (Peeters et al., 2004; Souty 2008; Boswald et al., 2006; Boswald and Govers, 2008; Klepka and Tadeusz, 2008; Peeters et al., 2009). Finally, it is worth noting that the OMA methods provide the modal properties that correspond to the real operation conditions of the structure. This allows the identification of more realistic modal models for in-operation structures. These conditions may differ significantly from the ones obtained during

laboratory forced excitation tests. Examples of this situation include the modal properties obtained for bridges using large exciters. Such modal analyses are usually performed under closed traffic conditions. For bridges that are open in traffic, one should expect changes in mass loading due to the vehicles passing through the bridge (Kim et al., 2001; Roberts, 2001). These changes alter the modal properties of the structure.

OMA proved very useful in civil engineering, where it is very difficult and expensive to excite constructions such as bridges and buildings with a hammer or shaker and to obtain artificially induced vibration levels that exceed the natural vibrations due to traffic or wind. Also in mechanical engineering, OMA is successfully applied to obtain data-based dynamic models of, for instance, a vehicle during road testing or an aircraft during flight tests.

The drawbacks of the operational modal analysis methods are the broadband assumptions on the unknown input and the low signal to noise ratios for the low level vibrations on which usually the measurements are made. In particular, all operational modal analysis methods are based on the fact that the unknown input forces can be adequately modeled by white noise processes. This condition is often violated since excitation forces may contain harmonic components which will appear as peaks in the spectra and may be erroneously identified by the methods as structural modes.

This chapter is concerned with developing methods for identification of non-classically modal modes using ambient vibrations. The evaluation of the actual dynamic characteristics of structures through measurements of their dynamic response induced by ambient excitations has been attracting an increasing research effort worldwide. There are a number of methods and respective software developed either in time or frequency domain for the identification of modal properties. The peak-picking method (Felber, 1993) is the simplest method to estimate the modal parameters of a structure subjected to ambient loading. It is based on the power spectra that are obtained from the measured time histories using discrete Fourier transform. The locations of the peaks of the power spectra give an estimate of the modal frequencies. The mode shapes are determined by computing the cross power spectral density functions between all outputs and a reference sensor. The method requires that the damping is low and the modes are well-separated. Violation of these two assumptions may lead to erroneous results. A disadvantage of the method is the subjective selection of modal frequencies and the lack of accurate damping estimates. However, the major advantage of the method is its speed. In general, the method identifies the operational deflection shapes instead of mode shapes, since there is no modal model that is fitted to the measured data. In particular, for the case of closely spaced modes such operational deflection shapes will be the superposition of the modeshapes of the multiple closely-spaced modes.

Nowadays, the stochastic subspace identification (Van Overschee and De Moor, 1996; Hermans and Van der Auweraer, 1999; Peeters and De Roeck, 1999; Basseville at al., 2001) has been well developed and widely used for identifying the modal properties from ambient vibration measurements. In this method, a stochastic state space model is identified directly from measured output data or output correlations. It can be shown that this stochastic state space model is a good representation of a vibrating structure, provided that the unknown excitation

forces can be modeled by white noise processes. Successful real-life modal analysis applications of stochastic subspace identification can be found in the literature (e.g. Hermans and Van der Auweraer, 1999; Peeters, 2000; Basseville at al., 2001).

Statistical methods for the estimation of the modal parameters based on output-only measurements have also been proposed. Frequency-domain maximum likelihood approaches for the estimation of modal parameters from output-only data were proposed by Hermans et al. (1998), Guillaume et al. (1999), Verboten (2002), Parloo (2003) and Cauberghe (2004). A Bayesian statistical approach for modal identification has also been proposed by Katafygiotis and Yuen (2001) using ambient data. The method is based on the statistics of an estimator of the spectral density. This approach allows for the direct calculation of the probability density functions (PDF) of the modal parameters which can then be approximated by an appropriately selected multi-variant Gaussian distribution.

Besides the aforementioned modal identification approaches, several methods proposed are based on fitting directly the measured data with modal model predicted data using least-squares type of approaches. In Beck et al. (1994) a methodology for modal identification is proposed using time-domain least-squares methods based on correlation functions of the output time histories. In Brinker et al. (2001), Verboten (2002) and Cauberghe (2004) frequency-domain least-squares methods based on full cross-power spectral densities (CPSD) are proposed. Peeters and Van der Auweraer (2005) have proposed a frequency-domain least-squares modal identification method based on half spectra. Finally, Devriendt and Guillaume (2008) have recently proposed an approach to identify modal parameters from scalar transmissibility measurements where the unknown ambient loads can be arbitrary (colored noise, swept sine, impact, etc.).

In this chapter a frequency domain least-squares approach is proposed to identify the modal parameters of a structure. A three step approach is proposed to solve the nonlinear optimization problem. The first step of the proposed algorithm provides estimates of the poles (modal frequencies and modal damping ratios) by solving a system of linear algebraic equations for the coefficients of the common denominator polynomial. Conventional stabilization diagrams are used to distinguish the physical from the spurious mathematical poles (Heylen et al., 1997). One of the novel parts of this chapter is the methodology that is developed based on the special structure of the common denominator polynomial that is revealed for the cross power spectral density matrices. Taking advantage of this special structure, one simplifies the system of normal equations used to compute the coefficients of the common denominator polynomial and also reduces considerably the number of spurious mathematical (non-physical) modes that are obtained using the conventional stabilization diagrams. Given the poles selected in the first step, the second step of the algorithm identifies the modeshapes and all other modal parameters that fully describe the modal model of the structure using two different approaches. Finally the third step of the algorithm solves a fully nonlinear optimization problem for the identification of all modal parameters simultaneously, with initial estimates the values obtained in the previews two steps. The third step is recommended to improve the estimates of the modal parameters especially for cases of closely and overlapping modes. The efficiency of the algorithm is tested using simulated measured data but also using real measured data from structures.

This chapter is organized as follows. Section 3.2 present the equations that relate the cross power spectral density to the modal parameters of a non-classically damped modal model of a structure. Available methods for estimating the CPSD using output measured response time histories are briefly reviewed in the Appendix 3.A. The least squares method for identifying/estimating the modal properties is formulated in Section 3.3. Section 3.4 presents the optimization algorithms and the three step approach. Section 3.5 illustrates the effectiveness of the methodology using simulated and real measurements from structures. Finally, conclusions of this work are presented in Section 3.6.

3.2 Modal decomposition of cross power spectral density functions

Consider a n DOF representation of a linear mechanical system given in (2.3). Let $\underline{f}(t) \in \mathbb{R}^{N_{in}}$ denote the force input vector at continuous time t and $\underline{x}(t) \in \mathbb{R}^n$ the output displacement vector. Let the $(N_{out} \times N_{in})$ Frequency Response Function (FRF) matrix between the outputs and inputs be given by equation (Heylen et al., 1997)

$$H(j\omega) = \sum_{r=1}^{m} \left[\frac{\underline{u}_r \underline{l}_r^T}{j\omega - \lambda_r} + \frac{\underline{u}_r^* \underline{l}_r^{*T}}{j\omega - \lambda_r^*} \right] \tag{3.1}$$

where λ_r, $\underline{u}_r$ and $\underline{l}_r$ are respectively the pole, mode shape and modal participation factor of mode r, and m is the number of contributing modes with $m \le n$.

It is known (Ljung, 1999; Lutes and Sarkani, 2004) that for stationary stochastic processes the cross power spectral density matrix $S_{xx}(j\omega) \in \mathbb{C}^{n \times n}$ of the response vector $x(t)$ can be written as a function of the transfer function $H(j\omega)$ and the cross power spectral density matrix $S_{ff}(j\omega)$ of the (unknown) force vector $\underline{f}(t)$ as follows:

$$S_{xx}(j\omega) = H(j\omega) S_{ff}(j\omega) H^{*T}(j\omega) \tag{3.2}$$

Assuming that the forces acting on the structure are independent white noise sequences, then the cross power spectral density matrix of the forces is constant, independent of $j\omega$, given by $S_{ff}(j\omega) = S_0$ that is diagonal and real. In this case equation (3.2) is written in the form

$$S_{xx}(j\omega) = H(j\omega) S_0 H^{*T}(j\omega) \tag{3.3}$$

It is shown in Heylen et al. (1997) and Ntotsios (2009) that by assuming white noise inputs and substituting (3.1) in (3.3) the cross power spectral density matrix $S_{xx}(j\omega)$ of the responses evaluated at frequency ω, can be modally decomposed as follows

$$S_{xx}(j\omega) = \sum_{r=1}^{n} \left[\frac{\underline{u}_r \underline{g}_r^T}{j\omega - \lambda_r} + \frac{\underline{u}_r^* \underline{g}_r^{*T}}{j\omega - \lambda_r^*} + \frac{\underline{g}_r \underline{u}_r^T}{-j\omega - \lambda_r} + \frac{\underline{g}_r^* \underline{u}_r^{*T}}{-j\omega - \lambda_r^*} \right] \tag{3.4}$$

where n is the number degrees of freedom, $\lambda_r = -\zeta_r \omega_r \pm j\omega_r \sqrt{1-\zeta_r^2}$ is the complex eigenvalue of the r-th contributing mode, ω_r is the r-th modal frequency, ζ_r is the r-th modal damping ratio, $\underline{u}_r \in \mathbb{C}^{N_{out}}$ is the complex modeshape of the r-th mode, $\underline{g}_r \in \mathbb{C}^{N_{out}}$ are vector quantities called operational reference vector, given in Ntotsios (2009), that depend on the characteristics of the modal model and the CPSD of the white noise input vector, while the symbol z^* denotes the complex conjugate of the complex number z.

The operational reference vector $\underline{g}_r$ for mode r is given by (Ntotsios, 2009)

$$\underline{g}_r^T = \underline{l}_r^T S_0 \begin{bmatrix} L_c^{*T} & L_c^T \end{bmatrix} \begin{bmatrix} h^*(-\lambda_r) & 0 \\ 0 & h(-\lambda_r) \end{bmatrix} \begin{bmatrix} U^{*T} \\ U^T \end{bmatrix} \in \mathbb{C}^{1\times n} \tag{3.5}$$

where

$$U = \left[\underline{u}_1, \ldots \underline{u}_n\right] \in C^{n\times m} \tag{3.6}$$

$$L_c = \begin{bmatrix} \underline{l}_1^T \\ \vdots \\ \underline{l}_{N_m}^T \end{bmatrix} \in R^{m\times n} \tag{3.7}$$

and $h(j\omega)$, $h^*(j\omega)$ are diagonal matrices given by

$$h(j\omega) = \begin{bmatrix} \frac{1}{j\omega - \lambda_1} & & 0 \\ & \ddots & \\ 0 & & \frac{1}{j\omega - \lambda_m} \end{bmatrix} \in \mathbb{C}^{m\times m} \tag{3.8}$$

and

$$h^*(j\omega) = \begin{bmatrix} \frac{1}{j\omega - \lambda_1^*} & & 0 \\ & \ddots & \\ 0 & & \frac{1}{j\omega - \lambda_m^*} \end{bmatrix} \in \mathbb{C}^{m\times m} \tag{3.9}$$

The reference vector $\underline{g}_r$ is a complex function of the cross power spectrum matrix of the unknown random input forces and the modal parameters of the structure. Its physical interpretation is less obvious than the modal participation factors.

It should be noticed that the modal decomposition of the power densities of the outputs has a symmetry in the poles i.e. both the positive and negative poles are present in the model. This symmetry is referred to as a 4-quadrant symmetry. Given this similarity between the modal decomposition of the cross spectral densities of the output time histories and the modal decomposition of the FRFs, the modal parameter estimation techniques developed for FRFs can be extended to handle the case where the cross power spectral density matrix is available from output-only data.

In most modal identification applications the modal parameters are set to be identified within a specific frequency range of interest $[\omega_1, \omega_2]$. In those cases the CPSD function matrix can be written alternatively as

$$S(j\omega,\underline{\theta}) = \sum_{r=1}^{m}\left[\frac{\underline{u}_r \underline{g}_r^T}{j\omega-\lambda_r} + \frac{\underline{u}_r^* \underline{g}_r^{*T}}{j\omega-\lambda_r^*} + \frac{\underline{g}_r \underline{u}_r^T}{-j\omega-\lambda_r} + \frac{\underline{g}_r^* \underline{u}_r^{*T}}{-j\omega-\lambda_r^*}\right] - \frac{n_1(j\omega)}{n_2(j\omega)}A + n_1(j\omega)B \qquad (3.10)$$

where m is the number of contributing modes in the frequency range of interest and $A \in \mathbb{R}^{N_{out}\times N_{out}}$, $B \in \mathbb{R}^{N_{out}\times N_{out}}$ are real symmetric matrices, called the upper and lower residual term, accounting for the approximate contribution of the out-of-bound modes to the selected frequency range of interest (Heylen et al. 1997). For the case that the CPSD function matrix is given for the acceleration response, the frequency functions $n_1(j\omega)$ and $n_2(j\omega)$ are given by

$$n_1(j\omega) = 1 \qquad (3.11)$$

and

$$n_2(j\omega) = (j\omega)^4 = \omega^4 \in \mathbb{R} \qquad (3.12)$$

Note that the parameter set $\underline{\theta}$ has been introduced in (3.10) to include all the necessary modal and other parameters that completely define the CPSD matrix $S(j\omega,\underline{\theta})$. From the structure of the CPSD matrix in (3.10), the parameter set $\underline{\theta}$ includes the poles λ_r, the modeshape vectors $\underline{u}_r$, the reference vectors $\underline{g}_r$ and the elements of the real matrices A and B.

3.3 Identification of structural modes

A modal model output-error identification approach seeks the optimal values of the parameter set $\underline{\theta}$ that minimize a measure of fit between the CPSD matrix $S_k(\underline{\theta}) \equiv S_k(j\omega_k,\underline{\theta})$, $k = 1,\cdots,N_\omega$ predicted by the modal model and the corresponding CPSD matrix $\hat{S}_k \equiv \hat{S}_k(j\omega_k)$ estimated from the measured data at the N_{out} DOFs. That is, the modal model identification is formulated as a minimization problem of finding the values of $\underline{\theta}$ that minimizes the weighted measure of fit

$$J^{NL}(\underline{\theta}) = \frac{1}{V}\sum_{k=0}^{N_\omega} \mathrm{tr}\left\{\left[\varepsilon_k^{NL}\right]^{*T} W \left[\varepsilon_k^{NL}\right]\right\} = \frac{1}{V}\sum_{k=0}^{N_\omega}\left\|\underline{\varepsilon}_k^{NL}\right\|^2 \text{、} \qquad (3.13)$$

where

$$\varepsilon_k^{NL}\left(\underline{\theta}\right) = S_k\left(\underline{\theta}\right) - \hat{S}_k \tag{3.14}$$

is a nonlinear function of the parameter set $\underline{\theta}$, $S_k\left(\underline{\theta}\right) \equiv S\left(j\omega_k, \underline{\theta}\right)$, $\omega_k = k\Delta\omega$, $\Delta\omega$ is the frequency discretization step (sampling frequency interval), N_ω is the number of sample data over the analyzed frequency band, k is the frequency index set, $V = \sum_{k=0}^{N_\omega} \left\| \hat{S}_k \right\|^2$ is the normalization factor, and $\left\|\underline{Y}\right\|^2 = tr\left\{\underline{Y}^T W \underline{Y}\right\}$ with $W \in \mathbb{R}^{N_{out} \times N_{out}}$ being a user selected weighting matrix. Herein, the weighting matrix W is selected to be the identity matrix, $W = I$.

From the computer implementation point of view, it is necessary to describe the modal model predicted CPSD function matrix $S_k\left(\underline{\theta}\right) \equiv S\left(j\omega_k, \underline{\theta}\right)$ in terms of real-valued variables in the parameter set $\underline{\theta}$. Introducing the modal frequencies ω_r and the modal damping ratios ζ_r, instead of the complex poles λ_r, as well as the real and imaginary parts of the modeshape vector $\underline{u}_r = \underline{u}_{r,\mathrm{Re}} + j\underline{u}_{r,\mathrm{Im}}$ and the reference vectors $\underline{g}_r^T = \underline{g}_{r,\mathrm{Re}}^T + j\,\underline{g}_{r,\mathrm{Im}}^T$, the CPSD matrix predicted by the modal model is completely described by the real parameter set

$$\underline{\theta} = \left\{ \omega_r,\ \ \zeta_r,\ \ \underline{u}_{r,\mathrm{Re}},\ \ \underline{u}_{r,\mathrm{Im}},\ \ \underline{g}_{r,\mathrm{Re}}^T,\ \ \underline{g}_{r,\mathrm{Im}}^T,\ \ r = 1,...,m,\ \ A,\ \ B \right\} \tag{3.15}$$

where m is the number of contributing modes which is also an unknown in the identification process. The total number of model parameter involved in the prediction of the response at N_{out} DOFs given m modes is $2m(1+2N_{out}) + N_{out}^2 + N_{out}$. Computational efficient algorithms for solving this highly nonlinear, non-convex optimization problem involving the objective function $J^{NL}\left(\underline{\theta}\right)$ in (3.13) with respect to the parameter set $\underline{\theta}$ in (3.15) are presented in the next Section 3.4.

In order to use equation (3.13) and (3.14) for the identification of modal parameters from output-only data, accurate estimates of the cross power spectral densities $\hat{S}_k$, between the responses, are to be obtained from finite sequences of measured time samples. Basically, two classical methods exist for the estimation of auto and cross power spectral density estimates (Marple 1987), the periodogram and the correlogram approach. The periodogram (Marple 1987) method operates directly on the data set to yield power spectrum estimates. The correlogram approach (Blackman and Tukey 1958) first makes an estimate of the correlation functions in the time-domain and then proceeds by Fourier transforming the correlation sequences into power spectral densities. For both approaches, the user is faced with a tradeoff to produce statistically reliable estimates of highest possible spectral resolution from finite sequences of measured time data. For completeness, these methods are briefly presented in Appendix 3.A.

3.4 Optimization algorithm

A three step approach is used to estimate the modal properties by minimising the objective function (3.13). The first step provides estimates of the modal frequencies and modal damping ratios by re-formulating the objective function in a convenient way so that these modal properties can be obtained by solving a system of linear algebraic equations using the common denominator model (Heylen et al., 1997). Stabilization diagrams are also used as part of the approach to estimate the number of contributing modes and distinguish between physical and mathematical modes. This first step is an extension of the PolyMAX or polyreference least-squares complex frequency domain method, developed by Peeters et al. (2004) for the case of frequency response functions. It is developed herein to treat the CPSD functions of non-classically damped modal models describing the system response characteristics based on ambient vibration data. In particular, advance is taken of the structure of the poles describing the CPSD functions of the discrete time system in order to simplify the estimation of the poles. The second step provides estimates of the modeshapes and the operational referense vectors given the estimates of the modal frequencies and modal damping ratios, by solving a system of linear algebraic equations. It should be noted that two different approaches have been developed for the computation of the modeshapes and operational referense vectors in this second step. In the first approach the residue matrices

$$R_r = \underline{u}_r \underline{g}_r^T \in \mathbb{C}^{N_{out} \times N_{out}} \tag{3.16}$$

are assumed to be the unknown parameters and the CPSD function matrix in (3.10) is given in the form

$$S(j\omega, \underline{\theta}) = \sum_{r=1}^{m} \left[\frac{R_r}{j\omega - \lambda_r} + \frac{R_r^*}{j\omega - \lambda_r^*} + \frac{R_r^T}{-j\omega - \lambda_r} + \frac{R_r^{*T}}{-j\omega - \lambda_r^*} \right] - \frac{n_1(j\omega)}{n_2(j\omega)} A + n_1(j\omega) B \tag{3.17}$$

Recognizing that the objective function in (3.13) is quadratic with respect to R_r, A and B, one can apply the stationarity conditions to estimate these residue terms, formulating and solving the resulting linear system of equations for R_r, A and B. Then the modeshapes $\underline{u}_r$ and the operational reference vectors $\underline{g}_r$ are derived directly by the Singular Value Decomposition (SVD) of the resulting numerator matrix R_r. In the second approach, advantage is taken of the fact that the error function in (3.13) with $S(j\omega, \underline{\theta})$ given by (3.10) is quadratic with respect to the modeshapes $\underline{u}_r$ and the matrices A and B. This observation is used to develop explicit expressions that relate the parameters $\underline{u}_r$, A and B to the vectors $\underline{g}_r$, the modal frequencies ω_r and the damping ratios ζ_r, so that the number of parameters involved in the optimization is reduced from $2m(1+2N_{out}) + N_{out}^2 + N_{out}$ to $2m(N_{out}+1)$. This reduction is considerable for a relatively large number of measurement points. The modeshapes $\underline{u}_r$ and the matrices A and B are computed by taking stationary conditions that lead to a linear system of equations from which these parameters are readily derived. The first two steps usually give accurate estimates of the modal characteristics. However, a third step is often recommended to improve these estimates,

especially for closely spaced and overlapping modes, by efficiently solving the full nonlinear optimization problem (3.13) with respect to all modal parameters ω_r, ζ_r, $\underline{u}_r$, $\underline{g}_r$, A and B involved in (3.10). The initial estimates of the modal parameters are those obtained from the first and second steps. Such initial estimates are very good estimates that guarantee accelarated convergence to the global optimum. These steps are described in more details in the sub-sections that follow.

3.4.1 Step 1: Identification of contributing modes, modal frequencies and damping ratios

Consider the modal decomposition of the CPSD matrix assuming white noise inputs given in (3.4) by means of a common-denominator function

$$S(j\omega,\underline{\theta}) = \sum_{r=1}^{m}\left[\frac{\underline{u}_r \underline{g}_r^T}{j\omega-\lambda_r} + \frac{\underline{u}_r^* \underline{g}_r^{*T}}{j\omega-\lambda_r^*} + \frac{\underline{g}_r \underline{u}_r^T}{-j\omega-\lambda_r} + \frac{\underline{g}_r^* \underline{u}_r^{*T}}{-j\omega-\lambda_r^*}\right] = \frac{N_m(s(j\omega))}{d_m(s(j\omega))} \qquad (3.18)$$

which is a rational fraction of two polynomials in $s = s(j\omega)$ of order $p = 2m$, of which the denominator polynomial $d_m(s) \in \mathbb{C}$ given by

$$d_m(s) = \sum_{r=0}^{p} s^r a_r^{[m]} \qquad (3.19)$$

is common for all output quantities, and the numerator polynomial matrix $N_m(j\omega) \in \mathbb{C}^{N_{out}\times N_{out}}$ given by

$$N_m(s) = \sum_{r=0}^{p} s^r \beta_r^{[m]} \qquad (3.20)$$

with $s = s(j\omega) = j\omega$ is the polynomial basis in the continuous time formulation, $s = s(j\omega) = \exp(j\omega\Delta t)$ is the polynomial basis in the discrete time formulation, while $\underline{\alpha} = (a_0, a_1, \cdots, a_p)^T \in \mathbb{R}^{p+1}$ and $\beta_r \in \mathbb{R}^{N_{out}\times N_{out}}$, $r = 0,\cdots,p$, are the coefficients of the denominator and numerator polynomials, respectively.

For the continuous time formulation given in (3.18), it is obvious that the poles of the structure are $\lambda_{1,r} = \lambda_r$, $\lambda_{2,r} = \lambda_r^*$, $\lambda_{3,r} = -\lambda_r$ and $\lambda_{4,r} = -\lambda_r^*$ for $r = 0,\cdots,m$. Using the discrete time formulation the poles μ_r of the structure are obtained from the transformation

$$\mu_r = e^{\lambda_r \Delta t} \qquad (3.21)$$

and thus correspond to μ_r, μ_r^*, $1/\mu_r$ and $1/\mu_r^*$.

Using the relation (3.18), it is clear that the poles of the structure are given by the roots of the denominator polynomial $d_m(s)$. Given the values of the coefficients $a_r^{[m]}$ of the denominator polynomial, these roots are readily obtained by the solution of an eigenvalue problem for the

companion matrix (Kailath, 1980; Haylen et al., 1997). So the problem of finding the poles is reduced to the problem of finding the coefficients of the denominator polynomial $d_m(s) \in \mathbb{C}$. This can be readily done by using the formulation for the CPSD functions matrix in (3.18) and substituting in the error function (3.14) to obtain

$$\varepsilon_k^{NL}\left(\underline{\theta}\right) = \frac{N_m(j\omega, \beta^{[m]})}{d_m(j\omega; \underline{\alpha}^{[m]})} - \hat{S}_k \tag{3.22}$$

where the parameters $\underline{\theta}$ in (3.22) consist of the coefficients $\underline{\alpha}^{[m]}$ and $\beta^{[m]}$, $r = 0, \cdots, p$.

It should be noted that the error function (3.22) is a nonlinear function of $\underline{\alpha}$ and a linear function of β_r, $r = 0, \cdots, p$. Instead of using the nonlinear error function (3.22), one can redefine the error function

$$\varepsilon_k^{L}\left(\underline{\theta}\right) = d_m(j\omega; \underline{\alpha}_r^{[m]})\varepsilon_k^{NL}\left(\underline{\theta}\right) = N_m(j\omega, \beta^{[m]}) - d_m(j\omega; \underline{\alpha}^{[m]})\hat{S}_k \tag{3.23}$$

which is a linear function of the parameters $\underline{\alpha}^{[m]}$ and $\beta_r^{[m]}$, $r = 0, \cdots, p$. So the optimization problem can be readily solved analytical and obtain the coefficients $\underline{\alpha}$ and β_r, $r = 0, \cdots, p$ from the solution of a linear system of equations. This linear system of equations is developed in the next subsection.

3.4.1.1 Reduced normal equations

Each row of the common denominator model in (3.18) can be expressed in the form:

$$\left\langle S_o\left(\omega\right)\right\rangle = \frac{\left\langle \underline{N}_o^T\left(\omega\right)\right\rangle}{d\left(\omega\right)}, \forall o = 1, 2, \cdots, N_{out} \tag{3.24}$$

where

$$\left\langle \underline{N}_{m,o}^T\left(\omega\right)\right\rangle = \sum_{r=0}^{p} s^r \left\langle \underline{\beta}_{or}^{[m]T}\right\rangle \tag{3.25}$$

$$d_m\left(\omega\right) = \sum_{r=0}^{p} s^r \alpha_r^{[m]} \tag{3.26}$$

The polynomial coefficients $\underline{\beta}_{or} \in \mathbb{R}^{N_{out}\times 1}$ and $a_r \in \mathbb{R}^{1\times 1}$ are assembled in the following matrices:

$$\underline{\beta}_o = \begin{pmatrix} \underline{\beta}_{o0} \\ \underline{\beta}_{o1} \\ \cdots \\ \underline{\beta}_{op} \end{pmatrix} \in \mathbb{R}^{\left(N_{out}(p+1)\right)\times 1} \quad , \forall o = 1, 2, \cdots, N_{out} \tag{3.27}$$

$$\underline{\alpha} = \begin{pmatrix} \alpha_0 \\ \alpha_1 \\ \cdots \\ \alpha_p \end{pmatrix} \in \mathbb{R}^{(p+1)\times 1} \tag{3.28}$$

$$\underline{\theta} = \begin{bmatrix} \underline{\beta}_1 \\ \vdots \\ \underline{\beta}_{N_{out}} \\ \underline{a} \end{bmatrix} \in \mathbb{R}^{\left(\left(N_{out}^2+1\right)(p+1)\right)\times 1} \tag{3.29}$$

Error functions for each ω_k can be written as a vector $\underline{E}_o^L(\theta) \in C^{N_\omega \times 1}$, of the form

$$\underline{E}_o^L(\underline{\theta}) = \begin{pmatrix} \varepsilon_o^L(\omega_1, \underline{\theta}) \\ \varepsilon_o^L(\omega_2, \underline{\theta}) \\ \cdots \\ \varepsilon_o^L(\omega_{N_\omega}, \underline{\theta}) \end{pmatrix} = \begin{bmatrix} X & Y_o \end{bmatrix} \begin{Bmatrix} \underline{\beta}_o \\ \underline{a} \end{Bmatrix} \tag{3.30}$$

and X and Y_o, $o = 1, \cdots, N_{out}$, are complex matrices given by

$$X = \begin{bmatrix} \left[\Omega_1(\omega_1) \cdots \Omega_p(\omega_1)\right] \\ \vdots \\ \left[\Omega_1(\omega_{N_\omega}) \cdots \Omega_p(\omega_{N_\omega})\right] \end{bmatrix} \in C^{N_\omega \times (N_{out}(p+1))} \tag{3.31}$$

$$Y_o = \begin{bmatrix} -\hat{S}_o(\omega_1)\left[\Omega_1(\omega_1) \cdots \Omega_p(\omega_1)\right] \\ \vdots \\ -\hat{S}_o(\omega_{N_\omega})\left[\Omega_1(\omega_{N_\omega}) \cdots \Omega_p(\omega_{N_\omega})\right] \end{bmatrix} \in C^{N_\omega \times (p+1)} \tag{3.32}$$

Similar to (3.13) the following cost function can be written according to the error function (3.23):

$$J^L(\underline{\theta}) = \sum_{o=1}^{l} \sum_{k=1}^{N_\omega} tr\left\{ \left(\varepsilon_o^L(\omega_k, \underline{\theta})\right)^H \left(\varepsilon_o^L(\omega_k, \underline{\theta})\right) \right\} \tag{3.33}$$

The minimization of the cost function leads to a Weighted Least-Squares Problem. Substituting equations (3.30), (3.31) and (3.32) in (3.33) yields

$$J^L(\underline{\theta}) = \sum_{o=1}^{N_{out}} tr\left\{\left(E_o^L(\underline{\theta})\right)^{*T}\left(E_o^L(\underline{\theta})\right)\right\} = \sum_{o=1}^{N_{out}} tr\left\{\left(\underline{\beta}_o^T \quad \underline{\alpha}^T\right)\begin{pmatrix} X^{*T} \\ Y_o^{*T}\end{pmatrix}\begin{pmatrix} X & Y_o\end{pmatrix}\begin{pmatrix}\underline{\beta}_o \\ \underline{\alpha}\end{pmatrix}\right\} = \sum_{o=1}^{N_{out}} tr\left\{\underline{\theta}^T J_o^{*T} J_o \underline{\theta}\right\} \tag{3.34}$$

where $J \in C^{N_\omega \times (N_{out}+1)(p+1)}$ is the Jacobian matrix

$$J_o = \begin{pmatrix} X & Y_o\end{pmatrix} \tag{3.35}$$

In case of real-valued coefficients $\underline{\theta}$, it can be shown that the expression $J_o^{*T} J_o$ can be substituted by its real part. Hence, the cost function (3.34) becomes

$$J^L(\underline{\theta}) = \sum_{o=1}^{N_{out}} tr\left\{\underline{\theta}^T \operatorname{Re}\left(J_o^{*T} J_o\right)\underline{\theta}\right\} \tag{3.36}$$

where

$$\operatorname{Re}(J_o^{*T} J_o) = \begin{pmatrix} R & Z_o \\ Z_o^T & T_o\end{pmatrix} \in \mathbb{R}^{(Nout+1)(p+1)\times(N_{out}+1)(p+1)} \tag{3.37}$$

with

$$R = \operatorname{Re}(X^{*T} X) \in \mathbb{R}^{N_{out}(p+1)\times N_{out}(p+1)} \tag{3.38}$$

$$Z_o = \operatorname{Re}(X^{*T} Y_o) \in \mathbb{R}^{N_{out}(p+1)\times(p+1)} \tag{3.39}$$

$$T_o = \operatorname{Re}(Y_o^{*T} Y_o) \in \mathbb{R}^{(p+1)\times(p+1)} \tag{3.40}$$

The cost function is minimized by setting the derivatives of (3.36) with respect to the unknown polynomial coefficients θ equal to zero:

$$\frac{\partial J^L(\underline{\theta})}{\partial \underline{\beta}_o} = 2(R\underline{\beta}_o + Z_o\underline{\alpha}) = 0 \qquad \forall o = 1,\cdots,N_{out} \tag{3.41}$$

$$\frac{\partial J^L(\underline{\theta})}{\partial \underline{\alpha}} = 2\sum_{o=1}^{l}(Z_o^T\underline{\beta}_o + T_o\underline{\alpha}) = 0 \qquad \forall o = 1,\cdots,N_{out} \tag{3.42}$$

These equations are the so - called normal equations which can be written (using equations (3.37) and (3.40)) in the form:

$$2\operatorname{Re}(J_o^{*T} J_o)\underline{\theta} = 0 \tag{3.43}$$

We focus on the polynomial denominator $\underline{\alpha}$ from which result the poles and the modal coefficients in order to set up a stabilization diagram. Consequently, least-squares problem can be simplified by substituting the coefficients $\underline{\beta}_o$, which result from (3.41)

$$\beta_o = -R^{-1} Z_o \alpha \tag{3.44}$$

into (3.42). Thus, equation (3.42) becomes:

$$\mathrm{M}\underline{\alpha} = \underline{0} \tag{3.45}$$

where $M \in \mathbb{R}^{(p+1)\times(p+1)}$ is given by

$$\mathrm{M} = 2\sum_{o=1}^{l}\left(\mathrm{T}_o - \mathrm{Z}_o^{\mathrm{T}}\mathrm{R}^{-1}\mathrm{Z}_o\right) \tag{3.46}$$

and can be computed from the measured data. The solution of this equation gives the denominator polynomial coefficients $\underline{\alpha}$ in a least-squares sense. To avoid finding the trivial solution $\underline{\alpha} = \underline{0}$, a constraint is imposed on the parameters. Such a constraint also removes the parameter redundancy that exists in the common denominator model (multiplying numerator and denominator with the same scalar yields different numerator and denominator polynomials, but the same CPSD function matrix). Specifically, to remove the parameter redundancy the value of the coefficient α_0 is selected to be $\alpha_0 = 1$.

Once these coefficients $\underline{\alpha}$ are obtained, the poles μ_r of the polynomial $d(s)$ are readily obtained by solving an eigenvalue problem of order $p = 4m$ of the companion matrix of the polynomial $d(s)$ (Heylen et al. 1997). The eigenvalues λ_r are obtained from μ_r using the relations (3.21).

3.4.1.2 Stabilization diagrams

In modal analysis applications the accuracy of the estimated modal parameters is important. When trying to estimate the modal parameters from real data, it is generally a good idea to over-specify the model order considerably, i.e. to try to fit high order models that contain much more modes than present in the measured data. Stabilization diagrams (Heylen et al., 1997) can be used to distinguish between the mathematical and the physical modes and eventually keep only the physical modes of the system. In particular, the poles corresponding to a certain model order are compared to the poles of a one order lower model. If their differences are within pre-set limits, the poles are considered as stable one. The spurious mathematical poles will not stabilize at all during this process and can be sorted out of the estimated modal parameter data set more easily. Thus the previous methodology not only provide estimates of the modal frequencies and modal damping ratios but also gives the number of contributing modes through the appropriate-conventional use of stabilization diagrams. Examples of stabilization diagrams will be shown in Section 3.5.

3.4.1.3 Simplification using special structure of common denominator model

It should be noted that the denominator polynomial $d_m(s)$ in (3.18) using the transformation (3.21) in the discrete time formulation can be given in the form

$$d_m(s) = \prod_{r=1}^{m} (s-\mu_r)(s-\mu_r^*)(s-\frac{1}{\mu_r})(s-\frac{1}{\mu_r^*}) \tag{3.47}$$

which is of order $p = 4m$. Carrying out the product of the factors, the denominator polynomial $d_m(s)$ can be written in the form

$$d_m(s) = \prod_{r=1}^{m} \left(a_{r,4}s^4 + a_{r,3}s^3 + a_{r,2}s^2 + a_{r,1}s \ + a_{r,0} \right) \tag{3.48}$$

with

$$a_{r,4} = a_{r,0} = 1 \tag{3.49}$$

$$a_{r,3} = a_{r,1} = \mu_r + \mu_r^* + \frac{1}{\mu_r} + \frac{1}{\mu_r^*} = 2\,\mathrm{Re}\left\{\mu_r\right\} + 2\,\mathrm{Re}\left\{\frac{1}{\mu_r}\right\} \tag{3.50}$$

$$a_{r,2} = \left|\mu_r\right|^2 + \frac{1}{\left|\mu_r\right|^2} + \left(\mu_r + \mu_r^*\right)\left(\frac{1}{\mu_r} + \frac{1}{\mu_r^*}\right) = \left|\mu_r\right|^2 + \frac{1}{\left|\mu_r\right|^2} + 2 + 2\,\mathrm{Re}\left\{\frac{\mu}{\mu^*}\right\} \tag{3.51}$$

Consequently equation (3.48) can be written in general form as

$$d_m(s) = \prod_{r=1}^{m} \left(a_{r,0}s^4 + a_{r,1}s^3 + a_{r,2}s^2 + a_{r,1}s \ + a_{r,0} \right) \tag{3.52}$$

Proposition: The polynomial $d_m(s)$ admits the representation

$$d_m(s) = \sum_{k=0}^{2m-1} a_k^{[m]} s^k + a_{2m}^{[m]} s^{2m} + \sum_{k=0}^{2m-1} a_k^{[m]} s^{4m-k} \tag{3.53}$$

which specifies that the coefficients of the term s^k are the same as the coefficients of the term s^{p-k}, that is, $a_k^{[m]} = a_{4m-k}^{[m]}$, $k = 0,1,\ldots,2m$.

Proof: The proposition will be shown to be true using mathematical induction.

For $m = 1$ the formulation (3.53) gives

$$d_1(s) = a_0^{[1]}s^4 + a_1^{[1]}s^3 + a_2^{[1]}s^2 + a_1^{[1]}s \ + a_0^{[1]} = \sum_{k=0}^{1} a_k^{[1]} s^k + a_2^{[1]}s^2 + \sum_{k=0}^{1} a_k^{[1]} s^{4-k} \tag{3.54}$$

which is true due to the representation (3.52) and selecting $a_0^{[1]} = a_{1,0}$, $a_1^{[1]} = a_{1,1}$ and $a_2^{[1]} = a_{1,2}$.

Assuming that formulation (3.53) holds for m it will be shown that it also stands for $m+1$, that is

$$d_{m+1}(s)=\sum_{k=0}^{2(m+1)-1}a_k^{[m+1]}s^k+a_{2(m+1)}^{[m+1]}s^{2(m+1)}+\sum_{k=0}^{2(m+1)-1}a_k^{[m+1]}s^{4(m+1)-k} \tag{3.55}$$

Using the representation (3.52) the denominator $d_{m+1}(s)$ can be written as

$$d_{m+1}(s)=d_m(s)\left(a_{m+1,0}s^4+a_{m+1,1}s^3+a_{m+1,2}s^2+a_{m+1,1}s\ +a_{m+1,0}\right) \tag{3.56}$$

Setting $b_1=a_{m+1,1}$, $b_2=a_{m+1,2}$, $a_{m+1,0}=1$ and substituting (3.53) into (3.56) yields

$$d_{m+1}(s)=\left(\sum_{k=0}^{2m-1}a_k^{[m]}s^k+a_{2m}^{[m]}s^{2m}+\sum_{k=0}^{2m-1}a_k^{[m]}s^{4m-k}\right)\left(s^4+b_1s^3+b_2s^2+b_1s\ +1\right) \tag{3.57}$$

and by multiplying the expressions in the parentheses yields

$$\begin{aligned}d_{m+1}(s)=&\sum_{k=0}^{2m-1}a_k^{[m]}s^k+\sum_{k=0}^{2m-1}b_1a_k^{[m]}s^{k+1}+\sum_{k=0}^{2m-1}b_2a_k^{[m]}s^{k+2}+\sum_{k=0}^{2m-1}b_1a_k^{[m]}s^{k+3}+\sum_{k=0}^{2m-1}a_k^{[m]}s^{k+4}+\\&a_{2m}^{[m]}s^{2m}+b_1a_{2m}^{[m]}s^{2m+1}+b_2a_{2m}^{[m]}s^{2m+2}+b_1a_{2m}^{[m]}s^{2m+3}+a_{2m}^{[m]}s^{2m+4}+\\&\sum_{k=0}^{2m-1}a_k^{[m]}s^{4(m+1)-k-4}+\sum_{k=0}^{2m-1}b_1a_k^{[m]}s^{4(m+1)-k-3}+\sum_{k=0}^{2m-1}b_2a_k^{[m]}s^{4(m+1)-k-2}+\\&\sum_{k=0}^{2m-1}b_1a_k^{[m]}s^{4(m+1)-k-1}+\sum_{k=0}^{2m-1}a_k^{[m]}s^{4(m+1)-k}\end{aligned} \tag{3.58}$$

Observing the symmetry in (3.58) where all pairs of order s^k, $s^{4(m+1)-k}$ for $\forall k=0,\ldots,2(m+1)$ have the same polynomial coefficients, with the only exception of the term $b_2a_{2m}^{[m]}s^{2m+2}$, the above equation can obviously be written in the general form (3.55), where the coefficients $a_k^{[m+1]}$ can be directly derived from the coefficients $a_k^{[m]}$ and the values of b_1 and b_2.

$$d_{m+1}(s)=\sum_{k=0}^{2(m+1)-1}a_k^{[m+1]}s^k+a_{2(m+1)}^{[m+1]}s^{2(m+1)}+\sum_{k=0}^{2(m+1)-1}a_k^{[m+1]}s^{4(m+1)-k} \tag{3.59}$$

This implementation reduces the number of the unknown polynomial coefficients $\underline{\alpha}=(\alpha_0,\ \alpha_1,\ldots,\ \alpha_{4m})^T$ in (3.45) from $p+1=4m+1$ to $\frac{p}{2}+1=2m+1$ coefficients $\underline{\alpha}'=(\alpha_0,\ \alpha_1,\ldots,\ \alpha_{2m})^T$ taking advantage of the fact that $\alpha_k=\alpha_{4m-k}$. Substituting $\alpha_k=\alpha_{4m-k}$ into (3.45) and considering only the first $2m+1$ equations, the unknown vector $\underline{\alpha}'=(\alpha_0,\ \alpha_1,\ldots,\ \alpha_{2m})^T$ of the coefficients defining the denominator polynomial $d_m(s)$ is given by the set of linear equations

$$\tilde{\mathrm{M}}\underline{\alpha}'=\underline{0} \tag{3.60}$$

where the matrix $\tilde{\mathrm{M}} \in \mathbb{R}^{(2m+1)\times(2m+1)}$ is derived from the elements of the matrix M as follows:

$$\begin{aligned} \tilde{\mathrm{M}}_{l,k} &= \mathrm{M}_{l,k} + \mathrm{M}_{l,tm-k} \ , \qquad k = 1,2,\ldots,2m \\ \tilde{\mathrm{M}}_{l,2m+1} &= \mathrm{M}_{l,2m+1} \end{aligned} \tag{3.61}$$

This special structure of the denominator polynomial $d_m(s)$ reduces by a factor of two the computational time for obtaining the modes of the structure using stabilization diagrams. In addition, the mathematical poles estimated using the special structure (3.60) of the reduced normal equations is a subset of the mathematical poles estimated with the original set (3.45) of reduced normal equations. This has an effect of limiting the number of spurious mathematical modes that are manifested in the stabilization diagrams. This results in better ways of distinguishing between the mathematical and the physical modes. It should be noted using the above simplified formulation for the denominator polynomial $d_m(s)$ given in (3.53) does not impose that the resulting poles to come in groups of four giving μ_r, μ_r^*, $1/\mu_r$ and $1/\mu_r^*$ for $r = 0,\cdots,m$. Such poles are also considered as spurious mathematical poles.

3.4.2 Step 2: Identification of modeshapes and operational reference vectors

In the second step, the number of contributing modes m and the estimated values of the poles λ_r are considered to be known and are used with (3.10) in order to obtain estimates of the remaining unknown modal parameters, the modeshapes $\underline{u}_r$, the operational reference vectors $\underline{g}_r$ and the real matrices A and B. Two different approaches have been developed for the computation of these quantities in this second step.

3.4.2.1 First approach

In the first approach, given the number of contributing modes m and the estimated values of the poles λ_r, estimates of the residue matrices R_r and the real matrices A and B are obtained by minimizing (3.13) with $\underline{\varepsilon}_k^{NL}(\underline{\theta})$ given by (3.14) with $S_k(\underline{\theta})$ given by

$$S(j\omega) = \sum_{r=1}^{m}\left[\frac{R_r}{j\omega-\lambda_r} + \frac{R_r^*}{j\omega-\lambda_r^*} + \frac{R_r^T}{-j\omega-\lambda_r} + \frac{R_r^{*T}}{-j\omega-\lambda_r^*}\right] - \frac{n_1(j\omega)}{n_2(j\omega)}A + n_1(j\omega)B \tag{3.62}$$

Note that (3.62) is the same as (3.10) with $\underline{u}_r\,\underline{g}_r^T$ replaced by R_r.

It is evident from the structure of the problem that the objective function is quadratic in the elements of R_r, A and B. So, using the stationarity conditions, one can develop systems of linear equations for the elements of R_r, A and B. For completeness, these systems of equations are given next as a function of the measurements and the values of the system poles λ_r. An important result of this approach is that the optimal estimates of R_r, A and B that

minimize the objective function (3.13) given the number of contributing modes and the values of λ_r are obtained by a non-iterative approach.

First the complex-valued matrix $R_r \;\; r=1,\ldots,m$ in (3.62) involved in the description of the modal model are expressed in terms of the real and imaginary parts as follows:

$$R_r = L_r + jG_r \tag{3.63}$$

with $L_r, G_r \in \mathbb{R}^{Nout \times Nout}$. The CPSD function matrix of equation (3.62) is then written as

$$S(j\omega) = \sum_{r=1}^{m} \left[L_r \mu_r^+ + G_r \mu_r^- + L_r^T k_r^+ + G_r^T k_r^- \right] - \frac{n_1(j\omega)}{n_2(j\omega)} A + n_1(j\omega) B \tag{3.64}$$

where

$$\mu_r^+ = n_1(j\omega) \left[\frac{1}{j\omega - \lambda_r} + \frac{1}{j\omega - \lambda_r^*} \right] \tag{3.65}$$

$$\mu_r^- = n_1(j\omega)\, j \left[\frac{1}{j\omega - \lambda_r} - \frac{1}{j\omega - \lambda_r^*} \right] \tag{3.66}$$

$$k_r^+ = n_1(j\omega) \left[\frac{1}{-j\omega - \lambda_r} + \frac{1}{-j\omega - \lambda_r^*} \right] \tag{3.67}$$

$$k_r^- = n_1(j\omega)\, j \left[\frac{1}{-j\omega - \lambda_r} - \frac{1}{-j\omega - \lambda_r^*} \right] \tag{3.68}$$

For the case that the CPSD function matrix is estimated using the acceleration response measurements, the frequency functions $n_1(j\omega)$ and $n_2(j\omega)$ are given by (3.11) and (3.12). It should be also noted that for the case that $n_1(j\omega) \in \mathbb{R}$ and $n_2(j\omega) \in \mathbb{R}$ are real the following relation holds true:

$$k_r^{+*} = \mu_r^+ \quad \text{and} \quad k_r^{-*} = \mu_r^- \tag{3.69}$$

Consider first the case $i \neq l$ and define the vectors of unknown quantities partitioned as follows:

$$\underline{z}_{li}^T = \left[L_{1,li} \cdots L_{m,li} \quad L_{1,il} \cdots L_{m,il} \quad G_{r=1,li} \cdots G_{m,li} \quad G_{1,il} \cdots G_{m,il} \quad A_{li} \quad A_{il} \quad B_{li} \quad B_{il} \right] \tag{3.70}$$

for $l = 1,\ldots,N_{out}$ and $i = 1,\ldots,N_{out}$, where $L_{r,li}$ is the (l,i) element of the matrix L_r involved in (3.63), while similar definitions hold for the quantities $G_{r,li}$, A_{li} and B_{li}. It can be readily shown that the stationarity conditions yield the group of $N_{out}(N_{out}-1)$ algebraic systems of equations

$$\begin{bmatrix} M & X \\ X^T & H \end{bmatrix} \underline{z}_{li} = \begin{Bmatrix} \underline{a}_{li}^{+} \\ \underline{a}_{li}^{-} \\ \underline{b}_{li} \end{Bmatrix} \quad , \quad l = 1,\ldots,N_{out}, \;\; l = 1,\ldots,N_{out}, \;\; l \neq i \tag{3.71}$$

where the left-hand side matrix, partitioned by the four submatrices M , X , X^T and H , is common for all the systems of equations. The submatrices are given by

$$M = \begin{bmatrix} \sum_{k=1}^{N_\omega} \mathrm{Re}\left\{\underline{\mu}^{+}\underline{\mu}^{+T}\right\} & \sum_{k=1}^{N_\omega} \mathrm{Re}\left\{\underline{\mu}^{+}\underline{k}^{+T}\right\} & \sum_{k=1}^{N_\omega} \mathrm{Re}\left\{\underline{\mu}^{+}\underline{\mu}^{-T}\right\} & \sum_{k=1}^{N_\omega} \mathrm{Re}\left\{\underline{\mu}^{+}\underline{k}^{-T}\right\} \\ \sum_{k=1}^{N_\omega} \mathrm{Re}\left\{\underline{\mu}^{+}\underline{k}^{+T}\right\} & \sum_{k=1}^{N_\omega} \mathrm{Re}\left\{\underline{\mu}^{+}\underline{\mu}^{+T}\right\} & \sum_{k=1}^{N_\omega} \mathrm{Re}\left\{\underline{\mu}^{+}\underline{k}^{-T}\right\} & \sum_{k=1}^{N_\omega} \mathrm{Re}\left\{\underline{\mu}^{+}\underline{\mu}^{-T}\right\} \\ \sum_{k=1}^{N_\omega} \mathrm{Re}\left\{\underline{\mu}^{-}\underline{\mu}^{+T}\right\} & \sum_{k=1}^{N_\omega} \mathrm{Re}\left\{\underline{\mu}^{-}\underline{k}^{+T}\right\} & \sum_{k=1}^{N_\omega} \mathrm{Re}\left\{\underline{\mu}^{-}\underline{\mu}^{-T}\right\} & \sum_{k=1}^{N_\omega} \mathrm{Re}\left\{\underline{\mu}^{-}\underline{k}^{-T}\right\} \\ \sum_{k=1}^{N_\omega} \mathrm{Re}\left\{\underline{\mu}^{-}\underline{k}^{+T}\right\} & \sum_{k=1}^{N_\omega} \mathrm{Re}\left\{\underline{\mu}^{-}\underline{\mu}^{+T}\right\} & \sum_{k=1}^{N_\omega} \mathrm{Re}\left\{\underline{\mu}^{-}\underline{k}^{-T}\right\} & \sum_{k=1}^{N_\omega} \mathrm{Re}\left\{\underline{\mu}^{-}\underline{\mu}^{-T}\right\} \end{bmatrix} \tag{3.72}$$

$$X = \begin{bmatrix} -\sum_{k=1}^{N_\omega} \mathrm{Re}\left\{\frac{n_1}{n_2}\underline{\mu}^{+}\right\} & \underline{0} & \sum_{k=1}^{N_\omega} \mathrm{Re}\left\{n_1\underline{\mu}^{+}\right\} & \underline{0} \\ \underline{0} & -\sum_{k=1}^{N_\omega} \mathrm{Re}\left\{\frac{n_1}{n_2}\underline{\mu}^{+}\right\} & \underline{0} & \sum_{k=1}^{N_\omega} \mathrm{Re}\left\{n_1\underline{\mu}^{+}\right\} \\ -\sum_{k=1}^{N_\omega} \mathrm{Re}\left\{\frac{n_1}{n_2}\underline{\mu}^{-}\right\} & \underline{0} & \sum_{k=1}^{N_\omega} \mathrm{Re}\left\{n_1\underline{\mu}^{-}\right\} & \underline{0} \\ \underline{0} & -\sum_{k=1}^{N_\omega} \mathrm{Re}\left\{\frac{n_1}{n_2}\underline{\mu}^{-}\right\} & \underline{0} & \sum_{k=1}^{N_\omega} \mathrm{Re}\left\{n_1\underline{\mu}^{-}\right\} \end{bmatrix} \tag{3.73}$$

and

$$H=\begin{bmatrix} \sum_{k=1}^{N_\omega}\mathrm{Re}\left\{\frac{n_1^2}{n_2^2}\right\} & 0 & -\sum_{k=1}^{N_\omega}\mathrm{Re}\left\{\frac{n_1^2}{n_2}\right\} & 0 \\ 0 & \sum_{k=1}^{N_\omega}\mathrm{Re}\left\{\frac{n_1^2}{n_2^2}\right\} & 0 & -\sum_{k=1}^{N_\omega}\mathrm{Re}\left\{\frac{n_1^2}{n_2}\right\} \\ -\sum_{k=1}^{N_\omega}\mathrm{Re}\left\{\frac{n_1^2}{n_2}\right\} & 0 & \sum_{k=1}^{N_\omega}\mathrm{Re}\left\{n_1^2\right\} & 0 \\ 0 & -\sum_{k=1}^{N_\omega}\mathrm{Re}\left\{\frac{n_1^2}{n_2}\right\} & 0 & \sum_{k=1}^{N_\omega}\mathrm{Re}\left\{n_1^2\right\} \end{bmatrix} \tag{3.74}$$

Using the relations in (3.69), it can be readily shown that the matrix M is symmetric, i.e. $M=M^T$ and can be written as

$$M=\sum_{k=1}^{N_\omega}\mathrm{Re}\left\{\underline{\rho}\ \underline{\rho}^T\right\} \tag{3.75}$$

with

$$\underline{\rho}=\begin{Bmatrix} \underline{\mu}^{+} \\ \underline{\mu}^{+*} \\ \underline{\mu}^{-} \\ \underline{\mu}^{-*} \end{Bmatrix} \tag{3.76}$$

Also, it is obvious from (3.74) that H is also symmetric. Thus, the system matrix in (3.71) is symmetric.

The right-hand side vector for each (l,i) system in (3.71) is partitioned by the three subvectors $\underline{a}_{li}^{+}$, $\underline{a}_{li}^{-}$ and $\underline{b}_{li}$ given by

$$\underline{a}_{li}^{+}=\begin{Bmatrix} \sum_{k=1}^{N_\omega}\mathrm{Re}\left\{\underline{\mu}^{+}\widehat{S}_{li}\right\} \\ \sum_{k=1}^{N_\omega}\mathrm{Re}\left\{\underline{\mu}^{+}\widehat{S}_{il}\right\} \end{Bmatrix} \tag{3.77}$$

$$\underline{a}_{li}^{-}=\begin{Bmatrix} \sum_{k=1}^{N_\omega}\mathrm{Re}\left\{\underline{\mu}^{-}\widehat{S}_{li}\right\} \\ \sum_{k=1}^{N_\omega}\mathrm{Re}\left\{\underline{\mu}^{-}\widehat{S}_{il}\right\} \end{Bmatrix} \tag{3.78}$$

and

$$\underline{b}_{li} = \begin{Bmatrix} -\sum_{k=1}^{N_\omega} \mathrm{Re}\left\{ \dfrac{n_1}{n_2} \widehat{S}_{li} \right\} \\ -\sum_{k=1}^{N_\omega} \mathrm{Re}\left\{ \dfrac{n_1}{n_2} \widehat{S}_{il} \right\} \\ \sum_{k=1}^{N_\omega} \mathrm{Re}\left\{ n_1 \widehat{S}_{li} \right\} \\ \sum_{k=1}^{N_\omega} \mathrm{Re}\left\{ n_1 \widehat{S}_{il} \right\} \end{Bmatrix} \tag{3.79}$$

Finally, the vectors $\underline{\mu}^{\pm}$ and $\underline{k}^{\pm}$ involved in all above equations are given as

$$\underline{\mu}^{\pm} = \begin{Bmatrix} \mu_1^{\pm} \\ \vdots \\ \mu_m^{\pm} \end{Bmatrix} \text{ and } k^{\pm} = \begin{Bmatrix} k_1^{\pm} \\ \vdots \\ k_m^{\pm} \end{Bmatrix} \tag{3.80}$$

where m is the number of contributing modes .

Consider next the case of $l = i$ and define the vectors of the rest of the unknown quantities

$$\underline{z}_{ii}^T = \begin{bmatrix} L_{1,ii} \cdots L_{m,ii} & G_{1,ii} \cdots G_{m,ii} & A_{ii} & B_{ii} \end{bmatrix} \tag{3.81}$$

for $i = 1, \ldots, N_{out}$. It can be readily shown that the stationarity conditions yield a group of $N_{out} / 2$ algebraic systems of equations given by

$$\begin{bmatrix} M_d & X_d \\ X_d^T & H_d \end{bmatrix} \underline{z}_{ii} = \begin{Bmatrix} \underline{a}_{ii}^{+} \\ \underline{a}_{ii}^{-} \\ \underline{b}_{ii} \end{Bmatrix} \tag{3.82}$$

where the left-hand side matrix, partitioned by the four submatrices M_d , X_d , X_d^T and H_d , is common for all the systems of equations. The matrices are given by

$$M_d = \begin{bmatrix} \sum_{k=1}^{N_\omega} \mathrm{Re}\left\{ \underline{\mu}^{+} \underline{\mu}^{+T} \right\} + \sum_{k=1}^{N_\omega} \mathrm{Re}\left\{ \underline{\mu}^{+} \underline{k}^{+T} \right\} & \sum_{k=1}^{N_\omega} \mathrm{Re}\left\{ \underline{\mu}^{+} \underline{\mu}^{-T} \right\} + \sum_{k=1}^{N_\omega} \mathrm{Re}\left\{ \underline{\mu}^{+} \underline{k}^{-T} \right\} \\ \sum_{k=1}^{N_\omega} \mathrm{Re}\left\{ \underline{\mu}^{-} \underline{\mu}^{+T} \right\} + \sum_{k=1}^{N_\omega} \mathrm{Re}\left\{ \underline{\mu}^{-} \underline{k}^{+T} \right\} & \sum_{k=1}^{N_\omega} \mathrm{Re}\left\{ \underline{\mu}^{-} \underline{k}^{-T} \right\} + \sum_{k=1}^{N_\omega} \mathrm{Re}\left\{ \underline{\mu}^{-} \underline{\mu}^{-T} \right\} \end{bmatrix} \tag{3.83}$$

$$X_d = \begin{bmatrix} -\sum_{k=1}^{N_\omega} \mathrm{Re}\left\{ \frac{n_1}{n_2} \underline{\mu}^{+} \right\} & \sum_{k=1}^{N_\omega} \mathrm{Re}\left\{ n_1 \underline{\mu}^{+} \right\} \\ -\sum_{k=1}^{N_\omega} \mathrm{Re}\left\{ \frac{n_1}{n_2} \underline{\mu}^{-} \right\} & \sum_{k=1}^{N_\omega} \mathrm{Re}\left\{ n_1 \underline{\mu}^{-} \right\} \end{bmatrix} \tag{3.84}$$

and

$$H_d = \frac{1}{2} \begin{bmatrix} \sum_{k=1}^{N_\omega} \mathrm{Re}\left\{ \frac{n_1^2}{n_2^2} \right\} & -\sum_{k=1}^{N_\omega} \mathrm{Re}\left\{ \frac{n_1^2}{n_2} \right\} \\ -\sum_{k=1}^{N_\omega} \mathrm{Re}\left\{ \frac{n_1^2}{n_2} \right\} & \sum_{k=1}^{N_\omega} \mathrm{Re}\left\{ \frac{n_1^2}{n_2^2} \right\} \end{bmatrix} \tag{3.85}$$

Using the relations in (3.69), it can be readily shown that the matrix M_d is symmetric, i.e. $M_d = M_d^T$. Also, it is obvious from (3.85) that H_d is also symmetric. Thus, the system matrix in (3.82) is symmetric.

The right-hand side vector for each (i,i) system in (3.82) is partitioned by the three subvectors $\underline{a}_{ii}^{+}$, $\underline{a}_{ii}^{-}$ and $\underline{b}_{ii}$ given by

$$\underline{a}_{ii}^{+} = \left\{ \sum_{k=1}^{N_\omega} \mathrm{Re}\left\{ \underline{\mu}^{+} \widehat{S}_{ii} \right\} \right\} \tag{3.86}$$

$$\underline{a}_{ii}^{-} = \left\{ \sum_{k=1}^{N_\omega} \mathrm{Re}\left\{ \underline{\mu}^{-} \widehat{S}_{ii} \right\} \right\} \tag{3.87}$$

and

$$\underline{b}_{ii} = \frac{1}{2} \begin{Bmatrix} -\sum_{k=1}^{N_\omega} \mathrm{Re}\left\{ \frac{n_1}{n_2} \widehat{S}_{ii} \right\} \\ \sum_{k=1}^{N_\omega} \mathrm{Re}\left\{ n_1 \widehat{S}_{ii} \right\} \end{Bmatrix} \tag{3.88}$$

The vectors $\underline{\mu}^{\pm}$ and $\underline{k}^{\pm}$ are given in (3.80).

The solutions of the systems of equations in (3.71) and (3.82) provide estimates of the residue matrices R_r and the real matrices A and B. Given the residue matrices R_r and noting that it admits the representation $R_r = \underline{u}_r \underline{g}_r^T$, i.e. is expected to be of rank one, the modeshapes $\underline{u}_r$ and the operational reference vectors $\underline{g}_r$ are obtained by applying singular value decomposition SVD on each $R_r \equiv R$

$$R = U \Sigma V^T \tag{3.89}$$

where $U = \left(\underline{u}_1 \cdots \underline{u}_{N_{out}}\right),\ V = \left(\underline{v}_1 \cdots \underline{v}_{N_{out}}\right),\ \Sigma = diag(\sigma_i),$ and $\left|\sigma_1\right| \geq \ldots \geq \left|\sigma_{N_{out}}\right|$. The modeshape vector $\underline{u}_r$ corresponds to the larger singular value σ_1 and is given by $\underline{u}_r = \sigma_1 \underline{u}_1$, while the operational reference vectors $\underline{g}_r$ is given by $\underline{g}_r = \underline{v}_1$. However, for the case of closely spaced and overlapping modes this approach sometimes fail to estimate all contributing closely spaced modes. An example of this case will be presented in subsection 3.5.2.

3.4.2.2 Second approach

In the second approach, given the number of contributing modes m and the estimated values of the poles λ_r, estimates of the modeshapes $\underline{u}_r$, the operational reference vectors $\underline{g}_r$ and the real matrices A and B are obtained by minimizing (3.13) with $\underline{\varepsilon}_k^{NL}\left(\underline{\theta}\right)$ given by (3.14) and $S_k\left(\underline{\theta}\right)$ given by

$$S(j\omega,\underline{\theta}) = \sum_{r=1}^{m}\left[\frac{\underline{u}_r \underline{g}_r^T}{j\omega-\lambda_r} + \frac{\underline{u}_r^* \underline{g}_r^{*T}}{j\omega-\lambda_r^*} + \frac{\underline{g}_r \underline{u}_r^T}{-j\omega-\lambda_r} + \frac{\underline{g}_r^* \underline{u}_r^{*T}}{-j\omega-\lambda_r^*}\right] - \frac{n_1(j\omega)}{n_2(j\omega)}A + n_1(j\omega)B \qquad (3.90)$$

The number of parameters that are involved in the optimization using the formulation in (3.90) is $2m(1+2N_{out}) + N_{out}^2 + N_{out}$. By recognizing that the the error function in (3.13) is quadratic with respect to the modeshapes $\underline{u}_r$, A and B, advantage is taken to develop explicit expressions that relate the parameters $\underline{u}_r$, A and B to the vectors $\underline{g}_r$ and the poles λ_r, so that the number of parameters involved in the optimization is reduced to $2m(N_{out}+1)$. This reduction is considerable for a relatively large number of measurement points. So, using the stationarity conditions, one can develop a system of linear equations for the elements of $\underline{u}_r$, A and B with respect to the vectors $\underline{g}_r$ and the poles λ_r. For completeness, this system of equations is given next as a function of the measurements, the vectors $\underline{g}_r$ and the values of the system poles λ_r. First the complex-valued modeshape $\underline{u}_r$ $r = 1,\ldots,m$ involved in the description of the modal model (3.90) are expressed in terms of the real and imaginary parts as follows:

$$\underline{u}_r = \underline{\phi}_r + j\underline{\psi}_r \qquad (3.91)$$

with the vectors $\underline{\phi}_r, \underline{\psi}_r \in \mathbb{R}^{Nout}$. The CPSD function matrix of equation (3.90) is then written as

$$S(j\omega) = \sum_{r=1}^{m}\left[\underline{\phi}_r \underline{\mu}_r^{+T} + \underline{\psi}_r \underline{\mu}_r^{-T} + \underline{k}_r^{+} \underline{\phi}_r^T + \underline{k}_r^{-} \underline{\psi}_r^T\right] - \frac{n_1(j\omega)}{n_2(j\omega)}A + n_1(j\omega)B \qquad (3.92)$$

where

$$\underline{\mu}_r^{+} = n_1(j\omega)\left[\frac{\underline{g}_r}{j\omega-\lambda_r}+\frac{\underline{g}_r^{*}}{j\omega-\lambda_r^{*}}\right] \tag{3.93}$$

$$\underline{\mu}_r^{-} = n_1(j\omega)\, j\left[\frac{\underline{g}_r}{j\omega-\lambda_r}-\frac{\underline{g}_r^{*}}{j\omega-\lambda_r^{*}}\right] \tag{3.94}$$

$$\underline{k}_r^{+} = n_1(j\omega)\left[\frac{\underline{g}_r}{-j\omega-\lambda_r}+\frac{\underline{g}_r^{*}}{-j\omega-\lambda_r^{*}}\right] \tag{3.95}$$

$$\underline{k}_r^{-} = n_1(j\omega)\, j\left[\frac{\underline{g}_r}{-j\omega-\lambda_r}-\frac{\underline{g}_r^{*}}{-j\omega-\lambda_r^{*}}\right] \tag{3.96}$$

For the case that the CPSD function matrix is given for the acceleration response the frequency functions $n_1(j\omega)$ and $n_2(j\omega)$ are already given by (3.11) and (3.12). It should be also noted that $n_1(j\omega)\in\mathbb{R}$ and $n_2(j\omega)\in\mathbb{R}$ are real the following relation holds true:

$$k_r^{+*} = \mu_r^{+} \quad \text{and} \quad k_r^{-*} = \mu_r^{-} \tag{3.97}$$

Define the vector of unknown quantities partitioned as follows:

$$\underline{x} = \begin{Bmatrix} vec\left\{\Phi^T\right\} \\ vec\left\{\Psi^T\right\} \\ vec\left\{A^T\right\} \\ vec\left\{B^T\right\} \end{Bmatrix} \in \mathbb{R}^{2N_{out}(N_{out}+m)} \tag{3.98}$$

where

$$\Phi = \left[\underline{\phi}_1 \quad \ldots \quad \underline{\phi}_m\right] \in \mathbb{R}^{N_{out}\times m} \tag{3.99}$$

$$\Psi = \left[\underline{\psi}_1 \quad \ldots \quad \underline{\psi}_m\right] \in \mathbb{R}^{N_{out}\times m} \tag{3.100}$$

The stationarity conditions with respect in the parameters in $\underline{x}$ yield the algebraic system of $2N_{out}(N_{out}+m)$ equations for $\underline{x}$:

$$\begin{bmatrix} L_{11} & L_{12} & L_{13} & L_{14} \\ L_{21} & L_{22} & L_{23} & L_{24} \\ L_{31} & L_{32} & L_{33} & L_{14} \\ L_{41} & L_{42} & L_{43} & L_{44} \end{bmatrix} \underline{x} = \begin{Bmatrix} \underline{b}_1 \\ \underline{b}_2 \\ \underline{b}_3 \\ \underline{b}_4 \end{Bmatrix} \tag{3.101}$$

where the left-hand side matrix is partitioned by the submatrices $L_{p,q} \quad p,q = 1,\ldots,4$ given by

$$L_{11} = \mathrm{Re}\left\{ \sum_{k=1}^{N_f} \left[M^{+T} \otimes M^{+} + M_I^{+T} \left(I_{N_{out}} \otimes K^{+} \right) \right] \right\} \in \mathbb{R}^{mN_{out} \times mN_{out}} \tag{3.102}$$

$$L_{12} = \mathrm{Re}\left\{ \sum_{k=1}^{N_f} \left[M^{+T} \otimes M^{-} + M_I^{+T} \left(I_{N_{out}} \otimes K^{-} \right) \right] \right\} \in \mathbb{R}^{mN_{out} \times mN_{out}} \tag{3.103}$$

$$L_{13} = -\mathrm{Re}\left\{ \sum_{k=1}^{N_f} \frac{n_1}{n_2} M^{+T} \otimes I_{N_{out}} \right\} \in \mathbb{R}^{mN_{out} \times N_{out}^2} \tag{3.104}$$

$$L_{14} = \mathrm{Re}\left\{ \sum_{k=1}^{N_f} n_1 M^{+T} \otimes I_{N_{out}} \right\} \in \mathbb{R}^{mN_{out} \times N_{out}^2} \tag{3.105}$$

$$L_{21} = \mathrm{Re}\left\{ \sum_{k=1}^{N_f} \left[M^{-T} \otimes M^{+} + M_I^{-T} \left(I_{N_{out}} \otimes K^{+} \right) \right] \right\} \in \mathbb{R}^{mN_{out} \times mN_{out}} \tag{3.106}$$

$$L_{22} = \mathrm{Re}\left\{ \sum_{k=1}^{N_f} \left[M^{-T} \otimes M^{-} + M_I^{-T} \left(I_{N_{out}} \otimes K^{-} \right) \right] \right\} \in \mathbb{R}^{mN_{out} \times mN_{out}} \tag{3.107}$$

$$L_{23} = -\mathrm{Re}\left\{ \sum_{k=1}^{N_f} \frac{n_1}{n_2} M^{-T} \otimes I_{N_{out}} \right\} \in \mathbb{R}^{mN_{out} \times N_{out}^2} \tag{3.108}$$

$$L_{24} = \mathrm{Re}\left\{ \sum_{k=1}^{N_f} n_1 M^{-T} \otimes I_{N_{out}} \right\} \in \mathbb{R}^{mN_{out} \times N_{out}^2} \tag{3.109}$$

$$L_{31} = -\mathrm{Re}\left\{ \sum_{k=1}^{N_f} \frac{n_1}{n_2} \left[I_{Nout} \otimes M^{+T} + K_I^{+} \right] \right\} \in \mathbb{R}^{mN_{out} \times N_{out}^2} \tag{3.110}$$

$$L_{32} = -\mathrm{Re}\left\{ \sum_{k=1}^{N_f} \frac{n_1}{n_2} \left[I_{Nout} \otimes M^{-T} + K_I^{-} \right] \right\} \in \mathbb{R}^{mN_{out} \times N_{out}^2} \tag{3.111}$$

$$L_{33} = \mathrm{Re}\left\{ \sum_{k=1}^{N_f} \frac{n_1^2}{n_2^2} I_{N_{out}^2} \right\} \in \mathbb{R}^{N_{out}^2 \times N_{out}^2} \tag{3.112}$$

$$L_{34} = -\mathrm{Re}\left\{\sum_{k=1}^{N_f} \frac{n_1^2}{n_2} I_{N_{out}^2}\right\} \in \mathbb{R}^{N_{out}^2 \times N_{out}^2} \tag{3.113}$$

$$L_{41} = \mathrm{Re}\left\{\sum_{k=1}^{N_f} n_1 \left[I_{Nout} \otimes M^{+} + K_I^{+}\right]\right\} \in \mathbb{R}^{mN_{out} \times N_{out}^2} \tag{3.114}$$

$$L_{42} = \mathrm{Re}\left\{\sum_{k=1}^{N_f} n_1 \left[I_{Nout} \otimes M^{-} + K_I^{-}\right]\right\} \in \mathbb{R}^{mN_{out} \times N_{out}^2} \tag{3.115}$$

$$L_{43} = -\mathrm{Re}\left\{\sum_{k=1}^{N_f} \frac{n_1^2}{n_2} I_{N_{out}^2}\right\} \in \mathbb{R}^{N_{out}^2 \times N_{out}^2} \tag{3.116}$$

and

$$L_{44} = \mathrm{Re}\left\{\sum_{k=1}^{N_f} n_1^2 I_{N_{out}^2}\right\} \in \mathbb{R}^{N_{out}^2 \times N_{out}^2} \tag{3.117}$$

The right-hand side vector of the system in (3.101) is partitioned by the four subvectors $\underline{b}_1$, $\underline{b}_2$, $\underline{b}_3$ and $\underline{b}_4$ given by

$$\underline{b}_1 = \mathrm{Re}\left\{\sum_{k=1}^{N_f} \left(M^{+T} \otimes I_{N_{out}}\right) vec\left\{\hat{S}^T\right\}\right\} \in \mathbb{R}^{mN_{out}} \tag{3.118}$$

$$\underline{b}_2 = \mathrm{Re}\left\{\sum_{k=1}^{N_f} \left(M^{-T} \otimes I_{N_{out}}\right) vec\left\{\hat{S}^T\right\}\right\} \in \mathbb{R}^{mN_{out}} \tag{3.119}$$

$$\underline{b}_3 = -\mathrm{Re}\left\{\sum_{k=1}^{N_f} \frac{n_1}{n_2} vec\left\{\hat{S}^T\right\}\right\} \in \mathbb{R}^{N_{out}^2} \tag{3.120}$$

$$\underline{b}_4 = \mathrm{Re}\left\{\sum_{k=1}^{N_f} n_1 vec\left\{\hat{S}^T\right\}\right\} \in \mathbb{R}^{N_{out}^2} \tag{3.121}$$

and the matrices $M^{\pm}$, $K^{\pm}$, $M_I^{\pm T}$ and $K_I^{\pm T}$ are given by

$$M^{\pm} = \left[\underline{\mu}_1^{\pm} \quad \ldots \quad \underline{\mu}_m^{\pm}\right] \in \mathbb{C}^{N_{out} \times m} \tag{3.122}$$

$$K^{\pm} = \left[\underline{k}_1^{\pm} \quad \ldots \quad \underline{k}_m^{\pm}\right] \in \mathbb{C}^{N_{out} \times m} \tag{3.123}$$

$$M_I^{\pm T} = \begin{bmatrix} I_{N_{out}} \otimes \underline{\mu}_1^{\pm} \\ \vdots \\ I_{N_{out}} \otimes \underline{\mu}_m^{\pm} \end{bmatrix} \in \mathbb{C}^{mN_{out} \times N_{out}^2} \tag{3.124}$$

$$K_I^{\pm T} = \begin{bmatrix} I_{N_{out}} \otimes \left\langle K^{\pm} \right\rangle_1 \\ \vdots \\ I_{N_{out}} \otimes \left\langle K^{\pm} \right\rangle_{N_{out}} \end{bmatrix} \in \mathbb{C}^{N_{out}^2 \times mN_{out}} \tag{3.125}$$

where the $\otimes$ denotes the Kronecker product, $I_{N_{out}}$ denotes the identity matrix dimensioned $N_{out} \times N_{out}$ and $\left\langle Z \right\rangle_l$ denotes the l row of matrix Z.

For given the number of m contributing modes and values of the poles estimated in the first step of the algorithm, the solution of the system of equations in (3.101) gives the modeshape components of the structure at the measured DOF with respect to the vectors $\underline{g}_r$. The optimal values of the modeshapes that minimize the objective described in (3.13) with $\underline{\varepsilon}_k^{NL}\left(\underline{\theta}\right)$ given by (3.14) are computed by nonlinear optimization algorithms with respect to the elements of the complex vectors $\underline{g}_r$. For this, the complex-valued vectors $\underline{g}_r \quad r = 1,\ldots,m$ involved in the optimization are expressed in terms of the real and imaginary parts so the resulting number of parameters involved in the optimization algorithm is $2mN_{out}$. Each iteration of the optimization procedure demand the solution of the system of equations in (3.101) of size $2N_{out}(N_{out}+m)$.

3.4.3 Step 3: Modal identification by full nonlinear optimization

For closely spaced and overlapping modes, the two step approach may not be adequate. In this case the full nonlinear optimization problem can be solved for the identification of all modal parameters. Specifically, the modal parameters in the set $\underline{\theta}$ are identified by minimizing the objective function (3.13) with $\varepsilon_k^{NL}\left(\underline{\theta}\right)$ given by (3.14). The number of contributing modes m are obtained using the stabilization diagrams in the first step of the algorithm. The initial estimates for the parameters involved in the optimization problem can be obtained by the first and second steps of the algorithm, assisting the convergence of the optimization algorithm and reducing the computational cost. Two approaches are next introduced depending on the form of the CPSD function $S(j\omega,\underline{\theta})$ and the type of the modal parameters involved.

3.4.3.1 First approach

In the first second approach the CPSD function is given by (3.17). The modal parameter set $\underline{\theta}$ to be identified contains the parameters ω_r, ζ_r, R_r, $r = 1,\cdots,m$, A and B that completely

define the CPSD matrix in (3.17). The total number of parameters is $2m(1+N_{out}^2)+N_{out}^2+N_{out}$ for non-classically damped modal models.

The minimization of the objective function (3.13) can be carried out efficiently, significantly reducing the computational cost, by recognizing that the error function in (3.13) is quadratic with respect to the complex matrices R_r and the elements in the matrices A and B. This observation is used to develop explicit expressions that relate the parameters R_r, A and B to the modal frequencies ω_r and the damping ratios ζ_r, so that the number of parameters involved in the optimization is reduced to $2m$. This reduction is considerable for a relatively large number of measurement points. Applying the optimality conditions with respect to the components of R_r, A and B, linear systems of equations result for obtaining R_r, A and B with respect to ω_r and ζ_r, $r=1,\cdots,m$. These linear systems are given in (3.71) and (3.82). The resulting nonlinear optimization problem with respect to the remaining variables ω_r and ζ_r, $r=1,\cdots,m$, is solved in Matlab using available gradient-based optimisation algorithms. The starting values of the parameters required in the optimization are obtained from the estimates provided by the first and second steps. These starting values are usually very close to the optimal values for most of the modes and thus the optimization algorithm converges in a relatively few iterations. Noting that the matrices R_r admit the representation $R_r=\underline{u}_r\underline{g}_r^T$, $r=1,\cdots,m$, the modeshapes $\underline{u}_r$ and the operational reference vectors $\underline{g}_r$ are derived directly by the Singular Value Decomposition (SVD) for the resulting numerator matrices R_r using the left-hand and right-hand singular vectors corresponding to the highest singular value.

3.4.3.2 Second approach

In the second approach the CPSD function is given by (3.10). The modal parameter set $\underline{\theta}$ to be identified contains the parameters ω_r, ζ_r, $\underline{u}_r$, $\underline{g}_r$, $r=1,\cdots,m$, A and B that completely define the CPSD matrix in (3.10). The total number of parameters is $2m(1+2N_{out})+N_{out}^2+N_{out}$ for non-classically damped modal models.

The minimization of the objective function (3.13) can be carried out efficiently, significantly reducing the computational cost, by recognizing that the error function in (3.13) is quadratic with respect to the complex modeshapes $\underline{u}_r$ and the elements in the matrices A and B. This observation is used to develop explicit expressions that relate the parameters $\underline{u}_r$, A and B to the vectors $\underline{g}_r$, the modal frequencies ω_r and the damping ratios ζ_r, so that the number of parameters involved in the optimization is reduced to $2m(N_{out}+1)$. This reduction is considerable for a relatively large number of measurement points. Applying the optimality conditions with respect to the components of $\underline{u}_r$, A and B, a linear system of equations results for obtaining $\underline{u}_r$, A and B with respect to the $\underline{g}_r$, ω_r and ζ_r, $r=1,\cdots,m$. These linear systems are given in (3.101). The resulting nonlinear optimization problem with respect to the

remaining variables $\underline{g}_r$, ω_r and ζ_r, $r = 1, \cdots, m$, is solved in Matlab using available gradient-based optimisation algorithms. The starting values of the parameters required in the optimization are obtained from the estimates provided by the first and second steps. These starting values are usually very close to the optimal values for most of the modes and thus the optimization algorithm converges in a relatively few iterations.

3.5 Validation using simulated and measured ambient vibrations

In the remaining sections of this chapter the proposed identification techniques are validated by means of three examples. First the methodology that has been developed for the first step of the algorithm and presented in Sections 3.4.1.1, 3.4.1.2 and 3.4.1.3 is tested using simulated ambient vibration measurements. Specifically, the methodology that is developed in Section 3.4.1.3 based on the special structure of the common denominator polynomial is applied and compared with the conventional methodology for the identification of the structural poles. Next, the proposed three step algorithm is applied and its efficiency is tested for the identification of closely spaced and overlapping modes using simulated measurement data of the response of a model structure. Finally, a real-life example for the identification of the modal properties of a full-scale bridge using ambient response measurements is presented.

3.5.1 Identification of structural poles using simulated measurement data

This example is concentrated on the efficiency of the first step of the proposed modal identification algorithm where the poles of the structure are identified creating stabilization diagrams. The methodology developed in Section 3.4.1.3 based on the special structure of the common denominator polynomial is applied and compared with the conventional methodology for the identification of the structural poles developed in Section 3.4.1.1. A three dimensional beam model of a two-span bridge-like structure, shown in Figure 3.1, is considered in the simulation studies. The simulated measurement data used for the modal identification are the vibration responses predicted at several locations by a finite element model of a structure. These vibrations are induced by excitation forces applied at the deck and modeled by white noise processes. The “measured” CPSD function matrices used for the simulation are derived directly using equation (3.3) where the Frequency Response Function is calculated from the finite element model of the structure using a modal damping ratio of 2% and the intensity of the white noise excitation is 1.

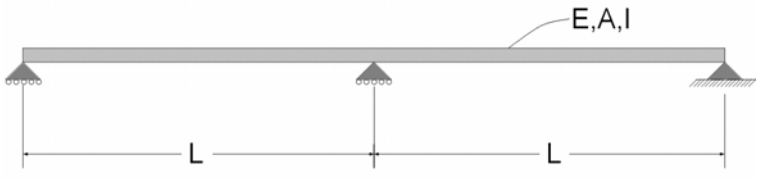

3.1: Two-span model of a bridge-like structure.

The first step of the proposed identification algorithm described in Section 3.4.1 is applied in the frequency band that contain the first four modes of the structure for identifying the structural poles that yield the modal frequencies ω_r and the modal damping ratios ζ_r. The stabilization diagram that is constructed by solving sequentially the system of linear equations in (3.60) and using the simplification presented in Section 3.4.1.3 increasing the order of the common denominator polynomial order with maximum value of order $p=100$ is presented in Figure 3.2. In Figure 3.2 the green cross $(+)$ marker represent the poles that do not derive in groups of four μ_r, μ_r^*, $1/\mu_r$ and $1/\mu_r^*$ for the discrete time models described in Section 3.4.1.1 and are ignored in the stabilization procedure. All other markers represent the poles that appear in groups of four with the red square markers representing the poles stabilized considering the modal frequencies and the red triangular markers representing the poles stabilized considering both the modal frequencies and modal damping ratios. The magenta xi $(\times)$ markers correspond to non stabilized spurious mathematical poles that comes in groups of four μ_r, μ_r^*, $1/\mu_r$ and $1/\mu_r^*$.

For the conventional case, the stabilization diagram constructed in the same way by solving sequentially the system of linear equations in (3.45) but without using the simplification presented in Section 3.4.3, is presented in Figure 3.3. Similar to Figure 3.2 the green cross (+) marker in Figure 3.3 represent the poles that are not derived in groups of four μ_r, μ_r^*, $1/\mu_r$ and $1/\mu_r^*$ for the discrete time models described in Section 3.4.1 and are ignored in the stabilization procedure. All other markers represent the poles that appear in groups of four with the red square markers representing the poles stabilized considering the modal frequencies and the red triangular markers representing the poles stabilized considering both the modal frequencies and modal damping ratios. It should be noted that in the conventional method the poles are never derived exactly following the form of μ_r, μ_r^*, $1/\mu_r$ and $1/\mu_r^*$, but they have small computational errors, due to the fact that such a sequence of four poles has not being enforced in the conventional method. In order to be grouped and accepted as physical poles, a tolerance criterion must be implemented when comparing the poles computed with the ideal case of μ_r, μ_r^*, $1/\mu_r$ and $1/\mu_r^*$. For the case of Figure 3.3 the tolerance is selected to be $tol=3\%$ and the four poles are assumed to approximately form a sequence of μ_r, μ_r^*, $1/\mu_r$ and $1/\mu_r^*$ if $\dfrac{\left|\lambda_r\right|-\left|\tilde{\lambda}\right|_r}{\left|\lambda_r\right|}<tol$ with λ_r are the poles in the continuous time formulation given by

$$\lambda_r=\frac{\ln\mu_r}{\Delta t} \tag{3.126}$$

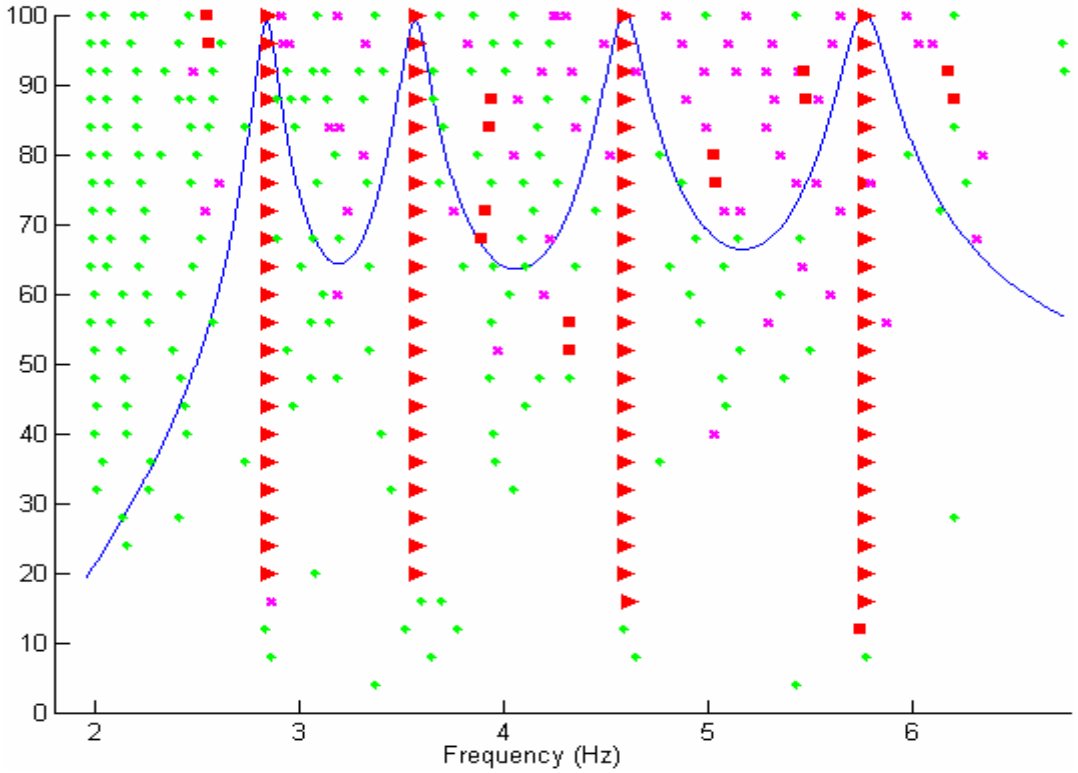

Figure 3.2: Stabilization Diagram constructed using the simplification presented in Section 3.4.1.3.

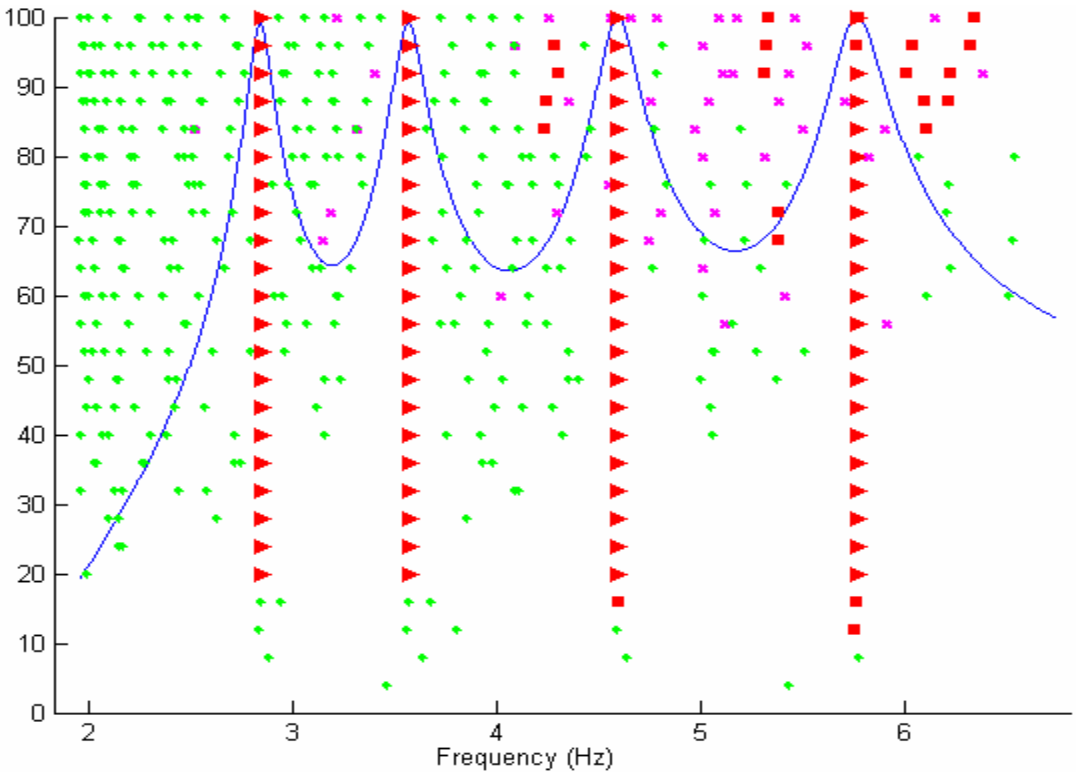

Figure 3.3: Stabilization Diagram constructed using the conventional method.

Comparing the stabilization diagrams presented in Figures 3.2 and 3.3 it is observed that several spurious mathematical modes appear for both the cases of the new and the conventional methods. The number of spurious mathematical modes for the case of the conventional method is significantly higher than the corresponding number for the new method. Also, both methods converge fast as the value of p increases. Specifically, for both methods the physical modes have been identified and the procedure has converged for values of $p = 20$. It has been observed that, for the conventional method, by decreasing the tolerance criterion, the order of the polynomial in which all four physical modes are computed is increased. Finally, the predictions of the modal frequencies and damping ratios obtained from the new and the conventional method for $p = 20$ and $p = 40$ are presented in Table 3.1 for the new method and in Table 3.2 for the conventional method. The accuracy of the predictions is inferred by comparing these predicted values with the actual values obtained from the eigenvalue analysis of the finite element model of the structure. It is observed that both methodologies in this case of simulated experimental data easily identify the modes of the structure giving accurate results for the values of the modal frequencies and the modal damping ratios. Generally, both methodologies appear to work adequately, easily identifying the modes of the structure. The new method is more efficient since it takes advantage of the special structure of the denominator polynomial in CPSD to converge faster and provide accurate results consistent with the structure of the denominator polynomial.

Table 3.1: Comparison between the identified values of the modal frequencies and modal damping ratios and the nominal values estimated by the FEM, for the new method.

	1st mode		2nd mode		3rd mode		4th mode	
	ω_1 (Hz)	ζ_1 (%)	ω_2 (Hz)	ζ_2 (%)	ω_3 (Hz)	ζ_3 (%)	ω_4 (Hz)	ζ_4 (%)
FEM	2.842	2.00	3.569	2.00	4.595	2.00	5.769	2.00
$p = 20$	2.844	2.04	3.570	2.00	4.596	2.00	5.770	1.99
$p = 40$	2.845	2.00	3.570	2.00	4.596	2.00	5.770	2.00

Table 3.2: Comparison between the identified values of the modal frequencies and modal damping ratios and the nominal values estimated by the FEM, for the conventional method.

	1st mode		2nd mode		3rd mode		4th mode	
	ω_1 (Hz)	ζ_1 (%)	ω_2 (Hz)	ζ_2 (%)	ω_3 (Hz)	ζ_3 (%)	ω_4 (Hz)	ζ_4 (%)
FEM	2.842	2.00	3.569	2.00	4.595	2.00	5.769	2.00
$p = 20$	2.845	2.02	3.570	2.00	4.596	2.00	5.770	2.00
$p = 40$	2.845	2.00	3.570	2.00	4.596	2.00	5.770	2.00

It should be noted that the aforementioned results are based on simulated CPSD functions that are computed directly from the finite element model of the structure and the PSD of the white noise excitation. Next, the identification of the first four modes of the same model is performed again but this time the simulated CPSD functions are computed using simulated vibration response time histories predicted at same locations as before. These vibrations are induced by excitation forces applied at the deck and modeled by discrete white noise processes. The equations of motion are then solved to compute the acceleration response time histories. The CPSD function matrices of the acceleration response of the model are estimated from these simulated time histories using the methodologies described in Appendix 3.A.

The stabilization diagrams for new method (see Section 3.4.1.3) and the conventional (see Section 3.4.1.1) are constructed with maximum value of order $p = 100$ and presented in Figures 3.4 and 3.5, respectively. The interpretation of the symbols (markers) green cross (+), red square and red triangular in these figures is kept the same as the one used for Figures 3.2 and 3.3. It should be noted that applying the conventional method for the first step of the algorithm the poles estimated are not obtained in groups of four μ_r, μ_r^*, $1/\mu_r$ and $1/\mu_r^*$ for the discrete time models and the same tolerance criterion of $tol = 3\%$ is used. This makes the distinction between physical and mathematical more difficult resulting in many spurious mathematical poles that can not be removed easily from the stabilization procedure. Compared to Figures 3.4 and 3.5, it can be seen that a slower converge is observed as the value of p increases, especially for the conventional method. Specifically, for the conventional method the stabilization of the poles seem not to be as efficient as for the new method even for high order denominator models.

Both methods seem to have been converged in modal frequencies for values of $p = 20$ but it should be noted that for both methods higher order denominator models seem to provide poles that makes the stabilization procedure not very reliable. This problem could be solved and eliminate the spurious modes appearing for high values of p by implementing another criterion in the stabilization procedure that takes into account the comparison of the modeshapes computed by the poles of order p and $p-1$. Specifically the modal assurance criterion (MAC) could be implemented for comparing two modeshapes in the stabilization procedure but this requires the estimation of all modeshapes given the poles. These modeshapes can be estimated using the techniques described in Section 3.4.2, increasing significantly the computational cost of the procedure.

The accuracy of the predictions of the modal frequencies and damping ratios obtained from the new and the conventional methods for $p = 20$ and $p = 40$ is presented in Table 3.3 and 3.4 and compared to the actual values obtained from the eigenvalue analysis of the finite element model of the structure. It is observed that both methods fail to give sufficiently accurate estimates of the modal damping ratios for all four modes. Generally, the new method is more efficient and accurate since it has faster converge properties and provide accurate results for the modal frequencies and damping ratios of all four modes.

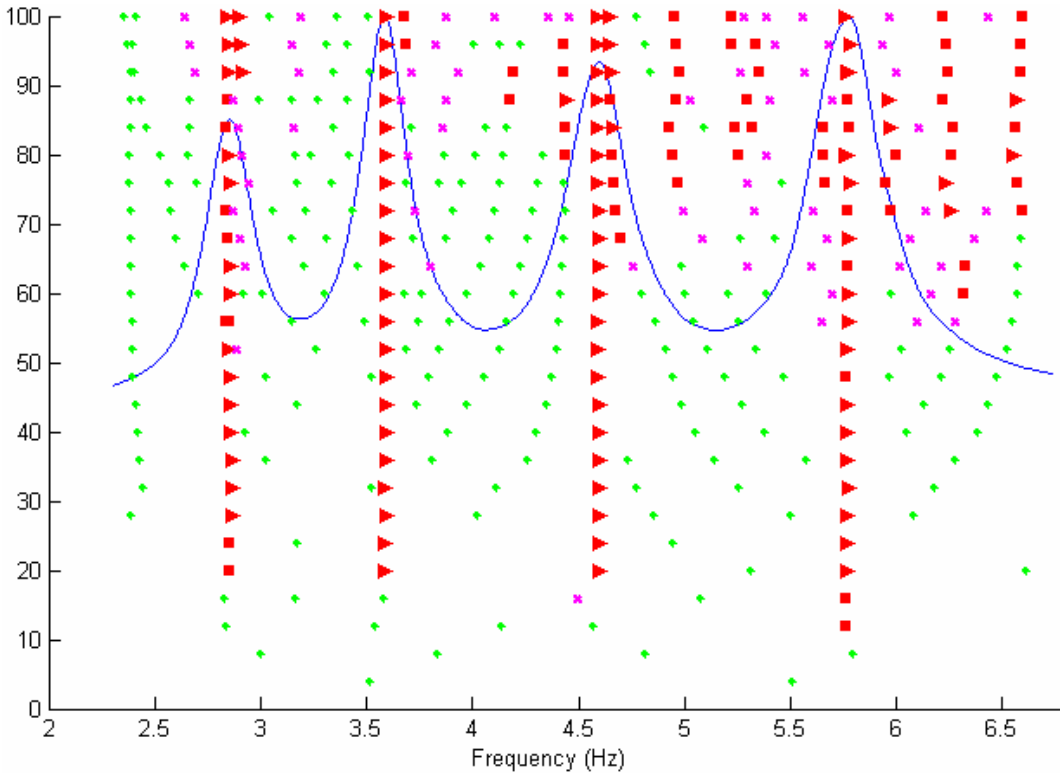

Figure 3.4: Stabilization Diagram constructed using the simplification presented in Section 3.4.1.3.

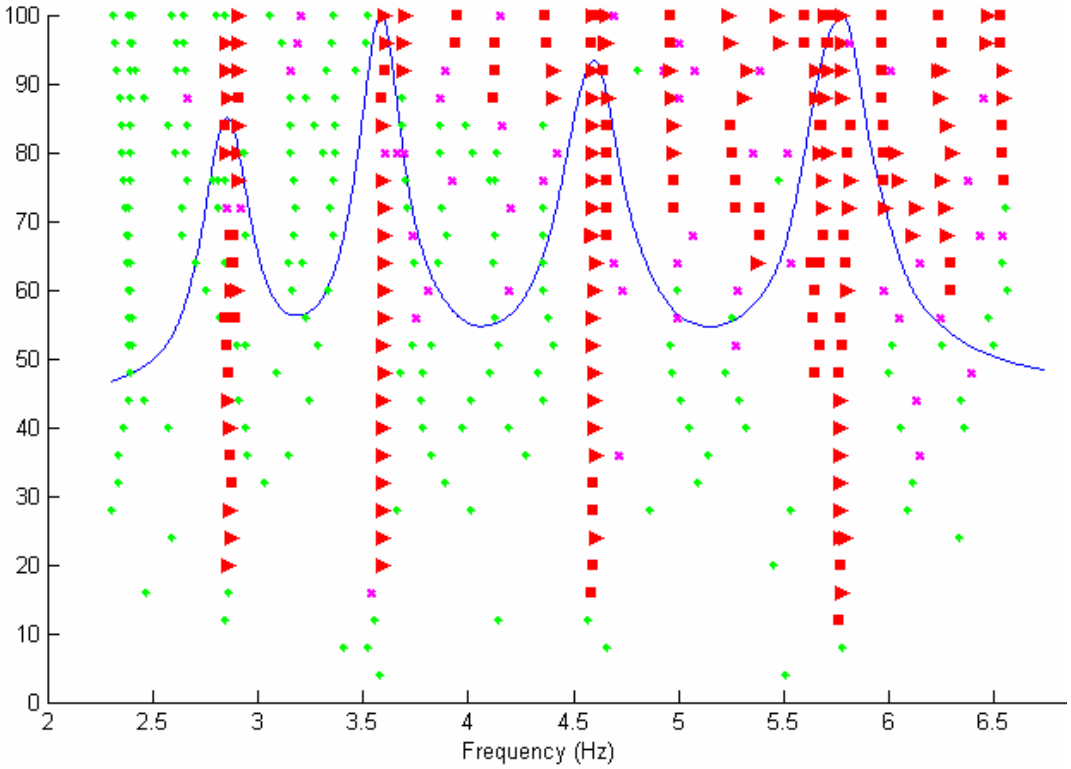

Figure 3.5: Stabilization Diagram constructed using the conventional method.

Table 3.3: Comparison between the identified values of the modal frequencies and modal damping ratios and the nominal values estimated by the FEM, for the new method.

	1st mode		2nd mode		3rd mode		4th mode	
	ω_1 (Hz)	ζ_1 (%)	ω_2 (Hz)	ζ_2 (%)	ω_3 (Hz)	ζ_3 (%)	ω_4 (Hz)	ζ_4 (%)
FEM	2.842	2.00	3.569	2.00	4.595	2.00	5.769	2.00
$p = 20$	2.853	2.09	3.589	1.78	4.592	2.30	5.766	2.07
$p = 40$	2.857	2.01	3.585	1.79	4.591	2.33	5.763	1.97

Table 3.4: Comparison between the identified values of the modal frequencies and modal damping ratios and the nominal values estimated by the FEM, for the conventional method.

	1st mode		2nd mode		3rd mode		4th mode	
	ω_1 (Hz)	ζ_1 (%)	ω_2 (Hz)	ζ_2 (%)	ω_3 (Hz)	ζ_3 (%)	ω_4 (Hz)	ζ_4 (%)
FEM	2.842	2.00	3.569	2.00	4.595	2.00	5.769	2.00
$p = 20$	2.855	2.18	3.585	1.77	4.595	2.30	5.767	2.03
$p = 40$	2.842	1.97	3.569	1.76	4.595	2.31	5.769	1.75

3.5.2 Identification of closely spaced and overlapping modes using simulated measurement data

In this section the methodologies will be tested for closely spaced and overlapped modes. The modal identification of a structure that has closely and overlapping modes is always a challenging problem. This problem is studied in this subsection in detail. Specifically, the proposed three step algorithm is applied and its efficiency is tested for the identification of closely spaced modes using simulated measurement data of the response of a model structure. In the literature, a two step algorithm is commonly used for modal identification. This example demonstrates that the first two identification steps are sometimes inadequate especially for the case of closely and overlapping modes. For this case the application of the third step is necessary and is shown to improve significantly the modal identification results.

A three dimensional beam model of a two-span bridge-like structure, shown in Figure 3.6, is considered in the simulation studies. The two spans are weakly connected and almost similar in properties. This has an effect of having pairs of two very closely-spaced bending modes. The dynamics of the structure considered in this artificial example is encountered in existing bridge structures. Specifically, the behavior of the two span bridge resembles the behavior observed for the four span G2 Kavala bridge of Egnatia Odos Motorway (Ntotsios et al. 2009). The four-span Kavala bridge has four closely spaced bending modes due to the almost similar properties of the four spans and the fact that these spans are weakly connected with each other. A finite element model for the simulated two-span bridge is constructed. The simulated measurement data used for the modal identification are the vibration responses predicted at several locations by the finite element model of a structure. These vibrations are induced by excitation forces applied at the deck and modeled by white noise processes. The “measured” CPSD function matrices used for

the simulation is derived directly using equation (3.3) where the Frequency Response Function is calculated from the finite element model of the structure using a modal damping ratio of 2% and the intensity of the white noise excitation is 1. The model of the structure has been properly selected to have pairs of closely spaced and overlapping modes.

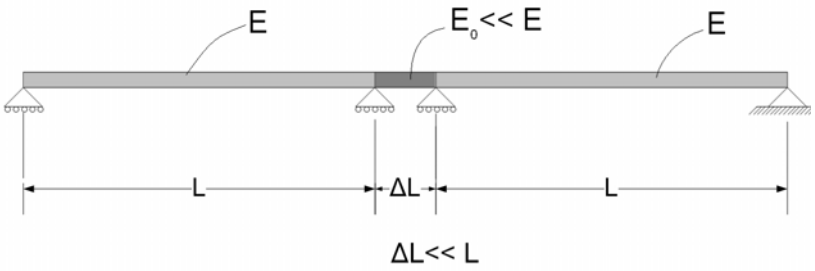

Figure 3.6: Two-span model of a bridge-like structure.

The first step of the proposed identification algorithm described in Sections 3.4.1.1 to 3.4.1.3 is next applied in the frequency band that contain the first two pairs of closely spaced and overlapping modes for identifying the structural poles that yield the modal frequencies ω_r and the modal damping ratios ζ_r. The stabilization diagrams for new method (see Section 3.4.1.3) and the conventional (see Section 3.4.1.1) are constructed with maximum value of order $p=100$ and presented in Figures 3.7 and 3.8, respectively. The interpretation of the symbols (markers) green cross (+), red square and red triangular in these figures is kept the same as the one used for Figures 3.2 to 3.5. It should be noted that applying the conventional method for the first step of the algorithm the poles estimated are not obtained in groups of four μ_r, μ_r^*, $1/\mu_r$ and $1/\mu_r^*$ for the discrete time models. This makes the distinction between physical and mathematical more difficult resulting in many spurious mathematical poles that can not be removed easily from the stabilization procedure.

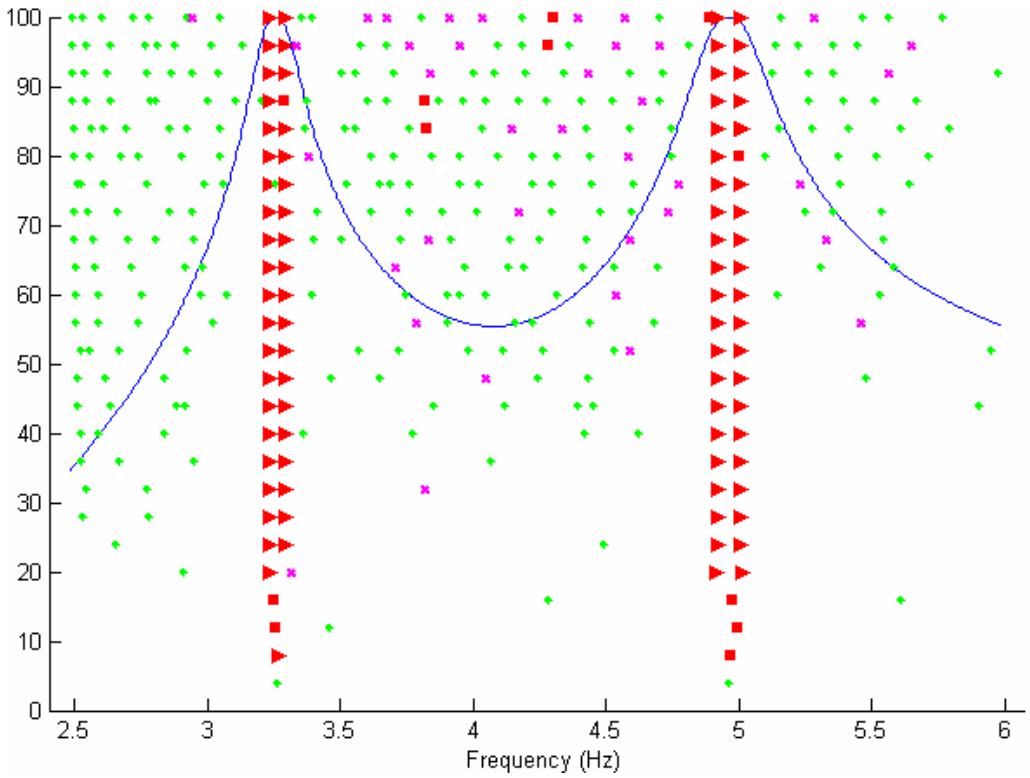

Figure 3.7: Stabilization Diagram constructed using the simplification presented in Section 3.4.1.3

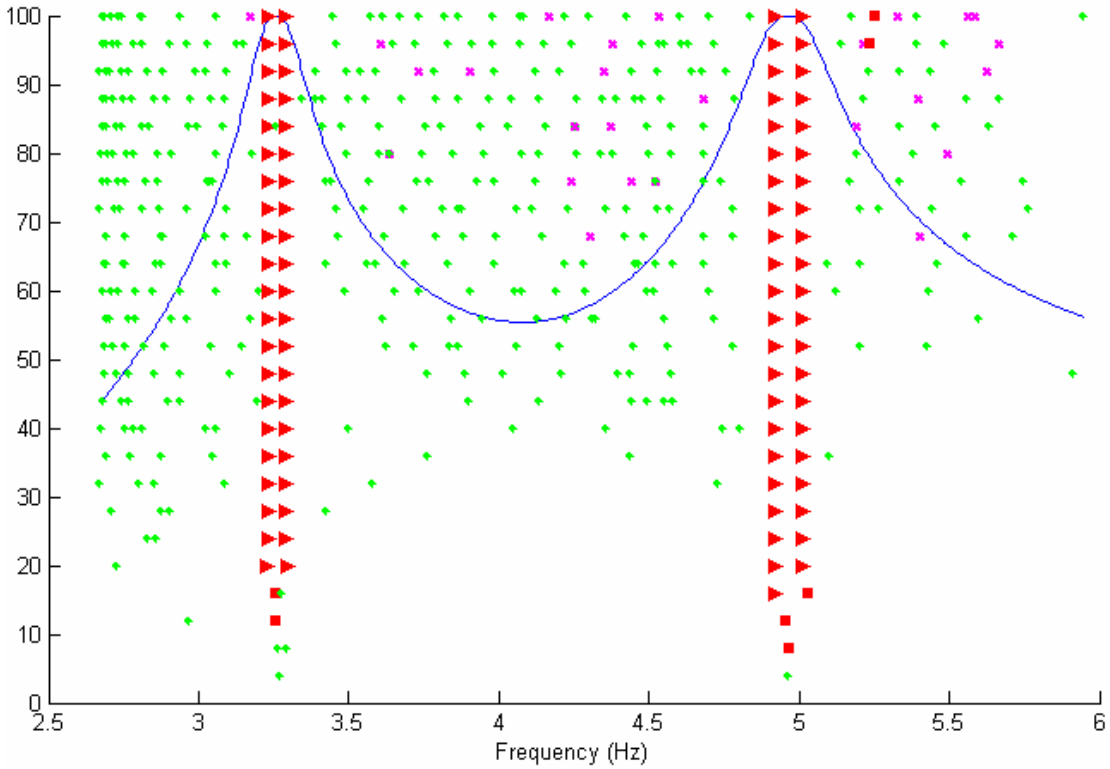

Figure 3.8: Stabilization Diagram constructed using the conventional method

Comparing the stabilization diagrams presented in Figures 3.7 and 3.8 it is observed that several spurious mathematical modes appear for both the cases of the new and the conventional methods. The number of spurious mathematical modes for the case of the conventional method is significantly higher than the corresponding number for the new method. For both methods the physical modes have been identified and the procedure has converged for values of $p = 20$. For the conventional method, the convergence is slower increasing the lowest order of the common denominator polynomial in which all four modes of the structure first appear stabilized. Finally, the predictions of the modal frequencies and damping ratios obtained from the new method and the conventional method for $p = 20$ and $p = 40$ is presented in Tables 3.5 and 3.6 respectively. The accuracy of these prediction is inferred by comparing the predicted values to the actual values obtained from the eigenvalue analysis of the finite element model of the structure. It is observed that generally, the both methods are efficient and accurate with fast converge properties and provide accurate results for the two pairs of closely-spaced modes.

Table 3.5: Comparison between the identified values of the modal frequencies and modal damping ratios and the nominal values estimated by the FEM, for the new method.

	1st mode		2nd mode		3rd mode		4th mode	
	ω_1 (Hz)	ζ_1 (%)	ω_2 (Hz)	ζ_2 (%)	ω_3 (Hz)	ζ_3 (%)	ω_4 (Hz)	ζ_4 (%)
FEM	3.228	2.00	3.286	2.00	4.916	2.00	5.004	2.00
$p = 20$	3.221	1.94	3.293	1.98	4.916	2.02	5.008	1.97
$p = 40$	3.231	2.00	3.288	2.00	4.917	2.00	5.006	2.00

Table 3.6: Comparison between the identified values of the modal frequencies and modal damping ratios and the nominal values estimated by the FEM, for the conventional method.

	1st mode		2nd mode		3rd mode		4th mode	
	ω_1 (Hz)	ζ_1 (%)	ω_2 (Hz)	ζ_2 (%)	ω_3 (Hz)	ζ_3 (%)	ω_4 (Hz)	ζ_4 (%)
FEM	3.228	2.00	3.286	2.00	4.916	2.00	5.004	2.00
$p = 20$	3.225	2.05	3.293	1.98	4.916	2.02	5.008	1.97
$p = 40$	3.231	2.00	3.288	2.00	4.917	2.00	5.006	2.00

From the results, it can be concluded that both methodologies appear to work adequately, easily identifying the modes of the structure. The new method is more efficient since it takes advantage of the special structure of the denominator polynomial in CPSD to converge faster and provide accurate results consistent with the structure of the denominator polynomial.

Next, in order to account of the fact that the existence of measurement noise may hinder the identification of the structural modes, the identification will also be based on simulated acceleration time histories generated by solving the equations of motion of the structure to discrete white noise excitation. For this, the identification of the modes of the bridge shown in

Figure 3.6 is performed again but this time the simulated CPSD functions are computed using simulated vibration response time histories predicted at same locations as before. These vibrations are induced by excitation forces applied at the deck and modeled by discrete white noise processes. The equations of motion are then solved to compute the acceleration response time histories. The CPSD function matrices of the acceleration response of the model are estimated from these simulated time histories using the methodologies described in Appendix 3.A.

In generating the simulated acceleration response time signals to be used for identification using OMA, it should be noted that in order to clearly identify the closely spaced modes, the time duration of these responses should be several times greater than $(2\pi/\Delta\omega)$, where $\Delta\omega$ is the distance between the modal frequencies of the closely spaced modes. It is expected that the larger the duration of the measured response in relation to $(2\pi/\Delta\omega)$, the better the estimates of the closely spaced modal properties. As the duration is increased, the measurements tend to contain the necessary information for the distinction of the closely and overlapped modes.

The first two steps of the proposed identification algorithm described in Section 3.4.2 are applied in the frequency band that contain the closely spaced modes for identifying the modal properties ω_r, ζ_r, $\underline{u}_r$, $\underline{g}_r$, A and B that define the CPSD matrix. The third step of the algorithm described in Section 3.4.3 is also applied, where the original non-linear optimization problem (3.13) is solved with respect to the parameters ω_r, ζ_r and $\underline{g}_r$, using as initial values for the minimization algorithm the values of the parameters already computed by the first two steps of the identification algorithm.

Specifically, the first step of the proposed identification algorithm described in Sections 3.4.1.1 to 3.4.1.3 is applied in the frequency band that contain the first two pairs of closely spaced and overlapping modes for identifying the structural poles that yield the modal frequencies ω_r and the modal damping ratios ζ_r. The stabilization diagrams for the new method (see Section 3.4.1.3) and the conventional one (see Section 3.4.1.1) are constructed with maximum value of order $p=100$ and presented in Figures 3.9 and 3.10, respectively. Comparing the stabilization diagrams it is observed that several spurious mathematical modes appear for both the cases of the new and the conventional methods. The number of spurious mathematical modes for the case of the conventional method is significantly higher than the corresponding number for the new method. It should be noted that for both methods higher order denominator models seem to provide poles that makes the stabilization procedure not very reliable. As before, this problem could be solved by implementing another criterion in the stabilization procedure that takes into account the comparison of the modeshapes computed by the poles of order p and $p-1$.

Also, the new method converges much faster as the value of p increases. Specifically, for the new method the physical modes have been identified and the procedure has converged for values of $p=68$ for the first pair of closely spaced modes and $p=40$ for the second pair of closely spaced modes. For the conventional method, the convergence is much slower and seems to fail to identify the first pair of closely spaced modes.

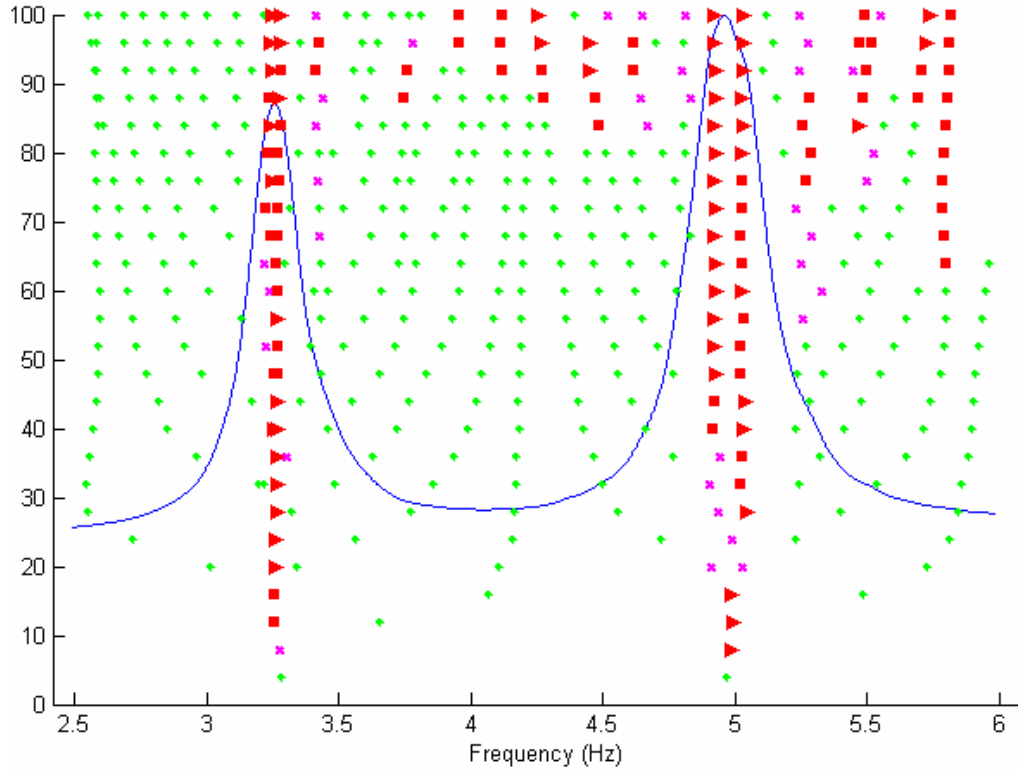

Figure 3.9: Stabilization Diagram constructed using the simplification presented in Section 3.4.1.3

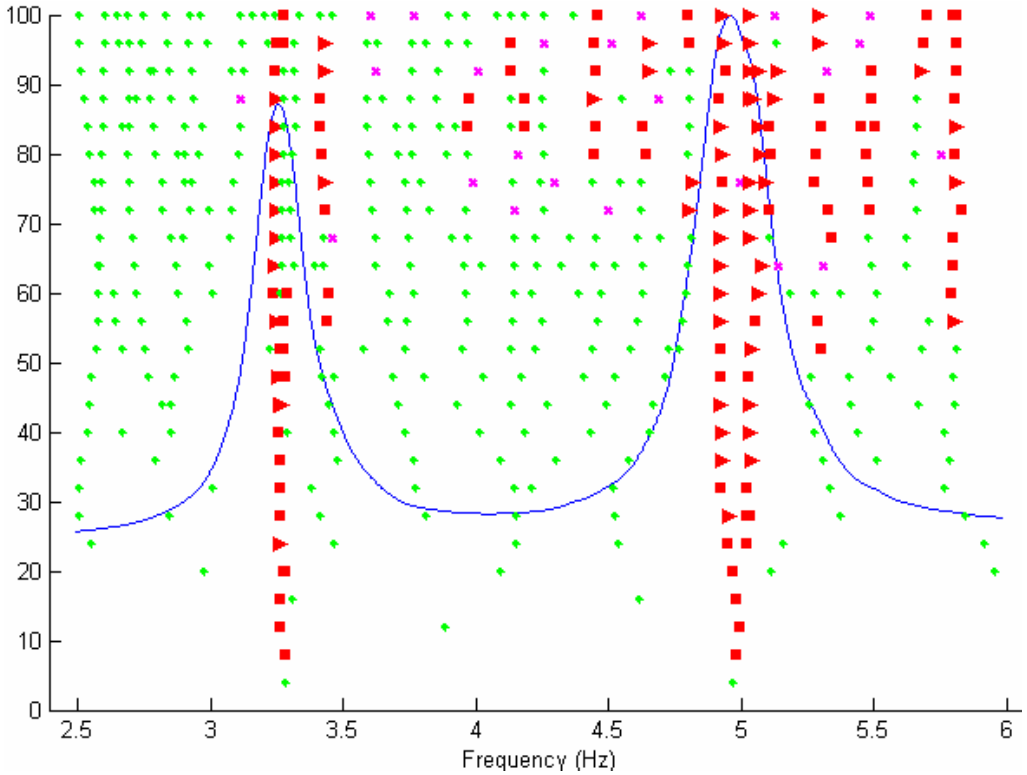

Figure 3.10: Stabilization Diagram constructed using the conventional method

The accuracy of the predictions of the modal frequencies and damping ratios obtained from the new method for $p = 40$ and $p = 100$ is presented in Table 3.7. The accuracy of the predictions of the modal frequencies and damping ratios obtained from the conventional method for $p = 40$ and $p = 100$ is presented in Table 3.8. In both tables the identified values are compared to the actual values obtained from the eigenvalue analysis of the finite element model of the structure. It is obvious that the new method performs much better for closely spaced modes. However, the accuracy of the modal frequencies and damping ratios of the closely spaced modes identified by the new method are not as good, especially for the modal damping ratios. To improve the accuracy of the modal frequencies and damping ratios, third step of the proposed nonlinear optimization algorithm is necessary.

Table 3.7: Comparison between the identified values of the modal frequencies and modal damping ratios and the nominal values estimated by the FEM, for the new method.

	1st mode		2nd mode		3rd mode		4th mode	
	ω_1 (Hz)	ζ_1 (%)	ω_2 (Hz)	ζ_2 (%)	ω_3 (Hz)	ζ_3 (%)	ω_4 (Hz)	ζ_4 (%)
FEM	3.228	2.00	3.286	2.00	4.916	2.00	5.004	2.00
$p = 40$	3.253	0.36	3.266	1.91	4.918	1.32	5.028	1.66
$p = 100$	3.248	1.32	3.278	1.29	4.920	1.25	5.030	1.60

Table 3.8: Comparison between the identified values of the modal frequencies and modal damping ratios and the nominal values estimated by the FEM, for the conventional method.

	1st mode		2nd mode		3rd mode		4th mode	
	ω_1 (Hz)	ζ_1 (%)	ω_2 (Hz)	ζ_2 (%)	ω_3 (Hz)	ζ_3 (%)	ω_4 (Hz)	ζ_4 (%)
FEM	3.228	2.00	3.286	2.00	4.916	2.00	5.004	2.00
$p = 20$	3.266	1.96	-	-	4.922	1.23	5.027	1.64
$p = 100$	3.280	2.47	-	-	4.922	1.29	5.029	1.61

Next, the accuracy of the identified modal values using the first two steps is compared to the accuracy of the identified modal values using all three steps. Using the stabilization diagram of Figure 3.9, the two pairs of closely and overlapping modes are identified and used in the second step of the identification algorithm for the estimation of the modeshapes and the reference vectors. Both approaches, termed 1st and 2nd approach, presented in Section 3.4.1.2 are applied. The resulting modal fits are shown in Figures 3.11 and 3.12 in the vicinity of the two pairs of closely spaced modes. Specifically, Figures 3.11 and 3.12 shows the comparison between the absolute value $\left\|\hat{S}(k\Delta\omega)\right\|$ of the measured CPSD functions and the absolute value $\left\|S(k\Delta\omega;\underline{\theta})\right\|$ of the CPSD functions predicted by the identified modal model. The third step of the identification algorithm is also applied and the resulted modal fits are also shown in Figures 3.11 and 3.12 for

the acceleration responses concentrated in the frequency band of the closely spaced and overlapping modes. For the third step, also the two approaches, termed 1st and 2nd approach, that have been introduced in Section 3.4.1.3 are applied. Table 3.9 summarizes the results for the modal frequencies and the modal damping ratios estimated by the third step of the algorithm using both the first and the second approach. It can be seen that the estimated values are very close to the exact values predicted by the finite element model used to generate the measurements especially when using the second approach

.

Table 3.9: Comparison between the identified values of the modal frequencies and modal damping ratios and the nominal values estimated by the FEM, using the three step algorithm.

	1st mode		2nd mode		3rd mode		4th mode	
	ω_1 (Hz)	ζ_1 (%)	ω_2 (Hz)	ζ_2 (%)	ω_3 (Hz)	ζ_3 (%)	ω_4 (Hz)	ζ_4 (%)
FEM	3.228	2.00	3.286	2.00	4.916	2.00	5.004	2.00
1st Approach	3.243	1.71	3.293	1.74	4.921	1.79	5.037	1.74
2nd Approach	3.234	2.00	3.287	2.09	4.913	1.93	5.013	1.86

It can be easily observed in the Figures 3.11 and 3.12 that for the case of closely and overlapping modes the modal model identified by applying only the first two steps of the algorithm is quite inadequate compared to the modal model identified using the third step (2nd approach) algorithm. It can also be observed that the modal model identified when applying the first approach of the three step algorithm can not predict the response of the structure as good as the modal model identified when applying the second approach. This has been observed for many cases of closely spaced and overlapping modes and is due to the assumption that the residue matrix R_r is of rank 1. For the case where the third step of the algorithm is used with the second approach outlined in Section 3.4.1.3, the identified modal model predicts very efficiently the closely spaced modes, while the corresponding CPSD predicted by the modal model provides a very good fit to the measured CPSD functions.

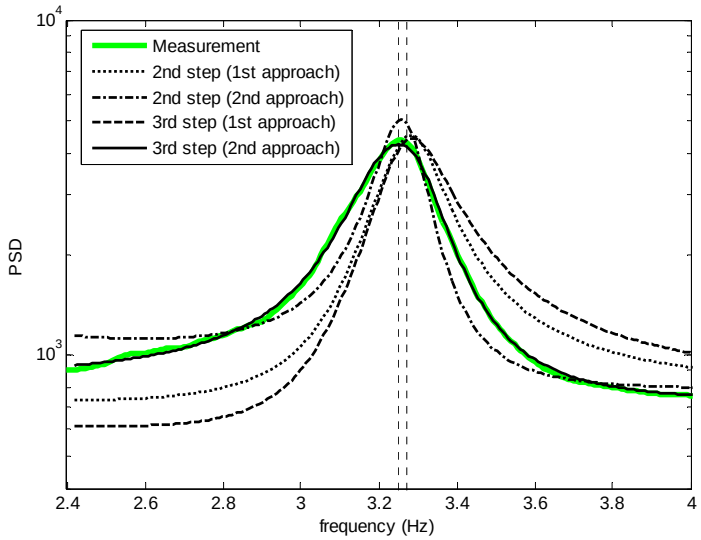

Figure 3.11: Comparison between the measured CPSD function and the CPSD functions predicted by the modal model that was identified by applying the two step and the three step algorithms in the frequency band of the first pair of closely-spaced modes.

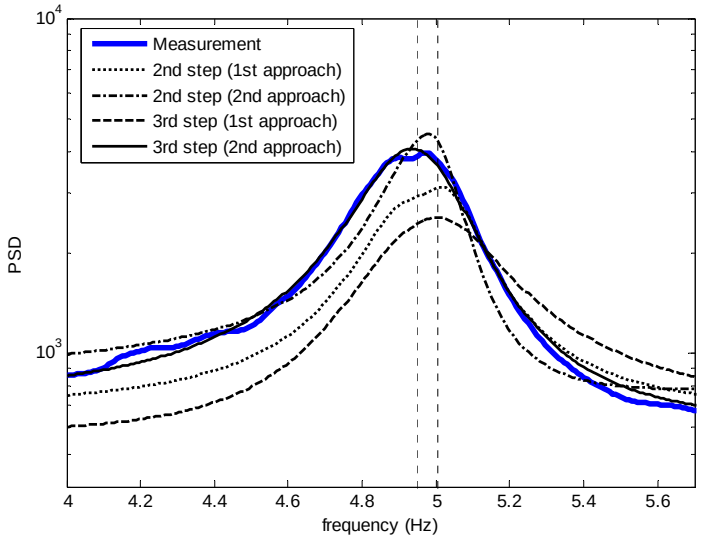

Figure 3.12: Comparison between the measured CPSD function and the CPSD functions predicted by the modal model that was identified by applying the two step and the three step algorithms in the frequency band of the second pair of closely-spaced modes.

3.5.3 Identification of structural poles using real measurement data

This section applies the developed modal identification methodologies for estimating the dynamic modal characteristics of the Metsovo bridge, shown in Figure 3.13, using ambient vibration measurements. Specifically, six uniaxial accelerometers were installed inside the box beam cantilever M3 of the left carriageway of Metsovo bridge when the carriageway was under construction. The part of the bridge that was constructed and instrumented is the one highlighted

in Figure 3.13. This subsection is concentrated in the efficiency of the proposed three step modal identification algorithm and thus complete description of the bridge and the instrumentation procedure are not given here. A fully detailed study on this bridge is presented in the work Panetsos et al. (2009) and Ntotsios (2009).

Figure 3.13: General view of the under construction Metsovo ravine bridge (November 2007)

The CPSD function matrix of the six measured acceleration responses of the bridge are first estimated using the methodologies described in Appendix 3.A. Then the first step of the proposed identification algorithm described in Sections 3.4.1 to 3.4.3 is applied in the frequency band 0 to 1 Hz for identifying the structural poles that yield the modal frequencies ω_r and the modal damping ratios ζ_r. The stabilization diagrams for the new method (see Section 3.4.1.3) and the conventional one (see Section 3.4.1.1) are constructed with maximum value of order $p=100$ and presented in Figures 3.14 and 3.15, respectively. The interpretation of the symbols (markers) green cross (+), red square and red triangular in these figures is kept the same as the one used for Figures 3.2 to 3.5. Comparing the stabilization diagrams presented in Figures 3.14 and 3.15 it is observed that the number of spurious mathematical modes for the case of the conventional method is significantly higher than the corresponding number for the new method. Also, much clearer stabilization diagrams are observed for the new method compared to the conventional method. In addition, the new method converges faster as the value of p increases. Specifically, for the new method the physical modes have been identified and the procedure has converged for values of $p=20$. For the conventional method, the convergence is slower since the lowest order of the common denominator polynomial in which all four modes of the structure first appear stabilized is $p=24$ using the tolerance of $tol=3\%$.

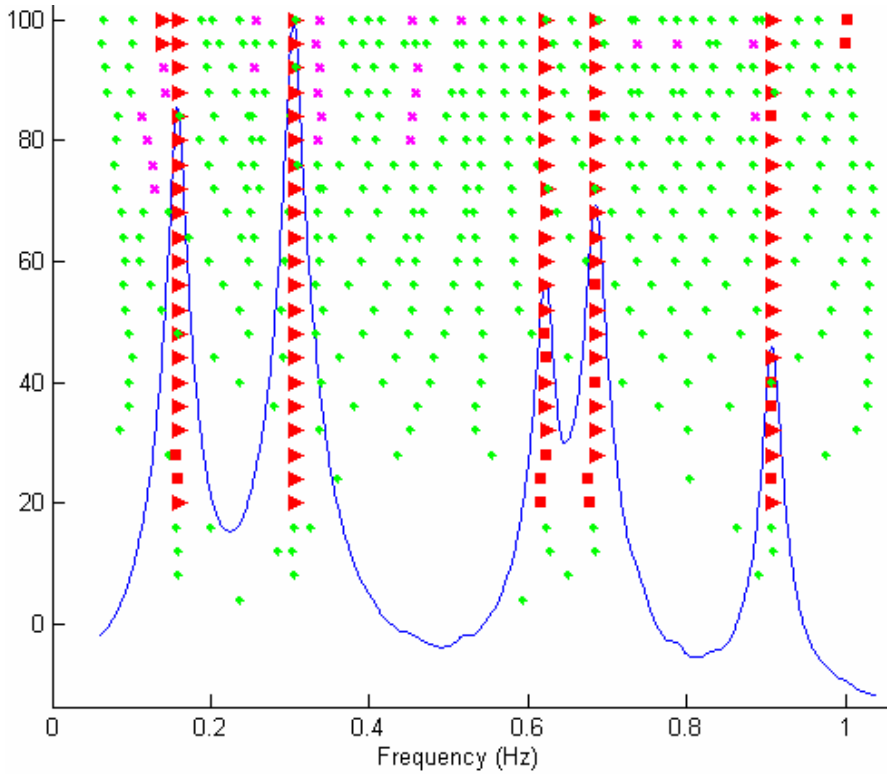

Figure 3.14: Stabilization Diagram constructed using the simplification presented in Section 3.4.1.3

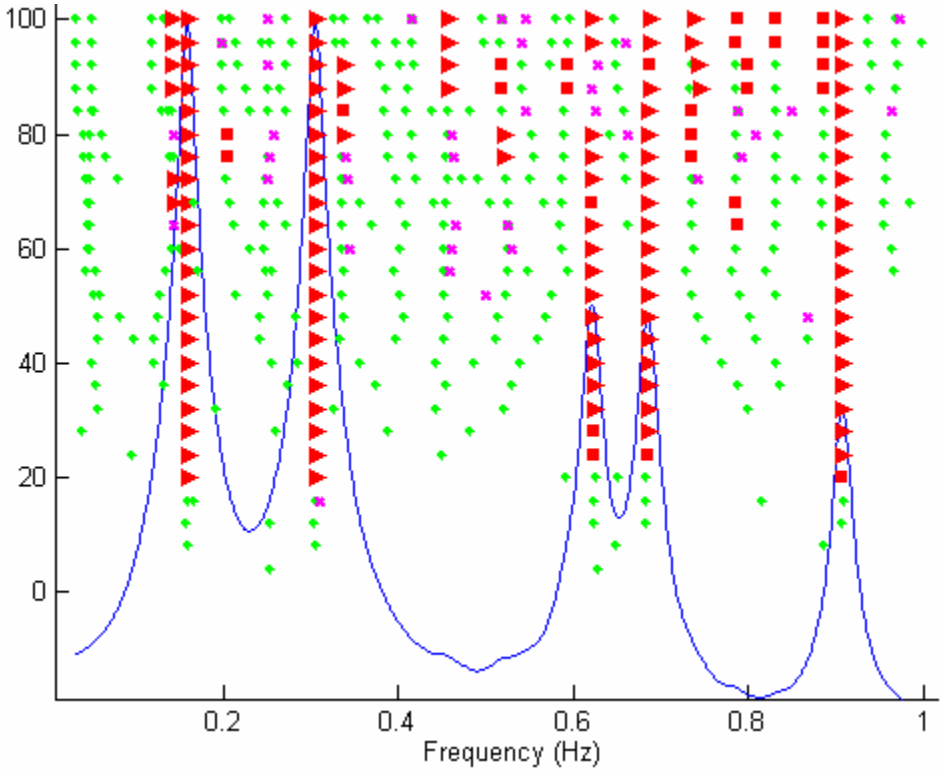

Figure 3.15: Stabilization Diagram constructed using the conventional method

The accuracy of the predictions of the modal frequencies and damping ratios obtained from the new method for $p=20$ and $p=100$ is presented in Table 3.10 and from the conventional method for $p=24$ and $p=100$ is presented in Table 3.11. It can be seen that both the new and the conventional method provide the same estimate of the modal frequencies for values of p as low as $p=20$ and $p=24$, respectively. Increasing the order of p does not improve the predictions. The values of the damping ratios differ slightly depending on the method and the order p used. Specifically, on can observe that both the new and the conventional method provide the same estimate of the modal damping ratios for values of p as high as $p=100$. For low values of $p=20$ for the new method and $p=24$ for the conventional method, the predictions differ significantly. Despite these differences, the predictions of the modal damping ratios even for the low p values are considered to be acceptable.

Table 3.10: Identified values of the modal frequencies and modal damping ratios for the case of the new method

	1st mode		2nd mode		3rd mode		4th mode		5th mode	
	ω_1 (Hz)	ζ_1 (%)	ω_2 (Hz)	ζ_3 (%)	ω_3 (Hz)	ζ_3 (%)	ω_4 (Hz)	ζ_4 (%)	ω_5 (Hz)	ζ_5 (%)
$p=20$	0.158	0.41	0.305	0.20	0.623	0.34	0.685	0.39	0.907	0.21
$p=100$	0.158	0.29	0.305	0.17	0.622	0.47	0.685	0.35	0.907	0.28

Table 3.11: Identified values of the modal frequencies and modal damping ratios for the case of the conventional method

	1st mode		2nd mode		3rd mode		4th mode		5th mode	
	ω_1 (Hz)	ζ_1 (%)	ω_2 (Hz)	ζ_3 (%)	ω_3 (Hz)	ζ_3 (%)	ω_4 (Hz)	ζ_4 (%)	ω_5 (Hz)	ζ_5 (%)
$p=24$	0.158	0.45	0.305	0.20	0.622	0.47	0.684	0.54	0.908	0.34
$p=100$	0.158	0.27	0.305	0.18	0.622	0.45	0.685	0.37	0.907	0.26

Next, using the stabilization diagram of Figure 3.16, five modes of the bridge are identified in the [0,1] Hz frequency band and used in the second step of the identification algorithm for the estimation of the modeshapes and the reference vectors. The first approach presented in Section 3.4.2.1 is applied. In addition, the third step of the identification algorithm is also used to improve the estimate of the modal model. The measured PSD function $\left\|\hat{S}(k\Delta\omega)\right\|$ is compared in Figure 3.11 for three measured acceleration responses concentrated in the frequency band 0 to 1 Hz to the PSD functions $\left\|S(k\Delta\omega;\underline{\theta})\right\|$ predicted by identified modal model using the two-step and the three-step algorithms. It can be observed that for this case of real measurement data with non-closely spaced and non-overlapping modes, and despite the noise in the signals resulted from the actual measurements, the modal model identified by the two step algorithm provides an excellent

fit to the measured PSDs which is almost identical to the fit provided by the modal model identified from the three step algorithm.

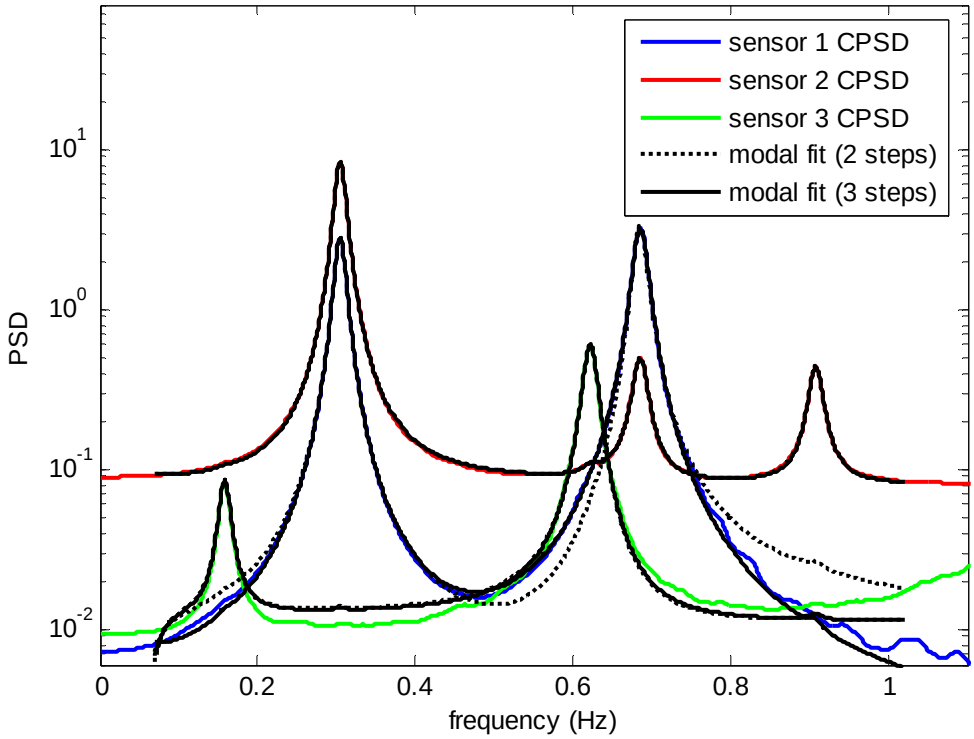

Figure 3.16: Comparison between the measured CPSD function and the CPSD functions predicted by the modal model that was identified by applying the two step and the three step algorithms.

3.6 Conclusions

Frequency domain least squares methods for the identification of non-classically damped modal models of linear structures using ambient vibration measurements were developed. The identification was based on minimizing the square difference between the measured CPSD matrix estimated from the available output only measurements and the CPSD matrix predicted by a modal model. The identification involves the estimation of the number of contributing modes, the modal frequencies, the modal damping ratios and the complex modeshapes of the contributing modes. Computational efficient algorithms for solving the resulting, highly non-convex, nonlinear optimization problem were proposed, including features of automatically estimating the number of contributing modes, as well as the modal frequencies and the damping ratios of the physical modes without or minimal user intervention.

A three-step approach was proposed to carry out efficiently the optimization. In the first step, the modal frequencies and modal damping ratios are estimated by solving a system of linear algebraic equations using the description of the CPSD matrix as a rational fraction of polynomials with common the denominator polynomial for all entries of the CPSD matrix. One of the novel

contributions is the methodology based on the special structure of the common denominator polynomial that is revealed by examining the dependence of the CPSD matrices on the eigenvalues for the discrete time formulation. Taking advantage of this special structure, one simplifies the system of normal equations used to compute the coefficients of the common denominator polynomial and also reduces considerably the number of spurious mathematical (non-physical) modes that are obtained using the conventional methodology. The modal frequencies and the damping ratios of the structure are obtained from the roots of the common denominator polynomial estimated using the eigenvalues of the companion matrix. Stabilization diagrams are used to estimate the number of contributing modes by distinguishing between physical and mathematical modes. In the second step, two alternative approaches were introduced to estimate the modeshapes of the structure. The first approach is non-iterative and estimates the modal residue matrices by solving a linear system of equations given the values of the modal frequencies and damping ratios estimated in the first step. Singular value decomposition on the residue matrices provides the complex modeshapes of the structure. The second approach is a least squares optimization approach that takes advantage of the quadratic dependence of the objective function on the modeshapes and other matrices to reduce the number of parameters involved in the nonlinear optimization to the smallest possible number.

The estimates provided from the first two steps are in most cases very close to the optimal estimates. In order to improve the estimates, the full non-convex nonlinear optimization problem has to be solved in the third step by using the initial estimates of the parameters obtained in the first two steps to accelerate convergence of the optimization algorithm. Two very efficient solution approaches were proposed for the third step. It is demonstrated that for closely-spaced and overlapping modes the third step improves significantly the accuracy of the modal characteristics.

The efficiency of the algorithm is tested using simulated ambient vibration data generated by simple structural models, as well as real measured ambient vibration data available for a full scale structure. The results showed that generally the proposed method for the identification of the structural poles in the first step is computationally much more efficient and accurate than existing methods since it has faster converge properties and provide accurate results for the modal frequencies and damping ratios. For the case of closely-spaced and overlapping modes it was demonstrated that the first two steps fail to accurately estimate the modal characteristics of the closely spaced modes. The third step of the proposed algorithm is required to improve significantly the estimates of the modal characteristics for closely spaced and overlapping modes. Finally, the proposed modal identification methodology applied on real measurement data from a full scale structure was shown to be very accurate since the fit between the measured and the modal model predicted CPSD functions was excellent.

Appendix 3.A

Estimation of auto and cross power spectral densities

Parts of the presentation that follows have been taken from the work of Parloo (2003) and Cauberghe (2004).

3.A.1 The periodogram approach

The periodogram method is a popular method for the estimation of auto and cross power spectral densities (Marple, 1987). Let $x_o(m)$, $m=0,\cdots,M-1$, $o=1,\cdots,N_{out}$ be an assembly of N_{out} discrete time-domain output sequences. Let $\underline{x}^{ref}(m)$ be a sub-vector of $\underline{x}(m)$ containing the time sequences of N_{ref} outputs which are serving as reference-responses for the measured data set. The basic idea of the periodogram method is to divide the data sequence for each measured output of M samples into P non-overlapping segments of D samples each, so that $DP \le M$. As an alternative to choosing no common samples between adjacent segments, a small overlap can be used (Welch, 1967). For each segment s, $s=0,\cdots,P-1$, the discrete Fourier transform of the signal $x_o(m)$ for all considered responses o, $o=1,\cdots,N_{out}$, weighted with a time window W of length D, can be computed as

$$X_o^s(j\omega) = T_s\left(\sum_{k=0}^{D-1} W(k)x_o(sD+k)e^{-j\omega kT_s}\right) \tag{3.127}$$

A similar expression can be found for all reference responses i, $i=1,\cdots,N_{ref}$, assembled in the sub-vectors $\underline{x}^{ref}(m)$

$$X_o^{s,ref}(j\omega) = T_s\left(\sum_{k=0}^{D-1} W(k)x_i^{ref}(sD+k)e^{-j\omega kT_s}\right) \tag{3.128}$$

An estimate of the entries of the $(N_{out}\times N_{ref})$ cross power spectral density matrix $S(j\omega)$ for each response reference-response combination, evaluated at discrete frequency ω, is given by

$$S_{o,i}(j\omega) = \frac{1}{P}\sum_{s=0}^{P-1}\left[X_o^s(j\omega)\left(X_i^{s,ref}(j\omega)\right)^*\right] \tag{3.129}$$

where $X_o^s(j\omega)$ and $X_i^{s,ref}(j\omega)$ are respectively the $(N_{out}\times 1)$ and $(N_{ref}\times 1)$ vectors computed in (3.127) and (3.128).

The time window W (e.g., Hanning window) is used to reduce the negative effect of leakage. Choosing a higher amount of data samples D in each segment, at the expense of the number of averages P, will reduce the effect of leakage. Moreover, a higher spectral resolution will be obtained in the frequency-domain. However, the resulting decrease in the number of averages P leads to a higher stochastic uncertainty on the estimates. In practice, a trade-off will have to be made between these contradicting aspects.

Note that the basic idea behind allowing an overlap between the data segments consists in allowing a better contribution of all samples of the raw time history response data to the averaged estimate. If no overlap is considered, the contribution of samples near the edges of the segments will be suppressed by the presence of the Hanning window.

3.A.2 The correlogram approach

The periodogram approach can be used as an alternative to the periodogram method for the estimation of cross power spectra of the response signals. This method computes the unbiased discrete-time domain correlation estimate between the signal $x_o(m)$, $m = 0, \cdots, M-1$, of a response o and the signal $x_i^{ref}(m)$ of a reference-response i. This correlation estimate is given by

$$\begin{cases} R_{o,i}(k) = \dfrac{1}{M-k} \displaystyle\sum_{m=0}^{M-k-1} x_o(m+k) x_i^{ref}(\mathrm{m}) & \text{for } 0 \le k \le M\text{-}1 \\ R_{o,i}(k) = \dfrac{1}{M-|k|} \displaystyle\sum_{m=0}^{M-|k|-1} x_i^{ref}(m+|k|) x_o(\mathrm{m}) & \text{for } -(M\text{-}1) \le k \le 0 \end{cases} \tag{3.130}$$

with k the correlation time. The biased correlation estimate uses $1/M$ rather than $1/(M-k)$. The cross power spectral density function matrix estimates can then be obtained by Fourier transforming the correlation functions obtained from (3.130)

$$S_{o,i}(j\omega) = T_s \sum_{k=-M}^{M} W(k) R_{o,i}(k) e^{-j\omega T_s} \tag{3.131}$$

where $R(k)$ is the $(N_{out} \times N_{ref})$ matrix that contains the correlation estimates calculated in (3.130) and $W(k)$ is a $(2M+1)$ point time window.

The window reduces the effect of leakage due to the large side lobes of the implicit rectangular window and therefore the bias error in the cross power spectral density estimate. The use of an adequate window (e.g., Hanning, Hamming, etc), symmetric around the origin, is advisable. For instance, applying a Hanning window to the correlation estimate will force the correlation to zero at the higher lags. Moreover, the application of such a window reduces the stochastic uncertainty on the cross power estimate due to the presence of a higher stochastic uncertainty near the higher lags of the correlation function estimate. However, when applying a time window, the poles (and especially the damping) of the underlining system will be affected. However, for an exponential window, the poles can be compensated exactly for the added damping. This is not the case for other windows such as Hanning or Hamming.

Hence, for the purpose of modal parameter estimation, the correlogram approach is best combined with the use of an exponential window. Given the form of the correlation function estimates, a double sided exponential time data window centered around 0,

$$W_m = e^{-\beta|m|T_s} \qquad \text{with} \qquad -\mathrm{M} \le \mathrm{m} \le +\mathrm{M} \tag{3.132}$$

with β a decay factor, can be used. The poles λ_r^{est} extracted from the estimates can be compensated (corrected) for the artificial damping added by the window by using the value of the β factor as follows

$$\lambda_r^{cor} = \lambda_r^{est} + \beta \tag{3.133}$$

Although an averaging procedure is usually not strictly required, the possibility exists to use an averaging similar to the periodogram approach. If the time history response sequences consist of M samples, every response sequence can be divided into P non-overlapping segments of D samples each so that $DP \le M$. Correlogram estimates of the auto- and cross power spectra $S_{o,i}^s$, between the responses o, $o = 1, \cdots, N_{out}$, and a subset of reference responses i, $i = 1, \cdots, N_{ref}$, can be obtained using equations (3.130) and (3.131) for each segments s, $s = 0, \cdots, P-1$. An averaged correlogram estimate of the auto- and cross power spectra is then given by

$$S_{o,i} = \sum_{s=0}^{P-1} S_{o,i}^s \tag{3.134}$$

It should be noted that averaging the correlogram estimates decreases the spectral resolution of the resulting estimate. Reducing the number of samples used for the computation of the correlation functions also increases the bias error due to leakage on these estimates.

3.A.3 The 'positive' power spectra approach

For the identification of modal parameters from output-only measurements, several frequency-domain identification methods are based on the cross power spectral densities satisfying (3.4). However, this technique has several disadvantages:

- The power spectra have a 4-quadrant symmetry i.e. the modal model contains as poles the values λ_r, λ_r^*, $-\lambda_r$ and $-\lambda_r^*$. This results in a model order, which is twice the modal order needed to model FRFs. For all identification methods based on the full spectra, this higher model order results in an increasing calculation time and in a less good numerical conditioning.
- The power spectra contain both stable λ_r, λ_r^* and unstable poles $-\lambda_r$, $-\lambda_r^*$ poles in its model. This results in less interesting properties for the interpretation of stabilization diagrams, when distinguishing physical from mathematical poles.
- Power spectra estimated from a limited amount of data are typically characterized by high noise levels compared to FRFs. Therefore, an additional noise reduction would be preferable.
- When using the periodogram approach to estimate the power spectra, a tradeoff must be made between the stochastic uncertainties and the bias errors introduced by leakage.

Some of these disadvantages can be overcome by starting from the first M positive lags of the correlation function R_n given by (3.130). Using the correlogram approach it is sufficient to estimate the so called *positive spectra (*or half spectra), which are obtained by using only the correlation having a positive time lag (Cauberghe 2004, Peeters and Van der Auwearer 2005) in (3.131) as follows

$$S_{o,i}^{++}(j\omega) = \frac{W(0)R_{o,i}(0)}{2} + T_s \sum_{k=1}^{M} W(k)R_{o,i}(k)e^{-j\omega T_s} \tag{3.135}$$

The relation between half spectra (3.135) and the full spectra (3.131) is the following:

$$S_{o,i}(j\omega) = S_{o,i}^{++}(j\omega) + \left(S_{o,i}^{++}(j\omega)\right)^{*T} \tag{3.136}$$

The modal decomposition of these half spectra only consists of the first two terms in (3.4), that is,

$$S_{xx}^{++}(j\omega) = \sum_{r=1}^{N_m} \left[\frac{\underline{u}_r \underline{g}_r^T}{j\omega - \lambda_r} + \frac{\underline{u}_r^* \underline{g}_r^{*T}}{j\omega - \lambda_r^*} \right] \tag{3.137}$$

The advantage in modal analysis is that models of low order can be fitted without affecting the quality.

Under the white noise input assumption, the output correlations are equivalent to impulse response. So, just like in impact testing, it is logical to apply an exponential window $W(k)$ to the correlations before computing the DFT in equation (3.135). The exponential window reduces the effect of leakage and the influence of the higher time lags, which have a larger variance. Moreover, the application of an exponential window to impulse responses or correlations is compatible with the modal model and the pole estimates can be corrected using equation (3.133).

3.A.4 Choosing reference responses

Similar to choosing position(s) for the input force(s) (so-called references) during input-output modal testing, the choice of good reference response signals during output-only modal testing can be important for obtaining high quality data sets.
If all N_{out} responses of a structure under test are measured simultaneously, each of the structural responses can be used as a reference response. This approach results in a $N_{out} \times N_{out}$ power spectrum matrix $S(j\omega)$. If the number of outputs is large, the latter approach can lead to a high computational burden especially during the parametric estimation.

Instead of using all outputs as reference responses, a small number of responses in suitable locations of the structure can be chosen as reference responses. Note that the nodal points of structural modes should be avoided to be used as reference positions. Moreover, responses with a signal to noise ratio superior (or at least equal) compared to the other responses should be preferred when choosing reference responses in order to increase the quality of the auto and cross power spectral density estimates. If the reference response signals are chosen carefully,

similar quality modal information can be extracted from data sets obtained with a limited number of references as from data sets where the maximum number of references was used.

The idea of the reference sensors can be used to obtain measurements for a structure using a small number of sensors compared to the measurement locations that one would like to identify the modeshape components. In this case the available sensors are divided into two groups. One group constitutes the reference group and the sensors are placed at reference locations which remain fixed during the measurements. The other group constitutes the moving group and the sensors in this group are moved from measurement to measurement to new locations until all desirable measurements locations are covered by the available number of moving sensors. The measurements from the moving sensors are combined into the vector $\underline{x}(m)$, while the measurements from the reference sensors constitute the vector of measurements $\underline{x}^{ref}(m)$. In choosing the reference locations care should be taken so that nodal points are avoided.

Chapter 4

Structural identification methods for finite element model updating and prediction variability

4.1 Introduction

Structural model updating methods (e.g. Mottershead and Friswell, 1993; Farhat and Hemez, 1993; Capecchi and Vestroni, 1993; Link, 1998; Yuen et al., 2006) have been proposed in the past to reconcile mathematical models, usually discretized finite element models, with experimental data. Each model updating method has its own advantages and shortcomings, but there is no universally acceptable methodology for treating the model updating problem. Comprehensive reviews of structural model updating methods can be found in the work by Mottershead and Friswell (1993) and Doebling et al. (1998). The estimate of the optimal model is sensitive to uncertainties that are due to limitations of the mathematical models used to represent the behavior of the real structure, the presence of measurement noise from ambient excitations and the processing errors in estimating the modal data. Also, optimal model estimates are sensitive to the number and type of measured response time histories or modal data used in the reconciling process, as well as the norms used to measure the fit between measured and model predicted response time histories or modal properties. The optimal structural models resulting from such methods can be used for improving the model response and reliability predictions, as well as accounting for the uncertainties in these predictions (Beck and Katafygiotis, 1998; Papadimitriou et al., 2001; Beck and Au, 2002). Moreover, these optimal structural models can be used for structural health monitoring applications (Sohn and Law, 1997; Fritzen et al., 1998; Vanik et al., 2000; Teughels and De Roeck 2005) and structural control (Yuen and Beck 2003).

Structural model parameter estimation problems based on measured data, such as modal characteristics (e.g. Mottershead and Friswell, 1993; Hjelmstad and Shin, 1996; Alvin, 1997; Bohle and Fritzen, 2003) or response time history characteristics (Beck and Katafygiotis, 1998), are often formulated as weighted least-squares problems in which metrics, measuring the residuals between measured and model predicted characteristics, are build up into a single weighted residuals metric formed as a weighted average of the multiple individual metrics using weighting factors. Standard optimization techniques are then used to find the optimal values of the structural parameters that minimize the single weighted residuals metric representing an overall measure of fit between measured and model predicted characteristics. Due to model error and measurement noise, the results of the optimization are affected by the values assumed for the weighting factors. The choice of the weighting factors depends on the model adequacy and the uncertainty in the available measured data, which are not known apriori. Different values of the weights result in different optimal models and consequently different predictions from the optimal models.

The model updating problem has also been formulated in a multi-objective context (Haralampidis et al., 2005) that allows the simultaneous minimization of the multiple metrics, eliminating the need for using arbitrary weighting factors for weighting the relative importance of each metric in

the overall measure of fit. The multi-objective parameter estimation methodology provides multiple Pareto optimal structural models consistent with the data and the residuals used in the sense that the fit each Pareto optimal model provides in a group of measured modal properties cannot be improved without deteriorating the fit in at least one other modal or response time history group.

Each optimal model in the Pareto set can alternatively be obtained by solving the weighted least-squares problem for a particular choice of the weight values. The whole Pareto optimal set could be estimated by varying the weight values from 0 to 1, excluding the case for which all weight values are simultaneously equal to zero. The final task of rationally selecting a unique set of weight values on which to base the estimation of the optimal structural model using the weighted least-squares method or, equivalently, the task of selecting an optimal structural model among all Pareto optimal models, is subjective and is usually left to the experience of the structural analysts.

In this chapter, the structural model updating problem using modal residuals is first formulated as a multi-objective optimization problem and then as a single-objective optimization with the objective formed as a weighted average of the multiple objectives using weighting factors. The problem of rationally estimating the optimal values of the weights or, equivalently, selecting the most probable structural model among the Pareto optimal models utilising the available measured data is addressed. Thus, the selection of the optimal structural model is based on weight values that are estimated based on the data, avoiding an arbitrary a priori selection of these weight values. In addition, a Bayesian statistical framework (Beck, 1989; Beck and Katafygiotis, 1998; Katafygiotis et al., 1998; Sohn and Law, 1997) for structural model parameter identification is used to identify the values of the weights. Using Bayes theorem, the probability distribution of the weight values based on the data is formulated as a probability integral over the structural model parameters (Christodoulou and Papadimitriou, 2007). An asymptotic approximation is presented to analytical approximate this probability distribution. The best values of the weights are selected as the ones that maximize the probability distribution of the weights.

Theoretical and computational issues arising in multi-objective identification are addressed and the correspondence between the multi-objective identification and the weighted residuals identification is established. Emphasis is given in addressing issues associated with solving the resulting multi-objective and single-objective optimization problems. In addition, efficient methods are proposed for estimating the gradients and the Hessians of the objective functions using the Nelson's method (Nelson, 1976) for finding the sensitivities of the eigenproperties to model parameters.

This chapter is organized as follows. In Section 4.2 the structural identification problem using modal residuals is first formulated as a multi-objective optimization problem and then as an equivalent single-objective optimization with the objective formed as a weighted average of the multiple objectives using weighting factors. For this, the modal properties are assigned into groups and each objective involved in the optimization measures the residuals of the difference between the experimental and the model predicted modal properties involved in a modal group. The correspondence between the multi-objective identification and the weighted modal residuals

identification is also established. A novel optimally weighted modal residuals method is proposed. In Section 4.3, a Bayesian statistical system identification framework for structural parameter estimation is reviewed to address the problem of estimating the probability distribution and the optimal values of the weights based on the measured data. Using asymptotic approximations the resulting probability integrals describing the probability distribution of the weight values are estimated. Two algorithms are proposed for estimating the optimal values of the weights and the corresponding optimal structural model based on the measured modal data. In Section 4.4, theoretical and computational issues associated with solving the resulting single-objective and multi-objective optimization problems are addressed, including issues related to estimation of global optima, convergence of the proposed algorithms, and identifiability. In Chapter 4.5 emphasis is given in addressing the problem of structural model updating for the case of closely spaced modes. Finally, in Section 4.6, theoretical and computational issues are illustrated by applying the methodology for updating two model classes, a simple three degrees-of-freedom (DOF) model and a much higher fidelity finite element model class, using experimentally obtained modal data from a small-scaled three-story laboratory steel building structure tested at a reference and a mass modified configuration. Validation studies are performed to show the applicability of the methodologies, the advantages of the multi-objective identification, and the performance of the most preferred Pareto optimal model. Emphasis is given in investigating the variability of the Pareto optimal models and the variability of the response predictions from these Pareto optimal models. Comparisons between the results from a simple 3-DOF model class and a much higher fidelity finite element model class, are used to assess the effect of model error uncertainty on model updating and model response prediction variability. The conclusions are summarized in Section 4.7.

4.2 Model updating based on modal residuals

4.2.1 Modal groups and residuals

Let $D = \{\hat{\omega}_r^{(k)}, \underline{\hat{\phi}}_r^{(k)} \in R^{N_0},\ r = 1,\cdots,m,\ k = 1,\cdots,N_D\}$ be the measured modal data from a structure, consisting of modal frequencies $\hat{\omega}_r^{(k)}$ and modeshape components at N_0 measured DOFs, where m is the number of observed modes and N_D is the number of modal data sets available. Consider a parameterized class of linear structural models used to model the dynamic behavior of the structure and let $\underline{\theta} \in R^{N_\theta}$ be the set of free structural model parameters to be identified using the measured modal data. The objective in a modal-based structural identification methodology is to estimate the values of the parameter set $\underline{\theta}$ so that the modal data $\{\omega_r(\underline{\theta}),\ \underline{\phi}_r(\underline{\theta}) \in R^{N_d}, r = 1,\cdots,m\}$, where N_d is the number of model degrees of freedom (DOF), predicted by the linear class of models best matches, in some sense, the experimentally obtained modal data in D. For this, let

$$\varepsilon_{\omega_r}(\underline{\theta}) = \frac{\omega_r^2(\underline{\theta}) - \hat{\omega}_r^2}{\hat{\omega}_r^2} \quad \text{and} \quad \varepsilon_{\underline{\phi}_r}(\underline{\theta}) = \frac{\left\| \beta_r(\underline{\theta}) L\underline{\phi}_r(\underline{\theta}) - \hat{\underline{\phi}}_r \right\|}{\left\| \hat{\underline{\phi}}_r \right\|} \tag{4.1}$$

$r = 1, \cdots, m$, be the measures of fit or residuals between the measured modal data and the model predicted modal data for the r-th modal frequency and modeshape components, respectively, where $\| \underline{z} \|^2 = \underline{z}^{\mathrm{T}} \underline{z}$ is the usual Euclidian norm, and $\beta_r(\underline{\theta}) = \hat{\underline{\phi}}_r^T L\underline{\phi}(\underline{\theta})_r / \left\| L\underline{\phi}_r(\underline{\theta}) \right\|^2$ is a normalization constant that guaranties that the measured modeshape $\hat{\underline{\phi}}_r$ at the measured DOFs is closest to the model modeshape $\beta_r(\underline{\theta}) L\underline{\phi}_r(\underline{\theta})$ predicted by the particular value of $\underline{\theta}$. The matrix $L \in R^{N_0 \times N_d}$ is an observation matrix comprised of zeros and ones that maps the N_d model DOFs to the N_0 observed DOFs.

In order to proceed with the model updating formulation, the measured modal properties are grouped into n groups. Each group contains one or more modal properties. The modal properties assigned in the ith group are identified by the set $g_i(k)$, $i = 1, \cdots, n$ and $k = 1, 2$, with any element in the set $g_i(k)$ is an integer from 1 to m. An element in the set $g_i(k)$ with $k = 1$ refer to the number of the measured modal frequency assigned in the group i, while the elements of the set $g_i(k)$ with $k = 2$ refer to the number of the measured modeshape assigned in the group i. For the ith group, a norm $J_i(\underline{\theta})$ is introduced to measure the residuals of the difference between the measured values of the modal properties involved in the group and the corresponding modal values predicted from the model class for a particular value of the parameter set $\underline{\theta}$. The measure of fit in a modal group is the sum of the individual square errors in (4.1) for the corresponding modal properties involved in the modal group. Specifically, the measure of fit is given by

$$J_i(\underline{\theta}) = \sum_{r \in g_i(1)} \varepsilon_{\omega_r}^2(\underline{\theta}) + \sum_{r \in g_i(2)} \varepsilon_{\underline{\phi}_r}^2(\underline{\theta}) \tag{4.2}$$

The grouping of the modal properties $\{\omega_r(\underline{\theta}), \underline{\phi}_r(\underline{\theta}), r = 1, \cdots, m\}$ into n groups and the selection of the measures of fit (residuals) $J_1(\underline{\theta}), \cdots, J_n(\underline{\theta})$ are usually based on user preference. The modal properties assigned to each group are selected by the user according to their type and the purpose of the analysis.

The aforementioned analysis accommodates general grouping schemes and objective functions. For demonstration purposes, a specific grouping scheme is next defined by grouping the modal properties into two groups as follows. The first group contains all modal frequencies, with the measure of fit $J_1(\underline{\theta})$ selected to represent the difference between the measured and the model predicted frequencies for all modes, while the second group contains the modeshape components for all modes with the measure of fit $J_2(\underline{\theta})$ selected to represents the difference between the measured and the model predicted modeshape components for all modes. Specifically, the two measures of fit are given by

$$J_1(\underline{\theta}) = \sum_{r=1}^{m} \varepsilon_{\omega_r}^2(\underline{\theta}) \quad \text{and} \quad J_2(\underline{\theta}) = \sum_{r=1}^{m} \varepsilon_{\underline{\phi}_r}^2(\underline{\theta}) \tag{4.3}$$

The aforementioned grouping scheme is used in the application section for demonstrating the features of the proposed model updating methodologies.

4.2.2 Multi-objective identification

The problem of identifying the model parameter values $\underline{\theta}$ that minimize the modal or response time history residuals can be formulated as a multi-objective optimization problem stated as follows (Haralampidis et al., 2005). Find the values of the structural parameter set $\underline{\theta}$ that simultaneously minimizes the objectives

$$\underline{y} = \underline{J}(\underline{\theta}) = (J_1(\underline{\theta}), \cdots, J_n(\underline{\theta})) \tag{4.4}$$

subject to inequality constrains $\underline{c}(\underline{\theta}) \le \underline{0}$ and parameter constrains $\underline{\theta}_{low} \le \underline{\theta} \le \underline{\theta}_{upper}$, where $\underline{\theta} = (\theta_1, \cdots, \theta_{N_\theta}) \in \Theta$ is the parameter vector, Θ is the parameter space, $\underline{y} = (y_1, \cdots, y_n) \in Y$ is the objective vector, Y is the objective space, $\underline{c}(\underline{\theta})$ is the vector function of constrains, and $\underline{\theta}_{low}$ and $\underline{\theta}_{upper}$ are respectively the lower and upper bounds of the parameter vector. For conflicting objectives $J_1(\underline{\theta}), \cdots, J_n(\underline{\theta})$, there is no single optimal solution, but rather a set of alternative solutions, known as Pareto optimal solutions, that are optimal in the sense that no other solutions in the parameter space are superior to them when all objectives are considered.

Using multi-objective terminology, the Pareto optimal solutions are the non-dominating vectors in the parameter space Θ, defined mathematically as follows. A vector $\underline{\theta} \in \Theta$ is said to be non-dominated regarding the set Θ if and only if there is no vector in Θ which dominates $\underline{\theta}$. A vector $\underline{\theta}$ is said to dominate a vector $\underline{\theta}'$ if and only if

$$J_i(\underline{\theta}) \le J_i(\underline{\theta}') \quad \forall i \in \{1, \cdots, n\} \quad \text{and} \quad \exists\ j \in \{1, \cdots, n\} \ :\ J_j(\underline{\theta}) < J_j(\underline{\theta}') \tag{4.5}$$

The set of objective vectors $\underline{y} = \underline{J}(\underline{\theta})$ corresponding to the set of Pareto optimal solutions $\underline{\theta}$ is called Pareto optimal front. The characteristics of the Pareto solutions are that the modal residuals cannot be improved in any modal group without deteriorating the modal residuals in at least one other modal group. Specifically, using the objective functions in (4.3), all optimal models that trade-off the overall fit in modal frequencies with the overall fit in the modeshapes are estimated.

The multiple Pareto optimal solutions are due to modelling and measurement errors. The level of modelling and measurement errors affect the size and the distance from the origin of the Pareto front in the objective space, as well as the variability of the Pareto optimal solutions in the parameter space. The variability of the Pareto optimal solutions also depends on the overall sensitivity of the objective functions or, equivalently, the sensitivity of the modal properties, to model parameter values $\underline{\theta}$. Such variabilities were demonstrated for the case of two-

dimensional objective space and one-dimensional parameter space in the work by Christodoulou and Papadimitriou (2007).

It should be noted that in the absence of modelling and measurement errors, there is an optimal value $\hat{\underline{\theta}}$ of the parameter set $\underline{\theta}$ for which the model based modal frequencies and modeshape components match exactly the corresponding measured modal properties. In this case, all objective functions $J_1(\hat{\underline{\theta}}),\cdots,J_n(\hat{\underline{\theta}})$ take the value of zero and, consequently, the Pareto front consists of a single point at the origin of the objective space. In particular, for identifiable problems (Katafygiotis, 1991; Katafygiotis and Beck 1998), the solutions in the parameter space consist of one or more isolated points for the case of a single or multiple global optima, respectively. For non-identifiable problems (Katafygiotis et al., 1998; Katafygiotis and Lam 2002), the Pareto optimal solutions form a lower dimensional manifold in the parameter space.

4.2.3 Weighted modal residuals identification

The parameter estimation problem is traditionally solved by minimizing the single objective

$$J(\underline{\theta};\underline{w}) = \sum_{i=1}^{n} w_i J_i(\underline{\theta}) \tag{4.6}$$

formed from the multiple objectives $J_i(\underline{\theta})$ using the weighting factors $w_i \geq 0$, $i=1,\cdots,n$, with $\sum_{i=1}^{n} w_i = 1$. The objective function $J(\underline{\theta};\underline{w})$ represents an overall measure of fit between the measured and the model predicted characteristics. The relative importance of the residual errors in the selection of the optimal model is reflected in the choice of the weights. The results of the identification depend on the weight values used. Conventional weighted least squares methods assume equal weight values, $w_1 = \cdots = w_n = 1/n$. This conventional method is referred herein as the equally weighted modal residuals method.

4.2.4 Comparison between multi-objective and weighted modal residuals identification

Formulating the parameter identification problem as a multi-objective minimization problem, the need for using arbitrary weighting factors for weighting the relative importance of the residuals $J_i(\underline{\theta})$ of a modal group to an overall weighted residuals metric is eliminated. An advantage of the multi-objective identification methodology is that all admissible solutions in the parameter space are obtained.

It can be readily shown that the optimal solution to the problem (4.6) is one of the Pareto optimal solutions. For this, let $\hat{\underline{\theta}}$ be the global optimal solution that minimizes the objective function $J(\underline{\theta};\underline{w})$ in (4.6) for given $\underline{w}$. Then this solution is also a Pareto optimal solution since otherwise there would exist another solution, say $\hat{\underline{\theta}}'$, for which equation (4.5) will be satisfied for $\underline{\theta} = \hat{\underline{\theta}}'$ and $\underline{\theta}' = \hat{\underline{\theta}}$, that is, $J_i(\hat{\underline{\theta}}') \leq J_i(\hat{\underline{\theta}}) \quad \forall i \in \{1,\cdots,n\}$ and $\exists\ j \in \{1,\cdots,n\} : J_j(\hat{\underline{\theta}}') < J_j(\hat{\underline{\theta}})$.

As a result of this and the fact that $w_i \geq 0$, it is readily derived using the form of $J(\underline{\theta};\underline{w})$ in (4.6) that $J(\underline{\hat{\theta}}';\underline{w}) < J(\underline{\hat{\theta}};\underline{w})$. The last inequality implies that $\underline{\hat{\theta}}'$, instead of $\underline{\hat{\theta}}$, is the global solution optimizing $J(\underline{\theta};\underline{w})$, which is a contradiction.

Thus, solving a series of single objective optimization problems of the type (4.6) and varying the values of the weights w_i from 0 to 1, excluding the case for which the values of all weights are simultaneously equal to zero, Pareto optimal solutions are alternatively obtained. These solutions for given $\underline{w}$ are denoted by $\underline{\hat{\theta}}(\underline{w})$. It should be noted, however, that there may exist Pareto optimal solutions that do not correspond to solutions of the single-objective weighted modal residuals problem (Christodoulou et al. 2008).

The single objective is computationally attractive since conventional minimization algorithms can be applied to solve the problem. However, a severe drawback of generating Pareto optimal solutions by solving the series of weighted single-objective optimization problems by uniformly varying the values of the weights is that this procedure often results in cluster of points in parts of the Pareto front that fail to provide an adequate representation of the entire Pareto shape. Thus, alternative algorithms dealing directly with the multi-objective optimization problem and generating uniformly spread points along the entire Pareto front should be preferred. Special algorithms are available for solving the multi-objective optimization problem. Computational algorithms and related issues for solving the single-objective and the multi-objective optimization problems are discussed in Section 4.4.

4.2.5 Identification based on optimally weighted modal residuals

The Pareto optimal models $\underline{\hat{\theta}}(\underline{w})$ along the Pareto front trade-off the fit between measured and model predicted modal data for different modal groups. The objective of this section is to address the problem of rationally selecting the optimal value $\underline{\hat{w}}$ of the weighting parameter set $\underline{w} = (w_1, \cdots, w_n)$ in (4.6) and subsequently estimating the most preferred structural model $\underline{\hat{\theta}}_{opt} \equiv \underline{\hat{\theta}}(\underline{\hat{w}})$ among the Pareto optimal models $\underline{\hat{\theta}}(\underline{w})$, utilizing the measured data and the selected model class. The decision for selecting a single most preferred model $\underline{\hat{\theta}}_{opt} \equiv \underline{\hat{\theta}}(\underline{\hat{w}})$, among the Pareto optimal models $\underline{\hat{\theta}}(\underline{w})$, for further use in model-based prediction studies and reliability assessment, depends on the user preferences.

From the computational point of view, it is desirable that the selection of the most preferred optimal model does not necessitate the computation of the whole Pareto front and Pareto solutions, since this can be a very time consuming task for more than a few objectives and, therefore, such lengthy computations should be avoided. Moreover, it is desirable that the most preferred optimal model is not biased from measured modal properties that contain significant measurement and processing error or measured modal properties that cannot be well represented by the selected model class. For this, it is reasonable to weight the contribution of the modal group residuals $J_i(\underline{\theta})$ in the total residual measure (4.6) according to their residual error corresponding to the most preferred model. Specifically, modal groups with larger residual

errors should be given less weight than modal groups with smaller residual errors. A rational choice is to select the weights to be inversely proportional to the values of the modal group residuals obtained for the most preferred model. Specifically, the i-th optimal weight value $\hat{w}_i$ could be chosen to be inversely proportional to the average value of the total residual error of the modal properties involved in the i-th modal group. That is, the optimal values $\hat{w}_i$ of the weights are chosen to satisfy the set of equations

$$w_i = \alpha_i / J_i(\underline{\hat{\theta}}(\underline{w})), \qquad i = 1, \cdots, n \tag{4.7}$$

where

$$\underline{\hat{\theta}}(\underline{w}) = \arg\min_{\underline{\theta}} J(\underline{\theta}; \underline{w}) \tag{4.8}$$

is the optimal model parameter value that corresponds to the weight values $\underline{w}$, and α_i is the number of modal properties in the group g_i. In particular, for the two objective functions in (4.3), $\alpha_1 = m$ and $\alpha_2 = mN_0$. Using (4.7), the optimal weights in (4.6) are given by $\hat{w}_i = \alpha_i / J_i(\hat{\theta}_{opt})$, while the optimal value $\underline{\hat{\theta}}_{opt} \equiv \underline{\hat{\theta}}(\underline{\hat{w}})$ minimizes the optimally weighted residuals $J(\underline{\theta}; \underline{\hat{w}})$ in (4.6), that is, $\underline{\hat{\theta}}_{opt} \equiv \underline{\hat{\theta}}(\underline{\hat{w}})$ is given by (4.8) for $\underline{w} = \underline{\hat{w}}$.

Since the most preferred Pareto optimal structural model is not known prior to the selection of the weights, the corresponding optimal values of the modal residual errors and so the optimal values of the weights are not known. Thus, the selection of the optimal weights should be made simultaneously with the selection of the optimal model so that at the optimum, the weight values are inversely proportional to the optimal residual errors as suggested in (4.7). Specifically, the optimal values $\underline{\hat{w}}$ and the most preferred Pareto optimal model $\underline{\hat{\theta}}_{opt} \equiv \underline{\hat{\theta}}(\underline{\hat{w}})$ are obtained by simultaneously solving the set of equations (4.7) and the optimization problem (4.8) with respect to $\underline{w}$ and $\underline{\theta}$. This is a nested optimization problem that is solved iteratively. Specifically, for each iteration on $\underline{w}$, required in satisfying (4.7), an optimization problem for estimating $\underline{\hat{\theta}}(\underline{w})$ needs to be solved.

It can be shown that the aforementioned problem is equivalent to the problem of finding $\underline{\hat{\theta}}_{opt}$ that minimizes the objective function

$$I(\underline{\theta}) = \sum_{i=1}^{n} \alpha_i \ln J_i(\underline{\theta}) \tag{4.9}$$

with respect to the parameter set $\underline{\theta}$ and then computing the optimal $\underline{\hat{w}}$ from $\hat{w}_i = \alpha_i / J_i(\hat{\theta}_{opt})$. This can be readily verified by noting that the stationarity conditions $\nabla_{\underline{\theta}} I(\underline{\theta})|_{\underline{\theta}=\underline{\theta}_{opt}} = \underline{0}$ for the objective function $I(\underline{\theta})$ in (4.9), where $\nabla_{\underline{\theta}}$ is the gradient vector with respect to $\underline{\theta}$, are given by

$$\left.\frac{\partial I(\underline{\theta})}{\partial \theta_j}\right|_{\underline{\theta}=\underline{\theta}_{opt}} = \sum_{i=1}^{n} \frac{\alpha_i}{J_i(\underline{\theta}_{opt})} \left.\frac{\partial J_i(\underline{\theta})}{\partial \theta_j}\right|_{\underline{\theta}=\underline{\theta}_{opt}} = 0, \qquad j=1,\cdots,n \tag{4.10}$$

which are exactly the same as the stationarity conditions $\nabla J(\underline{\theta};\underline{w})|_{\underline{\theta}=\underline{\hat{\theta}}(\underline{w})}=0$ for (4.6) with $\underline{w}$ replaced by the optimal $\hat{w}_i = \alpha_i / J_i(\underline{\hat{\theta}}_{opt})$ computed by (4.7). It should be noted that the direct optimization of $I(\underline{\theta})$ with respect to $\underline{\theta}$ is computationally much more efficient than the equivalent problem of solving simultaneously the set of equations (4.7) and the optimization problem (4.8).

The aforementioned method for selecting the most preferred model among the Pareto optimal models that satisfy (4.9) is referred to as the optimally weighted residual method. This choice corresponds to one out of the infinitely many Pareto optimal models. It is worth pointing out that the logarithmic estimator in (4.9) has also been shown to arise from a Bayesian statistical identification point of view (Christodoulou and Papadimitriou, 2007). Specifically, the most preferred optimal model is the most probable model that results asymptotically for large number of data from a Bayesian approach for structural identification. This Bayesian estimate, which is presented in Section 4.3.3, is based on the assumption of Gaussian and independent errors between the measured modal properties and the corresponding modal properties predicted by the model class.

4.3 Bayesian identification utilizing modal data

4.3.1 Probability distribution of structural parameter values utilizing modal data

The Bayesian approach to structural identification (Beck, 1989; Beck and Katafygiotis, 1998) uses probability distributions to quantify the plausibility of each possible value of the model parameters $\underline{\theta}$. Using Bayes' theorem, the updated (posterior) probability distribution $p(\underline{\theta}\,|\,D,\underline{\sigma},M)$ of the model parameters $\underline{\theta}$ based on the inclusion of the measured data D, the modeling assumptions M and the value of a parameter set $\underline{\sigma}$, is obtained as follows:

$$p(\underline{\theta}\,|\,D,\underline{\sigma},M) = cp(D\,|\,\underline{\theta},\underline{\sigma},M)\,p(\underline{\theta}\,|\,\underline{\sigma},M) \tag{4.11}$$

where $p(D\,|\,\underline{\theta},\underline{\sigma},M)$ is the probability of observing the data from a model corresponding to a particular value of the parameter set $\underline{\theta}$ conditioned on the modeling assumptions M and the value of $\underline{\sigma}$, $p(\underline{\theta}\,|\,\underline{\sigma},M)$ is the initial (prior) probability distribution of a model, and c is a normalizing constant selected such that the PDF $p(\underline{\theta}\,|\,D,\underline{\sigma},M)$ integrates to one. Herein, the modeling assumptions M refer to the structural modeling assumptions as well as those used to derive the probability distributions $p(D\,|\,\underline{\theta},\underline{\sigma},M)$ and the prior $p(\underline{\theta}\,|\,\underline{\sigma},M)$. The parameter set $\underline{\sigma}$ contains all parameters that need to be defined in order to completely specify the modeling assumptions M. Measured data are accounted for in the updated estimates through the term

$p\left(D \mid \underline{\theta}, \underline{\sigma}, M\right)$, while any available prior information is reflected in the term $p\left(\underline{\theta} \mid \underline{\sigma}, M\right)$. In order to simplify the notation, the dependence of the probability distributions on M is dropped in the analysis that follows.

The form of $p\left(D \mid \underline{\theta}, \underline{\sigma}, M\right) \equiv p\left(D \mid \underline{\theta}, \underline{\sigma}\right)$ is derived by using a probability model for the prediction error vector $\underline{u}^{(k)} = \left[\underline{u}_1^{(k)}, \ldots, \underline{u}_m^{(k)}\right]$, $k = 1, \ldots, N_D$, defined as the difference between the measured modal quantities involved in D for all m modes and the corresponding modal quantities predicted from a particular model within the model class. Specifically, the prediction error $\underline{u}_r^{(k)} = \left[u_{\omega_r}^{(k)} \;\; \underline{u}_{\underline{\phi}_r}^{(k)}\right]$ is given separately for the modal frequencies and the mode shapes by the prediction error equations:

$$\hat{\omega}_r = \omega_r(\underline{\theta}) + u_{\omega_r}^{(k)} \tag{4.12}$$

$$\underline{\hat{\phi}}_r = \beta_r L \underline{\phi}_r(\underline{\theta}) + \underline{u}_{\underline{\phi}_r}^{(k)} \tag{4.13}$$

where $u_{\omega_r}^{(k)}$ and $\underline{u}_{\underline{\phi}_r}^{(k)}$ are respectively the prediction errors for the modal frequency and modeshape components of the r-th mode.

Following the Bayesian methodology (Beck and Katafygiotis, 1998) the predictions errors are modeled by zero-mean Gaussian vector variables. Specifically, the prediction error $u_{\omega_r}^{(k)}$ for the r-th modal frequency is assumed to be a zero mean Gaussian variable, $u_{\omega_r}^{(k)} \sim N\left(0, \sigma_{\omega_r}^2 \hat{\omega}_r^{(k)2}\right)$, with standard deviation $\sigma_{\omega_r} \hat{\omega}_r^{(k)}$. The prediction error parameter σ_{ω_r} represents the fractional difference between the measured and the model predicted frequency of the r-th mode. The prediction error for the r-th truncated modeshape vector $\underline{u}_{\underline{\phi}_r}^{(k)} \in R^{N_0}$ is also assumed to be zero mean Gaussian vector, $\underline{u}_{\underline{\phi}_r}^{(k)} \sim N\left(\mathbf{0}, C_{\underline{\phi}_r}^{(k)}\right)$, with covariance matrix $C_{\underline{\phi}_r}^{(k)} \in R^{N_0 \times N_0}$, where $N(\boldsymbol{\mu}, \Sigma)$ denotes the multidimensional normal distribution with mean $\boldsymbol{\mu}$ and covariance matrix Σ. In the analysis that follows, a diagonal covariance matrix $C_{\underline{\phi}_r}^{(k)} = \sigma_{\underline{\phi}_r}^2 \left\|\underline{\hat{\phi}}_r^{(k)}\right\|_{N_0}^2$ is assumed, where $\left\|\underline{\hat{\phi}}_r^{(k)}\right\|_{N_0}^2 = \left\|\underline{\hat{\phi}}_r^{(k)}\right\|^2 / N_0$. The prediction error parameter $\sigma_{\underline{\phi}_r}$ represents the difference between the measured and the model predicted component of the r-th modeshape relative to an average value $\left\|\underline{\hat{\phi}}_r^{(k)}\right\|_{N_0}$ of the modeshape components. The parameters σ_{ω_r} and $\sigma_{\underline{\phi}_r}$, represent the prediction error estimates of the measured modal frequencies and modeshapes involved in D.

In the analysis that follows, the parameter set $\underline{\sigma}$, introduced in (4.11), is taken to contain the parameters $\sigma_r = \sigma_{\omega_r}$ and $\sigma_{m+r} = \sigma_{\underline{\phi}_r}$, $r = 1, \ldots, m$. Given the values of the parameter set $\underline{\sigma}$, assuming independence of the prediction errors in $\underline{u}_r^{(k)}$, and using the Gaussian choice for the probability distribution of the prediction errors $u_{\omega_r}^{(k)}$ and $\underline{u}_{\underline{\phi}_r}^{(k)}$, the probability $p\left(D \mid \underline{\theta}, \underline{\sigma}\right)$ of

observing the data D is readily obtained in the form (e.g. Vanik et al., 2000; Papadimitriou and Katafygiotis, 2004)

$$p\left(D \mid \underline{\theta}, \underline{\sigma}\right) = \frac{1}{b(\sqrt{2\pi})^{NN_D}\rho(\underline{\sigma})} \exp\left[-\frac{NN_D}{2} J_D\left(\underline{\theta};\underline{\sigma}\right)\right] \tag{4.14}$$

where

$$J_D\left(\underline{\theta};\underline{\sigma}\right) = \sum_{i=1}^{n} \frac{\alpha_i}{\sigma_i^2} J_i\left(\underline{\theta}\right) \tag{4.15}$$

with $J_i\left(\underline{\theta}\right) = J_{\omega_i}\left(\underline{\theta}\right)$, $J_{m+i}\left(\underline{\theta}\right) = J_{\underline{\phi}_i}\left(\underline{\theta}\right)$, $r = 1,\ldots,m$, $n = 2m$ represents the weighted measure of fit between the measured modal data and modal data predicted by a particular model within the selected model class

$$\rho(\underline{\sigma}) = \prod_{i=1}^{n} (\sigma_i)^{\alpha_i NN_D} \tag{4.16}$$

is a function of the prediction error parameters $\underline{\sigma}$, $N = m(N_0 + 1)$ is the number of measured data per modal set, $\alpha_r = 1/N$ and $\alpha_{m+r} = N_0/N$, $r = 1,\cdots,m$, satisfying $\sum_{i=1}^{n} \alpha_i = 1$, represent the number of data contained in each modal group in relation to the total number N of data in a modal set, and $b = \prod_{r=1}^{m}\prod_{k=1}^{N_D} \hat{\omega}_r^{(k)} \left(\left\|\underline{\hat{\phi}}_r^{(k)}\right\|_{N_0}\right)^{N_0}$ is a constant.

Given the values of the prediction error parameters $\underline{\sigma}$, the optimal value of the model parameter set $\underline{\theta}$ corresponds to the most probable model maximizing the updated PDF $p(\underline{\theta} \mid D, \underline{\sigma}, M)$ given in (4.11). In particular, using (4.14) and assuming a non-informative prior distribution $p(\underline{\theta} \mid \underline{\sigma}, M) = \pi_\theta(\underline{\theta})$, the optimal values $\hat{\underline{\theta}}$ of the model parameters $\underline{\theta}$ are equivalently obtained by minimizing the measure of fit $J_D(\underline{\theta};\underline{\sigma})$ defined in (4.15), i.e.

$$\hat{\underline{\theta}}(\underline{\sigma}) = \arg\min_{\underline{\theta}} J_D(\underline{\theta};\underline{\sigma}) \tag{4.17}$$

The notation $\hat{\underline{\theta}}(\underline{\sigma})$ is used to indicate that the optimal value $\hat{\underline{\theta}}$ depends on the value of the prediction error parameter set $\underline{\sigma}$.

4.3.2 Relation between weights and prediction error parameter

It should be noted that the overall measure of fit $J_D(\underline{\theta};\underline{\sigma})$ between the experimental and model predicted modal data is constructed as a weighted sum of the individual measures of fit for each group of modal properties involved in the data set D, with the weights to be inversely proportional to the squares of the prediction error parameters. Comparing $J_D(\underline{\theta};\underline{\sigma})$ and $J(\underline{\theta};\underline{w})$ given in (4.15) and (4.6), respectively, it is clear that they are exactly the same provided

that the weights w_i are chosen to be inversely proportional to the prediction error parameters σ_i^2, i.e.

$$w_i = \frac{\alpha_i}{\sigma_i^2} \quad \text{and} \quad J(\underline{\theta};\underline{\alpha}/\underline{\sigma}^2) = J_D(\underline{\theta};\underline{\sigma}) \tag{4.18}$$

where the vector notation $\underline{\alpha}/\underline{\sigma}^2 = (\alpha_1/\sigma_1^2,\cdots,\alpha_n/\sigma_n^2)$ was introduced in (4.18) for convenience. Thus, the problem of estimating the weight values in the weighted residuals metric defined in (4.6) is equivalent to the problem of estimating the prediction error parameters in the Bayesian formulation.

The formulation presented is general and applicable to other grouping schemes. Specifically, the formulation for the grouping scheme introduced in (4.3), is obtained by assuming that the prediction error parameters $\sigma_{\omega_r} = \sigma_1$, $r = 1,\cdots,m$, are the same for all the modal frequencies, and that $\sigma_{\phi_r} = \sigma_2$, $r = 1,\cdots,m$, are the same for all modeshapes. In this case, $n = 2$, the prediction error parameters are $\underline{\sigma} = (\sigma_1,\sigma_2)$, and the exponents α_i appearing in (4.16) are given by $\alpha_1 = m/N$ and $\alpha_2 = mN_0/N$.

4.3.3 Probability distribution of prediction error parameter values utilizing modal data

The Bayesian framework has been extended (Christodoulou and Papadimitriou, 2007) to rationally estimate the optimal values of the prediction error parameters $\underline{\sigma}$ and the weights $\underline{w}$ from the available measured data D, taking into account modeling error and measurement noise. Similar to the case of the parameter set $\underline{\theta}$, probability distributions are used to quantify the uncertainty in the values of the parameter set $\underline{\sigma}$. Using Bayes' theorem, the posterior probability distribution $p(\underline{\sigma}\,|\,D)$ of the parameter set $\underline{\sigma}$ given the data D is given by

$$p(\underline{\sigma}\,|\,D) = \frac{p(D\,|\,\underline{\sigma})\;\pi_\sigma(\underline{\sigma})}{d} \tag{4.19}$$

where $p(D\,|\,\underline{\sigma})$ is the probability of observing the data given the values of the parameter set $\underline{\sigma}$, $\pi_\sigma(\underline{\sigma})$ is the prior probability distribution of the parameter set $\underline{\sigma}$ before the collection of data, while d is a normalizing constant given by $d = \int p(D\,|\,\underline{\sigma})\;\pi_\sigma(\underline{\sigma})\,d\underline{\sigma}$ so that the probability density function in (4.19) integrates to one.

Using the total probability theorem, the quantity $p(D\,|\,\underline{\sigma})$ is given by

$$p(D\,|\,\underline{\sigma}) = \int_\Theta p(D\,|\,\underline{\theta},\underline{\sigma})\;\pi(\underline{\theta})\,d\underline{\theta} \tag{4.20}$$

where it is assumed that the prior probability distribution $p(\underline{\theta}\,|\,\underline{\sigma}) = \pi(\underline{\theta})$ is independent of $\underline{\sigma}$. Replacing $p(D\,|\,\underline{\theta},\underline{\sigma})$ in (4.20) by (4.14) and then substituting (4.20) into(4.19), one readily derives that

$$p(\underline{\sigma}\,|\,D) = c_0 \frac{\pi_\sigma(\underline{\sigma})}{\rho(\underline{\sigma})} \int_{\Theta} \pi(\underline{\theta})\ \exp\left[-0.5NN_D\ J_D(\underline{\theta};\underline{\sigma})\right]\ d\underline{\theta} \tag{4.21}$$

where $c_0^{-1} = d\ b\left(\sqrt{2\pi}\right)^{NN_D}$. The optimal value $\hat{\underline{\sigma}}$ of the prediction error parameter set $\underline{\sigma}$ given the data D is the one that maximizes the function $p(\underline{\sigma}\,|\,D)$.

In order to compute the value of the function $p(\underline{\sigma}\,|\,D)$ for given $\underline{\sigma}$, one needs to estimate a multi-dimensional integral over the parameter space Θ. This makes the approach computationally very demanding and in most cases inefficient. Asymptotic approximations have been introduced (Christodoulou and Papadimitriou, 2007) to approximate analytically the integrals and, thus, provide a more efficient algorithm for finding the PDF $p(\underline{\sigma}\,|\,D)$ of the parameter set $\underline{\sigma}$ and the optimal value $\hat{\underline{\sigma}}$ of the parameter set $\underline{\sigma}$. Specifically, as $NN_D \to \infty$, i.e. for large number of data, the Lapalce method of asymptotic approximation (Bleistein and Handelsman, 1986) can be applied for the integral in (4.21) to yield (Christodoulou and Papadimitriou, 2007)

$$p(\underline{\sigma}\,|\,D) \sim c_0 (2\pi)^{N_\theta} \frac{\pi_\sigma(\underline{\sigma})}{\rho(\underline{\sigma})} \frac{\pi_\theta(\hat{\underline{\theta}}(\underline{\sigma}))\ \exp[-0.5NN_D\ J_D(\hat{\underline{\theta}}(\underline{\sigma});\underline{\sigma})]}{\sqrt{\left|H_D(\hat{\underline{\theta}}(\underline{\sigma});\underline{\sigma})\right|}} \tag{4.22}$$

where $\hat{\underline{\theta}}(\underline{\sigma})$ is the value that minimizes the function $J_D(\underline{\theta};\underline{\sigma})$ with respect to $\underline{\theta}$ for given value of $\underline{\sigma}$, that is, $\hat{\underline{\theta}}(\underline{\sigma})$ is given by (4.17), $H_D(\hat{\underline{\theta}}(\underline{\sigma});\underline{\sigma})$ is the Hessian of the function $0.5NN_D\ J_D(\underline{\theta};\underline{\sigma})$ evaluated at $\hat{\underline{\theta}}(\underline{\sigma})$.

Using the relation (4.19) between the weight values $\underline{w}$ and the prediction error parameter set $\underline{\sigma}$ one can readily develop the PDF $p(\underline{w}\,|\,D)$ of the weights given the data. The PDFs $p(\underline{\sigma}\,|\,D)$ or $p(\underline{w}\,|\,D)$ quantify the uncertainty in the values of the prediction error parameters or the weight values respectively, which in turn quantify the uncertainty in the corresponding Pareto optimal models and predictions from these models.

Assuming that the prior distributions $\pi_\theta(\underline{\theta})$ and $\pi_\sigma(\underline{\sigma})$ are non-informative uniform distributions over the domain of variation of the structural parameter set $\underline{\theta}$ and the prediction error parameter set $\underline{\sigma}$, respectively, one may set $\pi_\theta(\underline{\theta}) = c_\theta = \text{constant}$ and $\pi_\sigma(\underline{\sigma}) = c_\sigma = \text{constant}$ in (4.22). The optimal value $\hat{\underline{\sigma}}$ of the prediction error parameter set $\underline{\sigma}$ is the one that maximizes $p(\underline{\sigma}\,|\,D)$ in (4.22) or, equivalently, the one that minimizes the function

$$G_D(\underline{\sigma}) = -\ln p(\underline{\sigma}\,|\,D) + \kappa = \frac{NN_D}{2} J_D(\hat{\underline{\theta}}(\underline{\sigma});\underline{\sigma}) + \ln \rho(\underline{\sigma}) + \frac{1}{2}\ln\left|H_D(\hat{\underline{\theta}}(\underline{\sigma});\underline{\sigma})\right| \tag{4.23}$$

where $\kappa = \ln(c_0 c_\theta c_\sigma) + N_\theta \ln(2\pi)$ is a constant that does not affect the selection of the optimal $\hat{\underline{\sigma}}$. The optimization of the function in (4.23) can readily be carried out numerically using any available algorithm for optimizing a nonlinear function of several variables. It should be noted that in evaluating the objective function $G_D(\underline{\sigma})$ for given value of $\underline{\sigma}$, an internal minimization problem is involved for finding $\hat{\underline{\theta}}(\underline{\sigma})$ from (4.17). Moreover, the evaluation of the Hessian $H_D(\hat{\underline{\theta}}(\underline{\sigma});\underline{\sigma})$ is also needed.

For non-informative uniform priors, the optimal estimate $\hat{\underline{\sigma}}$ that minimizes the function in (4.23) can equivalently be obtained using the maximum likelihood approach. However, the proposed Bayesian methodology provides the complete probability distribution $p(\underline{\sigma} \mid D)$, given in (4.22), as well as the optimal estimate $\hat{\underline{\sigma}}$ that maximizes this distribution for general non-uniform prior distributions of the structural model and prediction error parameters.

Alternatively, applying the stationarity conditions in (4.19) with respect to the elements of $\underline{\sigma}$ and using Laplace method of asymptotic approximation (Bleistein and Handelsman, 1986), valid for large number of data, $NN_D \to \infty$ to the resulting integrals, one readily derives that the optimal values $\hat{\underline{\sigma}}$ of the parameter set $\underline{\sigma}$ satisfies the set of equations (Christodoulou and Papadimitriou, 2007)

$$\sigma_i^2 = J_i(\hat{\underline{\theta}}(\underline{\sigma})), \qquad i = 1, \cdots, 2m \tag{4.24}$$

where $\hat{\underline{\theta}}(\underline{\sigma})$ is given by (4.17). The result (4.24) indicates that the optimal value $\hat{\sigma}_i^2 = J_i(\hat{\underline{\theta}}(\hat{\underline{\sigma}}))$ of the prediction error variance σ_i^2 for the i-th modal group involved in the data is the optimal residual value between the data involved in the i-th group and the prediction from the optimal model $\hat{\underline{\theta}}_{opt} \equiv \hat{\underline{\theta}}(\hat{\underline{\sigma}})$.

Using (4.18) and (4.24), the optimal weights in (4.6) are given by $\hat{w}_i = \alpha_i / J_i(\hat{\underline{\theta}}_{opt})$, while the optimal value $\hat{\underline{\theta}}_{opt} \equiv \hat{\underline{\theta}}(\hat{\underline{\sigma}})$ which minimizes $J_D(\underline{\theta};\hat{\underline{\sigma}})$, also minimizes the optimally weighted residuals $J(\underline{\theta};\hat{\underline{w}})$ in (4.6), that is, $\hat{\underline{\theta}}_{opt} \equiv \hat{\underline{\theta}}(\hat{\underline{w}})$, where $\hat{\underline{\theta}}(\underline{w}) = \arg\min_{\underline{\theta}} J(\underline{\theta};\underline{w})$.

It should be noted that the optimal values $\hat{\underline{\sigma}}$ and $\hat{\underline{\theta}}_{opt} \equiv \hat{\underline{\theta}}(\hat{\underline{\sigma}})$ are obtained by simultaneously solving (4.24) and (4.17) with respect to $\underline{\sigma}$ and $\underline{\theta}$. Equivalently, the optimal values $\hat{\underline{w}}$ and $\hat{\underline{\theta}}_{opt} \equiv \hat{\underline{\theta}}(\hat{\underline{w}})$ are obtained by simultaneously solving $w_i = \alpha_i / J_i(\hat{\underline{\theta}}(\underline{w}))$, $i = 1, \cdots, 2m$ and $\hat{\underline{\theta}}(\underline{w}) = \arg\min_{\underline{\theta}} J(\underline{\theta};\underline{w})$ with respect to $\underline{w}$ and $\underline{\theta}$. It can be shown that both problems are equivalent to the problem of finding $\hat{\underline{\theta}}_{opt}$ that minimizes the objective function

$$I(\underline{\theta}) = \sum_{i=1}^{n} \alpha_i \ln J_i(\underline{\theta}) \tag{4.25}$$

with respect the parameter set $\underline{\theta}$ and then computing the optimal $\hat{\underline{\sigma}}$ from $\hat{\sigma}_i^2 = J_i(\hat{\underline{\theta}}_{opt})$ or the optimal $\hat{\underline{w}}$ from $\hat{w}_i = \alpha_i / J_i(\hat{\underline{\theta}}_{opt})$. This can be readily verified by noting that the stationarity conditions $\underline{\nabla}_{\underline{\theta}} I(\underline{\theta})|_{\underline{\theta}=\underline{\theta}_{opt}} = 0$ for the objective function $I(\underline{\theta})$, where $\underline{\nabla}_{\underline{\theta}}$ is the gradient vector with respect to $\underline{\theta}$, are exactly the same as the stationarity conditions $\underline{\nabla} J_D(\underline{\theta};\underline{\sigma})|_{\underline{\theta}=\hat{\underline{\theta}}(\underline{\sigma})} = 0$ for (4.17) with $\underline{\sigma}^2$ replaced by the optimal $\hat{\sigma}_i^2 = J_i(\hat{\underline{\theta}}_{opt})$ computed by (4.24).

It should be pointed out that the objective function (4.25) does not require information from the weights $\underline{w}$ or the prediction error parameters $\underline{\sigma}$. The optimization of $I(\underline{\theta})$ with respect to $\underline{\theta}$ can readily be carried out numerically using any available algorithm for optimizing a nonlinear function of several variables. The optimization of $I(\underline{\theta})$ is computationally much more efficient than the equivalent problem of solving simultaneously the set of equations (4.24) and the optimization problem (4.17).

Comparing the computational time involved in estimating the optimal weight vector $\hat{\underline{\sigma}}$ using (4.23) and (4.25), it is worth noting that for (4.23), each function evaluation involved in the optimization of the objective $G_D(\underline{\sigma})$ with respect to the prediction error parameters $\underline{\sigma}$ requires the solution of an inner optimization problem (4.17) for minimizing the measure of fit $J_D(\underline{\theta};\underline{\sigma})$ with respect to the parameter set $\underline{\theta}$ given the current value of $\underline{\sigma}$. However, (4.25) involves a single optimization of $I(\underline{\theta})$ and thus, it is computationally much more efficient than (4.23).

4.4 Computational issues related to model updating formulations

The proposed single and multi-objective identification problems are solved using available single- and multi-objective optimization algorithms. These algorithms are next reviewed and various implementation issues are addressed, including estimation of global optima from multiple local/global ones, as well as convergence problems. In addition, for gradient-based optimization algorithms, computationally efficient formulas are given to estimate the gradients and Hessians of the objectives. These formulas are useful for significantly reducing the computational time for the case of large number of parameters and very large number of model degrees of freedom. It shold be noted that the Hessians of the objective functions are used in (4.22) to obtain the PDF $p(\underline{\sigma}|D)$ of the prediction error parameters $\underline{\sigma}$.

4.4.1 Single-objective identification

The optimization of $J(\underline{\theta};\underline{w})$ in (4.6) with respect to $\underline{\theta}$ for given $\underline{w}$ and the optimization of $I(\underline{\theta})$ in (4.9) with respect to $\underline{\theta}$ can readily be carried out numerically using any available algorithm for optimizing a nonlinear function of several variables. These single objective optimization problems may involve multiple local/global optima. Conventional gradient-based local optimization algorithms lack reliability in dealing with the estimation of multiple local/global optima observed in structural identification problems (Christodoulou and Papadimitriou, 2007; Teughels et al., 2003),

since convergence to the global optimum is not guaranteed. Evolution strategies (Zitzler and Thiele, 1999) are more appropriate and effective to use in such cases. Evolution strategies are random search algorithms that explore the parameter space for detecting the neighborhood of the global optimum, avoiding premature convergence to a local optimum. A disadvantage of evolution strategies is their slow convergence at the neighborhood of an optimum since they do not exploit the gradient information. A hybrid optimization algorithm should be used that exploits the advantages of evolution strategies and gradient-based methods. Specifically, an evolution strategy is used to explore the parameter space and detect the neighborhood of the global optimum. Then the method switches to a gradient-based algorithm starting with the best estimate obtained from the evolution strategy and using gradient information to accelerate convergence to the global optimum.

4.4.2 Multi-objective identification

The set of Pareto optimal solutions can be obtained using available multi-objective optimization algorithms. Among them, the evolutionary algorithms, such as the strength Pareto evolutionary algorithm (Zitzler and Thiele, 1999), are well-suited to solve the multi-objective optimization problem. The strength Pareto evolutionary algorithm, although it does not require gradient information, it has the disadvantage of slow convergence for objective vectors close to the Pareto front (Haralampidis et al., 2005) and also it does not generate an evenly spread Pareto front, especially for large differences in objective functions.

Another very efficient algorithm for solving the multi-objective optimization problem is the Normal-Boundary Intersection (NBI) method (Das and Dennis, 1998) which produce an evenly spread of points along the Pareto front, even for problems for which the relative scaling of the objectives are vastly different. For completeness and for the purpose of demonstrating the implementation issues arising in multi-objective structural model updating, the idea of the NBI method is briefly illustrated geometrically with the aid of the two-dimensional Pareto front shown in Figure 4.1. For this, let $\underline{\hat{\theta}}^{(i)}$, $i=1,\cdots,n$, be the global optimal values of the parameter set that minimize the individual objectives $J_i(\underline{\theta})$, $i=1,\cdots,n$, respectively. The Pareto points $\underline{\hat{J}}^{(i)}=\underline{J}(\underline{\hat{\theta}}^{(i)})$, shown in Figure 1, determine the location of the boundaries of the Pareto front in the objective space. These edge points of the Pareto front are estimated using the single-objective optimization algorithms outlined in Section 4.4.1. The utopia point $\underline{\hat{J}}=[\hat{J}_1,\cdots,\hat{J}_n]^T$, shown in Figure 4.1, is introduced as the point in the objective space with coordinates the individual minima $\hat{J}_i=J_i(\underline{\hat{\theta}}^{(i)})$ of the objectives. Let Φ be the $n\times n$ matrix with the i-th column equal to the vector $\underline{\hat{J}}^{(i)}$. The set of points in the objective space that are convex combinations of $\underline{\hat{J}}^{(i)}-\underline{\hat{J}}$, obtained by the points $\{\Phi\underline{\beta}:\underline{\beta}\in R^n,\sum_{i=1}^{n}\beta_i=1,\beta_i\geq 0\}$, is referred to as the Convex Hull of Individual Minima (CHIM). These points are all points along the line segment AB in Figure 4.1. The Pareto points consist of points on the intersection of the boundary ∂Y of the objective space Y and the normal initiating from any point in the CHIM and pointing towards the origin of the objective space.

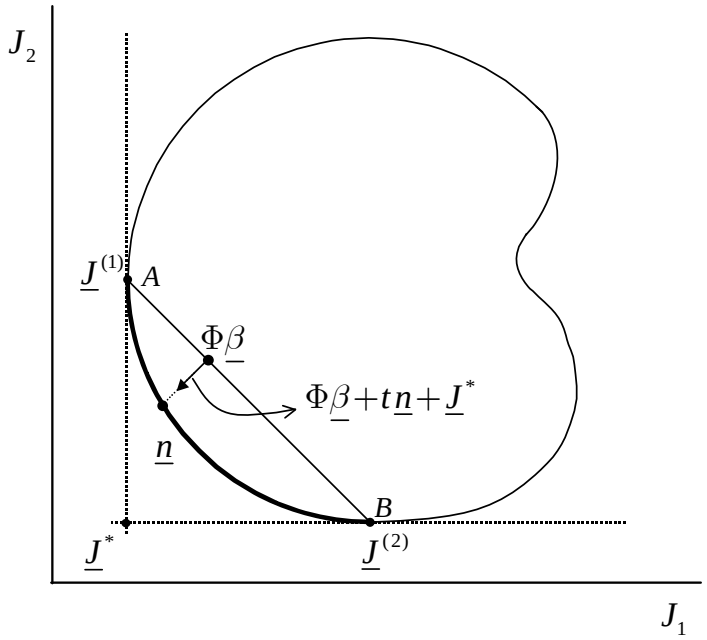

Figure 4.1: Geometric illustration of NBI Method in 2-dimensional objective space.

A point along the Pareto front can be found by solving a single-objective optimization problem. Given the coordinates $\underline{\beta}$, $\Phi\underline{\beta}$ represents a point on the CHIM and $\Phi\underline{\beta}+t\underline{n}$, where $t \in R$ and $\underline{n}$ the normal to the CHIM, represents the set of points on the normal to the CHIM at the point $\Phi\underline{\beta}$. The point of intersection of the normal and the bounbary ∂Y, closest to the origin, is the global solution of the commonly referred as NBI $_{\underline{\beta}}$ optimization problem (Das and Dennis, 1998):

$$\max_{\underline{\theta},t} t \tag{4.26}$$

subject to the constrains

$$\Phi\underline{\beta}+t\underline{n}=\underline{J}(\underline{\theta})-\underline{J}^* \tag{4.27}$$

Any constrains from the original multi-objective optimization problem (4.4) can also be considered by adding them as constrains in the NBI $_{\underline{\beta}}$ optimization problem. By solving the optimization problems NBI $_{\underline{\beta}}$ for various $\underline{\beta}$ values in the set $\{\underline{\beta} \in R^n : \sum_{i=1}^{n} \beta_i = 1, \beta_i \geq 0\}$, a pointwise representation of the Pareto front is efficiently constructed. The values of the parameters $\underline{\beta}$ are selected so that an evenly spread points along the CHIM are obtained, resulting to an evenly spread points along the Pareto front, independently of the scales of the objective functions. For the two-dimensional objective space, this is achieved by selecting the values of the component β_2 of $\underline{\beta}=(\beta_1,\beta_2)$ to be uniformly spaced in the interval [0,1] with spacing length $\delta = 1/(N-1)$, where N is the number of points along the CHIM including the edge points. The

first component β_1 is selected to satisfy $\beta_1 + \beta_2 = 1$. More details about the method, the selection of $\underline{\beta}$ values for more than two objectives, advantages and drawbacks, can be found in the original paper by Das and Dennis (1998).

It is also of interest to compare the computational time involved for estimating the Pareto optimal solutions with the computational time required in conventional weighted residuals methods for estimating a single solution. This estimate can be made by noting that each Pareto optimal solutions is obtained by solving a single-objective optimization problem NBI$_{\underline{\beta}}$. Thus, this computational time is of the order of the number of points used to represent the Pareto front multiplied by the computational time required to solve a single-objective NBI$_{\underline{\beta}}$ problem for computing each point on the front. However, for the NBI method, convergence can be greatly accelerated by using a good starting value for the NBI$_{\underline{\beta}}$ optimization problem close to the optimal value. This is achieved by selecting the Pareto optimal solution obtained from the current NBI$_{\underline{\beta}}$ problem to be used as starting value for solving the next NBI$_{\underline{\beta}}$ problem.

4.4.3 Formulation for gradients of objectives

In order to guarantee the convergence of the gradient-based optimization methods for structural models involving a large number of DOFs with several contributing modes, the gradients of the objective functions with respect to the parameter set $\underline{\theta}$ has to be estimated accurately. It has been observed that numerical algorithms such as finite difference methods for gradient evaluation does not guarantee convergence due to the fact that the errors in the numerical estimation may provide the wrong directions in the search space and convergence to the local/global minimum is not achieved, especially for intermediate parameter values in the vicinity of a local/global optimum. Thus, the gradients of the objective functions should be provided analytically. Moreover, gradient computations with respect to the parameter set using the finite difference method requires the solution of as many eigenvalue problems as the number of parameters.

The gradients of the modal frequencies and modeshapes, required in the estimation of the gradient of $J(\underline{\theta};\underline{w})$ in (4.6) or $I(\underline{\theta})$ in (4.9) or the gradients of the objectives $J_i(\underline{\theta})$ in (4.4) are computed by expressing them exactly in terms of the values of the contributive modal frequencies, modeshapes and the gradients of the structural mass and stiffness matrices with respect to $\underline{\theta}$ using Nelson's method (Nelson, 1976). Special attention is given to the computation of the gradients and the Hessians of the objective functions for the point of view of the reduction of the computational time required. Analytical expressions for the gradient of the modal frequencies and modeshapes are used to overcome the convergence problems. In particular, Nelson's method (Nelson, 1976) is used for computing analytically the first derivatives of the eigenvalues and the eigenvectors. The advantage of the Nelson's method compared to other methods is that the gradient of eigenvalue and the eigenvector of one mode are computed from the eigenvalue and the eigenvector of the same mode and there is no need to know the eigenvalues and the eigenvectors from other modes. For each parameter in the set $\underline{\theta}$ this

computation is performed by solving a linear system of the same size as the original system mass and stiffness matrices. Nelson's method is also extended in Section 4.4.4 to compute the second derivatives of the eigenvalues and the eigenvectors.

The computation of the gradients and the Hessian of the objective functions is shown to involve the solution of a single linear system, instead of N_θ linear systems required in usual computations of the gradient and $N_\theta\left(N_\theta+1\right)$ linear systems required in the computation of the Hessian. This reduces considerably the computational time, especially as the number of parameters in the set $\underline{\theta}$ increase. The expressions for the first derivatives of the objective functions are next presented.

4.4.3.1 First derivatives of eigenvalues and eigenvectors using Nelson's method

Summarizing, Nelson's method (Nelson, 1976) specialized for symmetric mass and stiffness matrices computes the derivatives of the r-th eigenvalue and eigenvector with respect to a parameter θ_j in the parameter set $\underline{\theta}$ from the following formulas

$$\frac{\partial\omega_r^2}{\partial\theta_j}=\underline{\phi}_r^T(K_j-\omega_r^2M_j)\underline{\phi}_r \tag{4.28}$$

and

$$\frac{\partial\underline{\phi}_r}{\partial\theta_j}=(I-\underline{\phi}_r\underline{\phi}_r^TM)A_r^{*-1}\underline{F}_r^*-\frac{1}{2}\underline{\phi}_r\underline{\phi}_r^TM_j\underline{\phi}_r \tag{4.29}$$

where

$$A_r=K-\omega_r^2M \tag{4.30}$$

$$\underline{F}_{r,j}=-\frac{\partial A_r}{\partial\theta_j}\underline{\phi}_r=-(I-M\underline{\phi}_r\underline{\phi}_r^T)(K_j-\omega_r^2M_j)\underline{\phi}_r \tag{4.31}$$

$$M_j\equiv M_j(\underline{\theta})=\frac{\partial M(\underline{\theta})}{\partial\theta_j},\qquad K_j\equiv K_j(\underline{\theta})=\frac{\partial K(\underline{\theta})}{\partial\theta_j} \tag{4.32}$$

For notational convenience, the dependence of several variables on the parameter set $\underline{\theta}$ has been dropped. For an $n\times n$ matrix A_r referring to the formulation for the r-th mode, A_r^* is used to denote the modified matrix derived from the matrix A_r by replacing the elements of the k-th column and the k-th row by zeroes and the (k, k) element of A_r by one, where k denotes the element of the modeshape vector $\underline{\phi}_r$ with the highest absolute value. Also, the n vector $\underline{b}_r^*$ is used to denote the modified vector derived from $\underline{b}_r$ replacing the k-th element of the vector $\underline{b}_r$ by zero. More details can be found in the work by Nelson (Nelson, 1976).

4.4.3.2 Gradients of objectives

The gradient of the square error $\varepsilon_{\omega_r}^2(\underline{\theta})$ is given by

$$\frac{\partial \varepsilon_{\omega_r}^2(\underline{\theta})}{\partial \theta_j} = \frac{\partial \varepsilon_{\omega_r}^2(\underline{\theta})}{\partial \omega_r^2}\frac{\partial \omega_r^2}{\partial \theta_j} = \left[\frac{\partial \varepsilon_{\omega_r}^2(\underline{\theta})}{\partial \omega_r^2}\underline{\phi}_r^T\right](K_j - \omega_r^2 M_j)\underline{\phi}_r \tag{4.33}$$

and the gradient of the square error $\varepsilon_{\underline{\phi}_r}^2(\underline{\theta})$ is given by

$$\frac{\partial \varepsilon_{\underline{\phi}_r}^2(\underline{\theta})}{\partial \theta_j} = [\nabla_{\underline{\varphi}_r}^T \varepsilon_{\underline{\varphi}_r}^2(\underline{\theta})]\frac{\partial \underline{\varphi}_r}{\partial \theta_j} = [\nabla_{\underline{\varphi}_r}^T \varepsilon_{\underline{\varphi}_r}^2(\underline{\theta})]L\frac{\partial \underline{\phi}_r}{\partial \theta_j} \tag{4.34}$$

Substituting (4.29) into (4.34), the gradient of the square error $\varepsilon_{\underline{\phi}_r}^2(\underline{\theta})$ is simplified to

$$\frac{\partial \varepsilon_{\underline{\phi}_r}^2(\underline{\theta})}{\partial \theta_j} = \underline{x}_r^{*T}\underline{F}_{r,j} - \frac{1}{2}\underline{z}_r^T M_j \underline{\phi}_r \tag{4.35}$$

where $\underline{F}_{r,j}$ is given in (4.31),

$$\underline{z}_r^T = [\nabla_{\underline{\phi}_r}^T \varepsilon_{\underline{\phi}_r}^2(\underline{\theta})]L\underline{\phi}_r\underline{\phi}_r^T \tag{4.36}$$

and $\underline{x}_r$ is given by the solution of the linear system of equations

$$A_r^* X_r = D_r \tag{4.37}$$

with $D_r = (I - M\underline{\phi}_r\underline{\phi}_r^T)L^T\nabla_{\underline{\varphi}_r}\varepsilon_{\underline{\varphi}_r}^2(\underline{\theta})$ and X_r replaced by $\underline{x}_r$. The system of equations (4.37) can be viewed as the adjoint system for the model updating optimization problem based on modal residuals.

It should be noted that for the specific objective functions $\varepsilon_{\omega_r}^2(\underline{\theta})$ and $\varepsilon_{\underline{\varphi}_r}^2(\underline{\theta})$ given by (4.1), the aforementioned expressions for the gradients of the objective functions simplify further. Specifically, using (4.1) and noting that $\varepsilon_{\underline{\phi}_r}^T(\underline{\theta})L\underline{\phi}_r = \varepsilon_{\underline{\phi}_r}^T(\underline{\theta})\underline{\varphi}_r = 0$, one readily obtains that

$$\frac{\partial \varepsilon_{\omega_r}^2(\underline{\theta})}{\partial \omega_r^2} = \frac{2\varepsilon_{\omega_r}(\underline{\theta})}{\hat{\omega}_r^2} \tag{4.38}$$

$$\nabla_{\underline{\varphi}_r}\varepsilon_{\underline{\varphi}_r}^2(\underline{\theta}) = 2\underline{e}_{\underline{\varphi}_r}(\underline{\theta})\beta_r \tag{4.39}$$

where

$$\underline{e}_{\underline{\varphi}_r} = \frac{\beta_r L\underline{\phi}_r^T - \hat{\underline{\phi}}_r^T}{\left\|\hat{\underline{\varphi}}_r\right\|^2} \tag{4.40}$$

$\underline{z}_r^T = \underline{0}^T$ and D_r is given by the equation

$$D_r = L^T 2\beta_r e_{\underline{\varphi}_r}(\underline{\theta}) \tag{4.41}$$

The computation of the derivatives of the square errors for the modal properties of the r-th mode with respect to the parameters in $\underline{\theta}$ requires only one solution of the linear system (4.37), independent of the number of parameters in $\underline{\theta}$. For a large number of parameters in the set $\underline{\theta}$ the above formulation for the gradients of the mean errors in modal frequencies and in the modeshape components in (4.1) are computationally very efficient and informative. The dependence on θ_j comes through the term $K_j - \omega_r^2 M_j$ and the term M_j. For the case where the mass matrix is independent of $\underline{\theta}$, $M_j = 0$ and the formulation is further simplified.

It should be noted that for the special case of linear dependence between the global mass and stiffness matrices on the parameters in the set $\underline{\theta}$, that is, $M(\underline{\theta}) = M_0 + \sum_{j=1}^{N_\theta} M_j \theta_j$ and $K(\underline{\theta}) = K_0 + \sum_{j=1}^{N_\theta} K_j \theta_j$, the gradients of $M(\underline{\theta})$ and $K(\underline{\theta})$ are easily computed from the constant matrices M_0, K_0, M_j and K_j, $j = 1, \cdots, N_\theta$. In order to save computational time, these constant matrices are computed and assembled once and, therefore, there is no need this computation to be repeated during the iterations involved in optimization algorithms. For the general case of nonlinear dependence between the global mass and stiffness matrices on the parameters in the set $\underline{\theta}$, the matrices M_j and K_j involved in the formulation (see (4.32)) can be obtained numerically at the element level and assembled to form the global matrices.

4.4.4 Formulation for Hessian of objectives

4.4.4.1 Second derivatives of eigenvalues and eigenvectors extending Nelson's method

A similar analysis to that followed in Nelson's method (Nelson, 1976) for computing the first derivative can also be followed for computing the second derivatives of the eigenvalues and the eigenvectors, resulting in the following expressions for the second derivatives

$$\frac{\partial^2 \omega_r^2}{\partial \theta_i \partial \theta_j} = \underline{\phi}_r^T \underline{g}_{r,ij} \tag{4.42}$$

and

$$\frac{\partial^2 \underline{\phi}_r}{\partial \theta_i \partial \theta_j} = (I - \underline{\phi}_r \underline{\phi}_r^T M) A_r^{*-1} \underline{G}_r^* - \underline{\phi}_r d_{r,ij} \tag{4.43}$$

where

$$\underline{G}_r = -(I - M \underline{\phi}_r \underline{\phi}_r^T) \underline{g}_r \tag{4.44}$$

$$\underline{g}_{r,ij} = \frac{\partial A_r}{\partial \theta_i}\frac{\partial \underline{\phi}_r}{\partial \theta_j} + \frac{\partial A_r}{\partial \theta_j}\frac{\partial \underline{\phi}_r}{\partial \theta_i} + \left[\frac{\partial^2 K}{\partial \theta_i \partial \theta_j} - \lambda_r \frac{\partial^2 M}{\partial \theta_i \partial \theta_j} - \frac{\partial \lambda_r}{\partial \theta_i}\frac{\partial M}{\partial \theta_j} - \frac{\partial \lambda_r}{\partial \theta_j}\frac{\partial M}{\partial \theta_i}\right]\underline{\phi}_r \quad (4.45)$$

and

$$d_{r,ij} = \underline{\phi}_r^T \left[\frac{\partial M}{\partial \theta_i}\frac{\partial \underline{\phi}_r}{\partial \theta_j} + \frac{\partial M}{\partial \theta_j}\frac{\partial \underline{\phi}_r}{\partial \theta_i} + \frac{1}{2}\frac{\partial^2 M}{\partial \theta_i \partial \theta_j}\underline{\phi}_r\right] + \frac{\partial \underline{\phi}_r^T}{\partial \theta_i} M \frac{\partial \underline{\phi}_r}{\partial \theta_j} \quad (4.46)$$

4.4.4.2 Hessians of objectives

The Hessian of the objective functions $\varepsilon^2_{\omega_r}(\underline{\theta})$ and $\varepsilon^2_{\underline{\varphi}_r}(\underline{\theta})$ can be readily computed from the second derivatives of the eigenvalues and the eigenvectors, respectively. Specifically, the (i, j) element of the Hessian of $\varepsilon^2_{\omega_r}(\underline{\theta})$ is obtained by differentiating (4.33) with respect to θ_i, resulting in

$$\begin{aligned}\frac{\partial^2 \varepsilon^2_{\omega_r}(\underline{\theta})}{\partial \theta_i \partial \theta_j} &= \frac{\partial^2 \varepsilon^2_{\omega_r}(\underline{\theta})}{\partial (\omega_r^2)^2}\frac{\partial \omega_r^2}{\partial \theta_i}\frac{\partial \omega_r^2}{\partial \theta_j} + \frac{\partial \varepsilon^2_{\omega_r}(\underline{\theta})}{\partial \omega_r^2}\frac{\partial^2 \omega_r^2}{\partial \theta_i \partial \theta_j} \\ &= \frac{\partial^2 \varepsilon^2_{\omega_r}(\underline{\theta})}{(\partial \omega_r^2)^2}[\underline{\phi}_r^T (K_i - \omega_r^2 M_i)\underline{\phi}_r][\underline{\phi}_r^T (K_j - \omega_r^2 M_j)\underline{\phi}_r] + \frac{\partial \varepsilon^2_{\omega_r}(\underline{\theta})}{\partial \omega_r^2}\underline{\phi}_r^T \underline{g}_r\end{aligned} \quad (4.47)$$

The (i, j) element of the Hessian of $\varepsilon^2_{\underline{\varphi}_r}(\underline{\theta})$ is obtained by differentiating (4.34) with respect to θ_i, resulting in

$$\frac{\partial^2 \varepsilon^2_{\underline{\varphi}_r}(\underline{\theta})}{\partial \theta_i \partial \theta_j} = \frac{\partial \underline{\varphi}_r^T}{\partial \theta_i}[\underline{\nabla}_{\underline{\varphi}_r}\underline{\nabla}^T_{\underline{\varphi}_r}\varepsilon^2_{\underline{\varphi}_r}(\underline{\theta})]\frac{\partial \underline{\varphi}_r}{\partial \theta_j} + [\underline{\nabla}^T_{\underline{\varphi}_r}\varepsilon^2_{\underline{\varphi}_r}(\underline{\theta})]\frac{\partial^2 \underline{\varphi}_r}{\partial \theta_i \partial \theta_j} \quad (4.48)$$

Substituting (4.43) into (4.48) and using (4.37), the Hessian can be finally simplified to

$$\frac{\partial^2 \varepsilon^2_{\underline{\phi}_r}(\underline{\theta})}{\partial \theta_i \partial \theta_j} = \frac{\partial \underline{\phi}_r^T}{\partial \theta_i} L^T [\underline{\nabla}_{\underline{\phi}_r}\underline{\nabla}_{\underline{\phi}_r}\varepsilon^2_{\underline{\phi}_r}(\underline{\theta})]^T L \frac{\partial \underline{\phi}_r}{\partial \theta_j} - 2\underline{x}_r^{*T}(I - M\underline{\phi}_r\underline{\phi}_r^T)\underline{g}_r - 2[\underline{\nabla}^T_{\underline{\phi}_r}\varepsilon^2_{\underline{\phi}_r}(\underline{\theta})]L\underline{\phi}_r d_{r,ij} \quad (4.49)$$

It should be noted that for the specific objective functions $\varepsilon^2_{\omega_r}(\underline{\theta})$ and $\varepsilon^2_{\underline{\varphi}_r}(\underline{\theta})$ given by (4.1), the aforementioned expressions for the Hessian of the objective functions simplify further. Specifically, using (4.1) and noting that $\varepsilon^T_{\underline{\phi}_r}(\underline{\theta})L\underline{\phi}_r = \varepsilon^T_{\underline{\phi}_r}(\underline{\theta})\underline{\varphi}_r = 0$, one readily obtains that

$$\frac{\partial^2 \varepsilon^2_{\omega_r}(\underline{\theta})}{\partial (\omega_r^2)^2} = \frac{2}{\hat{\omega}_r^4} \quad (4.50)$$

$$\underline{\nabla}_{\underline{\varphi}_r}\underline{\nabla}^T_{\underline{\varphi}_r}\varepsilon^2_{\underline{\varphi}_r}(\underline{\theta}) = \frac{-2}{\left\|\underline{\hat{\varphi}}_r\right\|^2 \left\|\underline{\varphi}_r\right\|^2}\left[(2\beta_r\underline{\varphi}_r - \underline{\hat{\varphi}}_r)(2\beta_r\underline{\varphi}_r - \underline{\hat{\varphi}}_r)^T - \beta_r^2 \left\|\underline{\varphi}_r\right\|^2 I\right] \quad (4.51)$$

and $\frac{\partial^2 \varepsilon_{\underline{\phi}_r}^2(\underline{\theta})}{\partial\theta_i \partial\theta_j}$ in (4.49) simplifies to

$$\frac{\partial^2 \varepsilon_{\underline{\phi}_r}^2(\underline{\theta})}{\partial\theta_i \partial\theta_j} = -\frac{2}{\left\|\underline{\hat{\phi}}\right\|^2 \left\|L\underline{\phi}_r\right\|^2}\left(\underline{z}_r^{*T}\underline{F}_{r,i}\right)\left(\underline{z}_r^{*T}\underline{F}_{r,j}\right) - \beta_r^2 \left\|L\underline{\phi}_r\right\|^2 \underline{F}_{r,j}^{*T} X_r X_r^T \underline{F}_{r,i}^{*} - 2\underline{x}_r^{*T}(I - M\underline{\phi}_r\underline{\phi}_r^T)\underline{g}_r \tag{4.52}$$

where $\underline{z}_r$ is given by the solution of the linear system (4.37) with $D_r = \left(I - M^T\underline{\phi}_r\underline{\phi}_r^T\right)L^T\left(2\beta_r L\underline{\phi}_r - \underline{\hat{\phi}}_r\right)$ and X_r is given by (4.37) with $D_r = \left(I - M^T\underline{\phi}_r\underline{\phi}_r^T\right)L^T$.

It should be noted that only the last term in (4.47) and the last term in (4.52) depend explicitly on the derivatives $\partial\underline{\phi}_r / \partial\theta_i$. Numerical results suggest that the Hessian of $\varepsilon_{\omega_r}^2(\underline{\theta})$ and $\varepsilon_{\underline{\phi}_r}^2(\underline{\theta})$ can be adequately approximated in the form (4.47) and (4.52), ignoring the contribution from the last terms in (4.47) and (4.52). Thus the Hessian of $\varepsilon_{\omega_r}^2(\underline{\theta})$ and $\varepsilon_{\underline{\phi}_r}^2(\underline{\theta})$ can be computed from the solution of the system (4.37), estimates of the eigenvalues and eigenvectors of the mode r, and the sensitivities K_j and M_j of the global stiffness and mass matrices with respect to the parameters $\underline{\theta}$.

Summarizing, it should be noted that the computation of the first and second derivatives of the square errors for the modal properties of the r-th mode with respect to the parameters in $\underline{\theta}$ requires only the solutions of the linear system (4.37), independent of the number of parameters in $\underline{\theta}$. For a large number of parameters in the set $\underline{\theta}$, the above formulation for the gradients and Hessian of the mean errors in modal frequencies and in the modeshape components in (4.1) are computationally very efficient and informative.

4.5 Generalization of model updating method for closely spaced modes

4.5.1 Modeshape residuals

For the case of closely spaced modes, the modeshapes that are estimated experimentally using the modal identification techniques may not exactly correspond to the closely spaced modeshapes predicted by the finite element model. It has often been observed with real data that in such cases the MAC values for two modeshapes corresponding to two closely spaced modes are of the order of 0.5. This lack of correspondence between the experimental and and the model predicted modeshapes is due to the fact that the experimental modeshapes belong to the subspace spanned by the model predicted modeshapes for the case of closely spaced modes, something that it is expected for modes with multiplicity of two or higher. In this case it is not appropriate to use the modeshape residual (4.1) since a one to one correspondence is not

usually satisfied. In order to take into account this problem in the formulation one needs to generalize the definition of the modeshape residuals as follows.

Consider the modal group r containing the modal properties $r_1,\ldots,r_m$. This modal group is introduced herein to correspond to a set of closely spaced modes. However, in a more general setting it can be introduced to correspond to a set of arbitrary modes selected by the user. The modeshape residual for an experimentally obtained modeshape $\underline{\hat{\phi}}_{r_l}$ is constructed by comparing the experimentally obtained modeshape with a reference analytical modeshape $\underline{\phi}_{r_l,ref}(\underline{\theta})$ that belongs to the subspace spanned by the modeshapes $\underline{\phi}_{r_1}(\underline{\theta}),\ldots,\underline{\phi}_{r_m}(\underline{\theta})$ in the group r and is closest to the experimentally obtained modeshape. Thus the reference analytical modeshape is obtained by the expansion

$$\underline{\phi}_{r_l,ref}(\underline{\theta}) = \sum_{k=1}^{m} L\underline{\phi}_{r_k}(\underline{\theta})\beta_{k,r_l}(\underline{\theta}) = \Phi_r(\underline{\theta})\underline{\beta}_{r_l}(\underline{\theta}) \tag{4.53}$$

where

$$\Phi_r(\underline{\theta}) = \left[L\underline{\phi}_{r_1} \quad \cdots \quad L\underline{\phi}_{r_m} \right] \tag{4.54}$$

and $\underline{\beta}_{r_l}(\underline{\theta}) = [\beta_{1,r_l}(\underline{\theta}),\cdots,\beta_{m,r_l}(\underline{\theta})]^T$. The coefficients $\underline{\beta}_{r_l}(\underline{\theta})$ in the expansion (4.53) are selected so that $\underline{\phi}_{r_l}(\underline{\theta})$ is closest to $\underline{\hat{\phi}}_{r_l}$, that is,

$$\underline{\beta}_{r_l}(\underline{\theta}) = \arg\min_{\underline{\beta}_{r_l}} \left\| \Phi_r(\underline{\theta})\underline{\beta}_{r_l}(\underline{\theta}) - \underline{\hat{\phi}}_{r_l} \right\|^2 \tag{4.55}$$

One can readily show that (4.55) yields

$$\underline{\beta}_{r_l}(\underline{\theta}) = \left[\Phi_r^T(\underline{\theta})\Phi_r(\underline{\theta}) \right]^{-1} \Phi_r^T(\underline{\theta})\underline{\hat{\phi}}_{r_l} \tag{4.56}$$

The modal residual between the measured modal data and the model predicted modal data for the modeshape component $\underline{\hat{\phi}}_{r_l}$ involved in the modal group r is next defined by

$$\varepsilon^2_{\underline{\phi}_{r_l}} = \frac{\left\| \underline{\phi}_{r_l,ref}(\underline{\theta}) - \underline{\hat{\phi}}_{r_l} \right\|^2}{\left\| \underline{\hat{\phi}}_{r_l} \right\|^2} = \frac{\left\| \Phi_r(\underline{\theta})\underline{\beta}_{r_l}(\underline{\theta}) - \underline{\hat{\phi}}_{r_l} \right\|^2}{\left\| \underline{\hat{\phi}}_{r_l} \right\|^2} \tag{4.57}$$

These modal residuals for the individual modeshape in the group r are used to define the total modal residuals for all modeshapes in the group r by

$$\varepsilon^2_{\Phi_{r_l}}(\underline{\theta}) = \sum_{l=1}^{m} \varepsilon^2_{\underline{\phi}_{r_l}} = \sum_{l=1}^{m} \frac{\left\| \Phi_r(\underline{\theta})\underline{\beta}_{r_l}(\underline{\theta}) - \underline{\hat{\phi}}_{r_l} \right\|^2}{\left\| \underline{\hat{\phi}}_{r_l} \right\|^2} \tag{4.58}$$

It should be noted that for modes that are not closely spaced, the elements $\beta_{j,r_l}(\underline{\theta})$ of the normalization vector $\underline{\beta}_{r_l}(\underline{\theta})$ are expected to have values close to zero for $j \neq r_l$ and so the measure of fit $\varepsilon_{\underline{\phi}_r}(\underline{\theta})$ is approximately the same as $\varepsilon_{\underline{\phi}_r}(\underline{\theta}) = \left\| L\underline{\phi}_r(\underline{\theta})\beta_{rr}(\underline{\theta}) - \hat{\underline{\phi}}_r \right\| / \left\| \hat{\underline{\phi}}_r \right\|$ defined in (4.1).

4.5.2 Gradients of objectives

Next, the gradient of the modeshape residuals $\varepsilon^2_{\Phi_\eta}(\underline{\theta})$ with respect to the model parameters are obtained. Using (4.58), one has that

$$\frac{\partial \varepsilon^2_{\Phi_\eta}(\underline{\theta})}{\partial \theta_j} = \sum_{k=1}^{m} \underline{\rho}^T_{k,r} L \frac{\partial \underline{\phi}_{r_k}}{\partial \theta_j} \tag{4.59}$$

where

$$\underline{\rho}_{k,r} = \sum_{l=1}^{m} \underline{\nabla}_{\underline{\varphi}_{r_k}} \varepsilon^2_{\underline{\varphi}_{r_l}}(\underline{\theta}) \tag{4.60}$$

It should be noted that (4.59) is of the form (4.34) for one modal property with $m = 1$. For $r_1, \ldots, r_m$ modal properties, equation (4.34) can be written in the form

$$\sum_{l=1}^{m} \frac{\partial \varepsilon^2_{\underline{\phi}_{r_l}}(\underline{\theta})}{\partial \theta_j} = \sum_{l=1}^{m} \underline{\nabla}^T_{\underline{\varphi}_{r_k}} \varepsilon^2_{\underline{\varphi}_{r_k}}(\underline{\theta}) L \frac{\partial \underline{\phi}_{r_k}}{\partial \theta_j} = \sum_{k=1}^{m} \underline{\rho}^T_{k,r} L \frac{\partial \underline{\phi}_{r_k}}{\partial \theta_j} \tag{4.61}$$

with $\underline{\rho}_{k,r} = \underline{\nabla}_{\underline{\varphi}_{r_k}} \varepsilon^2_{\underline{\varphi}_{r_k}}(\underline{\theta})$. Note also that $\underline{\rho}_{k,r}$ is given by $\underline{\rho}_{k,r} = 2\underline{e}_{\underline{\varphi}_{r_k}}(\underline{\theta})\beta_{r_k}$ in (4.39).

Comparing (4.59), (4.60) with (4.61), it can be seen that the formulation for the gradients of the modeshapes presented in Section 4.4.3.2 can directly be used to handle the modeshape residuals (4.59) for closely spaced modes by replacing $\underline{\rho}_{k,r} = \underline{\nabla}_{\underline{\varphi}_{r_k}} \varepsilon^2_{\underline{\varphi}_{r_k}}(\underline{\theta})$ in the formulas presented in Section 4.4.3.2 by the quantity $\underline{\rho}_{k,r}$ given in (4.60).

Finally, it can be readily shown that the quantity $\underline{\rho}_{k,r}$ defined in (4.60) is given by

$$\underline{\rho}_{k,r} = \sum_{l=1}^{m} 2\underline{e}_{\underline{\varphi}_{r_l}} \beta_{k,r_l} = 2\mathrm{E}\underline{b}_k \tag{4.62}$$

where

$$\underline{e}_{\underline{\varphi}_{r_l}} = \frac{\Phi_r(\underline{\theta})\underline{\beta}_{r_l}(\underline{\theta}) - \hat{\underline{\phi}}_{r_l}}{\left\| \hat{\underline{\phi}}_{r_l} \right\|^2} \tag{4.63}$$

$$\mathrm{E} = \left[\underline{e}_{\underline{\varphi}_{r_1}} \quad \cdots \quad \underline{e}_{\underline{\varphi}_{r_m}} \right] \tag{4.64}$$

and

$$\underline{b}_k = \begin{Bmatrix} \beta_{k,r_1} \\ \vdots \\ \beta_{k,r_m} \end{Bmatrix} = \left[B_{k-row} \right]^T \tag{4.65}$$

with $\left[B_{k-row} \right]$ denoting the k row of matrix B given by $B = \left[\underline{\beta}_{r_1}(\underline{\theta}) \quad \cdots \quad \underline{\beta}_{r_m}(\underline{\theta}) \right]$.

4.6 Application on a scaled three-story building structure

Experimental data from a scaled three-story steel building structure are used to demonstrate the applicability and effectiveness of the proposed model updating methods, assess the effect of model error uncertainties on the variability of the Pareto optimal models, as well as investigate the response prediction accuracy and variability of the updated models.

4.6.1 Description of the laboratory structure

A schematic diagram of the side and the front views of the laboratory structure are given in Figure 4.2a. The floors of the building are made of identical steel beams of hollow orthogonal cross section. The two interstory columns that support each floor are made up of identical thin steel plates. The columns and beams are connected through angles with the help of bolts and nuts. The horizontal members are made to be much stiffer compared to the vertical structural elements so that the structural behaviour can be adequately represented by a shear beam building model. The total height of the structure is approximately 2.4m. The y direction of the frame is made to be stiffer to prevent coupling of motion with the x direction, the latter being the principal direction of interest. Detailed description and plans of the steel beams and columns can be found in Christodoulou (2007). The structure is considered as the reference structure and it is denoted by C_0.

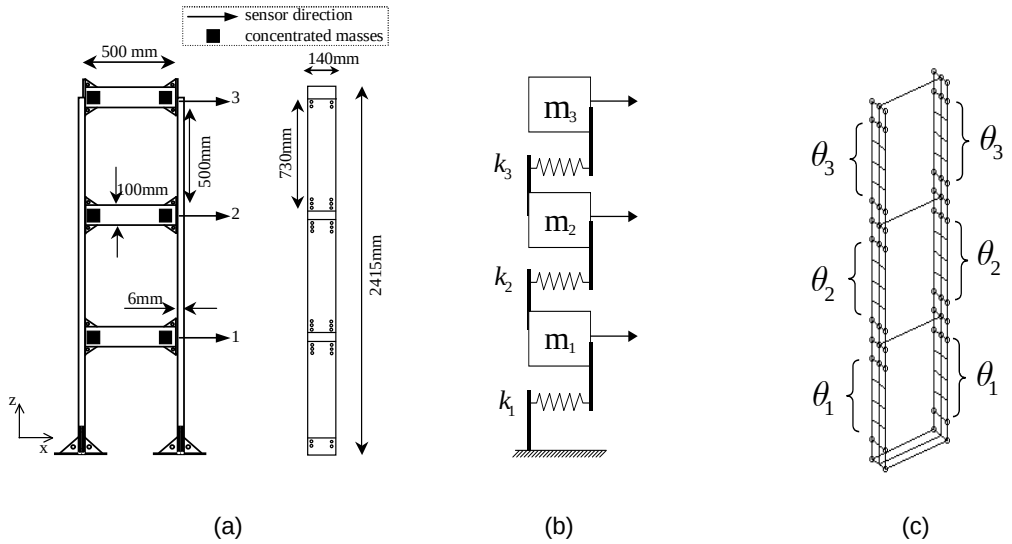

Figure 4.2: (a) Front and side views of 3-story building structure with added concentrated masses, (b) parameterized 3-DOF model class (c) parameterized 546 DOF finite element model class.

A second structural configuration is considered by adding concentrated masses made from lead in both sides of each floor of the reference structure as shown in Figure 4.2a. The added weight due to the concentrated masses is approximately 9.5 Kg per floor, while the total added mass corresponds to approximately 42% of the mass of the reference structure. The modified structural configuration with the concentrated masses is denoted by C_1.

4.6.2 Modal identification

The modal properties of the two structural configurations C_0 and C_1 are identified from frequency response functions that are obtained by processing the excitation force and acceleration response time histories generated from impulse hammer tests (Ewins, 2000). An array of three acceleration sensors located on the structure as schematically shown in Figure 1a, record the acceleration time histories during the test along the x direction. Multiple data sets are generated and processed that correspond to different excitation position of the impulse hammer at the second and third floor of the structure along the x direction. The common denominator least-squares complex frequency-domain method (Ntotsios, 2009) is used to obtain the optimal values of the modal parameters assuming classically damped modes. Table 4.1 reports the values of the identified modal frequencies and modeshape components at the measured locations of the lowest three bending modes for the reference C_0 and mass modified C_1 structural configurations.

Table 4.1: Lowest three bending modal frequencies and modeshapes identified for the reference and the mass modified structural configurations.

		Reference Structure C_0			Modified Structure C_1		
Mode #		1st	2nd	3rd	1st	2nd	3rd
Modal Freq. (Hz)		4.646	13.81	19.48	3.908	11.57	16.31
Modeshape Components	1st floor	0.4561	1.000	-0.7801	0.4408	1.000	-0.7892
	2nd floor	0.8069	0.3009	1.000	0.8219	0.3528	1.000
	3rd floor	1.000	-0.9026	-0.6448	1.000	-0.8709	-0.5708

4.6.3 Parameterized model classes

In order to investigate the effect of modelling error in model updating and model response prediction variability for each structural configuration, the following two parameterised model classes are introduced to represent the behaviour of the structure along the x direction.

The first model class, which is schematically shown in Figure 4.2b, is a simple 3-DOF mass-spring chain model. The modelling is based on the assumptions that the floors of the structure are rigid and that the stiffness is provided by the interstory plates. A lumped mass model is considered. Specifically, the i-th mass of the model includes the mass of the i-th floor and half of the mass of the interstory plates that are attached to the i-th floor. Thus, based on the weights of the structural elements, the masses m_1, m_2 and m_3 are taken to be equal to $m_1 = m_2 = m_0$ and $m_3 = 0.76m_0$, where $m_0 = 22.6$ Kg. The initial (nominal) values of the spring stiffnesses k_{01}, k_{02} and k_{03} are taken to be equal, that is, $k_{01} = k_{02} = k_{03} = k_0$. The ratio k_0 / m_0 was selected so as to minimize the difference between the first modal frequency predicted by the model and the first measured modal frequency for the structural configuration C_0.

The 3-DOF mass-spring chain model is parameterized introducing three parameters θ_1, θ_2 and θ_3, one for the stiffness of each spring modelling the interstory stiffness, so that $k_i = \theta_i k_{0i}$, for $i = 1, 2, 3$, where $k_{0i} = k_0$ is the nominal value of the stiffness of each spring in the nominal model and k_i is the updated value of the stiffness of each parameterised spring based on the measured data. This parameterized model class is denoted by M_0. For the modified structure C_1 with added concentrated masses, the 3-DOF model class is used with modified masses $m_1 + m_1'$, $m_2 + m_2'$ and $m_3 + m_3'$ that take into account the additional concentrated lead masses m_1', m_2' and m_3' added on the structure at each floor (see Figure 4.2a). The parameter set $\underline{\theta}$ is kept the same as the one used for the reference structure C_0. This parameterized model class for the modified structural configuration C_1 is denoted by M_1.

The second model class, which is schematically shown in Figure 4.2c, is a detailed finite element model. Each floor beam is modeled with a beam element, while the columns between each floor are modeled, due to its small thickness, with 12 plate elements each. The sizes of both types of

elements are calculated from the structural drawing. The modulus of elasticity and the density are based on the material properties. The plate elements near the joints, between columns and floors, are assumed to be very stiff compared to the interstory plate elements, in order to model the large rigidity in these parts of the structure. The FEM developed based on modeling assumptions, the structural drawings and the properties of the materials used, is referred to as the initial (nominal) FEM. The total number of DOF is 546.

The 546-DOF finite element model is parameterised introducing three parameters θ_1, θ_2 and θ_3, each one associated with the modulus of elasticity of the thin plate elements of first, second and third interstory columns, respectively, so that $E_i = \theta_i E_{0i}$, for $i = 1, 2, 3$, where $E_{0i} = E_0$ is the nominal value of the modulus of elasticity of interstory plate elements in the initial FE model and E_i is the updated value of the modulus of elasticity of each parameterised plate element. This parameterized model class is denoted by $M_{0,FE}$. The FEM of the modified structure C_1 with the additional concentrated masses is obtained by modifying the FEM of the reference structure, adding in the FEM the known values of the concentrated lead masses at the edge nodes of the horizontal beam elements used to model the stiffness of the floors. The parameter set $\underline{\theta}$ is kept the same as the one used for the reference structure. This parameterized model class for the modified structural configuration C_1 is denoted by $M_{1,FE}$.

The model within each of the defined model classes with parameter values $\theta_1 = \theta_2 = \theta_3 = 1$ correspond to the initial (nominal) model of the model class. It should be emphasized that the three parameters θ_1, θ_2 and θ_3 correspond to interstory stiffness properties of the three-story structure which are common for all four model classes introduced for the reference and mass modified configurations.

4.6.4 Structural model updating

Model updating results are computed for the model classes M_0 and $M_{0,FE}$ based on the experimental data in Table 4.1 available for the reference structural configuration C_0. Similarly, model updating results are computed for the model classes M_1 and $M_{1,FE}$ based on the experimental data in Table 4.1 available for the structural configuration C_1. The two objective functions in (4.1) are used for model updating. Thus, the objective space is two dimensional, while the parameter space is three dimensional. The Pareto optimal models are estimated from the proposed multi-objective identification method using the NBI algorithm and $N_P = 20$ points along the Pareto front. The estimation of the optimal models corresponding to the optimally-weighted and equally weighted residuals methods, as well as the optimal models corresponding to the edge points of the Pareto front, is based on the hybrid optimization method combining evolution strategies and gradient based methods.

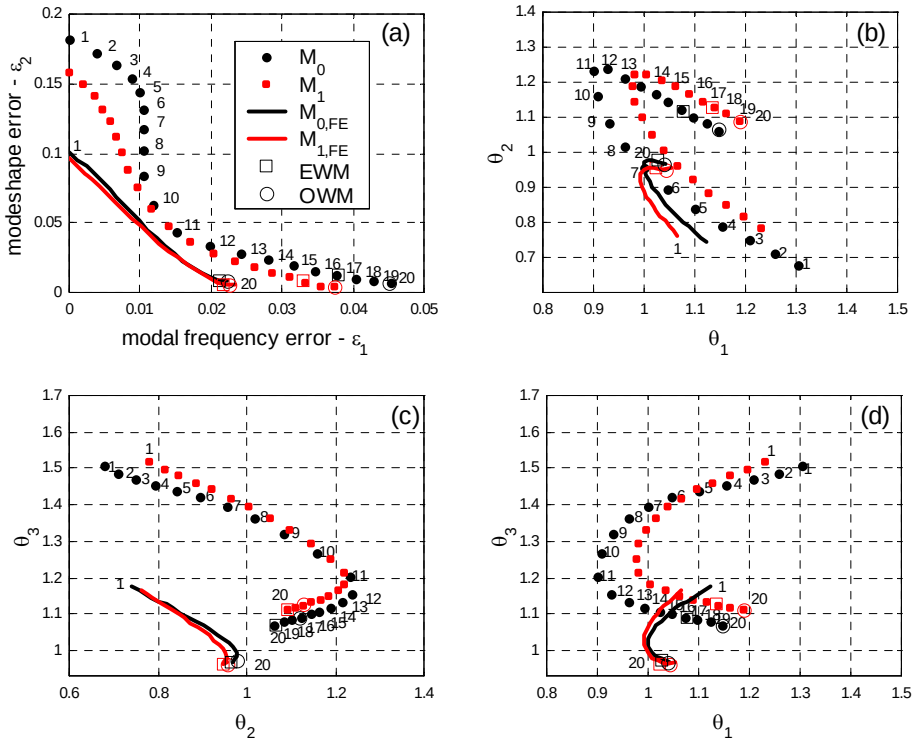

Figure 4.3: Pareto front and Pareto optimal solutions in the (a) objective space and (b-d) parameter space, along with optimal solutions obtained from the optimally and equally weighted modal residuals methods.

The results from the multi-objective identification methodology are shown in Figure 4.3. For each model class and associated structural configuration, the Pareto front, giving the Pareto solutions in the two-dimensional objective space, is shown in Figure 4.3a. Specifically, the results in Figure 4.3a are given for the functions $\varepsilon_1(\hat{\underline{\theta}}) = \sqrt{J_1(\hat{\underline{\theta}})/\alpha_1}$ and $\varepsilon_2(\hat{\underline{\theta}}) = \sqrt{J_2(\hat{\underline{\theta}})/\alpha_2}$ which, given the definition of the objective functions in (4.3), represent a measure of the average errors of the modal properties involved in the two modal groups. The non-zero size of the Pareto front and the non-zero distance of the Pareto front from the origin are due to uncertainties arising from modeling and measurement errors. Specifically, the distance of the Pareto points along the Pareto front from the origin is an indication of the size of the overall measurement and modeling error. The size of the Pareto front depends on the size of the model error and the sensitivity of the modal properties to the parameter values $\underline{\theta}$ (Christodoulou and Papadimitriou, 2007). It is observed that the average errors $\varepsilon_1(\hat{\underline{\theta}})$ and $\varepsilon_2(\hat{\underline{\theta}})$ between the measured and the model predicted modal properties obtained from the Pareto optimal models $\hat{\underline{\theta}}$ for the higher fidelity 546-DOF model classes $M_{0,FE}$ and $M_{1,FE}$ are significantly smaller than the residual errors corresponding to the 3-DOF model classes M_0 and M_1. Consequently, for the higher fidelity 546-DOF model classes, the Pareto front moves closer to the origin of the objective space. In

addition it is observed that the sizes of the Pareto fronts for the 546-DOF model classes $M_{0,FE}$ and $M_{1,FE}$ reduce to approximately one third to half the sizes of the Pareto fronts observed for the 3-DOF model classes M_0 and M_1. These results certify, as it should be expected based on the modeling assumptions in Section 5.3, that the 546-DOF model classes are higher fidelity model classes than the 3-DOF model classes. Also the results in Figure 4.3a quantify the quality of fit, acceptance and degree of accuracy of a model class in relation to another model class based on the measure data.

Figures 4.3b-d show the corresponding Pareto optimal solutions in the three-dimensional parameter space. For each model class, the Pareto optimal solutions are concentrated along a one-dimensional manifold in the three-dimensional parameter space. The Figures 4.3b-d show the projection of the Pareto solutions in the two-dimensional parameter spaces (θ_1,θ_2), (θ_2,θ_3) and (θ_1,θ_3). It is observed that a wide variety of Pareto optimal solutions are obtained for both model classes and structural configurations that are consistent with the measured data and the objective functions used. Comparing the Pareto optimal solutions for a model class, it can be said that there is no Pareto solution that improves the fit in both modal groups simultaneously. Thus, all Pareto solutions correspond to acceptable compromise structural models trading-off the fit in the modal frequencies involved in the first modal group with the fit in the modeshape components involved in the second modal group.

Comparing the Pareto front and Pareto optimal models for the 546-DOF model classes with the corresponding ones obtained for the 3-DOF model classes, it can be noted that the results are qualitatively similar. However, the size of the one dimensional optimal solutions manifolds for the 546-DOF model classes $M_{0,FE}$ and $M_{1,FE}$ are significantly smaller than the size of the manifolds for the 3-DOF model classes M_0 and M_1. These results clearly demonstrate that as the fidelity of the model class improves, the variability of the Pareto optimal models reduces. This has important implications in the selection of the weight values used in weighted modal residuals method for model updating and model-based prediction studies. Since the variability of the Pareto optimal solutions reduces as the fidelity of the models improves, the effect of the choice of weight on weighted modal residuals methods diminishes as the fidelity of the model increases.

Consider next the common parameter model classes M_0 and M_1 introduced for modeling the reference and modified structural configurations C_0 and C_1, respectively. The Pareto optimal values of the common parameter set $\underline{\theta}$ of the 3-DOF model classes M_0 and M_1 differ, despite the fact that the parameters for the two model classes M_0 and M_1 refer to the same interstory stiffnesses of the two different structural configurations. The differences can be attributed mainly to the size of modeling errors involved in the 3-DOF model classes. Instead, comparing the Pareto optimal values obtained from the common parameter 546-DOF model classes $M_{0,FE}$ and $M_{1,FE}$ for the two structural configurations C_0 and C_1, it is observed that the optimal solution manifolds for the 546-DOF model classes are significantly closer than the optimal solution manifolds for the 3-DOF model classes. This certifies that the higher fidelity model classes provide consistent estimates of the common parameters in model classes introduced to model

different structural configurations. Finally, it should be noted from the results in Figures 4.3b-d that the Pareto optimal values of the parameters predicted by the higher fidelity model classes $M_{0,FE}$ and $M_{1,FE}$ are significant different from the Pareto optimal values predicted by the simpler model classes M_0 and M_1. Thus, the model updating results and parameter estimates depend highly on the fidelity of the model class considered.

The optimal structural models corresponding to the optimally weighted (OWM) and the equally weighted (EWM) residuals methods for the 3-DOF and 546-DOF model classes are also shown in the Figure 4.3. It can be seen that these optimal models are points along the Pareto front, as it should be expected. The two methods, the OWM and the EWM, in general promote different Pareto optimal models for use in model-based prediction studies. For the example case considered, the Pareto solutions $\hat{\underline{\theta}}^{(owm)}$ provided by the optimally weighted residuals method for the 3-DOF model classes are close to the boundary solution $\hat{\underline{\theta}}^{(20)}$ for both structural configurations C_0 and C_1. Also, the Pareto points corresponding to the optimally weighted (OWM) and the equally weighted (EWM) residuals methods for the 546-DOF model classes are also shown in the Figure 4.3 to be closer than the corresponding Pareto points for the 3-DOF model classes.

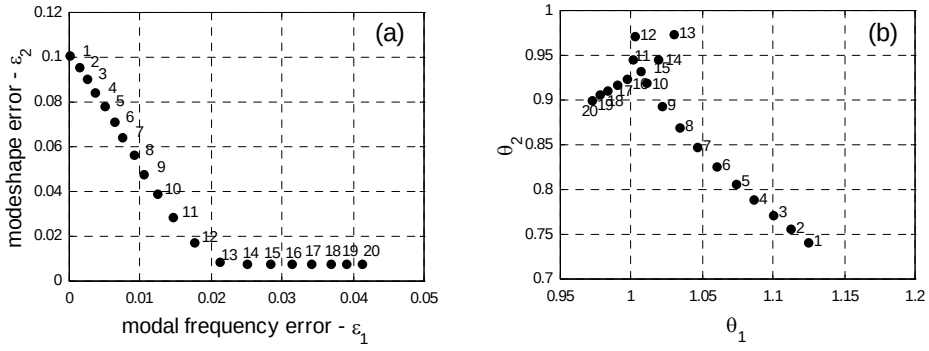

Figure 4.4: (a) Pareto front, (b) projection of Pareto optimal solutions in (θ_1, θ_2) plane for model class $M_{0,FE}$.

4.6.5 Unidentifiability issues

Unidentifiability issues are next discussed which were ignored in presenting the Pareto front for the model class $M_{0,FE}$ in Figure 4.3a. Figure 4.4a shows the Pareto front obtained by the application of the proposed NBI algorithm for the 546-DOF model class $M_{0,FE}$. It is observed that there is an almost flat part of the Pareto front at the lower right edge of Figure 3a. This is due to the unidentifiability problems (Katafygiotis et al., 1998; Katafygiotis and Lam, 2002) encountered in estimating the optimal model corresponding to the right edge point of the Pareto front. In this case, the right edge point of the Pareto front is obtained by optimizing the function $J_2(\underline{\theta})$. It turns

out that there is a lower dimensional manifold in the three-dimensional parameter space, shown in the two-dimensional projection (θ_1, θ_2) in Figure 4.4b to extend from point 13 to point 20, that give almost the same optimum for $J_2(\underline{\theta})$. Depending on the starting values of the parameter set $\underline{\theta}$, the gradient-based optimization algorithm converges to one of the infinite number of optimal models in this sub-manifold. As it is noted in Figure 4.4a, the flat unidentifiable portion of the Pareto front and the associated manifold in Figure 4.4b are readily obtained by the NBI method. From the engineering point of view, the most important point from this flat portion is the most left point 13 in Figure 4.4a since all other points in the flat portion deteriorate the fit in the objective function $J_1(\underline{\theta})$ without significantly altering the fit in $J_2(\underline{\theta})$. In order to generate points only on the identifiable portion of the Pareto front for pre-selected number of points on it (e.g. 20 points as shown in Figure 2a), the analyst can repeat the application of the NBI algorithm with edge points of the Pareto front selected to be the points 1 and 13 in Figure 3. It should be noted that in the results presented in Figure 4.3 for the model classes $M_{0,FE}$, only the identifiable part of the Pareto front is shown.

It is worth mentioning that unidentifiable portions of the Pareto front were not observed for the other three model classes which implies that the problem was identifiable for all three model classes.

4.6.6 Disconnected Pareto front

More careful examination of the optimal points resulted by the NBI method for the model class M_0 in Figure 4.3 reveals that the NBI points 6 and 7 for model class M_0 do not constitute Pareto points since it can be easily checked numerically that they do not satisfy conditions (4.5). Figure 4.5 shows the exact Pareto front and Pareto optimal solutions projected in the two-dimensional parameter space (θ_1, θ_2) using NBI method for $N_P = 40$ points. The NBI points that do not satisfy conditions (4.5) have been excluded from the Figures. It is clearly seen that the Pareto front in Figure 4.5a and the projection of the one-dimensional Pareto solution manifold in (θ_1, θ_2) plane in Figure 4.5b is disconnected. The missing portion in Figure 4.5 that does not belong to Pareto front is the portion of the Pareto front and Pareto solutions in Figure 4.3 that extends approximately from point 5 to point 8. From the previous results, it is evident that the NBI method, despite the disconnected manifolds that exists, is capable of fully describing the Pareto solutions.

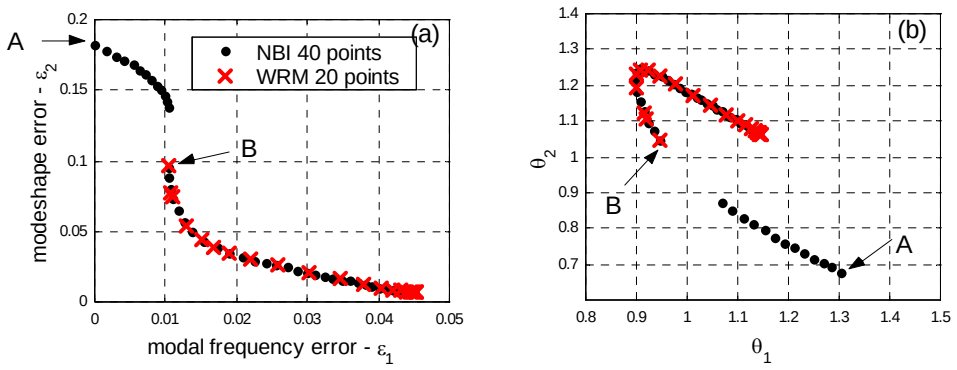

Figure 4.5: (a) Pareto front, (b) projection of Pareto optimal solutions in (θ_1, θ_2) plane for model class M_0.

4.6.7 Generation of Pareto points using the weighted residuals method

For comparison purposes, the weighted residuals method was also used to obtain the Pareto front by uniformly varying the weights in (4.6) from 0 to 1. Specifically, dividing the interval [0,1] for the weight w_1 into equally spaced sub-intervals using a step Δw, selecting the corresponding values of w_2 to satisfy the condition $w_1 + w_2 = 1$, and estimating the optimal solutions for the $1/\Delta w$ pairs of (w_1, w_2) values, the Pareto front and the Pareto solutions are obtained and shown in Figures 4.5a and 4.5b for model class M_0 for $\Delta w = 0.05$. It can be seen that varying the weights in the weighted residuals method, part of the Pareto points can be completely missed. Specifically, the top left portion of the Pareto front in Figure 4.5a has been missed. Attempts to recover this part by fully exploring the region in the parameter space that corresponds to the top left part of the Pareto front have failed. Such attempts included the use of different values of the weights $\underline{w}$ in (4.6), different starting values for solving the single-objective optimization problems, various sizes of Δw, and an increasing number of Pareto points. Numerically there is no point in the top left part of the Pareto front that corresponds to a weight value in the weighted residual method. This is in accordance with the fact that there may be Pareto solutions that do not correspond to solutions of the single-objective optimization involving the weighted residuals norm (4.6) for any values of the weights. It should however be noted that for weight values $w_1 = 1$ and $w_2 = 0$, there is a global optimal solution that corresponds to the edge Pareto point A shown in Figure 4.5, as well as a local solution that corresponds to the edge Pareto point B of the left portion of the Pareto front. Both solutions, although one global and one local for the same weight values $w_1 = 1$ and $w_2 = 0$, are Pareto optimal solutions because they correspond to different values of the second objective $J_2(\underline{\theta})$.

A final issue that is worth mentioning is that varying uniformly the weight values and computing the Pareto points using the weighted residuals method does not produce uniformly distributed points along the Pareto front. Instead, it may yield a cluster of points as it can be seen in Figure 4.5. As a consequence, part of the Pareto fronts can be misrepresented or completely missed.

4.6.8 Prediction variability using Pareto optimal structural models

The purpose of the identification is to construct faithful structural models, within a selected model class, that can be used for making improved structural performance predictions consistent with the measured data. The alternative models obtained along the Pareto front provide different performance predictions that are all acceptable based on the measured data and the measures of fit employed. The variability of these predictions is next explored.

The variability in the modal properties predicted by the Pareto optimal models is estimated for the model classes M_0 and $M_{0,FE}$ representing structural configuration C_0, and the model classes M_1 and $M_{1,FE}$ representing structural configuration C_1. The values of the three modal frequencies predicted by the Pareto optimal models from each model class, including the Pareto optimal models corresponding to the optimally weighted and equally weighted residuals methods, are shown in Figure 4.6. The measured modal frequencies for structural configurations C_0 and C_1 are also shown for comparison purposes. The variability of the corresponding MAC (Modal Assurance Criterion) values between the modeshape components predicted by the Pareto optimal models for each model class and the measured modeshapes for the three bending modes are shown in Figure 4.7.

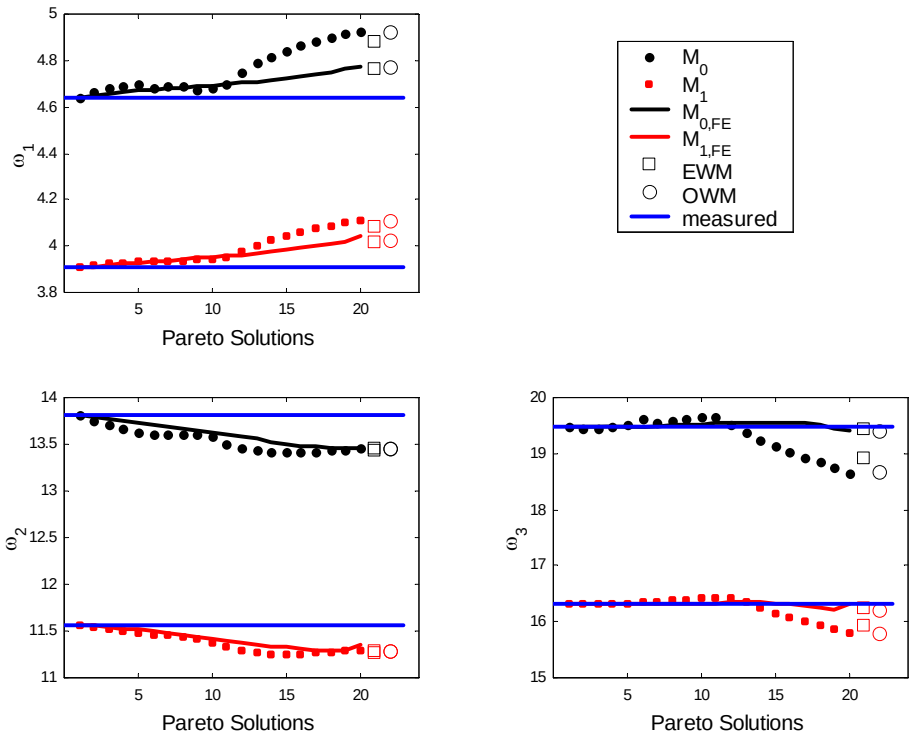

Figure 4.6: Variability of modal frequencies predicted by the Pareto optimal solutions corresponding to model classes M_0, M_1, $M_{0,FE}$ and $M_{1,FE}$. The corresponding measured modal frequencies are also presented.

For each model class, different Pareto optimal models along the Pareto front result in different predictions of the structural modal frequencies and MAC values. A relatively large variability in the predictions is observed for the 3-DOF model classes M_0 and M_1. The maximum percentage error values between the Pareto optimal model predictions for the first, second and third modal frequency are respectively of the order of 6.0%, 2.7% and 4.9% for the model class M_0 and of the order of 5.1%, 2.3% and 3.1% for the model class M_1. The MAC values corresponding to the first, second and third mode vary respectively from 0.990, 0.863 and 0.851 for the model classes M_0 and from 0.997, 0.895 and 0.884 for the model classes M_1 to values very close to 1.0.

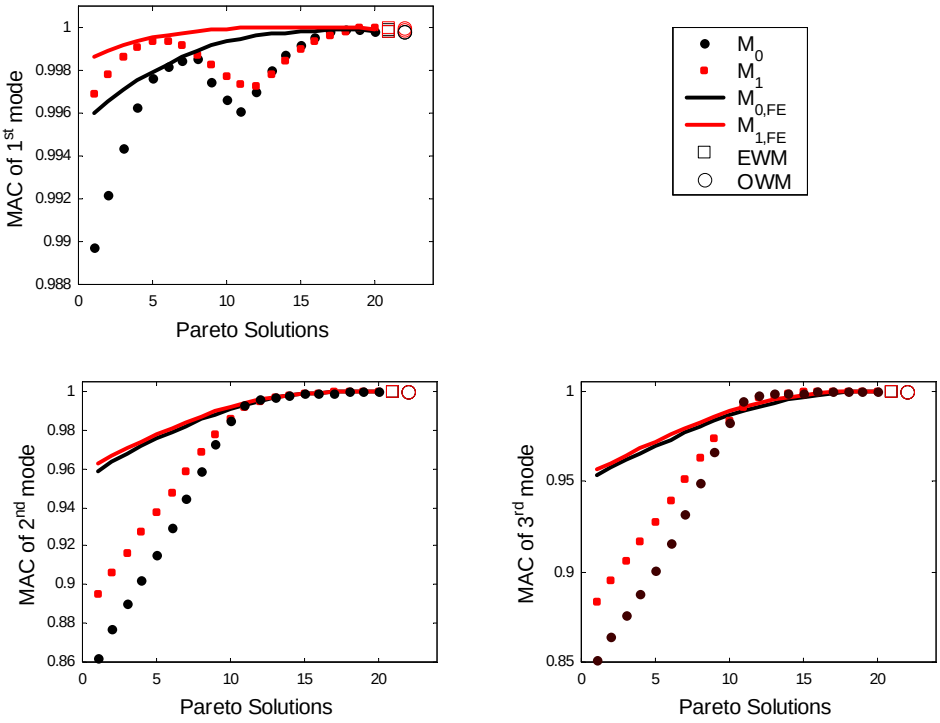

Figure 4.7: Variability of MAC values predicted by the Pareto optimal solutions corresponding to model classes M_0, M_1, $M_{0,FE}$ and $M_{1,FE}$.

It is clear that there is a trade off between the fit that the Pareto optimal models for model classes M_0 and $M_{0,FE}$ provide to the modal frequencies and the modeshapes. Specifically, the Pareto models with small numbers close to Pareto point 1 provide a very good fit to the modal frequencies in the expense of deteriorating the fit in the MAC values to values significantly smaller than one. The Pareto models with large numbers close to Pareto point 20 for model classes M_0 and $M_{0,FE}$ improve the MAC values to values very close to one in the expense of deteriorating the fit in the modal frequencies. Similar trade off in the fit is observed for the Pareto optimal models for model classes M_1 and $M_{1,FE}$.

Comparing the predictions in Figure 4.5 from the 3-DOF model classes and the 546-DOF model classes, the 546-DOF model classes $M_{0,FE}$ and $M_{1,FE}$ provide overall significantly better fit in the modal frequencies than the fit provided by the 3-DOF model classes M_0 and M_1. Also, comparing the results in Figure 4.7, it is observed that the higher fidelity 546-DOF model classes give MAC values between the Pareto optimal models and the measurements that are much closer to one than the MAC values obtained for the 3-DOF model class. These results verify that higher fidelity model classes tend to give better predictions that are less sensitive to selections required in model updating, such as the weight values used in weighted residuals methods.

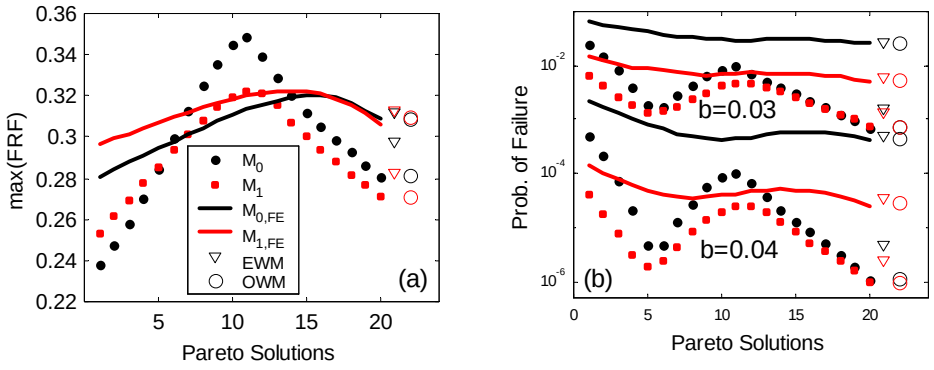

Figure 4.8: (a) Variability of the maximum of the frequency response function at first floor, (b) the probability of failure corresponding to allowable interstory drift levels $b = 0.03$ and $b = 0.04$.

Similar variability can be constructed for other structural performance indices. Figure 4.8a shows the variability of the maximum of the frequency response function at the first floor obtained for the Pareto optimal models for all model classes for damping values of $\zeta = 0.02$. Figure 4.8b shows the variability of the probability of failure of the structure to uncertain stochastic loads. Herein, failure is defined as the condition for which either one of interstory floor drifts exceeds a level b. The failure probability estimates are obtained for white noise excitation of duration $T = 30$ sec, strength $S = 0.001$ and for two allowable drift levels $b = 0.03$ and $b = 0.04$. The failure probability is obtained using efficient stochastic simulation methods available for linear systems [38-39] for 2000 samples. In particular, it is worth observing that a large variability in the maximum of the frequency response predictions, from [0.238 - 0.349] for the model class M_0 and [0.281 – 0.321] for the model class $M_{0,FE}$, and in the failure probabilities from [0.011x10^{-4} – 5.1x10^{-4}] for the model class M_0 and [0.4x10^{-3} – 2.1x10^{-3}] for the model class $M_{0,FE}$, are observed for the Pareto optimal models. Similar variability levels are observed for model classes M_1 and $M_{1,FE}$. These variabilities are larger than the variabilities in the modal frequencies shown in Figures 4.6.

Comparing the results in Figure 4.8 for the 3-DOF and the 546-DOF model classes, it is observed that the variability in the predictions of the maximum of the frequency response function and the probability of failure due to allowable drift exceedance levels of the 546-DOF model class is significantly smaller than the corresponding variability obtained from the 3-DOF model class.

Concluding, the predictions of the various performance indices from the Pareto optimal models may vary considerably. The variability in the predictions depends on the fidelity of the model class selected for identification. Higher fidelity model classes tend to reduce the variability in the predictions, diminishing the importance of selecting the weight values in weighted residuals methods.

4.7 Conclusions

Model updating methods were proposed to characterize and compute all Pareto optimal models from a model class, consistent with the measured data and the norms used to measure the fit between the measured and model predicted modal properties. The similarities with and differences from the conventional weighted modal residuals method were established. Based on a Bayesian statistical framework and the measured modal data, the most preferred Pareto optimal solution promoted by the proposed optimally weighted modal residuals method correspond to weight value for a modal group that is inversely proportional to the optimal residual between the measured and the model predicted properties involved in the modal group. The optimal values of the structural parameters for the most preferred Pareto optimal model are obtained by minimizing the sum of the logarithm of the modal residuals. The most preferred Pareto optimal model can be used for model-based predictions in case of more than a few objective functions for which the generation and visualization of Pareto optimal models in the multi-objective space is computationally less tractable. The Bayesian formulation also quantifies the uncertainty in the Pareto optimal models which can be used to further quantify the uncertainty in the response predictions from these Pareto optimal models. For this, an asymptotic approximation for the probability distribution of the weights has derived that depends on the optimal values of the model parameters and the Hessian of the residuals given a weight value.

Hybrid algorithms based on evolution strategies and gradient methods are necessary and well-suited optimization tools for solving the resulting non-convex single-objective optimization problem and identifying the global optimum from multiple local ones. The proposed NBI method is well-suited for solving the multi-objective optimization problem and effectively computing the useful identifiable part of the Pareto front, as well as portion of the unidentifiable part of the Pareto front at the edge points. Efficient algorithms are introduced for reducing the computational cost involved in estimating the gradients and Hessians of the objective functions. The computational cost for estimating the gradients and Hessians is shown to be independent of the number of structural model parameters. In addition to the optimization algorithm, the Hessian estimation is also used to estimate the probability distribution of the weights. The methodology is particularly efficient to system with several number of model parameters and large number of DOFs where repeated gradient evaluations are computationally quite time consuming.

Theoretical and computational issues were demonstrated by updating simple and higher fidelity model classes using experimental data from two configurations of a scaled three-story steel structure. A wide variety of Pareto optimal structural models consistent with the measured modal data was obtained. The variability in the Pareto optimal models is due to the model and measurement error. The large variability in the Pareto optimal models resulted in large variability in the response and structural reliability predictions. It has been demonstrated that higher fidelity model classes, tend to involve less model error, move the Pareto front towards the origin and reduce the size of the Pareto front in the objective space, reduce the variability of the Pareto optimal solutions, provide better fit to the measured quantities, and give much better predictions corresponding to reduced variability. In particular, as the fidelity of the model class improves, the importance of selecting the weight values in weighted residuals methods diminishes.

Chapter 5

Fatigue predictions of metallic structures using a limited number of vibration sensors

5.1 Introduction

Damage accumulation due to fatigue is an important safety-related issue in metallic structures. The linear Palmgren-Miner damage accumulation law (Palmgren, 1924; Miner, 1945) is often used to evaluate fatigue damage using available methods for cycle counting in variable amplitude measured stress response time histories and S-N curves obtained from laboratory experiments of simple specimens subjected to constant amplitude loads. The damage accumulation predictions are based on time histories measurements taken from a sensor network, consisting usually of strain rosettes, attached to the structure. Such predictions are only applicable for the locations where measurements are available. Due to practical and economical considerations, the number of sensors placed in a structure during operation is very limited and in most cases they do not cover all critical locations. Moreover, there are locations in the structure that one cannot install sensors such as submerged structures, underwater locations in offshore structures (oil refinery structures, offshore wind turbines, offshore steel jackets, etc.), heated structural components, internal points in solid structures, and non-approachable areas of large extended structures. Available fatigue prediction methods based only on measurements cannot be used to predict fatigue damage accumulation at such locations where measurements are not available. In order to infer damage due to fatigue at structural members where measurements are not available, one needs to predict the stress response time histories in these structural members using the available measurements obtained from the sensory system. In certain circumstances, such predictions can be possible if one combines the available measurements with the information obtained from a dynamic model (e.g. a finite element model) of the structure.

The methods for fatigue damage accumulation have been extended to treat the case that the excitations can be represented by a stochastic vector process with known correlation characteristics. Assuming that the structure behaves linearly and the excitation is modeled by a Gaussian stochastic vector process, the stress response at any point is a stochastic process that can be completely defined using the correlation characteristics of the stochastic excitations (Lutes and Sarkani, 2004). The fatigue damage accumulation at a structural location can then be computed using the characteristics of the stochastic processes of the components of the stress tensor at such a location. Methods for fatigue damage accumulation for Gaussian narrow-band stress processes have been introduced using the Rayleigh approximation and extended to handle the case of wide-band Gaussian stress processes (e.g. Wirsching and Light, 1980; Lutes et al., 1984; Lutes and Larsen 1990; Rychlik, 1993; Dirlik, 1985). A review and comparison of spectral methods for stochastic fatigue analysis based on wide-band Gaussian stochastic processes can be found in the work by Benasciutti and Tovo (2006). The formulations depend on the probability distribution of stress cycles corresponding to different stress levels in a stress response time history signal and the expected number of peaks per unit time of a stress process. Results for the

expected fatigue damage accumulation predicted by the Palmgren-Miner linear law have been presented in terms of the spectral moments of the stress process which are readily obtained from the power spectral density of the stress components involved. For the important case of wide band processes encountered often in applications, the simulation-inspired Dirlik approximation (Dirlik, 1985) is widely used and is considered to be the most accurate formula for modeling the probability of stress cycles in terms of the spectral moments of the stress process. It is worth noting that the aforementioned frequency domain methods based on the stress power spectral densities or spectral moments use no information available from a sensor network. Instead, their predictive accuracy depends on the assumptions employed for the excitation characteristics and the models representing the structural behavior. However, these predictions fail to integrate the information provided by a network of sensors. The sensor information is expected to update and improve the fatigue predictions, making them consistent with the available measurements.

In this chapter, the problem of estimating the expected damage accumulation or remaining lifetime due to fatigue in the entire body of a structure using output-only vibration measurements at a limited number of locations provided by a sensor network installed on the structure is addressed. The measurements may consist of response time histories such as e.g. strain, acceleration, velocity, displacement, etc. The expected fatigue damage accumulation in the entire structure is obtained by integrating (a) methods for predicting strain/stress response time histories and their correlation/spectral characteristics in the entire structure from output-only measured response time histories available at limited locations in the structure, and (b) frequency domain methods for estimating fatigue damage accumulation using the spectral characteristics of the predicted strain/stress response time histories. The idea is to use Kalman filter (Kalman and Bucy, 1961) methods to predict the strain/stress response time histories at various locations within structural components using the measurements available at a limited number of locations. A schematic diagram of the fatigue lifetime prediction in the entire structure from limited number of sensors using Kalman filter, along with its use in inspection/maintenance decisions, is shown in Figure 5.1. Response time history measurements are collected from a limited number of points $\mathrm{S}_1,\cdots,\mathrm{S}_n$, while stress time history predictions are made at any number of points $\mathrm{P}_1,\cdots,\mathrm{P}_m$. For each prediction point P, the fatigue damage accumulation, or remaining fatigue lifetime T, is obtained by combining the information in the stress tensor time history $\sigma(t)$ for the point P, fatigue data sets (e.g. S-N-curves) and a damage accumulation model (e.g. Palmgren-Miner rule). Such predictions are restricted here to the case of linear structures and excitations that can be adequately represented by Gaussian stationary stochastic processes. The excitation time histories applied in the structure are considered to be unknown. However, for several operational conditions of structures, the excitation time histories can be considered to be samples of a Gaussian stationary stochastic process with unknown intensity and frequency content. The proposed methodology is thus applicable for the case where the responses can be modeled by Gaussian stationary processes and the measured response time histories are long enough so that they can be considered to be samples of stationary processes.

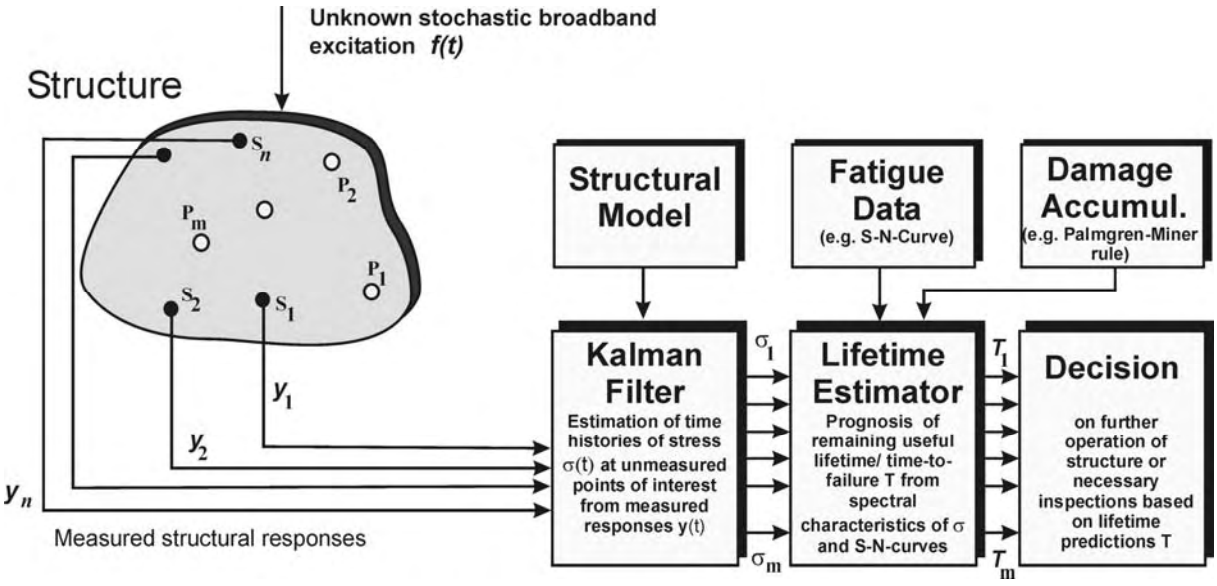

Figure 5.1: Scheme of life-time prediction from a limited number of sensors using a Kalman Filter.

The objective of this work is to formulate the fatigue prediction problem, illustrate the methodology and point out its use in evaluating the damage accumulation in the entire structure from a limited number of vibration measurements. For this, the present approach is limited to uni-axial stress processes and simplified models of structures. The extension to multi-axial stress processes can be accomplished by using recent developments in frequency domain methods for stochastic fatigue based on spectral techniques (Preumont and Piefort, 1994; You and Lee, 1996; Pitoiset and Preumont, 2000). These methods reduce the multi-axial stress state to an equivalent uniaxial stress state that can treated by available fatigue estimation techniques based on spectral methods. In addition, extension to non-Gaussian stress processes, known to significantly affect fatigue life predictions (Lutes et al., 1984; Sarkani et al., 1994) can also be accomplished by using recent approximations for the probability distribution of the stress cycles (Wang and Sun, 2005) in terms also of the higher moments of the stress process such as skewness and kurtosis.

This chapter is organized as follows. In Section 5.2, the frequency domain formulation for predicting damage due to fatigue in structural elements subjected to uniaxial stress state in linear structures under Gaussian stochastic excitations is reviewed. The formulation is applicable to Gaussian wide-band stress processes, often encountered in engineering applications, and damage accumulation due to fatigue depends on the spectral moments of the power spectral densities of the stress process at a location of a structure. Section 5.3 presents the formulation for predicting the strain/stress response time histories and the associated power spectral densities at all desirable locations of the structure using Kalman filter and the measured time histories at a limited number of locations in the structure. For this, first the state space formulation of the equations governing the vibrations of a structure is briefly summarized in Section 5.3.1. Using the discrete-time formulation of the state space approach, the Kalman filter approach for estimating the power spectral densities of the stresses in the entire body of the structure is

presented in Section 5.3.2 and 5.3.3. The approach considers that the unmeasured excitations can be represented by Gaussian stationary stochastic processes. Finally, Section 5.4 demonstrates the effectiveness of the proposed methodology using a chain-like mass-spring multi-degree-of-freedom (MDOF) structure and "measured" data that are simulated from various types of excitations, including white noise and filtered white noise excitations. Conclusions are summarized in Section 5.5.

5.2 Frequency domain method for fatigue estimation based on spectral moments

The Palmgren-Miner rule (Palmgren, 1924; Miner, 1945) is commonly used to predict the damage accumulation due to fatigue. According to this rule, a linear damage accumulation law at a point in the structure subjected to variable amplitude stress time history is defined by the formula

$$D = \sum_{i}^{m} \frac{n_i}{N_i} \tag{5.1}$$

where n_i is the number of cycles at a stress level σ_i, N_i is the number of cycles required for failure at a stress level σ_i, and m is the number of stress levels identified in a stress time history at the corresponding structural point. Available S-N fatigue curves, obtained from laboratory experiments on simple specimens that are subjected to constant amplitude loads, are used to describe the number of cycles N_i required for failure in terms of the stress level σ_i. The number of cycles n_i at a stress level σ_i are usually obtained using available stress cycle counting methods, provided that the stress time histories are available through measurements. Alternatively, for the cases where the stress response time histories are not available from measurements, frequency domain methods based on spectral moments (e.g. Lutes et al., 1984; Benasciutti and Tovo, 2006) can be used to predict the expected damage due to fatigue using the linear damage law (5.1). The methodology assumes that the power spectral density of the stress process at a structural location is available. For linear systems excited by time-varying loads that can be modeled by stationary stochastic processes, these power spectral densities can be straightforward computed using available random vibration results (Lutes and Sarkani, 2004).

The following section outlines such a frequency domain methodology based on spectral moments for fatigue estimation for structural members subjected to uniaxial stress state. For multi-axial stress states one can apply available methods (Preumont snd Piefort, 1994; You and Lee, 1996; Pitoiset and Preumont, 2000) to extend the applicability of the present methodology. Let $\sigma(t)$ be the uni-axial stress at a point in a structural element. The stress is considered to be a stationary Gaussian stochastic process. This is the case encountered in linear structures that are subjected to stationary Gaussian stochastic processes. Let $S_\sigma(\omega)$ be the power spectral density of the stationary Gaussian stochastic stress process $\sigma(t)$ of the uni-axial stress at a structural location and

$$\lambda_j = \int_{-\infty}^{\infty} |\omega|^j \, S_\sigma(\omega) d\omega \tag{5.2}$$

be the spectral moments of the process. Using frequency domain methods for fatigue estimation under stochastic excitations and the continuous version of the damage accumulation law (5.1), the expected fatigue damage accumulation for a uni-axial stochastic stress process is given by (Benasciutti and Tovo, 2006)

$$E[D] = \int_0^{\infty} \frac{n(\sigma)}{N(\sigma)} d\sigma = c^{-1} T E[P] \int_0^{\infty} \sigma^a \, p(\sigma) d\sigma \tag{5.3}$$

where $n(\sigma) = TE[P] p(\sigma) d\sigma$ is the number of cycles at stress levels within the stress interval $[\sigma, \sigma + d\sigma]$, $p(\sigma)$ is the probability distribution of the stress levels,

$$N(\sigma) = c\sigma^{-\alpha} \tag{5.4}$$

is the number of cycles for failure that correspond to a specific constant amplitude stress level σ obtained from available S-N curves, $E[P]$ is the expected number of peaks per unit time for the stress process, and T the period of observation. The parameters c and α are constants obtained from fatigue test experiments and depend on the material and the type of the test specimen.

The expected time of failure due to fatigue (fatigue lifetime) T_{life} corresponds to a critical expected damage value $E[D] = D_{cr}$ which is often set equal to unity ($D_{cr} = 1$). Using (5.3), the fatigue lifetime is given by

$$T_{life} = \frac{D_{cr}}{\bar{D}} \tag{5.5}$$

where $\bar{D}$ is the expected damage rate given by

$$\bar{D} = c^{-1} E[P] \int_0^{\infty} \sigma^{\alpha} \, p(\sigma) d\sigma \tag{5.6}$$

For Gaussian stochastic stress processes, the probability distribution of the stress range $\Delta\sigma = 2\sigma$, taken to be twice the random amplitude at stress level within $[\sigma, \sigma + d\sigma]$ in a stress process, is given by the Dirlik formula (Dirlik, 1985; Bishop and Sherrat, 1990; Benasciutti and Tovo, 2005) as

$$p(\Delta\sigma) = \frac{1}{2\sqrt{\lambda_0}} \left[\frac{d_1}{h} e^{-\frac{\Delta\sigma}{2h\sqrt{\lambda_0}}} + \frac{d_2 \Delta\sigma}{2r^2\sqrt{\lambda_0}} e^{-\frac{(\Delta\sigma)^2}{8r^2\lambda_0}} + \frac{d_3 \Delta\sigma}{2\sqrt{\lambda_0}} e^{-\frac{(\Delta\sigma)^2}{8\lambda_0}} \right] \tag{5.7}$$

where d_1, d_2, d_3, h and r are specific algebraic functions of the spectral moments λ_0, λ_1, λ_2, λ_4, given by

$$d_1 = \frac{2\left(x_m - \alpha_2^2\right)}{1+\alpha_2^2}, \qquad d_2 = \frac{1-\alpha_2-d_1+d_1^2}{1-r}, \qquad d_3 = 1-d_1-d_2 \tag{5.8}$$

$$h = \frac{1.25\left(\alpha_2 - d_3 - d_2 r\right)}{d_1}, \qquad r = \frac{\alpha_2 - x_m - d_1^2}{1-\alpha_2-d_1+d_1^2} \tag{5.9}$$

$$x_m = \frac{\lambda_1}{\lambda_0}\left[\frac{\lambda_2}{\lambda_4}\right]^{\frac{1}{2}} = \alpha_1\alpha_2, \qquad \alpha_1 = \frac{\lambda_1}{\sqrt{\lambda_0\lambda_2}}, \qquad \alpha_2 = \frac{\lambda_2}{\sqrt{\lambda_0\lambda_4}} \tag{5.10}$$

This is a semi-empirical probability density which is a mixture of one exponential and two Rayleigh distributions. It has been derived by fitting the shape of a rain-flow range distribution via minimizing the normalized error between the rain-flow ranges and the above density model. The spectral moments $\lambda_0, \lambda_1, \lambda_2, \lambda_4$ constitute a base for the construction of the approximate closed-form Dirlik formula for the probability density of the stress range. The Dirlik formula constitutes an extension of the Rayleigh distribution to non-narrow band processes. It is widely used for fatigue crack estimation under wide-band Gaussian stationary applied stress. Extension to non-Gaussian stress processes requiring the skewness and kurtosis of the stress process are available in the work by Wang and Sun (2005).

Using results from random vibration theory, the expected number of cycles $E[P]$ per second for a stochastic process is given by the spectral moments of the process in the form

$$E[P] = \frac{1}{2\pi}\sqrt{\frac{\lambda_4}{\lambda_2}} \tag{5.11}$$

Starting with (5.6) and noting that $p(\sigma) = p(\Delta\sigma)/2 = p(2\sigma)/2$, then substituting (5.11) and the Dirlik formula (5.7) into (5.6) and finally carrying out the integration in (5.6) analytically, the expected damage rate simplifies to (Benasciutti and Tovo, 2006)

$$\bar{D} = (8\pi c)^{-1}\sqrt{\frac{\lambda_4}{\lambda_2}}\lambda_0^{\alpha/2}\left[d_1 h^{\alpha}\Gamma(1+\alpha) + 2^{\alpha/2}\Gamma\left(1+\frac{\alpha}{2}\right)\left(d_2\,|\,r\,|^{a} + d_3\right)\right] \tag{5.12}$$

where d_1, d_2, d_3, h and r are defined in (5.8)-(5.10).

It is clear from the aforementioned formulation and equations (5.5) and (5.12) that the expected fatigue damage rate $\bar{D}$ and, consequently, the fatigue accumulation during a time interval T or the fatigue lifetime T_{life} at a point in the structure depends only on the spectral moments λ_i, $i = 0,1,2,4$, of the stress process $\sigma(t)$. Using the definition of the spectral moments in (5.2),

the spectral moments and the fatigue predictions at a point of a structure eventually depend only on the power spectral density $S_\sigma(\omega)$ of the stress process $\sigma(t)$.

The power spectral densities of the stress response processes at a point can be calculated from measurements, provided that these measurements are long enough to be considered stationary. However, there is a limited number of points that can be instrumented in the structure. For the points where measurements are not available, one has to make predictions of the stress process and subsequently the power spectral density of the stress process at a location, given the measurements at other locations. This issue of predicting the power spectral densities of the stress processes in the entire body of the structure using measurements at limited locations is addressed at the next Section 3. Once these measurements and predictions of the stresses are estimated at measured and unmeasured locations, the power spectral densities and the corresponding damage accumulation or lifetime due to fatigue are obtained, using (5.5) and (5.12), everywhere in the structure. In this way, fatigue damage accumulation maps for the entire structure are constructed from the limited number of ambient vibration measurements.

5.3 Response predictions in the entire structure using ambient vibration measurements

The objective of this section is to predict the stress response at all points in a structure using the measurements at a limited number of locations. This is achieved using an approach that is outlined in the next two subsection based on the commonly used Kalman filter method (Kalman and Bucy, 1961) for full state estimation of a linear system using limited number of measurements.

5.3.1 Equations of motion and state space formulation

Consider the dynamic response of a linear structural system subjected to deterministic and random excitations. Using a spatial discretization method, such as finite element analysis, the equations of motion are given by the following set of N second order differential equations

$$M\,\underline{\ddot{q}}(t) + C\,\underline{\dot{q}}(t) + K\,\underline{q}(t) = L_u\,\underline{u}(t) + L_w\,\underline{w}(t) \tag{5.13}$$

where $\underline{q}(t) \in \mathbb{R}^{N\times 1}$ is the displacement vector, M, C and $K \in \mathbb{R}^{N\times N}$ are respectively the mass, damping and stiffness matrices, $\underline{u}(t) \in \mathbb{R}^{N_{u,in}\times 1}$ and $\underline{w}(t) \in \mathbb{R}^{N_{w,in}\times 1}$ are the applied deterministic and stochastic excitation vectors of dimension $N_{u,in}$ and $N_{w,in}$, respectively, and $L_u \in \mathbb{R}^{N\times N_{u,in}}$ and $L_w \in \mathbb{R}^{N\times N_{w,in}}$ are matrices comprised of zeros and ones that map the $N_{u,in}$ and $N_{w,in}$ deterministic and stochastic excitation loads to the N output DOFs. Throughout the analysis, it is assumed that the system matrices M, C and K are symmetric. Let $\underline{y}(t) \in \mathbb{R}^{N_{meas}}$ be the vector that collects all measurements at different locations of the structure at time t.

These measurements are generally collected from sensors such as accelerometers, strain gauges, etc. For convenience and without loss of generality, it is assumed in the analysis that sensors placed in the structure measure the strains.

Introducing the state vector $\underline{x}^T = [\underline{q}^T \quad \underline{\dot{q}}^T] \in \mathbb{R}^{1\times 2N}$, the equation of motion can be written in the state space form

$$\underline{\dot{x}} = A_c \underline{x} + B_c \underline{u}(t) + G_c \underline{w}(t) \tag{5.14}$$

while the measured output vector $\underline{y}(t)$ is given by the observation equation

$$\underline{y}(t) = H \underline{x} + D\underline{u}(t) \tag{5.15}$$

where the state transition matrix A_c, and the matrices B_c and G_c are given by

$$A_c = \begin{bmatrix} 0 & I \\ -M^{-1}K & -M^{-1}C \end{bmatrix} \in \mathbb{R}^{2N\times 2N} \tag{5.16}$$

$$B_c = \begin{bmatrix} 0 \\ -M^{-1}L_u \end{bmatrix} \in \mathbb{R}^{2N\times N_{u,in}} \quad \text{and} \quad G_c = \begin{bmatrix} 0 \\ -M^{-1}L_w \end{bmatrix} \in \mathbb{R}^{2N\times N_{w,in}} \tag{5.17}$$

respectively, $H \in \mathbb{R}^{N_{meas}\times 2N}$ is the observation matrix and $D = 0 \in \mathbb{R}^{N_{meas}\times 2N_{u,in}}$ for strain measurements.

5.3.2 Kalman filter approach

Since measurements are available in digitized form, the presentation of the Kalman filter is next given in discrete time. Using the sampling rate $1/\Delta t$, the discrete-time state space model corresponding to (5.14) and (5.15) is

$$\underline{x}_k = A\underline{x}_{k-1} + B\underline{u}_{k-1} + G\underline{w}_{k-1} \tag{5.18}$$

$$\underline{y}_k = H\underline{x}_k + D\underline{u}_k + \underline{v}_k \tag{5.19}$$

where $\underline{x}_k = \underline{x}(k\Delta t)$ and $\underline{y}_k = \underline{y}(k\Delta t)$, $k = 1, \cdots, N_s$, are the digitized state and output vectors, and $A = e^{A_c \Delta t}$ is the state transition matrix for the discrete formulation. The random variables w_k and v_k represent the stochastic excitation and the measurement noise, respectively. They are assumed to be independent, white and following normal probability distributions $p(w_k) \sim N(0, Q)$ and $p(v_k) \sim N(0, R)$, where Q and R are the stochastic excitation and the measurement noise covariances assumed to be constant, independent of time.

Kalman filter is used to estimate the state $\underline{\hat{x}}_k$ of the system described by (5.18) using the measurements in the vector $\underline{y}_k$ in (5.19). Specifically, in the prediction step, an apriori state estimate $\underline{\hat{x}}_k^-$ of the state vector $\underline{x}_k$ of the system is estimated from equation (Franklin et al., 1990; Stengel, 1986)

$$\underline{\hat{x}}_k^- = A\underline{\hat{x}}_{k-1} + B\underline{u}_{k-1} \tag{5.20}$$

In the correction step, the measured value $\underline{y}_k$ is used to calculate a posteriori state estimate $\underline{\hat{x}}_k$, weighting the measured and estimated signals by the Kalman filter gain factor K_k. This is formulated by the equation

$$\underline{\hat{x}}_k = \underline{\hat{x}}_k^- + K_k[\underline{y}_k - H\underline{\hat{x}}_k^- - D\underline{u}_k] \tag{5.21}$$

where the Kalman gain factor is given by

$$K_k = P_k H^T [HP_k H^T + R]^{-1} \tag{5.22}$$

and, for steady state response, the error covariance matrix $P_k \equiv P = E[\underline{e}_k^-(\underline{e}_k^-)^T]$, where $\underline{e}_k^- = \underline{x} - \underline{\hat{x}}_k^-$ is the a priori error estimate, satisfies the discrete time Riccati equation:

$$P = APA^T - APH^T(HPH^T + R)^{-1}HPA^T + GQG^T \tag{5.23}$$

Let $\underline{\sigma}_k$ be a vector containing the digitized stresses at time $t = k\Delta t$ at various locations of the structure. Using structural mechanics theory, these stresses in the vector $\underline{\sigma}_k$ are related to the state vector through a linear transformation $\underline{\sigma}_k = \Sigma\underline{x}_k$, where Σ is the transformation matrix that associates the state vector to the desired stresses in the entire structure. Consequently, an estimate of the stresses $\underline{\hat{\sigma}}_k$ is related to the state vector estimate $\underline{\hat{x}}_k$ through the transformation:

$$\underline{\hat{\sigma}}_k = \Sigma\underline{\hat{x}}_k \tag{5.24}$$

Herein, the response prediction vector $\underline{\sigma}_k$ is restricted to stresses at elements subjected to uniaxial stress states required in lifetime fatigue estimation as described in Section 5.2.

Using the definition of the cross power spectral density (CPSD), the Kalman filter equations (5.20) and (5.21), the fact that $B = 0$ in (5.20) for the case of stochastic excitations and $D = 0$ in (5.21) for strain measurements, the CPSD $S_{\underline{\hat{\sigma}}}(\omega)$ of the stress response vector $\underline{\hat{\sigma}}_k$ can readily be obtained with respect to the CPSD $S_{\underline{y}}(\omega)$ of the measurement vector $\underline{y}_k$ in the form

$$S_{\underline{\hat{\sigma}}}(\omega) = \Sigma S_{\underline{x}}(\omega)\Sigma^T = \Sigma E^{-1}(j\omega)KS_{\underline{y}}(\omega)K^T E^{-T}(j\omega)\Sigma^T \tag{5.25}$$

where $E(j\omega)$ is the matrix given by

$$E(j\omega) = Ie^{j\omega\Delta t} - (I - KH)A \tag{5.26}$$

and I is the identity matrix. Equation (5.25) relates the power spectral densities of the components of the stress vector $\underline{\sigma}_k$ at various structural locations with the power spectral densities of the measured quantities involved in $\underline{y}_k$ available at the limited number of measured locations. This relation depends on the model (e.g. a finite element model) used to represent the behavior of the structure and the assumption that the excitation vector is broad-band so that the excitations can be modeled by zero-mean stationary white noise processes with spectral density described by $E[\underline{w}_k \underline{w}_l^T] = Q\delta_{kl}$, where δ_{kl} is the Kronecker delta.

It should be noted that in order to apply (5.23), an estimate of the zero-lag covariance matrix R of the measurement noise and the zero-lag covariance matrix Q of the unknown input stochastic vector process has to be provided. The values of the covariance matrix R which have to be chosen, affects the estimates of the cross power spectral density matrix $S_{\underline{\hat{\sigma}}}(\omega)$ in (5.25). However, an optimal estimate of the covariance matrix Q can be obtained using the strain measurements $\underline{y}(t)$ and the relation $Q_{yy} \equiv Q_{yy}(Q)$ between the covariance matrix Q_{yy} of the measurement vector $\underline{y}(t)$ and the covariance matrix Q of the excitation process. Using (5.19) with $D = 0$ for strain measurements, this relation is given by

$$Q_{yy} = HQ_{xx}H^T \tag{5.27}$$

where Q_{xx} is given by the discrete time Lyapunov equation for the system (5.18) in the form

$$A\,Q_{xx}A^T - Q_{xx} + GQG^T = 0 \tag{5.28}$$

The optimal values of the entries of the covariance matrix Q can be obtained by minimizing the difference between the covariance matrix $Q_{yy} \equiv Q_{yy}(Q)$ predicted by the linear model given Q and the covariance matrix $\hat{Q}_{yy} = (1/N_s)\sum_{k=1}^{N_s} \underline{y}_k \underline{y}_k^T$ obtained from the measurements in $\underline{y}_k$, $k = 1, \cdots, N_s$. That is, the optimal value Q_{opt} is obtained by minimizing the objective function

$$J(Q) = tr\,||\,Q_{yy}(Q) - \hat{Q}_{yy}\,||^2 \,/\, tr\,||\,\hat{Q}_{yy}\,||^2 \tag{5.29}$$

with respect to the elements in Q. The optimal value Q_{opt} of Q is then substituted in (5.23) to completely define the Riccati equation (5.23). The solution P of the Riccati equation is substituted in (5.22) in order to find K which is needed in (5.25). It should be noted that the optimal estimate of Q, as described above, assumes that the stochastic excitations in the vector

process $\underline{w}_k$ are sufficiently broadband so that they can be adequately approximated by white noise processes.

5.3.3 Estimation of power spectral densities of stresses

The cross power spectral density matrix $S_{\underline{y}}(\omega)$ of the sampled measurement vector $\underline{y}_k$, involved in (5.25), can be obtained using available signal processing techniques such as the Welch technique (Welch, 1967; Hayes, 1996). Once $S_{\underline{y}}(\omega)$ has been estimated from the measurements, equation (5.25) can be used to estimate the cross power spectral density $S_{\underline{\hat{\sigma}}}(\omega)$ of the stress response vector $\underline{\hat{\sigma}}_k$.

Alternatively, the PSD $S_{\underline{\hat{\sigma}}}(\omega)$ of the stress response vector $\underline{\hat{\sigma}}_k$ can be obtained by using equations (5.20) and (5.21) for the Kalman filter to provide estimates $\underline{\hat{x}}_k$ of the system state vector which are then used in equations (5.24) to estimate the stress vector $\underline{\hat{\sigma}}_k$. Finally, available signal processing techniques such as the Welch technique are used to compute the PSD $S_{\underline{\hat{\sigma}}}(\omega)$ from the sampled stress response vector $\underline{\hat{\sigma}}_k$. The length of the sampled time history should be sufficient large in order for the estimates to be accurate.

Once the cross power spectral density matrix $S_{\underline{\hat{\sigma}}}(\omega)$ of the stress vector process $\underline{\hat{\sigma}}_k$ containing the stresses at all desirable structural locations is obtained, the diagonal elements $diag[S_{\underline{\hat{\sigma}}}(\omega)]$ of the matrix $S_{\underline{\hat{\sigma}}}(\omega)$ contain the power spectral density estimates required for fatigue predictions at these structural location using equations (5.2), (5.5) and (5.12).

5.4 Application on spring-mass chain-like model

The applicability and effectiveness of the methodology is illustrated using simulated "measurements" from a simple class of N-DOF spring mass chain-like model fixed at the two ends as shown in Figure 5.2. The model is used to represent a structure consisting of a series of bar and body elements as shown in Figure 5.3. The structure consists of N bodies with the i-th body having mass m_i. The $i-1$ and the i bodies are connected by elastic bar elements which provide the stiffness to the system. The number of bar (or spring) elements of the chain model is $N+1$. The material of the bar elements is considered to be steel. For steel bar elements, the values of the fatigue constants in equation (5.4) are taken to be $c = 4.06 \times 10^{88}$ and $a = 9.82$. The i-th bar element has length L_i, cross-sectional area A_i and modulus of elasticity E_i. For simplicity, each bar element is represented by a spring element with stiffness $k_i = E_i A_i / L_i$ as shown in Figure 5.2. Also, the nodal mass m_i in Figure 5.2 includes the effect of the i body mass and the lumped mass arising from the bar elements connected to node i. The i component $q_i(t)$ of the vector $\underline{q}(t)$ corresponds to the displacement of the node i of the model. The system is subjected to an unmeasured excitation applied at node ρ. For the selected

structure, the stress state at critical bar locations is uniaxial so that the fatigue prediction methodology can be directly applied.

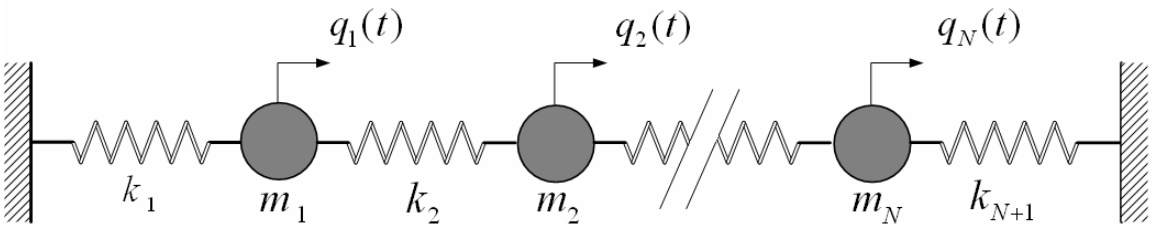

Figure 5.2: N -DOF spring mass chain-like model.

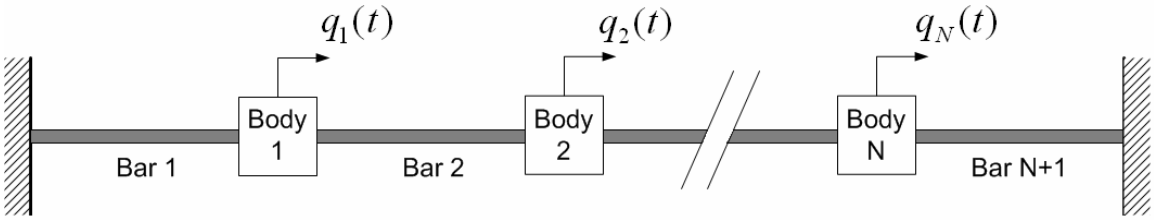

Figure 5.3: Structure consisting of a series of N masses and $N+1$ bar elements.

Fatigue predictions from the Kalman filter (KF) methodology are based on a nominal model of the structure that corresponds to nominal stiffness values $k_i = k_{0,i}$. The measurements that are collected from the actual structure are generated from a reference model introduced to simulate the actual behavior of the structure. In order to study the effects of the model error on the accuracy of the Kalman filter method for fatigue predictions, the reference model is selected to be different from the nominal model. Specifically, the reference model corresponds to the model shown in Figure 5.2 with stiffness values perturbed from the nominal stiffness values according to the expression $k_i = k_{0,i}(1+n_i)$, where $k_{0,i}$ are the nominal values used in KF-based fatigue predictions and $n_i \sim N(0, s_i^2)$ are samples from a zero mean normal distribution with variance s_i^2. The standard deviation s_i of the perturbed terms controls the size of the model error and reflects the differences observed in real applications between the predictions from a model of a structure and the actual behavior of the structure.

The measurements are assumed to be strain measurements. These measurements are simulated from the reference model of the structure using two types of excitations, referred to as Type I and Type II excitations. Type I excitations are assumed to be samples of a Gaussian white noise process, thus providing good approximation to an excitation whenever its correlation time is sufficiently small compared to the system time constants. In this case the excitation vector $\underline{u}(t)$

is modeled by samples generated by a Gaussian stationary white noise vector process $\underline{n}(t)$ with constant spectral density matrix $S_{\underline{u}} = S_0$. Type II excitations are assumed to be samples of a uni-modal filtered white noise excitation with characteristics given by the second order filter equation

$$\ddot{q}_f(t) + 2\zeta_f \omega_f \dot{q}_f(t) + \omega_f^2 q_f(t) = n(t) \tag{5.30}$$

$$u(t) = \ddot{q}_f(t) = -2\zeta_f \omega_f \dot{q}_f(t) - \omega_f^2 q_f(t) + n(t) \tag{5.31}$$

The characteristics of the excitation depend on the values of the filter parameters: the dominant frequency ω_f and the damping ratio ζ_f. The value of the power spectral density S_0 of the Gaussian stationary white noise process $n(t)$ controls the intensity of the excitation samples $u(t)$ generated by the second-order filter.

For type I excitation, the discrete state space formulation of the equations of motion for the reference model is used to simulated response time history data as well as compute estimates of the covariance responses and the power spectral density of the responses using the white noise excitation $n(t)$ applied at node ρ. For type II excitation, the responses from the reference model can readily be obtained by a discrete state space formulation of an augmented system which consists of the equations of motion (5.13) and the filter equations (5.30)-(5.31) excited by the white noise process $n(t)$. In this augmented system, the system states includes the states of the original system in (5.14) and the filter states arising from (5.30). For both excitation types, the strain and stress response time histories $\underline{\varepsilon}_k$ and $\underline{\sigma}_k$, respectively, are simulated at all bar elements using the discrete state space formulation. The time discretization step used in simulating the sampled data is $\Delta t = 0.5 \times 10^{-3}$. The simulated strain and stress response time histories are the reference stress response time histories that are considered to be the exact stress response time histories for the excitations used. These response time histories and the corresponding power spectral densities are also used with the fatigue methodology in Section 2 to compute the damage accumulation and lifetime of the entire body of the structure due to fatigue. Such predictions constitute the reference (exact) predictions against which the predictions from the proposed Kalman filter approach should be compared to for assessing the accuracy of the proposed methodology.

For convenience, the set o is introduced that contains the bar element numbers where the strains are measured. The measured strain response time histories $\underline{y}_k = \underline{\varepsilon}_k^{(o)}$ are the components of the reference response time history vector $\underline{\varepsilon}_k$ associated with the bar element numbers identified in the set o. In practice, these measurements are collected using appropriate sensors such as strain gauges. Let p be the set that contains the bar element numbers where the stresses will be predicted. Herein, the set p is selected to be $p = \{1, \cdots, N+1\}$, i.e. it is assumed that stresses are predicted at all bar elements.

Results demonstrating the effectiveness of the proposed methodology are first presented for a five degree of freedom system ($N = 5$) shown in Figure 5.2. The nominal values of the nodal

masses are $m_1 = m_5 = 21$ Kg, $m_2 = m_4 = 15$ Kg and $m_3 = 12$ Kg. A uniform distribution of the properties of the bar elements is assumed resulting in uniform stiffness $k_i = k_0$, $i = 1, \cdots, N$. The nominal values of the stiffness properties are chosen so that $k_0 = E_0 A_0 / L_0$, where $E_0 = 2.1 \times 10^{11} N/m^2$, $A_0 = \pi (0.0035)^2 m^2$ and $L_0 = 0.3m$ are same for all bar elements. For the mass and bar properties selected, the nominal values of the natural frequencies of the five degree of freedom system are 110.0 Hz, 193.4 Hz and 277.0 Hz, 344.3 Hz, 425.3 Hz. The damping matrix C in the equations of motion (5.13) is chosen assuming that the system is classically damped. Specifically, the damping matrix C is selected so that the values of the modal damping ratios are 1% for all contributing modes. A single excitation is considered which is applied at node $\rho = 5$. The measured strain response time histories $\underline{y}_k = \underline{\varepsilon}_k^{(o)}$ at the bar elements identified by the set o are used to predict the stress response time histories at all bar elements identified in the set p using the proposed Kalman filter approach. These predictions depend on the values of the measurement noise covariance R in the Kalman filter formulation. Herein, the noise covariance matrix R is selected to be a diagonal matrix of the form $R = \eta^2 diag(\hat{Q}_{yy})$, where ε gives the level of the observation error and $diag(\hat{Q}_{yy})$ denotes the diagonal matrix formed from $\hat{Q}_{yy}$ after setting the non-diagonal terms to zero. In the numerical results that follow, the values of $\eta = 0.1\%$ and $\eta = 10\%$ are used which corresponds to very small and relatively large observation errors, respectively.

The simulated measurements and the reference fatigue predictions are first obtained for the Type I white noise excitation. For demonstration purposes, comparison between the reference (exact) stress power spectral density (PSD) simulated by the model and the estimated PSD from the Kalman filter (KF) are given in Figure 5.4 for the bar elements $p = \{2, 4, 6\}$, assuming that the measured strains are at bar elements $o = \{1, 2\}$. Results are presented for the case of relatively large model error ($s_i = 5\%$) in Figures 5.4a-b at bar elements 2 and 4 and for the case of zero model error ($s_i = 0$) in Figures 5.4c-d at bar elements 4 and 6. It can be seen in Figure 5.4a for the case of relatively large model error that the estimated PSDs of the stress at the bar element 2, where measurements are available, almost coincides with the corresponding reference stress PSDs simulated by the model. At the bar element 4, where measurements are not available, there is a discrepancy between the estimated and reference (exact) stress PSDs as shown in Figure 5.4b. For the case of relatively large model error, the discrepancies observed in Figure 5.4b are mainly due to the fact that the nominal model used for PSDs predictions from the Kalman filter approach differs from the reference model used to simulate the reference PSDs. The size of the discrepancies depends on the size of the model error. Specifically, these discrepancies are shown in Figure 5.4b for relatively large model error ($s_i = 5\%$) to be significantly higher than the discrepancies observed in Figure 5.4c for zero model error ($s_i = 0$). For zero model error, the discrepancies shown in Figure 5.4c and 4d for bar elements 4 and 6, respectively, are due to the estimation error associated with the Kalman filter. However, it should be noted that the predictions of the PSD from the Kalman filter approach are quite good,

especially for the high amplitudes around the resonance peaks which mainly contribute to the fatigue process.

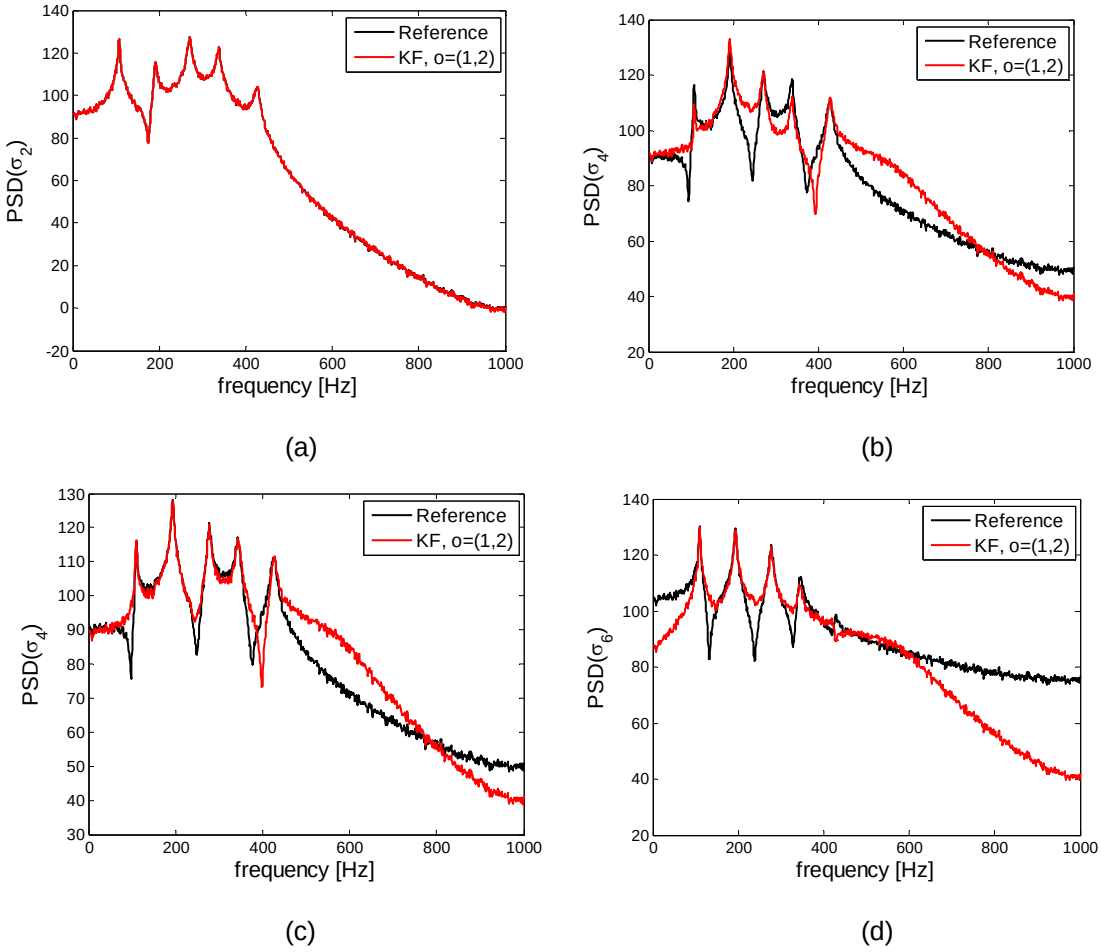

Figure 5.4: Comparison between reference and estimated from Kalman filter PSD of the stress response at bar elements 2, 4 and 6; (a,b) relatively large model error $s = 5\%$, (c,d) zero model error $s = 0\%$.

Lifetime predictions due to fatigue are next compared in Figures 5.5a-d for all six bar (spring) elements of the structure. The lifetime values in these figures are obtained using the fatigue prediction formula (5.5). For each bar element, there are six lifetime fatigue predictions. The first prediction is based on the reference time histories simulated by the reference model and it is used as the exact value against which to study the accuracy of the predictions from the proposed Kalman filter methodology. The other five fatigue-based lifetime estimates are the ones predicted by the methodologies based on the use of Kalman filter method and the nominal model to estimate the stress response time histories at all bar elements. To study the effect of the number and location of sensors on the accuracy of the predictions, the five fatigue lifetime estimates shown in Figures 5.5a to 5.5d correspond to the following five sensor configurations that differ from the number and location of sensors used: one sensor configuration $o = \{6\}$ involving one

sensor placed at location or bar element 6, two sensor configurations $o=\{1,2\}$ and $o=\{3,4\}$ each one involving two sensors placed at locations denoted in the set o, and two sensor configurations $o=\{1,2,3\}$ and $o=\{2,3,4\}$ each one involving three sensors. In order to study the effect of model error on the accuracy of the Kalman filter methodology, the results in Figures 5.5a-c are based on simulated measurements from the reference model chosen to involve zero ($s_i=0$), moderate ($s_i=2\%$) and relatively large ($s_i=5\%$) model error, while the observation error used for KF-based fatigue predictions is negligible ($\eta=0.1\%$). In order to study the effect of observation error in the accuracy of the Kalman filter methodology, the results in Figure 5.5d are based on simulated measurements from the reference model chosen to involve zero model error ($s_i=0$) and relatively large observation error ($\eta=10\%$) used for KF-based fatigue predictions.

It can be seen from the results for the fatigue predictions involving zero model error ($s_i=0$) shown in Figure 5.5a that the estimates based on the Kalman filter predictions are quite close to the reference fatigue values obtained from the actual (reference) response time histories. It also becomes clear that the accuracy of the Kalman filter predictions depend on the number and location of sensors in the structure. Specifically, the best predictions are obtained from one sensor placed at bar element 6. Similar accuracy in the predictions are obtained from the sensor configurations $o=\{3,4\}$ and $o=\{2,3,4\}$ involving two and three sensors. However, the sensor configurations $o=\{1,2\}$ and $o=\{1,2,3\}$ provide significantly less accurate predictions in the entire structure (all six bar elements) than the predictions provided by one sensor placed at location 6. Specifically, significant discrepancies between the reference and Kalman filter fatigue predictions from the sensor configurations $o=\{1,2\}$ and $o=\{1,2,3\}$ are observed in bar element 5 and 6. It becomes evident from the results in Figure 5.5a that the locations and number of sensors affect the accuracy of the fatigue lifetime predictions from the proposed Kalman filter approach. Optimal sensor location methodologies (Papadimitriou, 2004) may be advantageously used to obtain the most informative locations that give the best accuracy in the fatigue lifetime predictions with the least number of sensors.

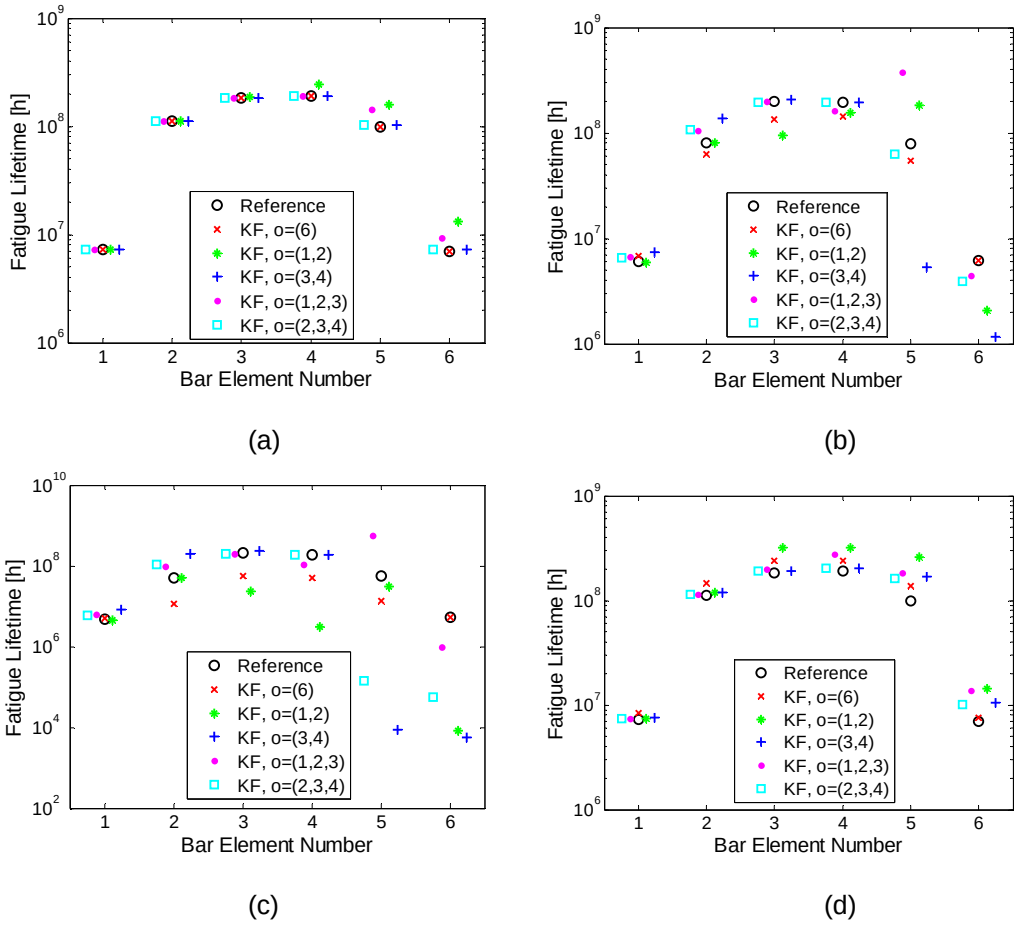

Figure 5.5: Comparison of reference fatigue-based lifetime estimates and the estimates predicted by the Kalman filter for the $N = 5$ DOF model as a function of the number and location of sensors.

(a) $s_i = 0$, $\eta = 0$, (b) $s_i = 2\%$, $\eta = 0$, (c) $s_i = 5\%$, $\eta = 0$, and (d) $s_i = 0$, $\eta = 10\%$.

Comparing the results in Figures 5.5a, 5.5b and 5.5c corresponding to zero ($s_i = 0$), moderate ($s_i = 2\%$) and larger ($s_i = 4\%$) model errors, it is evident that the size of model error affects the accuracy of the fatigue prediction provided by the proposed Kalman filter methodology. For a fixed sensor configuration, the accuracy of the fatigue predictions obtained from the Kalman filter methodology deteriorates as the size of the model error increases. Moreover, the accuracy of the predictions depends highly on the number and location of sensors. There are optimal sensor locations which give the most accurate fatigue predictions. Specifically, the most accurate predictions in the entire structure for the case of moderate model error ($s_i = 2\%$) are obtained from sensor configurations $o = \{6\}$ and $o = \{2,3,4\}$ involving one and three sensors, respectively. For the case of larger model error ($s_i = 5\%$), the most accurate predictions in the entire structure (all bar elements) are obtained from sensor configurations $o = \{6\}$ involving one sensor, followed by the predictions provided by the sensor configuration $o = \{1,2,3\}$ involving three sensors.

The effect of measurement error on the fatigue predictions provided by the Kalman filter approach is next considered by comparing the results in Figure 5.5d obtained for relatively large observation error of the order of $\eta = 10\%$ with the results in Figures 5.5a-c obtained for very small ($\eta = 0.1\%$) observation error. It can be seen that the accuracy of the fatigue predictions is less sensitive to the magnitude of the observation error than it is to the magnitude of the model error. In addition, the accuracy of the fatigue lifetime predictions provided by the Kalman filter for the different sensor configurations observed in Figure 5.5d for zero model error and significant observation error ($\eta = 10\%$) does not significantly deteriorate as compared to the accuracy of the predictions observed in Figure 5.5a provided by the methodology for zero model error and very small ($\eta = 0.1\%$) observation error.

Next, results are also presented for simulated measurements generated from the Type II filtered white noise excitation. In this case, one examines the effect of the characteristics of the excitation on the accuracy of the proposed methodology. As before, the excitations is applied at node $\rho = 5$. Figure 5.6 compares the reference fatigue estimates and the fatigue predictions provided by the Kalman filter methodology for three different excitation characteristics: broadband excitation corresponding to values $\omega_f = 200Hz$ and $\zeta_f = 0.4$ (Figure 5.6a), and two lightly damped excitations ($\zeta_f = 0.02$) with resonant frequencies close to the first, $\omega_f = \omega_1 \approx 110Hz$ (Figure 5.6b), and third $\omega_f = \omega_3 \approx 277Hz$ (Figure 5.6c), natural frequency of the structure. All results shown in Figures 5.6a-c are based on simulated measurements that involve zero model error ($s_i = 0$) and negligible measurement error $\eta = 0.1\%$. The results in Figure 5.6d are based on large model error ($s_i = 5\%$) and for the lightly damped excitation ($\zeta_f = 0.02$) with resonant frequency close to the third $\omega_f = \omega_3 \approx 277Hz$ natural frequency of the structure. All filtered white noise excitations correspond to the same variance. Given the values of ω_f and ζ_f, this is achieved by selecting appropriately the intensity of the white noise $n(t)$ so that the output $u(t)$ in (5.31) has the desired value of variance.

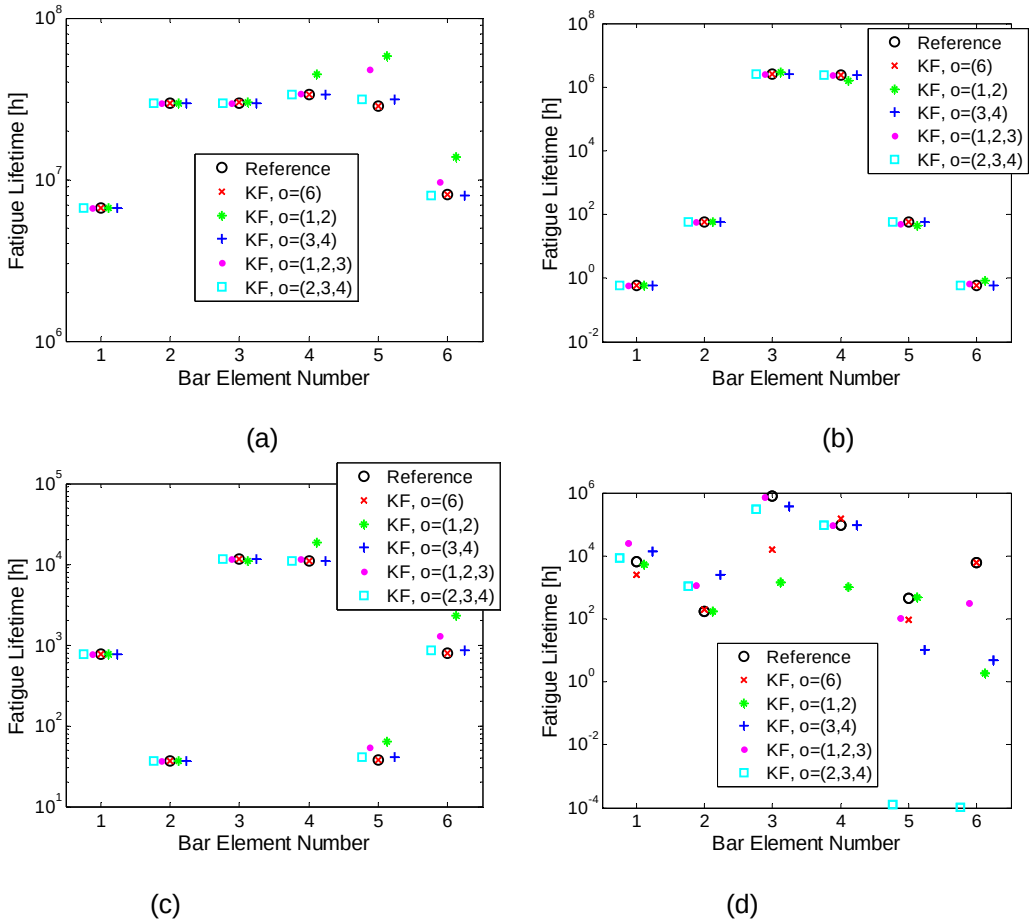

Figure 5.6: Comparison of reference fatigue-based lifetime estimates and the estimates predicted by the Kalman filter for the $N = 5$ DOF model as a function of the number and location of sensors.

(a) $\omega_f = 200Hz$, $\zeta_f = 0.4$, $s_i = 0$, (b) $\omega_f = \omega_1 \approx 110Hz$, $\zeta_f = 0.02$, $s_i = 0$, (c) $\omega_f = \omega_3 \approx 277Hz$, $\zeta_f = 0.02$, $s_i = 0$, and (d) $\omega_f = \omega_3 \approx 277Hz$ and $\zeta_f = 0.02$, $s_i = 5\%$.

It is clear in Figures 5.6a-c that for the case of zero model error the Kalman filter methodology gives very good predictions for a variety of excitation characteristics, including broad-band and lightly-damped excitations. As before, the accuracy of the predictions depends on the number and location of sensors. The most accurate predictions are obtained from the sensor configuration $o = \{6\}$ involving one sensor placed at location (bar element) 6, followed by the sensor configurations $o = \{3,4\}$ and $o = \{2,3,4\}$ involving two and three sensors. Less accurate predictions are obtained form the sensor configurations $o = \{1,2\}$ and $o = \{1,2,3\}$ involving two and three sensors, respectively. Obviously, optimizing the sensor placement in the structure can significantly improve the accuracy of the fatigue lifetime predictions provided by the Kalman filter methodology. Comparing the fatigue prediction results given in Figure 5.6d for large model error $s_i = 5\%$ to the fatigue prediction results in Figure 5.6c for zero model error, it is clear that the accuracy of the predictions from the Kalman filter methodology deteriorates as the model

error increases. Sensor configuration $o = \{6\}$ involving one sensor provides predictions with the best accuracy compared to the predictions provided by all other sensor configurations used in Figure 5.6.

For the two lightly damped excitations shown in Figures 5.6b and 5.6c, it is observed that the fatigue at each bar element depends on the mode excited. For the excitation with dominant frequency close to the first natural frequency (Figure 5.6b), the structure responds mainly to its first mode and the strains levels due to vibration, depending on the derivatives of the modeshape, are higher at bar elements 1 and 6, while due to symmetry they are lower at the middle bar elements 3 and 4. Consequently, the bar elements 1 and 6 are expected to have significantly less fatigue lifetime while the middle bar elements 3 and 4 are expected to have high fatigue lifetime, which is consistent with the results observed in Figure 5.6b. For the excitation with dominant frequency close to the third natural frequency, the structure respond mainly with its third mode and therefore high strain values are expected also to occur at internal bar elements 2 and 5, while due to symmetry the strains at the middle elements 3 and 4 are expected to be small. This is consistent with the small fatigue lifetime values predicted for the bar elements 2 and 5, and the high fatigue lifetime values predicted for the middle bar elements 3 and 4, as shown in Figure 5.6c.

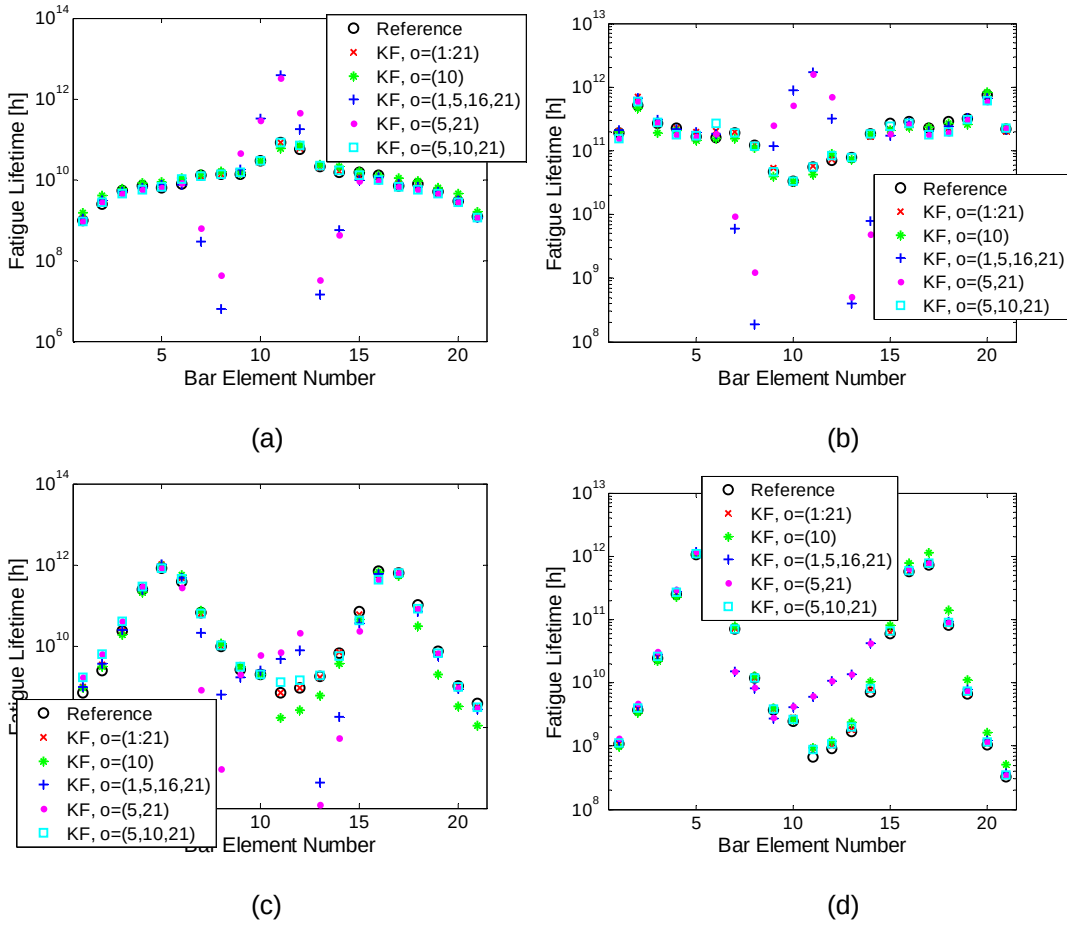

Figure 5.7: Comparison of reference fatigue-based lifetime estimates and the estimates predicted by the Kalman filter for the $N = 20$ DOF model as a function of the number and location of sensors.

(a) white noise, $s_i = 2\%$, $\eta = 0.1\%$, (b) $\omega_f = 110Hz$, $\zeta_f = 0.6$, $s_i = 2\%$, $\eta = 0.1\%$, (c) $\omega_f = \omega_2 \approx 44Hz$, $\zeta_f = 0.02$, $s_i = 2\%$, $\eta = 0.1\%$, (d) $\omega_f = \omega_2 \approx 44Hz$, $\zeta_f = 0.02$, $s_i = 0\%$, $\eta = 10\%$.

Finally, results demonstrating the effectiveness of the proposed methodology are presented for a twenty degree of freedom system ($N = 20$) shown in Figure 5.2. The nodal masses are assumed to be the same, i.e. $m_i = m_0$, $i = 1, \cdots, N$. A uniform distribution of the properties of the bar elements is also assumed resulting in uniform stiffness $k_i = k_0$, $i = 1, \cdots, N$. The nominal values of the mass and stiffness properties are chosen so that $m_0 = 30$ Kg and $k_0 = E_0 A_0 / L_0$, where $E_0 = 2.1 \times 10^{11} N/m^2$, $A_0 = \pi (0.0035)^2 m^2$ and $L_0 = 0.3m$ are same for all bar elements. For the mass and bar properties selected, the nominal values of the natural frequencies of the twenty degree of freedom system range from 22.5 Hz (minimum) to 300.8 Hz (maximum). The structure is subjected to either Type I stationary white noise excitation or Type II non-white excitation applied at node $\rho = 10$, with constant spectral density matrix equal to

$S_{\underline{u}} = S_0 = 10$. The strain response time histories $\underline{y}_k = \underline{\varepsilon}_k^{(o)}$ at the measured DOFs are used to predict the stress response time histories at all bar elements identified in the set $p = \{1, \cdots, 21\}$ using the Kalman filter approach.

Lifetime predictions due to fatigue are shown in Figure 5.7 for all twenty one bar (spring) elements of the structure. For each bar element, there are six lifetime fatigue predictions. The first prediction is based on the reference time histories simulated by the reference model and it is used as the exact value against which to study the accuracy of the predictions from the proposed Kalman filter methodology. The second fatigue lifetime prediction is based on the use of Kalman filter method and the nominal model using sensors at all 21 bar elements. This second prediction uses measurements from all 21 bar elements and thus represents the most accurate results that can be obtained from the Kalman filter methodology. The other four fatigue-based lifetime estimates are the ones predicted by the methodologies based on the use of Kalman filter method and the nominal model to estimate the stress response time histories at all bar elements using a limited number of sensors. To study the effect of the number and location of sensors on the accuracy of the predictions, the four fatigue lifetime estimates shown in Figures 5.7a to 5.7d in the entire structure (all 21 bar elements) correspond to the following four sensor configurations that differ from the number and location of sensors used: one sensor configuration $o = \{10\}$ involving one sensor placed at location or bar element 10, one sensor configuration $o = \{5, 21\}$ involving two sensors placed at locations 5 and 21, one sensor configuration $o = \{5, 10, 21\}$ involving three sensors, and one sensor configuration $o = \{1, 5, 16, 21\}$ involving four sensors. Figure 5.7a compares results for white noise excitation, Figure 5.7b compares results for broadband filtered white noise excitation ($\omega_f = 110Hz$, $\zeta_f = 0.6$), while Figures 5.7c-d compare results for lightly damped filtered white noise excitations ($\zeta_f = 0.02$) with dominant frequency close to the second natural frequency of the structure ($\omega_f = \omega_2 \approx 44Hz$). Predictions in Figure 5.7a-c correspond to moderate model error ($s_i = 2\%$) and very small observation error ($\eta = 0.1\%$). In order to study the effect of observation error in the accuracy of the Kalman filter methodology, predictions in Figure 5.7d correspond to zero model error ($s_i = 0\%$) and large observation error ($\eta = 10\%$).

It can be seen that despite the moderate model error considered in Figures 5.7a-c and the large measurement error considered in Figure 5.7d, the fatigue lifetime prediction values provided by the Kalman filter approach for a full sensor configuration involving 21 sensors installed in all 21 bar elements are quite close to the reference fatigue lifetime values. For given excitation case, it becomes clear that the accuracy of the fatigue lifetime predictions based on the Kalman filter approach using fewer than 21 sensors depend on the number and location of sensors in the structure. Specifically, the best predictions are obtained from the sensor configurations $o = \{10\}$ involving one sensor located at element 10 and the sensor configuration $o = \{5, 10, 21\}$ involving three sensors located at elements 5, 10 and 21. Such predictions are quite close to the reference fatigue values obtained from the actual (reference) response time histories and to the Kalman filter prediction provided by a full sensor configuration involving 21 sensors. It should be noted that the sensor configuration $o = \{5, 10, 21\}$ gives slightly better fatigue lifetime prediction

accuracy at all 21 bar elements than the sensor configuration $o=\{10\}$. This is due to the fact that the sensor configuration $o=\{5,10,21\}$ contains the sensor configuration $o=\{10\}$ and in addition it involves two extra sensors that provide additional information for reconstructing more accurately the response at unmeasured locations. However, the sensor configurations $o=\{5,21\}$ and $o=\{1,5,16,21\}$ involving two and four sensors, respectively, provide significantly less accurate predictions, especially at the bar elements 7 to 14, than the predictions provided by the sensor configurations $o=\{10\}$ and $o=\{5,10,21\}$ involving one and three sensors, respectively. It thus becomes evident from the results in Figure 5.7 that the location and number of sensors affect the accuracy of the fatigue lifetime predictions. Optimal sensor location strategies (Papadimitriou, 2004) may be advantageously used to obtain the most informative locations that give the best accuracy in the fatigue lifetime predictions with the least number of sensors.

The relative importance of the model and measurement error on the accuracy of the fatigue predictions provided by the Kalman filter is investigated by comparing the results in Figure 5.7d obtained for relatively large observation error of the order of $\eta=10\%$ and zero model error with the results in Figures 5.7c obtained for very small ($\eta=0.1\%$) observation error and moderate model error ($s_i=2\%$). It can be seen from these figures that the accuracy of the fatigue predictions are less sensitive to the size of the observation error. Specifically, the accuracy of the fatigue lifetime predictions provided by the Kalman filter for the different sensor configurations observed in Figure 5.7d for zero model error and significant observation error ($\eta=10\%$) does not significantly deteriorate as compared to the accuracy of the predictions observed in Figure 5.7c provided by the methodology for moderate model error ($s_i=2\%$) and very small observation error ($\eta=0.1\%$).

5.5 Conclusions

A methodology for estimating damage due to fatigue on the entire body of a structure using spectral methods and output only vibration measurements at a limited number of locations was presented. The fatigue predictions presented in this work were illustrated for structural members subjected to a uni-axial stress state. These predictions can be extended using available methods (You and Lee, 1996; Pitoiset and. Preumont, 2000) to structural members subjected to multi-axial stress state. Using the available response time history measurements and a model of the structure, a Kalman filter approach was used for predicting the power spectral densities of the stresses in the entire body of the structure needed in the spectral based fatigue prediction methodology. These power spectral density predictions were used to construct fatigue accumulation and lifetime prediction maps consistent with measurements provided by a monitoring system. Simulated measurements from a spring-mass chain-like structure suggest that the proposed methodology for lifetime fatigue prediction provide sufficiently accurate estimates even for the cases where the broadband assumptions of the stochastic excitation processes are violated. In particular, systematic numerical studies have demonstrated that the

accuracy of the proposed methodology depend on the size of the model and observation errors, as well as the number and location of sensors.

Chapter 6

Structural identification of an experimental vehicle model using measured modal characteristics

6.1 Introduction

In the present chapter, methods for modal identification and structural model updating are employed to develop high fidelity finite element models of an experimental vehicle model using acceleration measurements. The identification of modal characteristics of the vehicle is based on acceleration time histories obtained from impulse hammer tests. Modal identification methodologies are used to obtain the modal characteristics from the analysis of the various sets of vibration measurements. The modal characteristics are then used to update an increasingly complex set of finite element models of the vehicle. The multi-objective structural identification method developed in Chapter 4 is used for estimating the parameters of the finite element structural models based on minimizing the modal residuals.

The chapter is organized as follows. In Section 6.2 the description of the laboratory vehicle model and the available experimental configuration is presented. Modal identification methodologies are applied in Section 6.3 to identify the modal properties (modal frequencies, modal damping rations and modeshapes) of the laboratory vehicle structure using vibration measurements obtained from hammer tests. In Section 6.4 the proposed model updating methodologies in Chapter 4 are applied for updating a class of finite element models of the vehicle, demonstrating the applicability of the proposed model updating methods and the prediction accuracy of the Pareto optimal models.

6.2 Description of the laboratory vehicle structure and instrumentation

The vehicle structure, shown in Figure 6.1, is housed at the Machine Dynamics Laboratory of the Department of Mechanical Engineering in Aristotle University. Figure 6.2 also shows an overview of the experimental set up. In particular, the mechanical system tested consists of a frame substructure (parts with red, gray and black color), simulating the frame of a vehicle. The main experimental instruments used for performing the experimental measurements include the following:

- accelerometers Piezobeam 8632C10, 8690C10, 8634B5 and K-beam 8312A2 from Kistler Instrumente AG,
- load cell type 9712B250 from Kistler Instrumente AG,
- impulse force hammer type 9724A5000 from Kistler Instrumente AG,
- analog to digital converter cards, PCI -4551, PCI -4552 Dynamic signal acquisition and PCI-6552 E-series from National Instruments,
- data acquisition and signal processing software.

More details can be found in Giagopoulos and Natsiavas (2007).

Figure 6.2 presents details and the geometrical dimensions of the frame subsystem alone. The frame substructure is made of steel with Young's modulus $E = 2.1 \times 10^{11}\, N/m^2$, Poison's ratio $\nu = 0.3$ and density $\rho = 7850\, kg/m^3$. Moreover, the measurement points are indicated in Figure 6.3. Measurements are collected from 72 locations. Sensor locations have been chosen in such a way so as to gather as much information as possible about the structure's modal response.

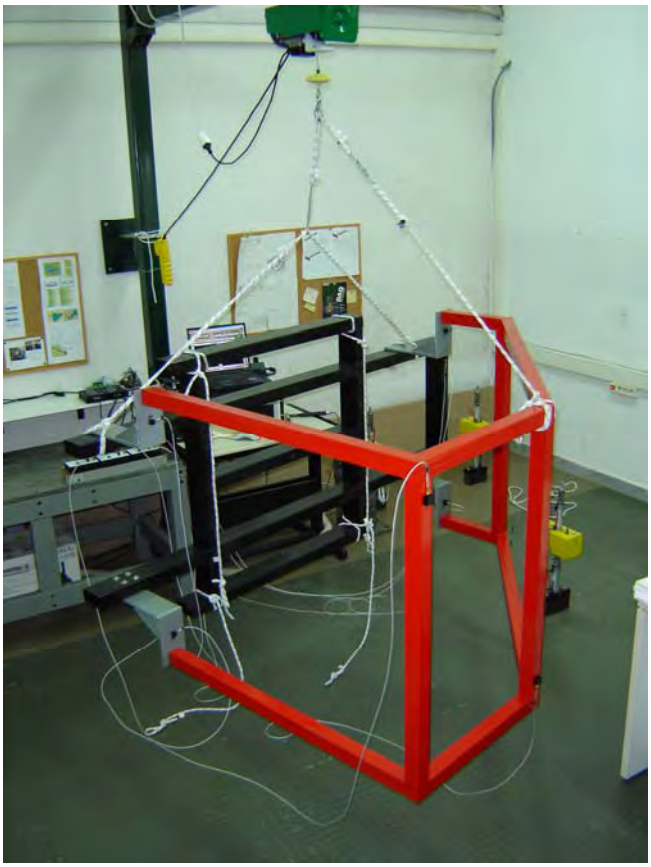

Figure 6.1: Scaled vehicle model and experimental set up.

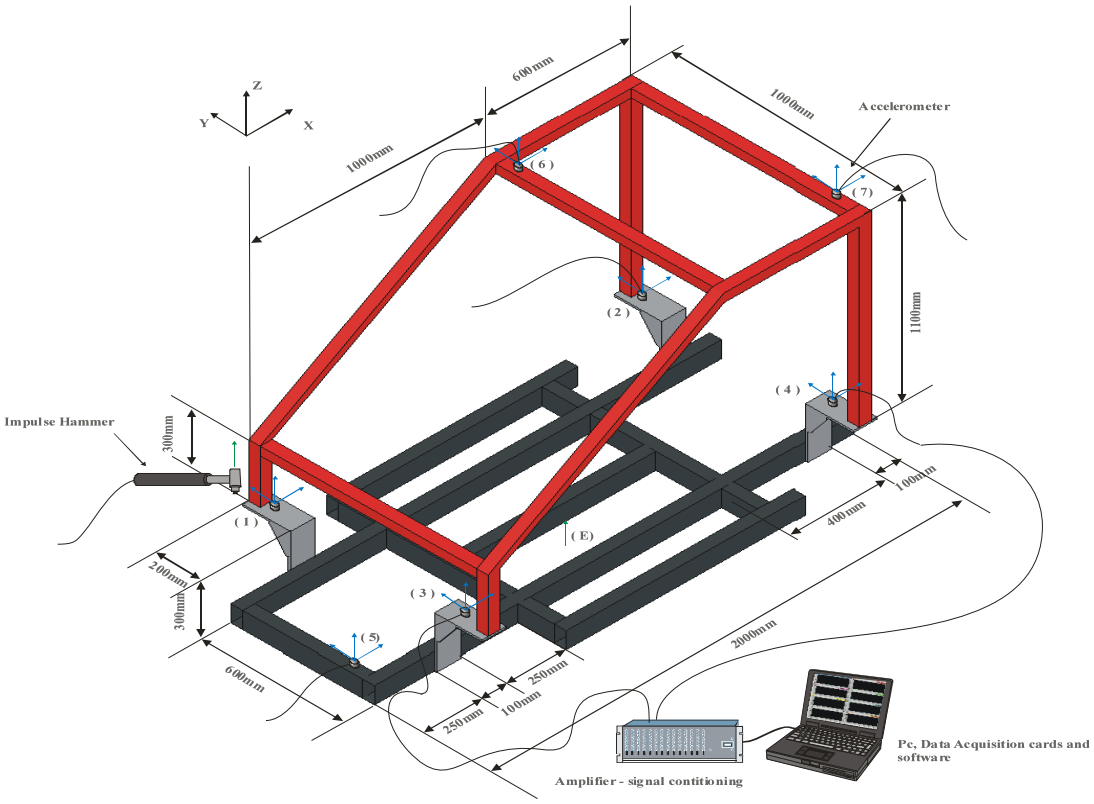

Figure 6.2: Dimensions of the frame substructure.

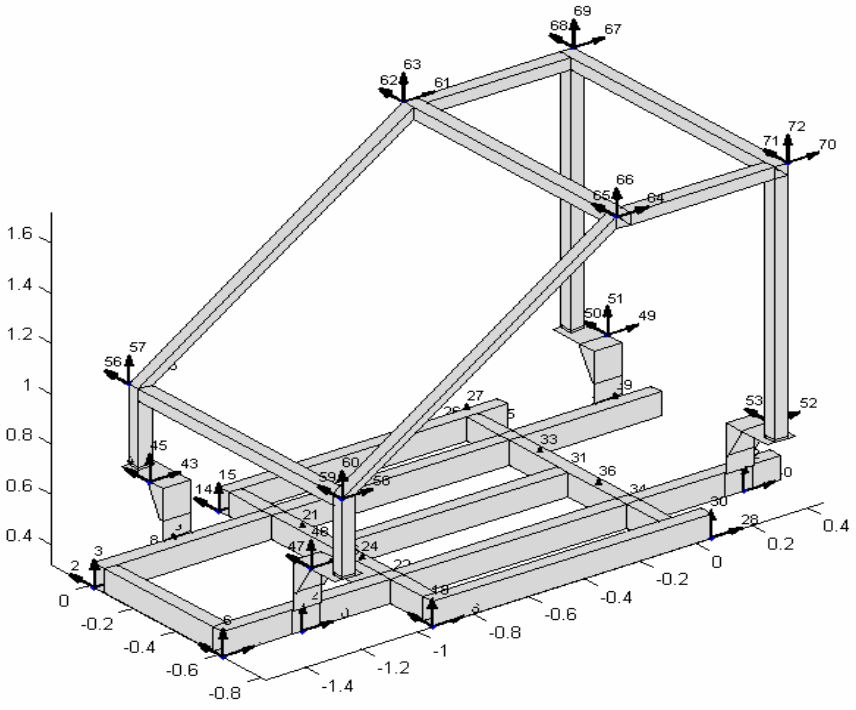

Figure 6.3: Measurement points on the frame substructure.

6.3 Modal identification

Using the available acceleration sensors to measure the vibrations induced by an applied impulse force, the frequency response functions (FRF) of the measured DOFs are estimated. These frequency response functions are used to estimate the modal properties using the Modal Identification Tool (MITooL) (Ntotsios 2009) developed by the System Dynamics Laboratory in University of Thessaly. The values of the modal frequencies, modal damping ratios, modeshape components and modal participation factors were estimated from the software in the 0 to 200 Hz frequency bandwidth. Figures 6.4, 6.5 and 6.6 compare the measured FRFs with the FRFs predicted by the identified optimal modal model for three representative sensors referred to as sensor 70, 71 and 72 respectively as shown in Figure 6.3. As it is seen a high modal density modal model is obtained. Moreover, the fit of the measured FRF is very good which validates the effectiveness of the modal identification software.

The identified values of the modal frequencies and the modal damping ratios are reported in Table 6.1. Twenty three modes were clearly identified in the frequency range 0 to 200 Hz with values of modal damping ratios of the order of 0.1% to 0.5%, which correspond to low relatively damping values. The identified modeshapes have also been recorded so that they can be used for updating the finite element models.

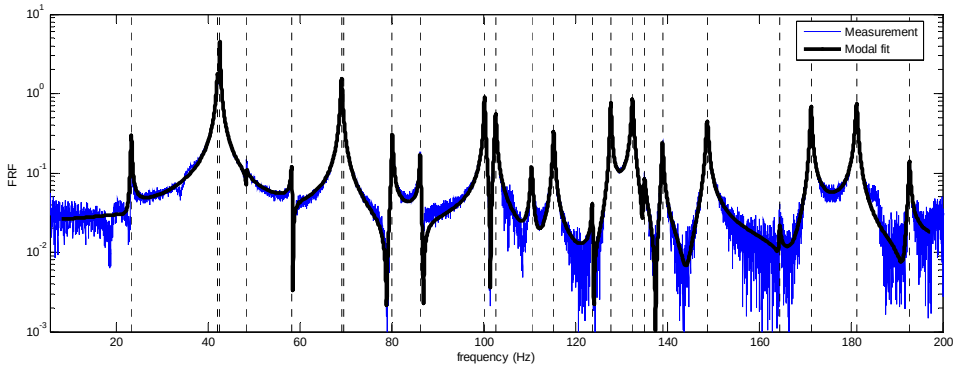

Figure 6.4: Comparison between measured and optimal modal model predicted FRF for sensor 70.

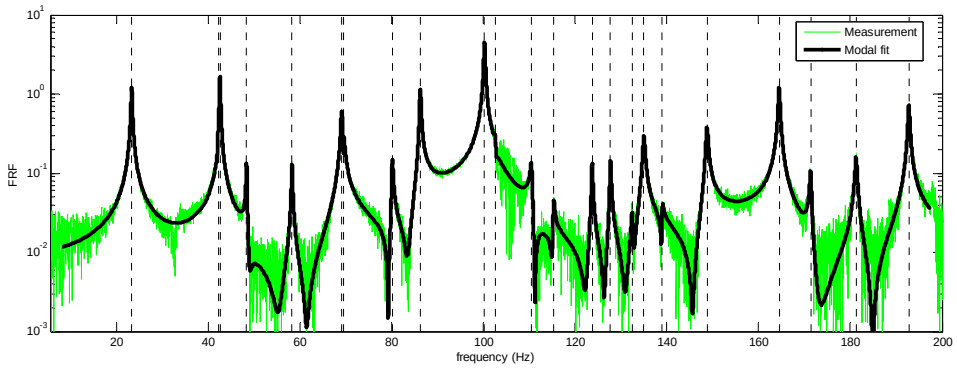

Figure 6.5: Comparison between measured and optimal modal model predicted FRF for sensor 71.

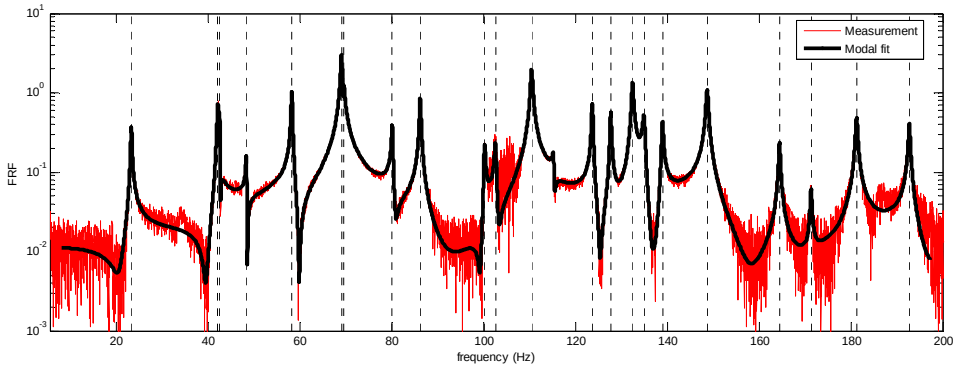

Figure 6.6: Comparison between measured and optimal modal model predicted FRF for sensor 72.

Table 6.1: Identified and nominal FE model predicted modal frequencies and damping ratios.

Mode	Identified Modal Frequency (Hz)	Identified Modal Damping Ratio (%)	Nominal FEM Predicted Frequency (Hz)	Difference between Identified and FE Predicted Modal Frequencies (%)	MAC between Identified & FE Predicted Modeshapes
1	23.2139	0.4799	23.2348	0.0902	0.9430
2	42.1225	0.3611	39.1265	-7.1126	0.9539
3	42.5020	0.2263	41.6084	-2.1024	0.9590
4	48.2753	0.2218	47.2930	-2.0349	0.9460
5	58.1552	0.1954	57.5692	-1.0077	0.9039
6	69.0429	0.2287	66.2020	0.0151	0.9503
7	69.4700	0.1662	69.0533	-4.7042	0.9030
8	80.0413	0.1651	80.4391	0.4969	0.9022
9	86.1449	0.1564	83.2491	-3.3615	0.9375
10	100.2428	0.1141	101.6080	1.3619	0.9585
11	102.5815	0.1714	105.9357	3.2701	0.9313
12	110.4424	0.1838	106.6243	-3.4572	0.7347
13	115.1205	0.1519	112.5407	-2.2409	0.8288
14	123.6425	0.0982	129.0741	4.3930	0.8474
15	127.6472	0.0977	121.7747	-4.6006	0.7592
16	132.4204	0.1347	131.7794	-0.4841	0.7743
17	134.9544	0.1673	133.8787	-0.7970	0.7532
18	138.9425	0.1066	137.3287	-1.1615	0.6472
19	148.6929	0.1474	146.5237	-1.4590	0.8077
20	164.3888	0.1026	160.8531	-2.1497	0.8351
21	171.3352	0.0898	155.7296	-9.1082	0.7465
22	181.2229	0.1197	169.1026	-6.6874	0.6299
23	192.7520	0.0819	193.9090	0.5995	0.8080

6.4 Updating of finite element vehicle models

Detailed finite element models were created that correspond to the model used for the design of the experimental vehicle. The structure was first designed in CAD environment and then imported in COMSOL Multiphysics (COMSOL, 2005) finite element modelling environment. The models were constructed based on the geometric details and the material properties of the structure. The finite element models for the vehicle were created using three-dimensional triangular shell finite elements to model the whole structure.

In order to investigate the sensitivity of the model error due to the finite element discretization, several models were created increasing the size of the elements in the finite element mesh. The resulted twelve finite element models consist of 886 to 44985 triangular shell elements corresponding to 2622 to 136074 DOF. The convergence in the first eleven modal frequencies predicted by the finite element models with respect to the number of models DOF is given in Figure 6.7. According to the results in Figure 6.7, a model of 15202 finite elements having 45564 DOF was chosen for the adequate modelling of the experimental vehicle. This model is shown in Figure 6.8 and for comparison purposes, Table 6.1 lists the values of the modal frequencies predicted by the nominal finite element models along with the percentage error between the identified and the nominal finite element model predicted modal frequencies. Also, Table 6.1 reports the MAC values between the identified and the nominal finite element model predicted modeshapes. Comparing with the identified modal frequency values it can be seen that, with the exception of the modes 21 and 22, the nominal FEM-based modal frequencies are fairly close to the experimental ones. Ten representative modeshapes predicted by the nominal finite element model for the ten lower frequency modes are shown in Figures 6.9 to 6.18.

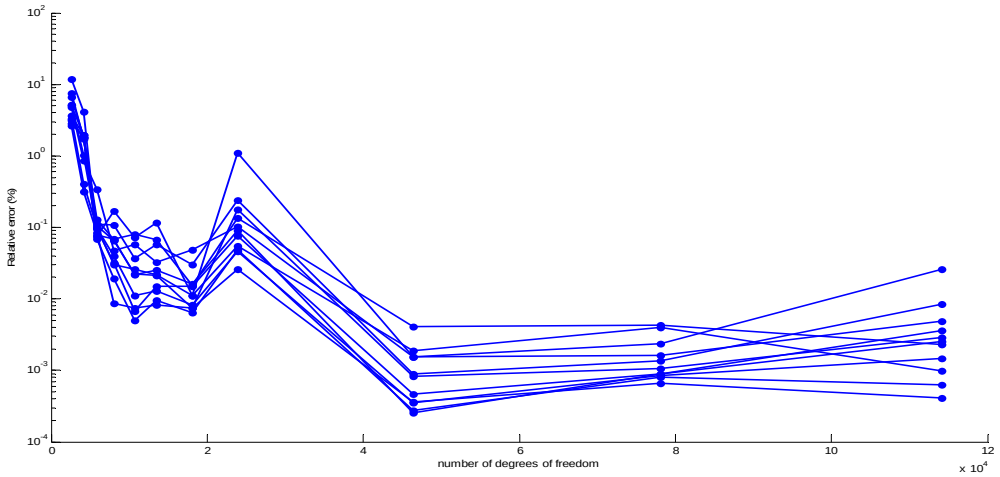

Figure 6.7: Relative error of the modal frequencies predicted by the finite element models with respect to the models' number of degrees of freedom.

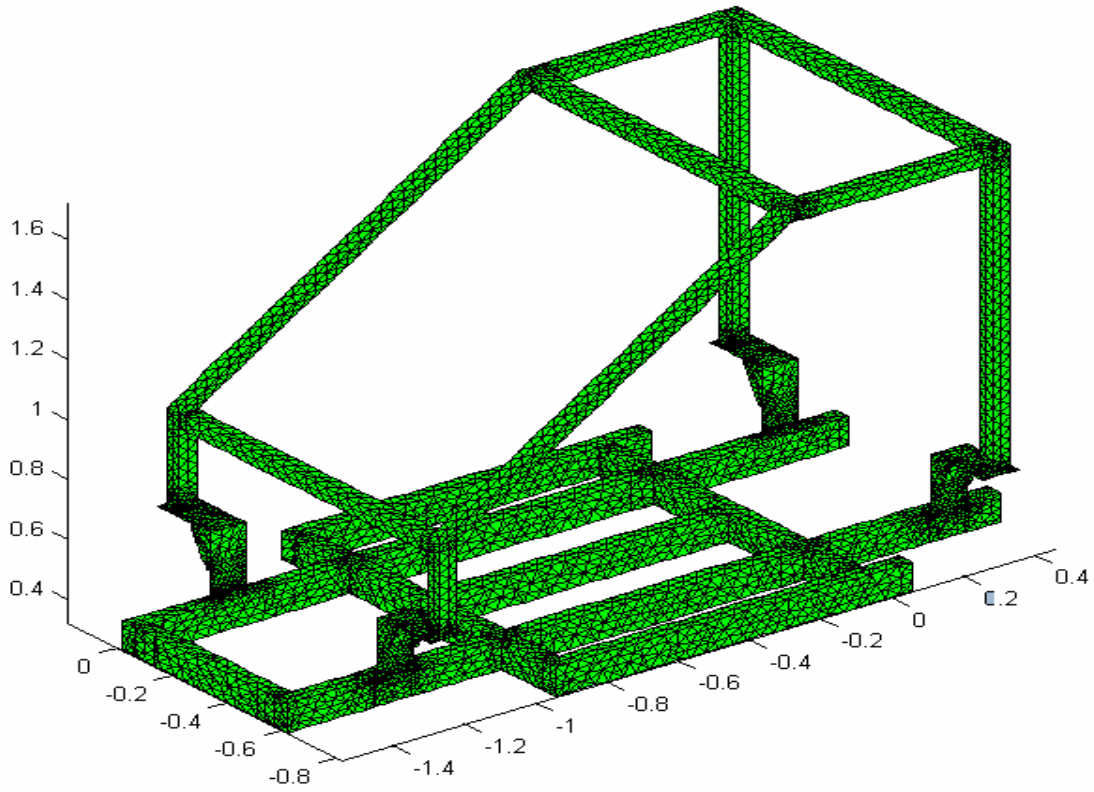

Figure 6.8: Finite element model of the experimental vehicle consisted of 15202 triangular shell elements and 45564 DOF.

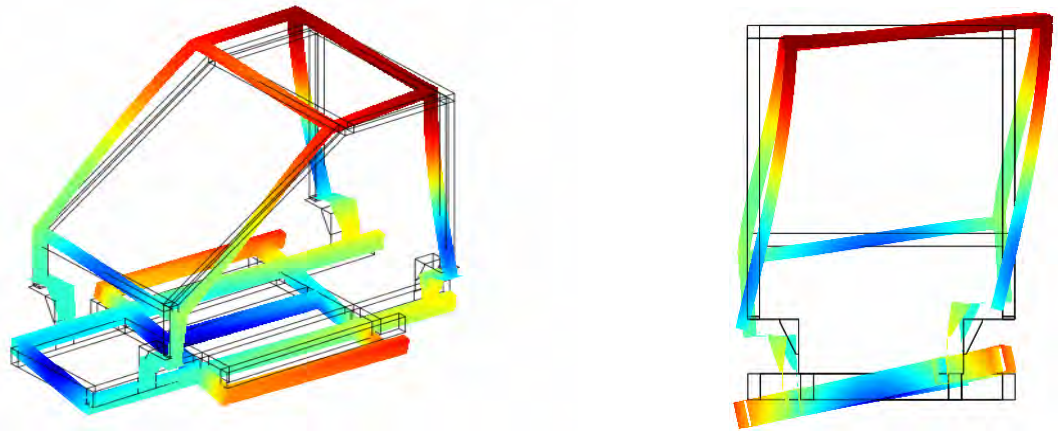

Figure 6.9: Modeshape predicted by the finite element model for the first mode at 23.23 Hz.

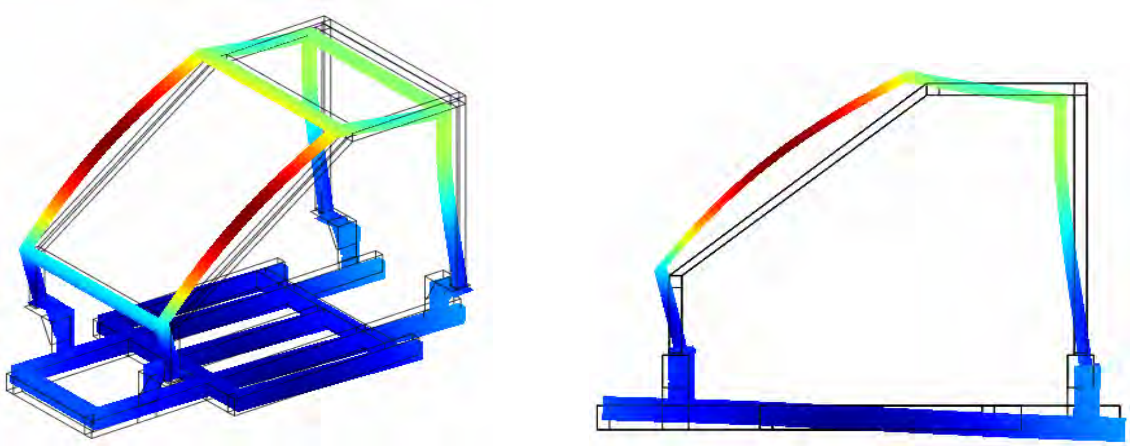

Figure 6.10: Modeshape predicted by the finite element model for the second mode at 39.13 Hz.

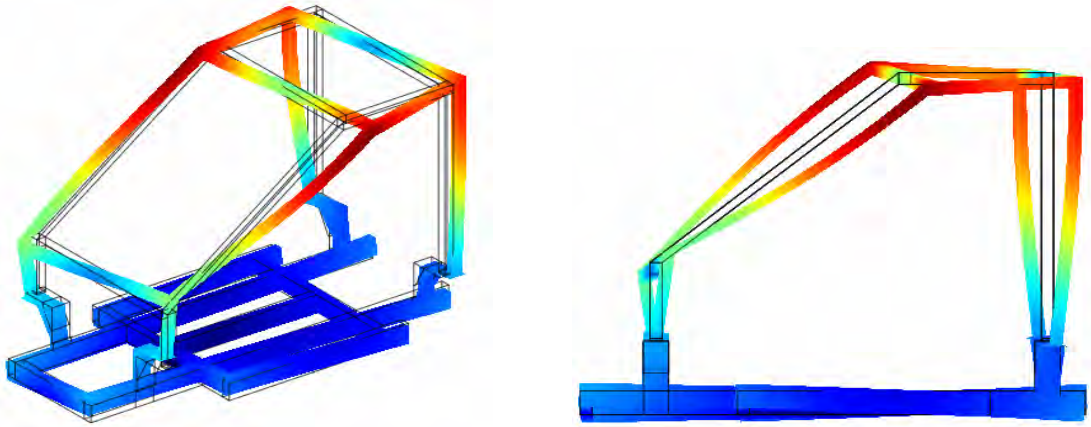

Figure 6.11: Modeshape predicted by the finite element model for the third mode at 41.61 Hz.

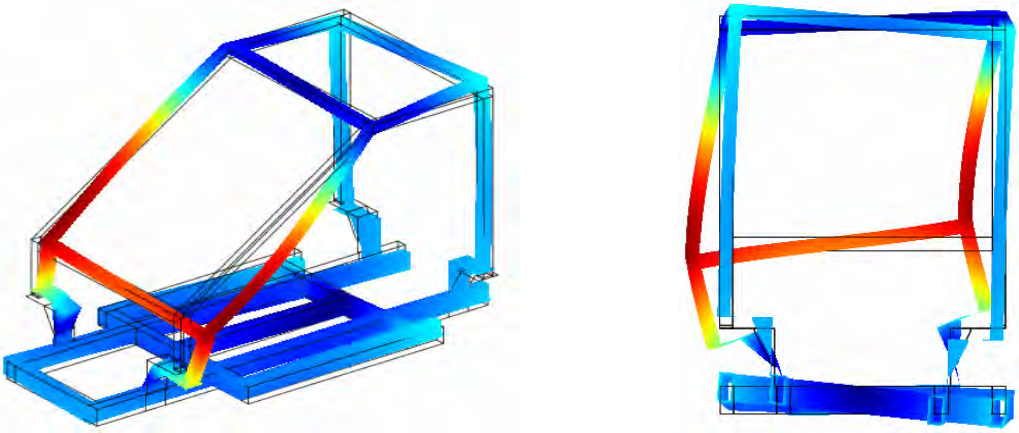

Figure 6.12: Modeshape predicted by the finite element model for the fourth mode at 47.29 Hz.

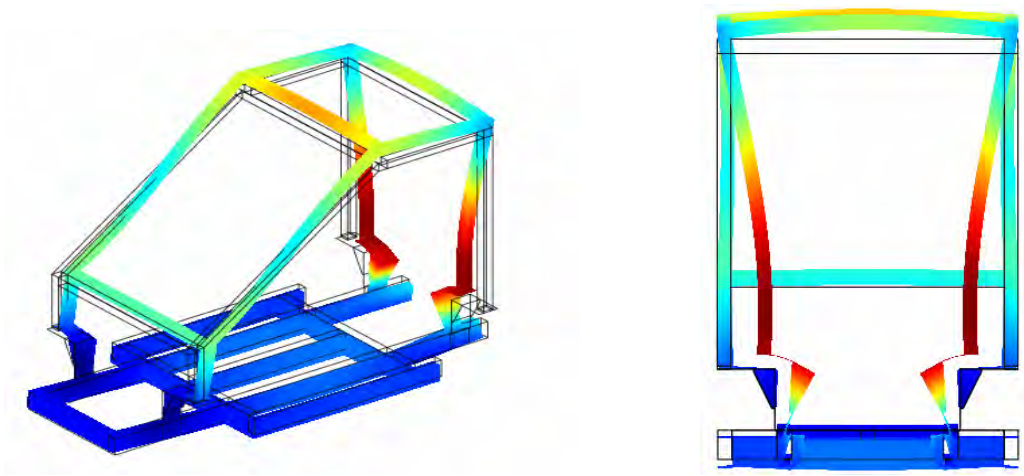

Figure 6.13: Modeshape predicted by the finite element model for the fifth mode at 57.57 Hz.

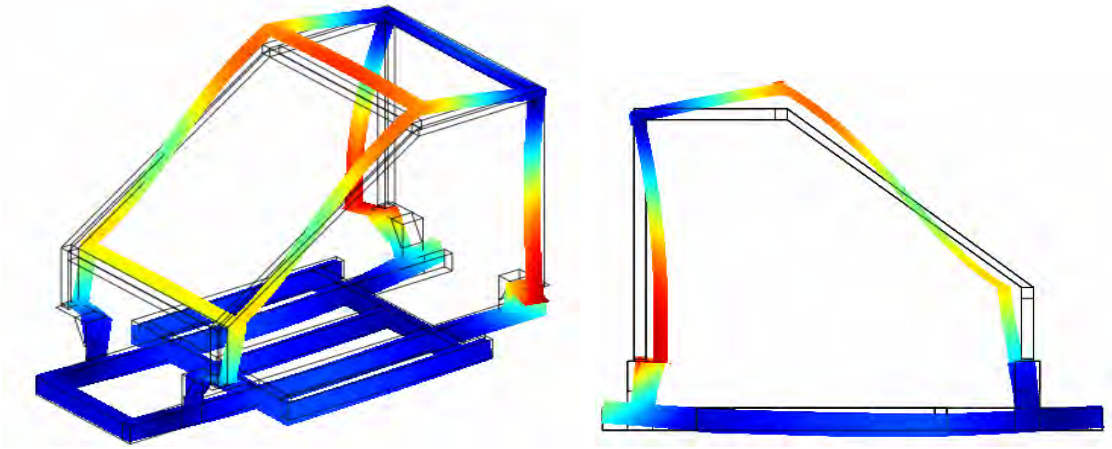

Figure 6.14: Modeshape predicted by the finite element model for the sixth mode at 66.20 Hz.

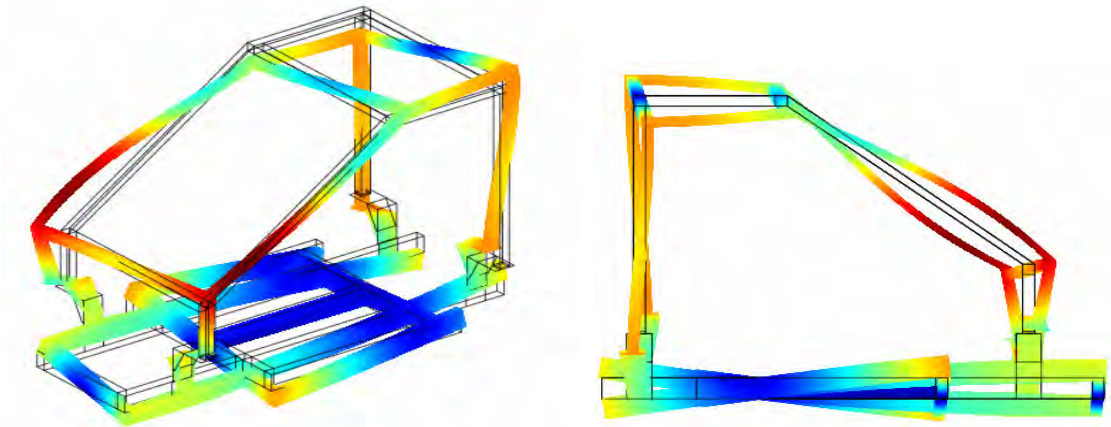

Figure 6.15: Modeshape predicted by the finite element model for the seventh mode at 69.05 Hz.

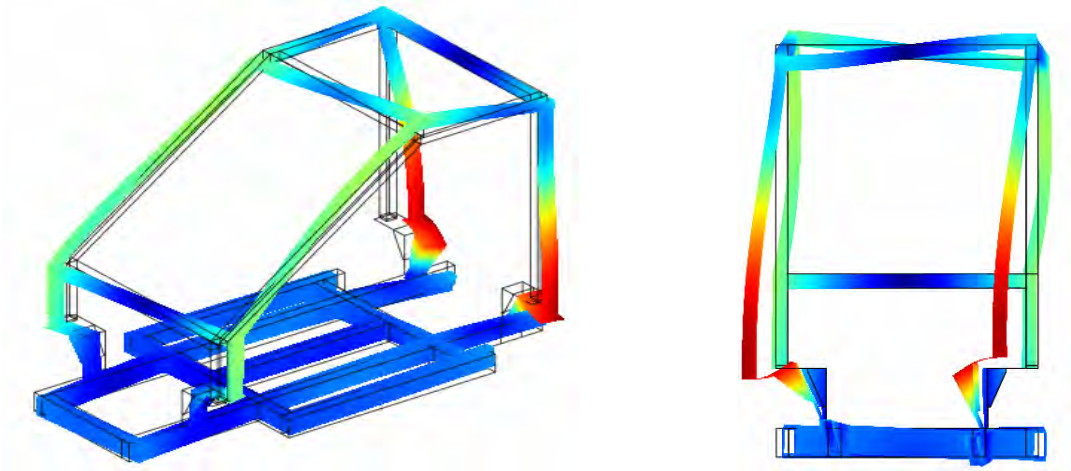

Figure 6.16: Modeshape predicted by the finite element model for the eight mode at 80.44 Hz.

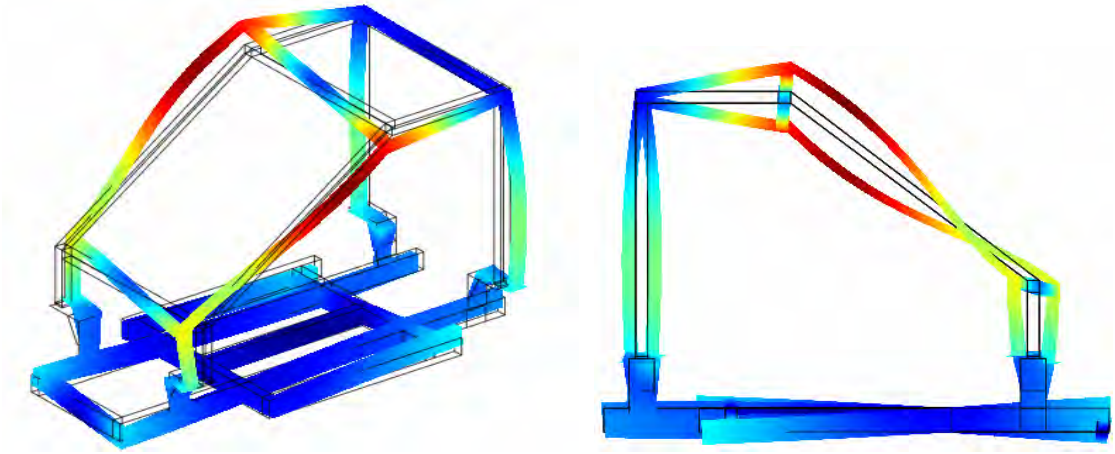

Figure 6.17: Modeshape predicted by the finite element model for the ninth mode at 83.25 Hz.

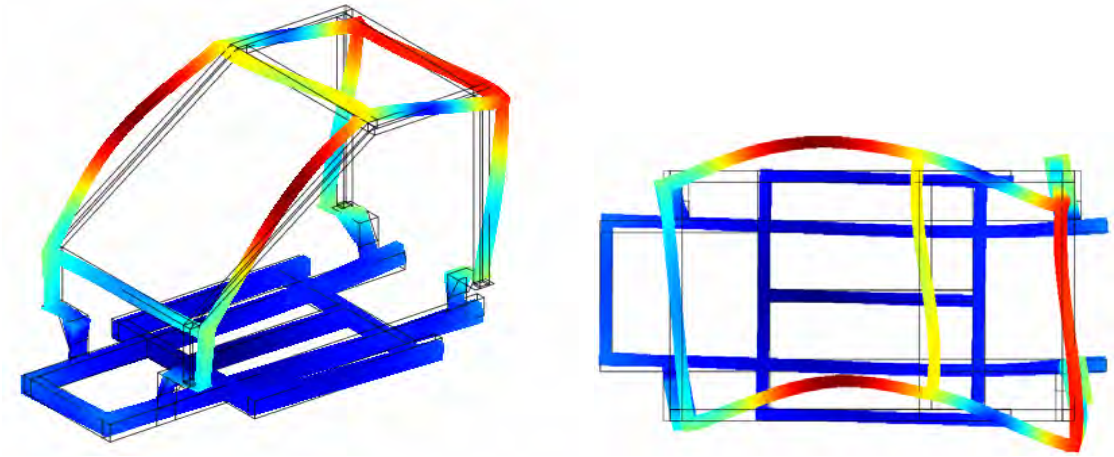

Figure 6.18: Modeshape predicted by the finite element model for the tenth mode at 101.60 Hz.

Five different parameterizations of the finite element model of the experimental vehicle are employed in order to demonstrate the applicability of the proposed finite element model updating methodologies, and point out issues associated with the multi-objective identification. The first parameterized model consists of three parameters, shown in Figure 6.19, where the first parameter θ_1 accounts for the modulus of elasticity of the lower part of the experimental vehicle, the second parameter θ_2 accounts for the modulus of elasticity of the parts (joints) that connect the lower part with the upper part (frame) of the experimental vehicle, while the third parameter θ_3 accounts for the modulus of elasticity of the upper part of the experimental vehicle. The second parameterized model consists of six parameters, shown in Figure 6.20, where the first parameter θ_1 accounts for the modulus of elasticity of the lower part of the experimental vehicle, the second parameter θ_2 accounts for the modulus of elasticity of the parts (joints) that connect the lower part with the upper part of the experimental vehicle, while the other four parameters θ_3, θ_4, θ_5 and θ_6 account for the modulus of elasticity of the different components of the upper part of the experimental vehicle as shown in Figure 6.20. The third parameterized model consists of eight parameters, shown in figure 6.21, where the first parameter θ_1 accounts for the modulus of elasticity of the lower part of the experimental vehicle, the second parameter θ_2 accounts for the modulus of elasticity of the parts (joints) that connect the lower part with the upper part of the experimental vehicle, while the other six parameters θ_3, θ_4, θ_5, θ_6, θ_7 and θ_8 account for the modulus of elasticity of the different components of the upper part of the experimental vehicle as shown in Figure 6.21. The forth parameterized model consists of nine parameters, shown in Figure 6.22, where the first parameter θ_1 accounts for the modulus of elasticity of the lower part of the experimental vehicle, the next four parameters θ_2, θ_3, θ_4 and θ_5 account for the modulus of elasticity of the parts (joints) that connect the lower part with the upper part of the experimental vehicle, while the other four parameters θ_6, θ_7, θ_8 and θ_9 account for the modulus of elasticity of the different components of the upper part of the experimental vehicle as shown in Figure 6.22. Finally, the fifth parameterized model consists of eleven parameters, shown in Figure 6.23, where the first parameter θ_1 accounts for the modulus of elasticity of the lower part of the experimental vehicle, the next four parameters θ_2, θ_3, θ_4 and θ_5 account for the modulus of elasticity of the parts (joints) that connect the lower part with the upper part of the experimental vehicle, while the other six parameters θ_6, θ_7, θ_8, θ_9, θ_{10} and θ_{11} account for the modulus of elasticity of the different components of the upper part of the experimental vehicle as shown in Figure 6.23. The nominal finite element models corresponds to values of $\theta_i = 1$ with $i = 1,\ldots,11$.

The parameterized finite element model classes are updated using the ten lowest modal frequencies and modeshapes obtained from the modal analysis, and the two modal groups with modal residuals given by (4.3).

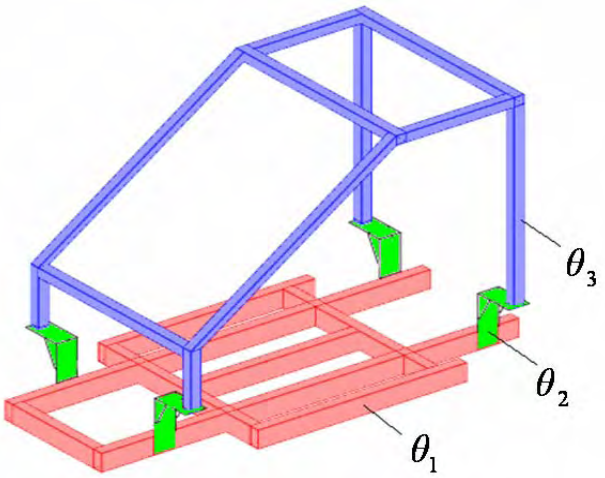

Figure 6.19: Three parameters finite element model class of the experimental vehicle.

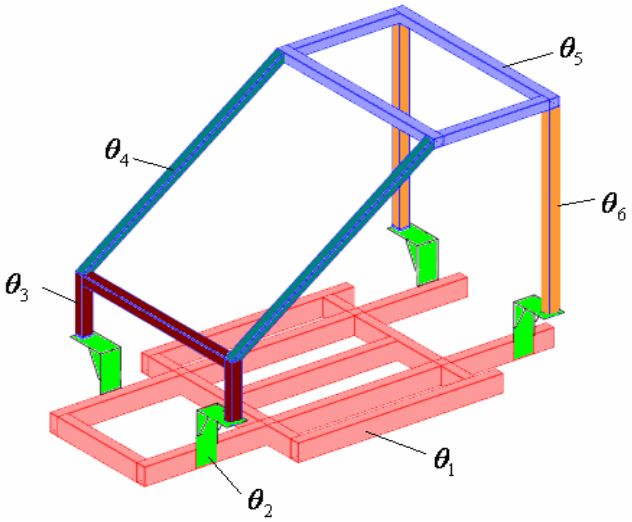

Figure 6.20: Six parameters finite element model class of the experimental vehicle.

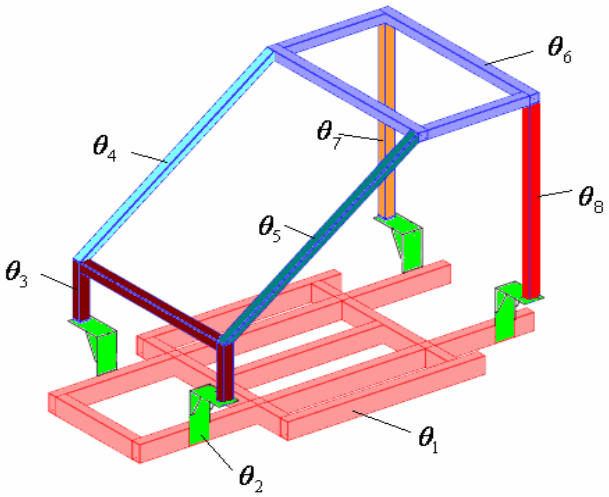

Figure 6.21: Eight parameters finite element model class of the experimental vehicle.

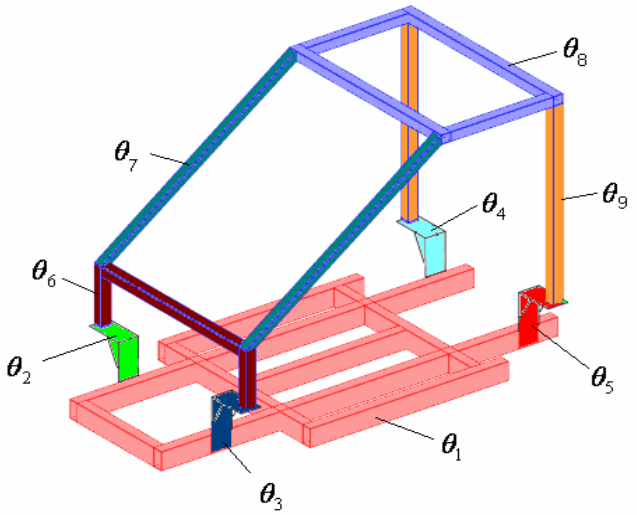

Figure 6.22: Nine parameters finite element model class of the experimental vehicle.

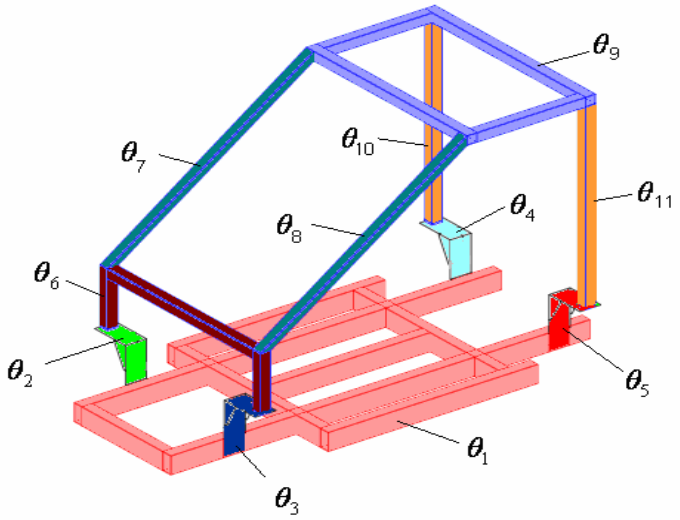

Figure 6.23: Eleven parameters finite element model class of the experimental vehicle.

The results from the multi-objective identification methodology is first presented for the case of the three parameter model shown in Figure 6.19. The NBI optimization algorithm was used to estimate the Pareto solutions. For each model class and associated structural configuration, the Pareto front, giving the Pareto solutions in the two-dimensional objective space, is shown in Figure 6.24a. The non-zero size of the Pareto front and the non-zero distance of the Pareto front from the origin are due to modeling and measurement errors. Specifically, the distance of the Pareto points along the Pareto front from the origin is an indication of the size of the overall measurement and modeling error. The size of the Pareto front depends on the size of the model error and the sensitivity of the modal properties to the parameter values $\underline{\theta}$ (Christodoulou and Papadimitriou 2007). Figures 6.24b-d show the corresponding Pareto optimal solutions in the three-dimensional parameter space. Specifically, these figures show the projection of the Pareto solutions in the two-dimensional parameter spaces (θ_1, θ_2), (θ_1, θ_3) and (θ_2, θ_3). It should be

noted that the equally weighted and the optimally solution is also computed and is shown in Figure 6.24.

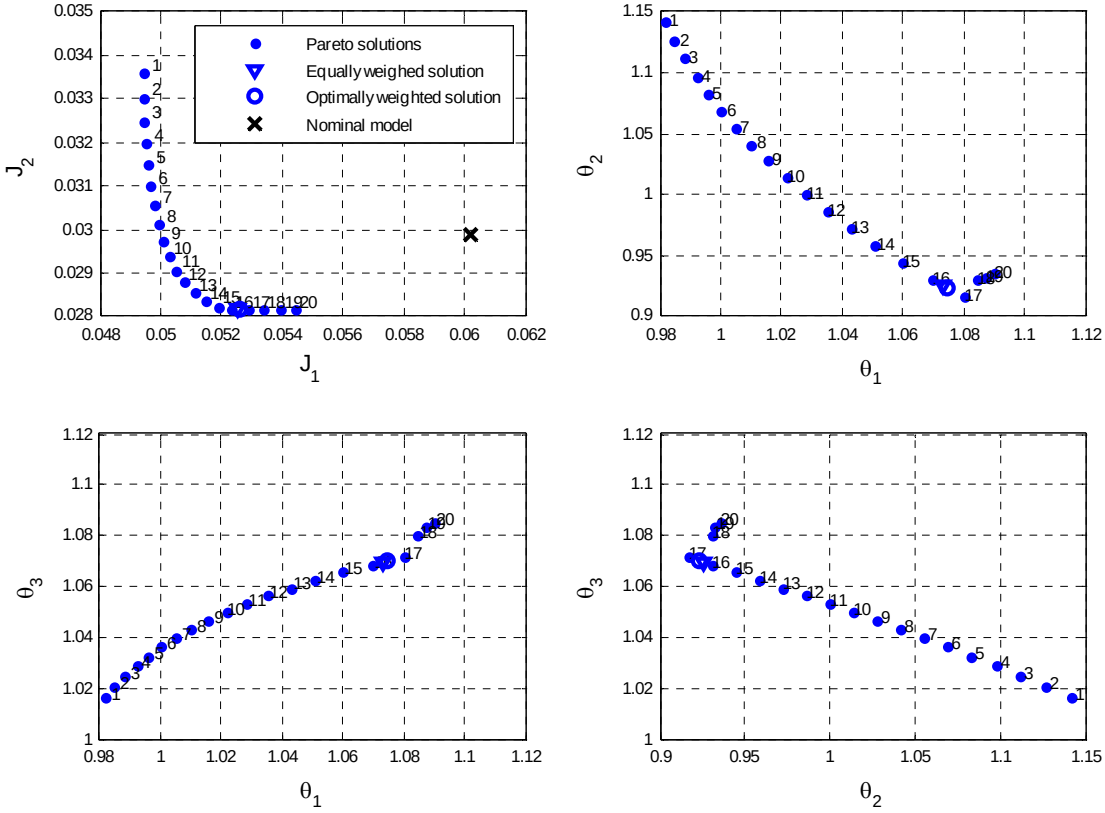

Figure 6.24: Pareto front and Pareto optimal solutions for the three parameter model classes in the (a) objective space and (b-d) parameter space.

It is observed that a wide variety of Pareto optimal solutions are obtained for different structural configurations that are consistent with the measured data and the objective functions used. The Pareto optimal solutions are concentrated along a one-dimensional manifold in the three-dimensional parameter space shown in Figure 6.25. Comparing the Pareto optimal solutions, it can be said that there is no Pareto solution that improves the fit in both modal groups simultaneously. Thus, all Pareto solutions correspond to acceptable compromise structural models trading-off the fit in the modal frequencies involved in the first modal group with the fit in the modeshape components involved in the second modal groups. The variability in the values of the model parameters are of the order of 10%, 22% and 7% for θ_1, θ_2 and θ_3 respectively.

It should be noted in Figures 6.25 and 6.24a that the Pareto solutions 17 to 20 form a one dimensional solution manifold in the parameter space that correspond to the non-identifiable solutions obtained by minimizing the second objective function $J_2(\underline{\theta})$. Specifically, it is observed that there is an almost flat part of the Pareto front at the lower right edge of Figure 6.24a. This is due to the unidentifiability problems (Katafygiotis et al. 1998, Katafygiotis and Lam 2002,

Christodoulou et al. 2008) encountered in estimating the optimal model corresponding to the right edge point of the Pareto front. In this case, the right edge point of the Pareto front is obtained by optimizing the function $J_2(\underline{\theta})$. Depending on the starting values of the parameter set $\underline{\theta}$, the gradient-based optimization algorithm converges to one of the infinite number of optimal models in this sub-manifold. As it is noted in Figure 6.24a, the flat unidentifiable portion of the Pareto front and the associated manifold in Figure 6.25 are readily obtained by the NBI method. From the engineering point of view, the most important point from this flat portion is the most left point 17 in Figure 6.24a since all other points in the flat portion deteriorate the fit in the objective function $J_1(\underline{\theta})$ without significantly altering the fit in $J_2(\underline{\theta})$. In order to generate points only on the identifiable portion of the Pareto front for pre-selected number of points on it (e.g. 20 points as shown in Figure 6.24a), the analyst can repeat the application of the NBI algorithm with edge points of the Pareto front selected to be the points 1 and 17 in Figure 6.24.

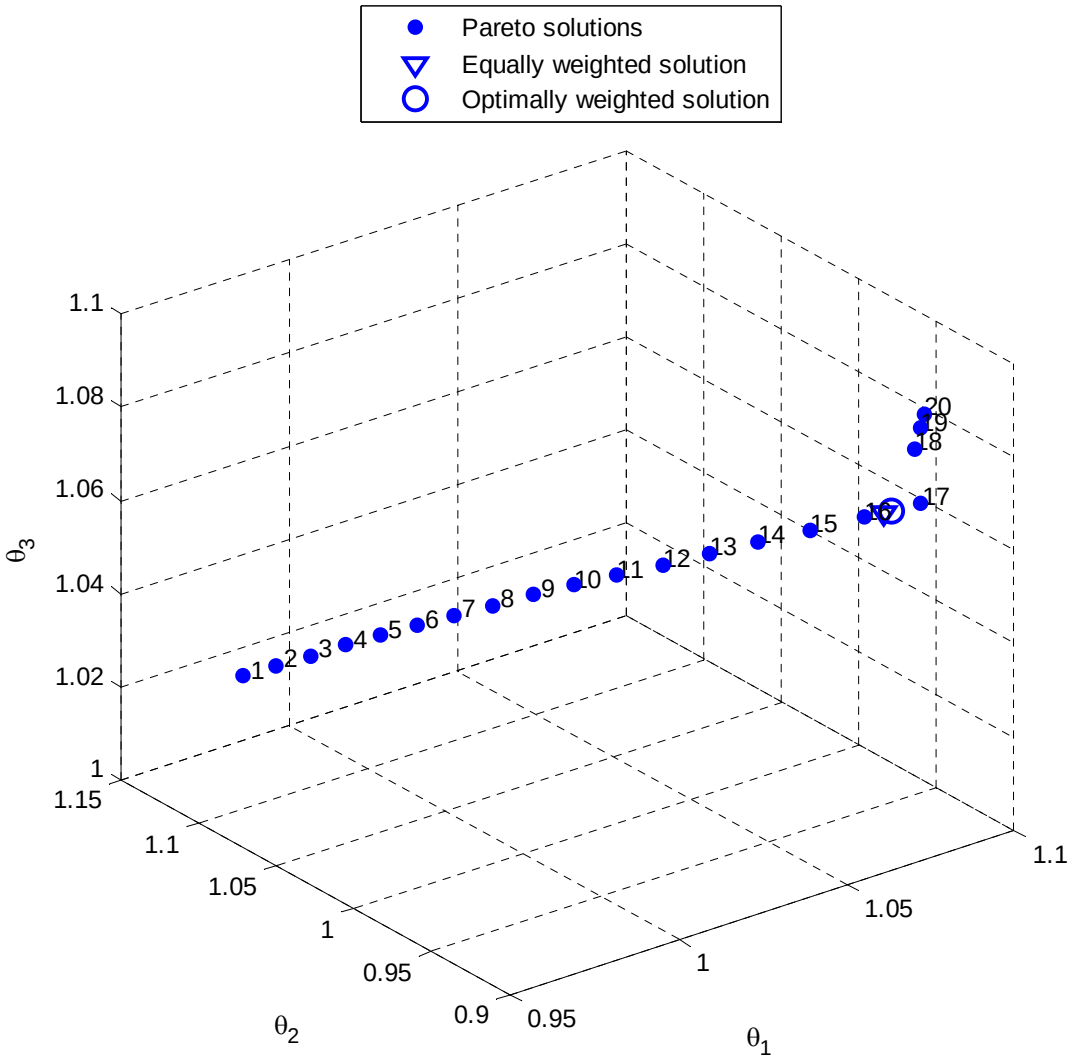

Figure 6.25: Pareto optimal solutions in the three-dimensional parameter space.

For the case of the six, eight, nine and eleven parameters, the Pareto fronts, giving the Pareto solutions in the two-dimensional objective space from the multi-objective identification methodology are shown in Figure 6.26. Comparing these results with the results in Figure 6.24a obtained for the case of the three parameter model it can be concluded that the model class with three parameters give a significantly worse fit to the experimental results considering both objectives J_1, J_2. In Figure 6.26 it is observed that generally the fit gets better when increasing the number of model parameters. However, the improvement obtained by increasing the number of parameters from six to eleven is not as significant as the improvement obtained by incrasing the number of parameters from three to six. Comparing the Pareto fronts in Figure 6.26 it can be observed that the nine and eleven parameter model classes are able to fit better the experimental results compared with the models with six and eight parameters. This is shown in Figure 6.26 observing that the distance from the origin of the Pareto fronts for the case of the nine and eleven parameter model classes is comparatively shorter than the six and eight parameter model classes.

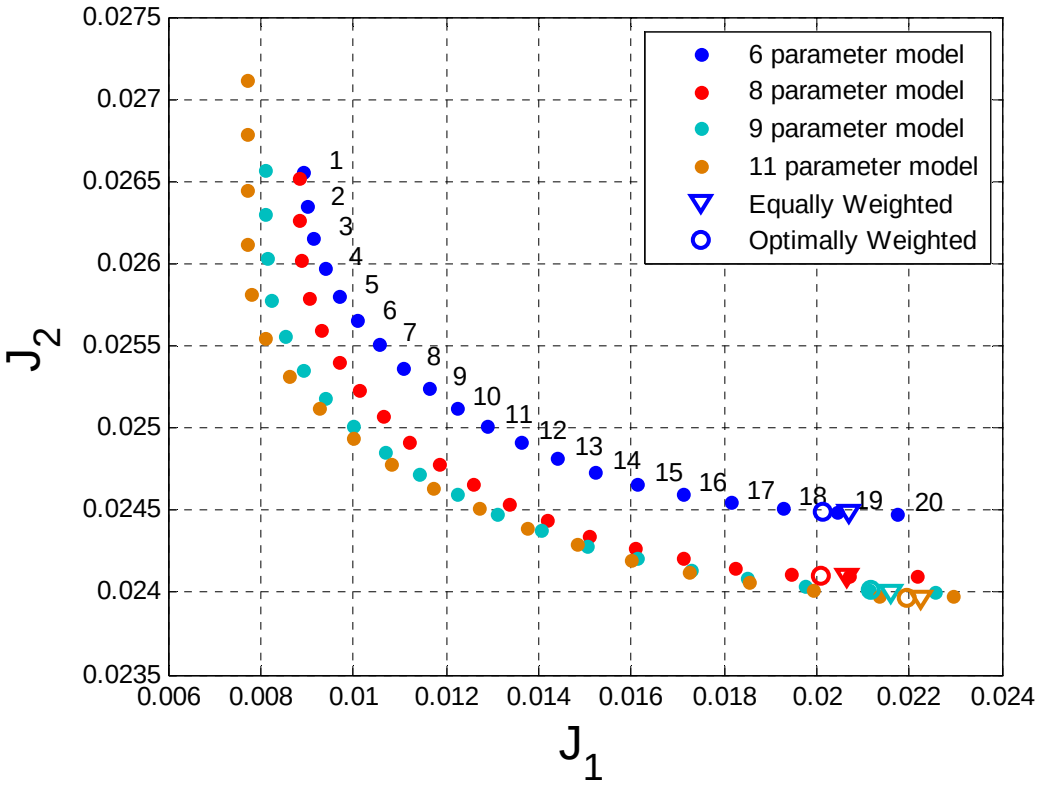

Figure 6.26: Pareto fronts for the six, eight, nine and eleven parameter model classes.

The corresponding Pareto optimal solutions for the six parameter model class are shown in Figure 6.27. The variability in the values of the model parameters are of the order of 9% for θ_1, 5% for θ_2, 29% for θ_3, 19% for θ_4, 7% for θ_5 and 17% for θ_6 respectively. It should be noted that the highest variability of 29% is observed at the stiffness of the members located at the front

part (Figure 6.20) of the vehicle. The lowest variability is observed in the stiffness of the connections between the lower and upper part of the vehicle shown in Figure 6.20.

For the case of the eight parameter model class the corresponding Pareto optimal solutions are shown in Figure 6.28. The variability in the values of the model parameters are of the order of 9% for θ_1, 5% for θ_2, 29% for θ_3, 24% for θ_4, 17% for θ_5, 7% for θ_6, 20% for θ_7 and 20% for θ_8 respectively. It should be noted that the highest variability of 29% is observed at the stiffness of the members located at the front part (Figure 6.21) of the vehicle. The lowest variability is observed in the stiffness of the connections between the lower and upper part of the vehicle shown in Figure 6.21.

For the case of the nine parameter model class the corresponding Pareto optimal solutions are shown in Figure 6.29. The variability in the values of the model parameters are of the order of 10% for θ_1, 19% for θ_2, 14% for θ_3, 7% for θ_4, 3% for θ_5, 34% for θ_6, 7% for θ_7, 5% for θ_8 and 4% for θ_9 respectively. It should be noted that the highest variability of 34% is observed at the stiffness of the members located at the front part (Figure 6.22) of the vehicle. The lowest variability is observed in the stiffness of the connections between the lower and upper part located at the rear part of the vehicle (3-7%), and the stiffness of the vertical members located at the rear part of the vehicle model (5-7%) shown in Figure 6.22.

For the case of the eight parameter model class the corresponding Pareto optimal solutions are shown in Figure 6.30. The variability in the values of the model parameters are of the order of 10% for θ_1, 17% for θ_2, 10% for θ_3, 18% for θ_4, 8% for θ_5, 37% for θ_6, 9% for θ_7, 9% for θ_8, 6% for θ_9, 13% for θ_{10} and 5% for θ_{11} respectively. It should be noted that the highest variability of 37% is observed at the stiffness of the members located at the front part (Figure 6.23) of the vehicle.

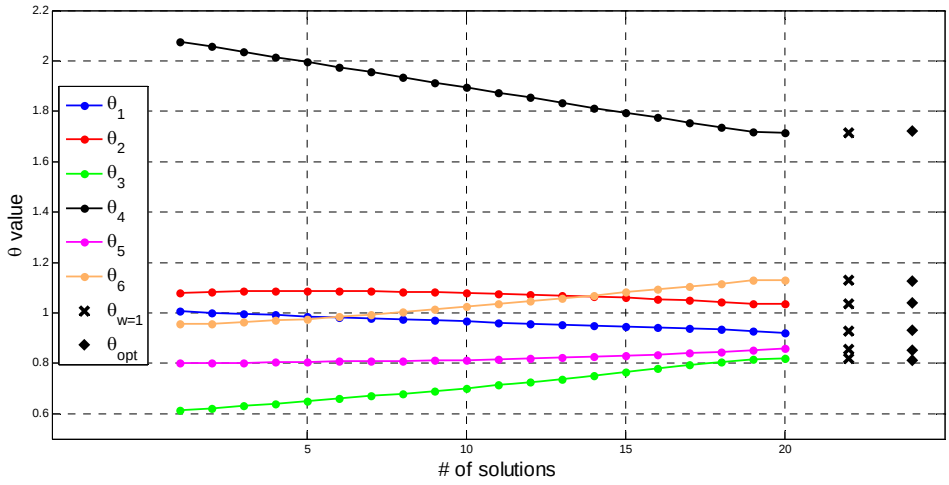

Figure 6.27: Pareto optimal solutions for the six parameter model.

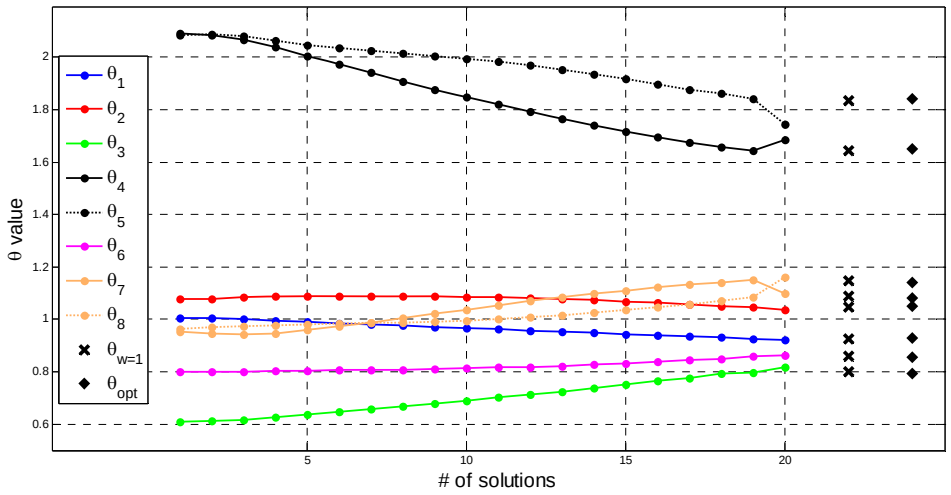

Figure 6.28: Pareto optimal solutions for the eight parameter model.

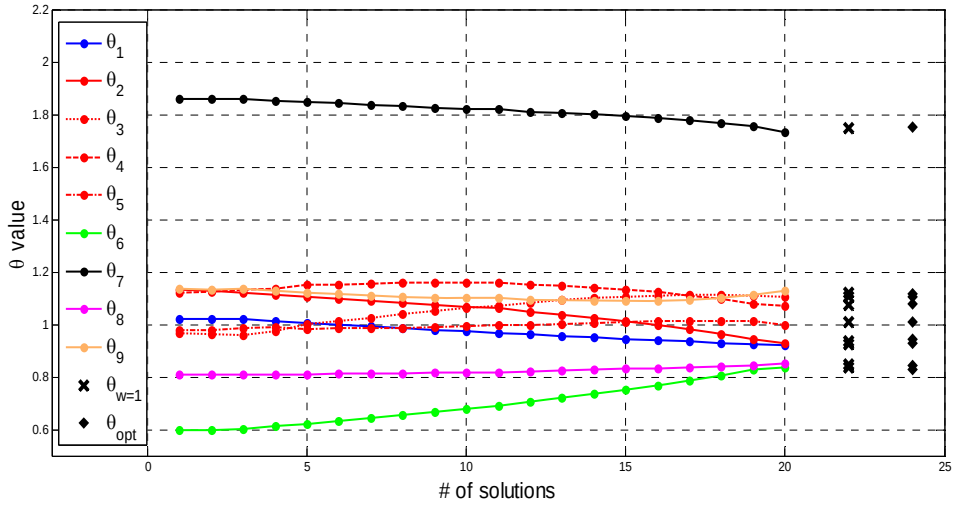

Figure 6.29: Pareto optimal solutions for the nine parameter model.

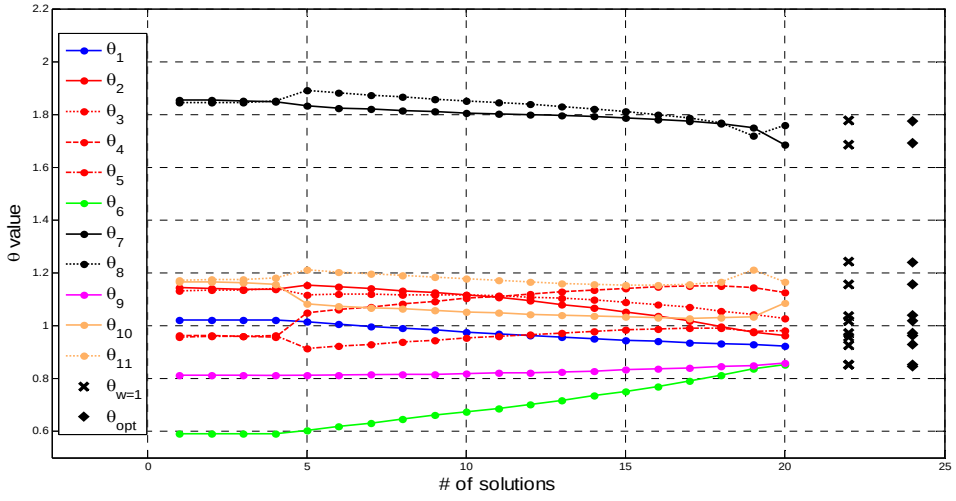

Figure 6.30: Pareto optimal solutions for the eleven parameter model.

The percentage error between the experimental (identified) values of the modal frequencies and the values of the modal frequencies predicted by the six, eight, nine and eleven parameter models for the nominal values of the parameters, the equally weighted solution and the Pareto optimal solutions 1, 5, 10, 15 and 20 are reported in Tables 6.2, 6.4, 6.6 and 6.8 respectively. Tables 6.3, 6.5, 6.7 and 6.9 reports the MAC values between the model predicted and the experimental modeshapes for the nominal, the equally weighted and the Pareto optimal models 1, 5, 10, 15 and 20 for the six, eight, nine and eleven parameter models respectively. It is observed that for the modal frequencies the difference between the experimental values and the values predicted by the Pareto optimal model vary between 0.01% and 2.09%. Specifically for the Pareto solution 1 that corresponds to the one that minimizes the errors in the modal frequencies (first objective function), the modal frequency errors are observed to be smaller than 0.8%. Highest modal frequencies errors up to 2.09% are observed as one moves towards Pareto solution 20 since such solutions are based on minimizing a weighted measure of the residuals in both the modal frequencies and the modeshapes. The errors from the Pareto solutions are significantly smaller than the errors observed for the nominal model which are as high as 7.11%. The MAC values between the experimental modeshapes and the modeshapes predicted by the Pareto optimal model 1 vary from 0.91 for the ninth mode to 0.98 for the tenth mode. The MAC values for all other modes (1 to 8) are approximately from 0.95 to 0.96. As one moves towards the Pareto solution 20 significantly improvement is observed only for the MAC value of the ninth mode. This value increases from 0.91 to 0.94. Concluding, it can be said that the six to nine parameter models give a very good fit to the experimentally identified modal data.

Table 6.2: Relative error between experimental and model predicted modal frequencies for the six parameters model.

Mode	Relative modal frequency error (%)							
	Nominal model	Equally weighted	Optimally weighted	Pareto solution 1	5	10	15	20
1	0.09	1.63	1.59	-0.43	0.02	0.57	1.16	1.69
2	-7.11	-0.64	-0.62	0.04	-0.05	-0.20	-0.41	-0.62
3	-2.10	1.38	1.36	0.54	0.70	0.92	1.17	1.37
4	-2.03	-0.76	-0.74	-0.49	-0.47	-0.54	-0.64	-0.77
5	-1.01	0.04	0.07	0.31	0.38	0.39	0.29	-0.04
6	0.02	-0.20	-0.17	0.61	0.47	0.27	0.05	-0.32
7	-4.70	-1.90	-1.87	-0.85	-1.10	-1.36	-1.63	-2.02
8	0.50	-0.55	-0.53	-0.14	-0.21	-0.30	-0.42	-0.61
9	-3.36	-0.34	-0.32	0.18	0.02	-0.12	-0.23	-0.40
10	1.36	1.03	0.96	0.17	0.19	0.28	0.52	1.19

Table 6.3: MAC values between experimental and model predicted modeshapes for the six parameters model.

Mode	MAC value							
	Nominal model	Equally weighted	Optimally weighted	Pareto solution 1	5	10	15	20
1	0.943	0.947	0.947	0.946	0.946	0.947	0.947	0.947
2	0.954	0.954	0.954	0.953	0.954	0.954	0.954	0.954
3	0.959	0.969	0.969	0.953	0.960	0.966	0.969	0.969
4	0.946	0.959	0.960	0.958	0.961	0.962	0.961	0.961
5	0.904	0.963	0.963	0.961	0.961	0.962	0.962	0.962
6	0.950	0.958	0.958	0.954	0.955	0.956	0.957	0.957
7	0.903	0.936	0.936	0.933	0.933	0.934	0.935	0.935
8	0.902	0.965	0.964	0.940	0.947	0.955	0.961	0.961
9	0.937	0.939	0.939	0.915	0.922	0.931	0.937	0.937
10	0.959	0.978	0.979	0.980	0.980	0.980	0.980	0.980

Table 6.4: Relative error between experimental and model predicted modal frequencies for the eight parameters model.

Mode	Relative modal frequency error (%)							
	Nominal model	Equally weighted	Optimally weighted	Pareto solution 1	5	10	15	20
1	0.09	1.57	1.52	-0.44	-0.10	0.50	1.11	1.65
2	-7.11	-0.65	-0.63	0.04	-0.05	-0.20	-0.41	-0.79
3	-2.10	1.31	1.29	0.54	0.66	0.89	1.14	1.34
4	-2.03	-0.72	-0.70	-0.49	-0.45	-0.51	-0.60	-0.81
5	-1.01	0.10	0.13	0.34	0.39	0.42	0.33	-0.07
6	0.02	-0.26	-0.23	0.58	0.47	0.25	0.00	-0.40
7	-4.70	-1.94	-1.92	-0.83	-1.03	-1.33	-1.66	-2.07
8	0.50	-0.49	-0.49	-0.14	-0.19	-0.29	-0.40	-0.63
9	-3.36	-0.36	-0.35	0.21	0.07	-0.10	-0.25	-0.43
10	1.36	1.14	1.07	0.16	0.18	0.28	0.58	1.21

Table 6.5: MAC values between experimental and model predicted modeshapes for the eight parameters model.

Mode	MAC value							
	Nominal model	Equally weighted	Optimally weighted	Pareto solution 1	5	10	15	20
1	0.943	0.947	0.947	.946	0.946	0.947	0.947	0.947
2	0.954	0.967	0.967	0.955	0.967	0.967	0.967	0.968
3	0.959	0.972	0.972	0.953	0.961	0.967	0.971	0.972
4	0.946	0.958	0.959	0.957	0.960	0.961	0.960	0.958
5	0.904	0.962	0.962	0.961	0.961	0.961	0.962	0.963
6	0.950	0.956	0.956	0.954	0.954	0.955	0.956	0.957
7	0.903	0.936	0.936	0.933	0.934	0.935	0.935	0.936
8	0.902	0.965	0.965	0.939	0.945	0.955	0.962	0.964
9	0.937	0.939	0.939	0.914	0.920	0.929	0.936	0.939
10	0.959	0.978	0.978	0.980	0.980	0.980	0.980	0.978

Table 6.6: Relative error between experimental and model predicted modal frequencies for the nine parameters model.

Mode	Relative modal frequency error (%)							
	Nominal model	Equally weighted	Optimally weighted	Pareto solution 1	5	10	15	20
1	0.09	1.67	1.63	-0.10	0.11	0.63	1.16	1.65
2	-7.11	-0.74	-0.71	0.19	0.15	-0.02	-0.30	-0.84
3	-2.10	1.60	1.55	0.22	0.36	0.70	1.10	1.48
4	-2.03	-1.00	-0.97	-0.52	-0.46	-0.45	-0.61	-1.15
5	-1.01	0.25	0.24	0.08	0.14	0.22	0.26	0.11
6	0.02	-0.28	-0.25	0.82	0.71	0.42	0.07	-0.45
7	-4.70	-1.92	-1.91	-0.72	-0.91	-1.32	-1.70	-2.09
8	0.50	-0.47	-0.47	-0.21	-0.26	-0.35	-0.42	-0.56
9	-3.36	-0.24	-0.25	0.09	-0.01	-0.17	-0.27	-0.38
10	1.36	0.84	0.83	0.13	0.13	0.26	0.56	0.89

Table 6.7: MAC values between experimental and model predicted modeshapes for the nine parameters model.

Mode	MAC value							
	Nominal model	Equally weighted	Optimally weighted	Pareto solution 1	5	10	15	20
1	0.943	0.947	0.947	0.946	0.947	0.947	0.947	0.947
2	0.954	0.967	0.967	0.950	0.968	0.968	0.967	0.967
3	0.959	0.972	0.972	0.962	0.968	0.971	0.971	0.972
4	0.946	0.959	0.959	0.962	0.963	0.962	0.960	0.959
5	0.904	0.961	0.961	0.960	0.960	0.960	0.961	0.961
6	0.950	0.957	0.957	0.953	0.954	0.955	0.956	0.957
7	0.903	0.938	0.938	0.931	0.933	0.935	0.937	0.938
8	0.902	0.967	0.967	0.936	0.943	0.955	0.963	0.968
9	0.937	0.941	0.940	0.911	0.916	0.928	0.937	0.941
10	0.959	0.978	0.978	0.979	0.979	0.979	0.979	0.977

Table 6.8: Relative error between experimental and model predicted modal frequencies for the eleven parameters model.

Mode	Relative modal frequency error (%)							
	Nominal model	Equally weighted	Optimally weighted	Pareto solution 1	5	10	15	20
1	0.09	1.75	1.73	-0.05	0.02	0.62	1.17	1.73
2	-7.11	-0.99	-0.96	0.19	0.16	-0.05	-0.40	-1.04
3	-2.10	1.64	1.60	0.17	0.25	0.66	1.11	1.60
4	-2.03	-1.05	-1.02	-0.51	-0.48	-0.45	-0.61	-1.06
5	-1.01	0.25	0.25	0.08	0.10	0.22	0.26	0.15
6	0.02	-0.34	-0.32	0.78	0.73	0.38	0.02	-0.40
7	-4.70	-1.83	-1.82	-0.67	-0.77	-1.23	-1.63	-1.95
8	0.50	-0.44	-0.44	-0.23	-0.23	-0.35	-0.41	-0.47
9	-3.36	-0.20	-0.21	0.11	0.08	-0.12	-0.23	-0.28
10	1.36	0.88	0.87	0.11	0.11	0.24	0.57	1.04

Table 6.9: MAC values between experimental and model predicted modeshapes for the eleven parameters model.

Mode	MAC value							
	Nominal model	Equally weighted	Optimally weighted	Pareto solution 1	5	10	15	20
1	0.943	0.947	0.947	0.946	0.947	0.947	0.947	0.947
2	0.954	0.968	0.968	0.936	0.968	0.968	0.968	0.967
3	0.959	0.971	0.972	0.958	0.966	0.970	0.971	0.972
4	0.946	0.959	0.959	0.963	0.962	0.962	0.960	0.959
5	0.904	0.961	0.961	0.960	0.958	0.959	0.960	0.961
6	0.950	0.957	0.957	0.953	0.953	0.955	0.956	0.957
7	0.903	0.939	0.939	0.931	0.934	0.936	0.938	0.939
8	0.902	0.966	0.966	0.936	0.941	0.955	0.963	0.967
9	0.937	0.941	0.940	0.910	0.912	0.927	0.936	0.940
10	0.959	0.978	0.978	0.978	0.979	0.979	0.979	0.977

The identified variability in Pareto optimal solutions has demonstrated in Christodoulou et al. (2008) to considerably affect the variability in the response predictions. Herein, the frequency response functions (FRF) predicted by the Pareto optimal solutions for the six, eight, nine and eleven parameter models are compared in Figures 6.31 to 6.34 respectively to the frequency response function computed directly from the measured data at sensor location 72 (see Figure 6.3) in the frequency range [20Hz, 105Hz] used for model updating. Compared to the initial nominal model, it is observed that the updated Pareto optimal models tend to considerably improve the fit between the model predicted and the experimentally obtained FRF in most frequency regions close to the resonance peaks. Also, it can be clearly seen that a variability in the predictions of the frequency response functions from the different Pareto optimal models is observed which is due to the variability in the identified Pareto optimal models. This variability is important to be taken into consideration in the predictions from updated models in model updating techniques. It should be noted that besides frequency response functions, similar variability is observed for other more important response quantities of interest such as the reliability of the structure against various modes of failure, as well as the fatigue accumulation and lifetime of the structure subjected to stochastic loads arising from the variability in road profiles.

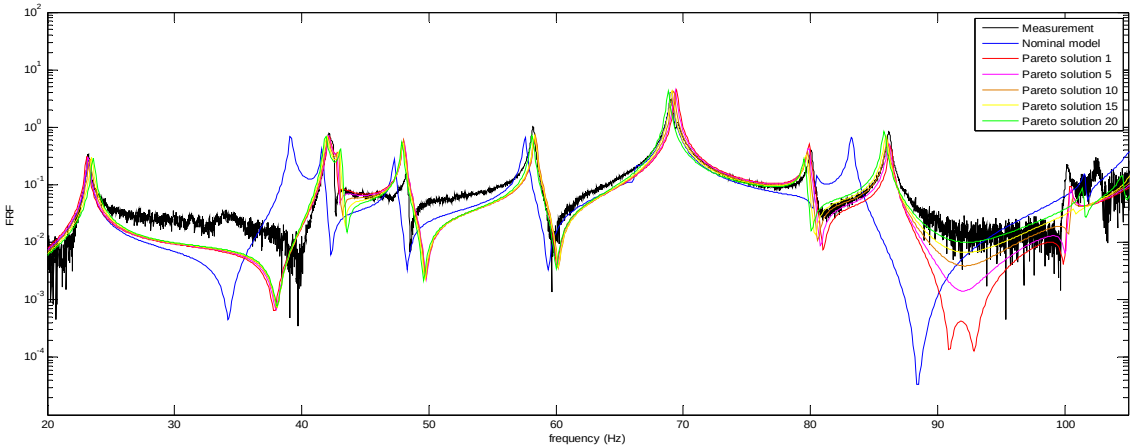

Figure 6.31: Comparison between measured and the predicted FRF from the Pareto models 1, 5, 10, 15, 20 for the six parameter model.

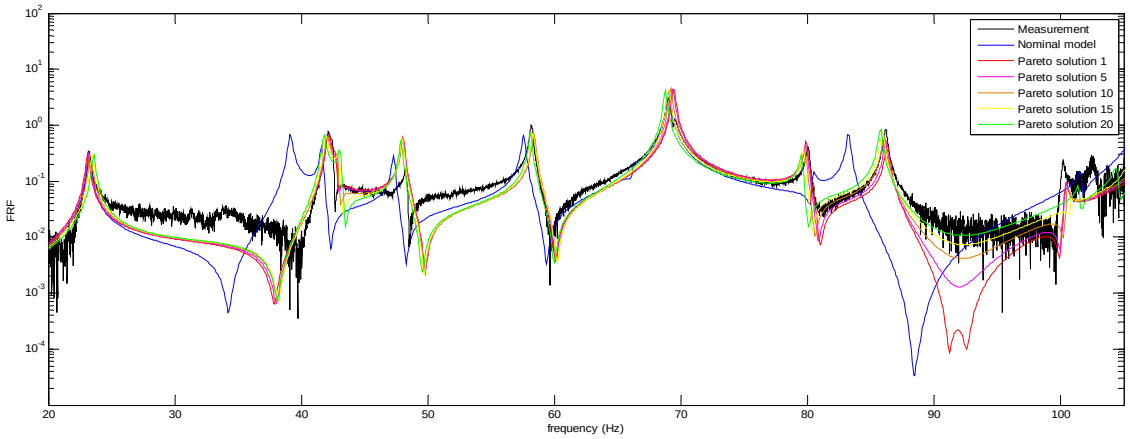

Figure 6.32: Comparison between measured and the predicted FRF from the Pareto models 1, 5, 10, 15, 20 for the eight parameter model.

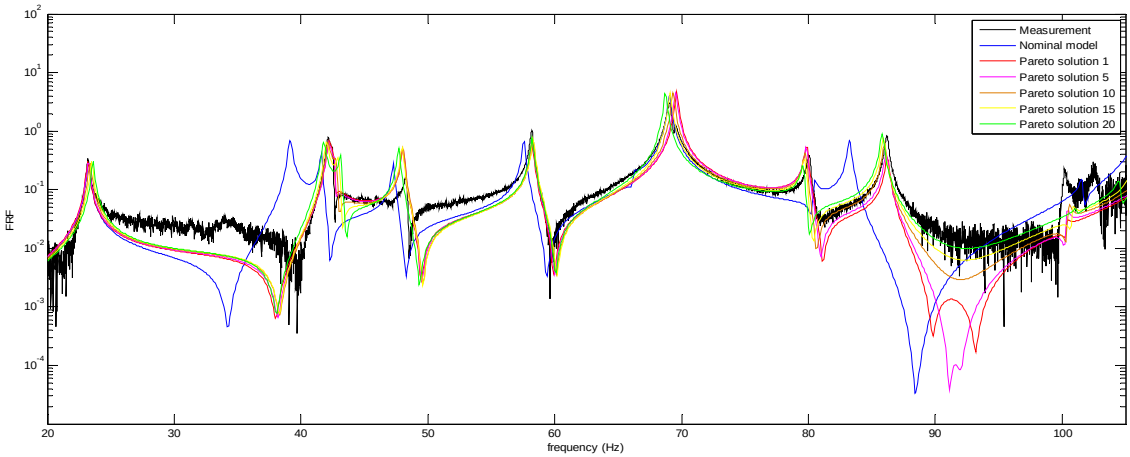

Figure 6.33: Comparison between measured and the predicted FRF from the Pareto models 1, 5, 10, 15, 20 for the eight parameter model.

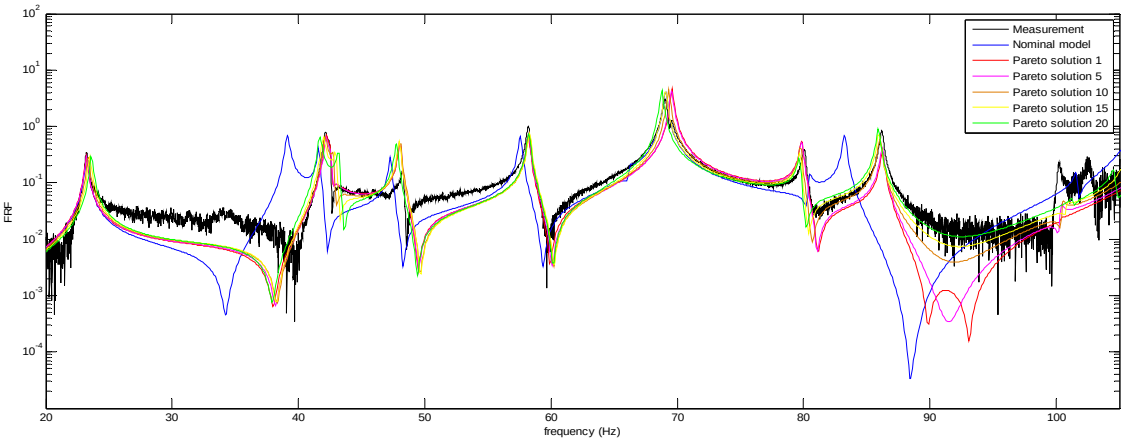

Figure 6.34: Comparison between measured and the predicted FRF from the Pareto models 1, 5, 10, 15, 20 for the eleven parameter model.

The discrepancies between the experimental and the model predicted modal frequencies as well as the deviations of the MAC values from unity are due to (a) the model error, (b) the parameterization employed, and (c) the measurement errors. Specifically, the model error arises from the assumptions used to construct the mathematical model of the structure. For the laboratory vehicle model one should emphasize that the sources of model error are due to the assumptions used to build up the connections between the various parts comprising the structure, as well as the use of shell elements to represent the members of the structure and the connections between the lower and the upper part of the model. Also, relative small errors results from the size of the finite elements employed in the discretization scheme. Another source that affects the model updating results and the errors between the model predictions and the measurements is the parameterization employed. A quite extensive search for the effect of the parameterization scheme (number and type of parameters) on the fidelity of the finite element model has been explored in this work. However, introducing more parameters to be updated will improve the fit and reduce the errors between the predictions and the experiment. However, these errors cannot be eliminated and the remaining errors could be attributed mainly to the model errors that arise from the assumptions made to build the mathematical model for the vehicle structure. The resulting errors provide guidance for modifying the assumptions made to build the model in an effort to further improve modeling and obtain higher fidelity models able to adequately represent the behavior of the experimental vehicle structure in the frequency range of interest.

6.5 Conclusions

Structural model updating method were used to develop high fidelity finite element models of an experimental vehicle model using the lowest ten modal characteristics of the structure. A multi-objective structural identification method was used for estimating the parameters of the finite element structural models based on minimizing two groups of modal residuals, one associated with the modal frequencies and the other with the modeshapes. The construction of high fidelity models consistent with the data depends on the assumptions made to build the mathematical model, the finite elements selected to model the different parts of the structure, the dicretization scheme controlling the size of the finite elements, as well as the parameterization scheme used to define the number and type of parameters to be updated by the methodology. In this work, a detailed finite element model with approximately 45000 DOF consisting of shell elements was build. The effect of the parameterization scheme on the Pareto optimal models and the model adequacy was explored. The multi-objective identification method resulted in multiple Pareto optimal structural models for each parameterization scheme that are consistent with the measured (identified) modal data and the two groups of modal residuals used to measure the discrepancies between the measured modal values and the modal values predicted by the model. These Pareto optimal models are due to uncertainties arising from model and measurement errors. A wide variety of Pareto optimal structural models was obtained that trade off the fit in various measured modal quantities. The size of observed variations in the Pareto optimal solutions depends on the information contained in the measured data, as well as the size of

model and measurement errors. The variability in the Pareto optimal vehicle models results in considerable variability in the predictions of the response, frequency response functions and reliability from these structural models. Such variability should be taken into consideration when using the updated models for predictions. Finally, a very good fit between the predictions from the Pareto optimal models and the measured modal data was obtained using six to nine parameter model classes. The discrepancies between the predicted and measured modal characteristics were very small. These small discrepancies verify the high fidelity of the model class used to model the vehicle.

Chapter 7

Conclusions and future work

7.1 Conclusions

The research work presented in the thesis contributes to the following three interrelated research areas of structural identification and response/damage prediction using vibration measurements: (1) identification of non-classically damped modal models of linear structures, (2) finite element structural model updating and prediction variability and (3) fatigue-based damage accumulation predictions in the entire body of metallic structures using a limited number of vibration sensors. Summarizing, the novel contributions in this thesis are as follows.

- Time and frequency domain least squares methods for identifying non-classically-damped modal models of linear structures from multiple-support excitations and multiple responses were proposed. A common structure of the time and frequency formulations is revealed and exploited to develop an identification software common for both formulations. A computationally very efficient three-step algorithm to solve the highly non-convex nonlinear optimization problem was developed. Specifically, the first step provides estimates of the modal frequencies and modal damping ratios by solving a system of linear algebraic equations. Stabilization diagrams are used to identify the number of contributing modes, distinguishing between physical and mathematical modes. The second step provides estimates of the modeshapes and the participation factors by solving a system of linear algebraic equations for the modal residue matrices of the contributing modes and using singular value decomposition to estimate the complex modeshapes and modal participation factors. The first two steps usually give fast and accurate estimates of the modal characteristics. A third step is added to improve the estimates of the modal characteristics for the case of closely spaced and overlapping modes by efficiently solving the original nonlinear optimization problem with initial estimates of the modal parameters those obtained from the two-step algorithm. Such choice of initial estimates significantly accelerates the convergence of gradient based acceleration algorithms. Analytical expressions for the gradient of the objective function with respect to the parameters are also integrated to further accelerate the convergence of the optimization.
- Frequency domain least squares methods for the identification of non-classically damped modal models of linear structures using ambient vibration measurements were also proposed. Computationally efficient two-step and three-step algorithms for solving the resulting, highly non-convex, nonlinear optimization problem were developed. The first step of the proposed algorithm provides estimates of the modal frequencies and modal damping ratios by solving a system of linear algebraic equations for the coefficients of the common denominator polynomial. Conventional stabilization diagrams are used to identify the number of contributing modes, distinguishing the physical from the spurious mathematical poles. Taking advantage of the special structure of the common

denominator polynomial that is revealed in this thesis for the analytical cross power spectral density matrices, one simplifies the system of normal equations used to compute the coefficients of the common denominator polynomial. This reduces considerably the computational time and the number of spurious mathematical (non-physical) modes that are obtained using the conventional stabilization diagrams. Given the poles selected in the first step, the second step of the algorithm identifies the modeshapes and all other modal parameters that fully describe the modal model of the structure using two different approaches, one non-iterative and one iterative. Finally the third step of the algorithm solves a fully nonlinear optimization problem for the identification of all modal parameters simultaneously, with initial estimates the values obtained from the two-step algorithm. Two very efficient solution schemes were proposed for the third step. Applications on simple structures with simulated measurements verify that the use of the third step is recommended to improve the estimates of the modal parameters for cases of closely and overlapping modes.

- Concerning the structural model updating problem using modal residuals, theoretical and computational issues arising in single-objective and multi-objective identification were addressed and the correspondence between the multi-objective identification, the weighted modal residuals identification and the Bayesian statistical identification was established. A novel optimally weighted modal residuals method was also proposed to select the most preferred Pareto model from the set of multiple Pareto optimal models available. Emphasis is given in addressing issues associated with solving the resulting multi-objective and single-objective optimization problems, including issues related to estimation of global optima, convergence of the proposed algorithms, and identifiability. Hybrid methods were developed to identify global optima and the normal boundary intersection method was adopted and integrated into the identification to efficiently estimate the Pareto front and the Pareto optimal models. In addition, efficient methods were proposed for estimating the gradients and the Hessians of the objective functions based on the Nelson's method for finding the sensitivities of the eigenproperties to model parameters. In particular, the Hessian computations are useful in the Bayesian asymptotic formulas for quantifying the uncertainty in the Pareto optimal models. Finally, in order to face the severe problems of corresponding measured and model predicted modes encountered for closely spaced modes, the definition of objectives in the aforementioned model updating methods was generalized and efficient gradient estimation algorithms were developed extending the use of the model updating methodology.

- A novel methodology was put forward for estimating damage accumulation due to fatigue in the entire body of a metallic structure using output-only vibration measurements from a sensor network installed at a limited number of structural locations. This was achieved by integrating (a) Kalman filter methods for predicting strain/stress response time histories and their correlation/spectral characteristics in the entire structure from output-only measured response time histories available at limited locations in the structure, and (b) frequency domain methods for estimating fatigue damage accumulation using the

spectral characteristics of the predicted strain/stress response time histories. Simulated measurements from simple structures subjected to uniaxial stress states demonstrate that the methodology is very promising in providing fatigue damage accumulation maps exploiting measured information collected from a sensor network under various operational conditions of the structure. The results are useful for fatigue lifetime prognosis and designing optimal maintenance strategies for critical components of metallic structures using vibration measurements.

- The applicability and effectiveness of the developed single- and multi-objective methodologies were explored using experimental modal data from a small-scale three-story building structure and a small-scale vehicle structure. Simple and higher fidelity finite element model classes with as high as tenths of thousands of degrees of freedom were updated. It was demonstrated that the Pareto optimal models differ significantly, resulting in large variability in response and reliability predictions from these Pareto optimal models. A wide variety of Pareto optimal structural models consistent with the measured modal data was obtained that trade-off the fit in various measured modal quantities. The variability in the Pareto optimal models is due uncertainties arising from model and measurement error. In particular, the size of observed variations in the Pareto optimal solutions depends on the information contained in the measured data, as well as the size of model and measurement errors. The variability in the Pareto optimal models may result in considerable variability in the predictions of the response and reliability from these Pareto structural models. Such variability should be taken into consideration when using the updated models for predictions. It has been demonstrated that higher fidelity model classes, tend to involve less model error, move the Pareto front towards the origin and reduce the size of the Pareto front in the objective space, reduce the variability of the Pareto optimal solutions, provide better fit to the measured quantities, and give much better predictions corresponding to reduced variability. In particular, as the fidelity of the model class improves, the importance of selecting the weight values in weighted residuals methods diminishes.

7.2 Future work

Concerning the work proposed about methods for the identification of non-classically-damped modal models of linear structures, an important direction for future work is to develop modal identification techniques to estimate the modal properties of fixed base structures using ambient vibration measurements and including the ambient measurements at the base as input measurements in the software. This is a challenging problem that remains unresolved. Such theoretical development along with the corresponding software will allow one to identify, in the expense of adding more sensors at the multiple bases of a structure, the modal properties of (a) the fixed base buildings and bridges using ambient vibration measurements, while ignoring the effects of soil structure interaction, and (b) fixed support vehicle bodies, ignoring the effects of the suspension system.

Another issue that it should be noted concerning the proposed model updating methods is that component mode synthesis methods dividing the structure to linear substructural components with fixed properties and linear substructural components with uncertain properties to be identified can be incorporated into the methodology to further reduce the computational effort required in optimization problems. The linear substructures with fixed properties can be represented by their lower contributing modes which remain unchanged during the model updating process. The method can be particular effective for finite element models with large number of DOF and for parameters that are introduced to monitor localized areas of a structure. This is usually the case for which the identification method are applied for locating damage in a structure.

The proposed model updating methodologies, such as multi-objective identification, Bayesian identification and optimally weighted residuals can be extended to handle nonlinear structures with localized nonlinearities. In this nonlinear case the measured data and the residuals are based directly on the measured response time histories instead of the modal characteristics. A challenging problem is to automate the computation of the gradients of the objective functions with respect to the model parameters since it requires developing of efficient methods for estimating the gradients of the response time histories for general nonlinear systems with various types of nonlinearities.

Another future direction is to extend the Bayesian model selection and parameter estimation to handle multiple sets of measurements corresponding to different operational conditions of the structure.

The method for predicting damage accumulation due to fatigue in the entire body of metallic structures exploiting measurements from a limited number of sensors can be extended to handle bi-axial stress states as well as to include more accurate rainflow counting methods. Also, the effectiveness of the proposed fatigue prediction methods should be explored for more complex structures, including realistic vehicle bodies and airframes. Finally, the fatigue damage accumulation methodology in the entire body of a structure can also be seen as a tool for a life-time prognosis within structural health monitoring concepts. Specifically, the proposed method can be used to estimate the accumulation of damage due to fatigue during operation in the entire body of a structure taking into account the actual conditions collected from a sensor network placed at limited number of locations. The fatigue accumulation and lifetime predictions provided by the proposed methodology in this thesis should be useful for designing optimal maintenance strategies for most critical components of metallic structures using information collected from a sensor network.

References

[1] Alvin K.F., (1997), “Finite element model update via Bayesian estimation and minimization of dynamic residuals,” *AIAA Journal*, Vol. 35, pp. 879-886.

[2] Arici Y. and Mosalam K.M., (2003), “System identification of instrumented bridge systems”, *Earthquake Engineering and Structural Dynamics*, Vol. 32, pp. 999–1020.

[3] Basseville M., Benveniste A., Goursat M., Hermans L., Mevel L., Van der Auweraer H., (2001), “Output-only subspace-based structural identification: from theory to industrial testing practice”, *ASME Journal of Dynamic Systems Measurement and Control*, Vol. 123 (4), pp. 668-676.

[4] Beck J.L., (1978), “Determining models of structures from earthquake records”, Report No. EELRL 78-01, Earthquake Engineering Research Laboratory, California Institute of Technology, Pasadena, CA.

[5] Beck J.L. and Jennings P.C., (1980), “Structural identification using linear models and earthquake records”, *Earthquake Engineering and Structural Dynamics*, Vol. 8, pp. 145-160.

[6] Beck J.L., (1989), “Statistical System Identification of Structures”, *Proceedings of the 5th International Conference on Structural Safety and Reliability* (ASCE), San Francisco, pp.1395-1402.

[7] Beck J.L., May B.S., Polidori D.C., (1994), “Determination of modal parameters from ambient vibration data for structural health monitoring”, *Proceedings of the 1st World Conference on Structural Control*, Los Angeles, USA, pp. 1395-1402.

[8] Beck J.L. and Katafygiotis L.S., (1998), “Updating models and their uncertainties- I: Bayesian statistical framework”, *Journal of Engineering Mechanics (ASCE)*, Vol. 124, pp. 455-461.

[9] Beck J.L. and Au S.K., (2002), “)Bayesian updating of structural models and reliability using Markov chain Monte Carlo simulation”, *Journal of Engineering Mechanics (ASCE)*, Vol. 128, pp. 380-391.

[10] Benasciutti D. and Tovo R., (2005), “Spectral methods for lifetime prediction under wide-band stationary random processes”, *International Journal of Fatigue*, Vol. 27, pp. 867–877.

[11] Benasciutti D. and Tovo R., (2006), “Comparison of spectral methods for fatigue analysis of broad-band Gaussian random processes”, *Probabilistic Engineering Mechanics*, Vol. 21, pp. 287–299.

[12] Bishop N.N.M. and Sherrat F., (1990), “A theoretical solution for the estimation of the rainflow ranges from power spectral density data”, *Fatigue and Fracture of Engineering Materials and Structures*, Vol. 13 (4), pp. 311-326.

[13] Blackman R.B. and Tukey J.W., (1958), *The measurement of power spectra from the point of view of communication engineering*, Dover Publications, Inc., New York.

[14] Bleistein N. and Handelsman R., (1986), Asymptotic expansions for integrals, Dover Publications, Inc., New York, USA.

[15] Bohle K. and Fritzen C.P., (2003), “Results obtained by minimizing natural frequencies and MAC-value errors of a plate model”, *Mechanical Systems and Signal Processing*, Vol. 17 (1), pp. 55-64.

[16] Boswald M., Goge D., Fullekrug U., Govers Y., (2006), “A review of experimental modal analysis methods with respect to their applicability to test data of large aircraft structures”, *International Conference on Noise and Vibration Engineering (ISMA2006),* Katholieke Universiteit Leuven, Leuven, Belgium.

[17] Boswald M. and Govers Y., (2008), “Taxi vibration testing - An alternative method to ground vibration testing of large aircraft”, *International Conference on Noise and Vibration Engineering (ISMA2008),* Katholieke Universiteit Leuven, Leuven, Belgium.

[18] Brincker R., Zhang L., Andersen P., (2001), “Modal identification of output-only systems using frequency domain decomposition”, *Smart Materials and Structures*, Vol. 10, pp. 441-445.

[19] Capecchi D. and Vestroni F., (1993), “Identification of finite-element models in structural dynamics”, *Engineering Structures*, Vol. 15 (1) , pp. 21-30.

[20] Cauberghe B., (2004), “Applied frequency-domain system identification in the field of experimental and operational modal analysis”, PhD Thesis, Department of Mechanical Engineering, Vrije Universiteit Brussel, Belgium.

[21] Chaudhary M.T.A., Abe M., Fujino Y., (2000), “System identification of two base-isolated buildings using seismic records”, *Journal of Structural Engineering (ASCE)*, Vol. 126(10), pp. 1187-1195.

[22] Chaudhary M.T.A., Abe M., Fujino Y. (2002), “Investigation of atypical seismic response of a base-isolated bridge”, *Engineering Structures*, Vol. 24, pp. 945–953.

[23] Christodoulou K. and Papadimitriou C., (2007), “Structural identification based on optimally weighted modal residuals”, Mechanical Systems and Signal Processing, Vol. 21, pp. 4-23.

[24] Christodoulou K., Ntotsios E., Papadimitriou C., Panetsos, P., (2008), "Structural Model Updating and Prediction Variability using Pareto Optimal Models." *Computer Methods in Applied Mechanics and Engineering*, Vol. 198 (1), pp.138-149.

[25] Clough R.W. and Penzien J., (1993), Dynamics of structures, McGraw-Hill.

[26] COMSOL AB, (2005), *COMSOL Multiphysics User’s Guide*. [http://www.comsol.com/].

[27] Das I., Dennis J.E., Jr., (1998), “Normal-Boundary Intersection: A new method for generating the Pareto surface in nonlinear multi-criteria optimization problems”, *SIAM Journal of Optimization*, Vol. 8, pp. 631-657.

[28] Devriendt C. and Guillaume P., (2008), “Identification of modal parameters from transmissibility measurements”, *Journal of Sound and Vibration*, Vol. 314 (1-2), pp. 343-356.

[29] Dirlik T., (1985), Applications of Computers to Fatigue Analysis, PhD Thesis, Warwick University.

[30] Doebling S.W., Farrar C.R. , Prime M.B., (1998), “A summary review of vibration-based damage identification methods”, *The Shock and Vibration Digest*, Vol. 30 (2), pp. 91-105.

[31] Ewins D.J., (2000), Modal Testing: Theory, Practice and Application, Second edition. Research Studies Press LTD.

[32] Farhat, C. and Hemez, P.M., (1993), “Updating Finite Element Dynamics Models Using an Element-by-Element Sensitivity Methodology”, *American Institute of Aeronautics and Astronautics Journal*, Vol. 31(9), pp. 1702-1711.

[33] Farrar C., Baker W., Bell T., Cone K., Darling T., Duffey, T., Eklund A., Migliori A., (1994), “Dynamic Characterization and Damage Detection in the I-40 Bridge over the Rio Grande”, Technical Report LA-12767-MS, Los Alamos National Laboratory.

[34] Felber A.J., (1993), “Development of a hybrid bridge evaluation system”, PhD Thesis, University of British Columbia, Vancouver, Canada.

[35] Franklin G.F., Powell J.D., Workman M.L., (1990), Digital Control of Dynamic Systems, Second Edition, Addison-Wesley.

[36] Fritzen C.P., Jennewein D., Kiefer T., (1998), “Damage detection based on model updating methods”, *Mechanical Systems and Signal Processing*, Vol. 12 (1), pp. 163-186.

[37] Giagopulos D. and Natsiavas S. (2007), “Hybrid (numerical-experimental) modeling of complex structures with linear and nonlinear components”, *Nonlinear Dynamics*, Vol. 47 (1-3), pp. 193-217.

[38] Guillaume P., Hermans L., Van der Auweraer H., (1999), “Maximum Likelihood Identification of Modal Parameters from Operational Data”, *Proceedings of the 17th International Modal Analysis Conference (IMAC17)*, pp. 1887-1893.

[39] Haralampidis Y., Papadimitriou C., Pavlidou M., (2005), “Multi-objective framework for structural model identification”, *Earthquake Engineering and Structural Dynamics*, Vol. 34 (6), pp. 665-685.

[40] Hermans L., Van der Auweraer H., Guillaume P., (1998), “A frequency-domain maximum likelihood approach for the extraction of modal parameters from output-only data”, *Proceedings of the 23rd International Seminar on Modal Analysis (ISMA23)*, pp. 367-376.

[41] Hermans L. and Van der Auweraer H., (1999), “Modal testing and analysis of structures under operational conditions: Industrial applications”, *Mechanical Systems and Signal Processing*, Vol 13 (2), pp. 193-216.

[42] Hayes M., (1996), Statistical Digital Signal Processing and Modeling, John Wiley & Sons.

[43] Heylen, W., Lammens, S., Sas, P. (1997), Modal Analysis Theory and Testing, Katholieke Universiteit Leuven, Department of Mechanical Engineering.

[44] Hjelmstad K.D. and Shin S.,(1996), “Crack identification in a cantilever beam from modal response”, *Journal of Sound and Vibration*, Vol. 198, pp. 527-545.

[45] Kailtath T., (1980), Linear systems, Prentice-Hall, New Jersey, U.S.

[46] Kalman R.E. and Bucy., R.S., (1961), “New results in linear filtering and prediction theory”, *J. of Basic Eng., Trans. ASME*, Series D, Vol. 83 (3), pp. 95–108.

[47] Katafygiotis L.S., (1991), Treatment of model uncertainties in structural dynamics, Technical Report EERL91-01, California Institute of Technology, Pasadena, CA.

[48] Katafygiotis L.S. and Beck J.L., (1998), “Updating models and their uncertainties. II: Model identifiability”, *Journal of Engineering Mechanics (ASCE)*, Vol. 124 (4), pp. 463-467.

[49] Katafygiotis L.S., Papadimitriou C., Lam H.F., (1998), “A probabilistic approach to structural model updating”, *International Journal of Soil Dynamics and Earthquake Engineering*, Vol. 17, pp. 495-507.

[50] Katafygiotis L.S. and Yuen K.V., (2001), “Bayesian spectral density approach for modal updating using ambient data”, *Earthquake Engineering and Structural Dynamics* Vol. 30 (8), pp. 1103-1123.

[51] Katafygiotis L.S. and Lam H.F., (2002), “Tangential-projection algorithm for manifold representation in unidentifiable model updating models”, *Earthquake Engineering and Structural Dynamics*, Vol. 31 (4), pp. 791-812.

[52] Klepka A. and Tadeusz U., (2008), “Hardware and software tools for in-flight flutter testing”, *International Conference on Noise and Vibration Engineering (ISMA2008),* Katholieke Universiteit Leuven, Leuven, Belgium, 15-17 September, 2008.

[53] Kim C., Kim N., Jung D., Yoon J., (2001), “Effect of vehicle mass on the measured dynamic characteristics of bridges from traffic-induced vibration test”, *Proceedings of the 19th International Modal Analysis Conference (IMAC19)*, pp. 1106-1111.

[54] Lin C.C., Hong L.L., Ueng J.M., Wu K.C., Wang C.E., (2005), “Parametric identification of asymmetric buildings from earthquake response records”, *Smart Materials and Structures*, Vol. 14, pp. 850-861.

[55] Link M., (1998), “Updating analytical models by using local and global parameters and relaxed optimization requirements”, *Mechanical Systems and Signal Processing*, Vol. 12 (1), pp. 7-22.

[56] Liu H., Yanga Z., Gaulkeb M.S., (2005), “Structural identification and finite element modeling of a 14-story office building using recorded data”, *Engineering Structures*, Vol. 27, pp. 463–473.

[57] Ljung L., (1999), System Identification: Theory for the User. Prentice-Hall, New York, USA.

[58] Lutes L.D., Corazao M., Hu S-L.J., Zimmerman J., (1984), “Stochastic fatigue damage accumulation”, *Journal of Structural Engineering ASCE*, Vol. 110 (11), pp. 2585-2601.

[59] Lutes L.D. and Larsen C.E., (1990), “Improved spectral method for variable amplitude fatigue prediction”, *Journal of Structural Engineering, ASCE*, Vol. 116 (4), pp. 1149-1164.

[60] Lutes L.D. and Sarkani S., (2004), Random Vibrations: Analysis of Structural and Mechanical Systems, Elsevier Butterworth-Heinemann.

[61] Lus H., Betti R., Longman R.W., (1999), “Identification of Linear Structural Systems using Earthquake-Induced Vibration Data”, *Earthquake Engineering and Structural Dynamics*, Vol. 28, pp. 1449–1467.

[62] Mahmoudabadi M., Ghafory-Ashtiany M., Hosseini M., (2007), “Identification of modal parameters of non-classically damped linear structures under multi-component earthquake loading”, *Earthquake Engineering and Structural Dynamics*, Vol. 36, pp. 765-782.

[63] Marple S.L., (1987), Digital spectral analysis, Prentice-Hall, New York, USA.

[64] McVerry G.H., (1980), “Structural identification in the frequency domain from earthquake records”, *Earthquake Engineering and Structural Dynamics*, Vol. 8, pp. 161-180.

[65] Miner M.A., (1945), “Cumulative damage in fatigue, Applied Mechanics”, *Transactions, ASME*, Vol. 12 (3), A159-A164

[66] Mottershead J.E., Friswell M.I., (1993), “Model updating in structural dynamics: A survey”, *Journal of Sound and Vibration*, Vol. 167, pp. 347-375.

[67] Natsiavas S., (1999), Ταλαντώσεις Μηχανικών Συστημάτων, Εκδόσεις Ζήτη.

[68] Nelson R.B., (1976), “Simplified calculation of eigenvector derivatives”, *AIAA Journal*, Vol. 14 (9), pp. 1201-1205.

[69] Nikolaou I., (2008), “Structural modal identification methods based on earthquake-induced vibrations”, MS Thesis Report No. SDL-08-2, Department of Mechanical and Industrial Engineering, University of Thessaly, Volos, Greece.

[70] Ntotsios E., Papadimitriou C., Panetsos P., Karaiskos G., Perros K., Perdikaris Ph., (2008), “Bridge health monitoring system based on vibration measurements”, *Bulletin of Earthquake Engineering*, doi: 10.1007/s10518-008-9067-4.

[71] Ntotsios E., (2009), “Experimental modal analysis using ambient and earthquake vibrations: Theory, Software and Applications”, MS Thesis Report No. SDL-08-1, Department of Mechanical and Industrial Engineering, University of Thessaly, Volos.

[72] Oden, J.T., Belytschko, T., Fish, J., Hughes, T.J.R., Johnson, C., Keyes, D., Laud, A., Petzold, L., Srolovitz, D., Yip, S., (2006), *Simulation-Based Engineering Science (SBES) – Revolutionizing Engineering Science through Simulation*, Report of the National Science Foundation: Blue Ribbon Panel on SBES.

[73] Palmgren A., (1924), Die Lebensdauer von Kugallagern, VDI-Zeitschrift, 68(14) 339-341.

[74] Panetsos P., Ntotsios E., Liokos N.A., Papadimitriou C., (2009), “Identification of Dynamic models of Metsovo (Greece) Bridge using Ambient Vibration Measurements”, *ECCOMAS Thematic Conference on Computational Methods in Structural Dynamics and Earthquake Engineering*, Rethymno, Rhodes, Greece.

[75] Parloo E., (2003), “Application of Frequency-domain System Identification in the Field of Operational Modal Analysis”, Ph.D. Thesis, Department of Mechanical Engineering, Vrije Universiteit Brussel, Belgium.

[76] Papageorgiou A.S., Lin B.C., (1989), “Influence of lateral-load-resisting system on the earthquake response of structures – A system identification study”, *Earthquake Engineering and Structural Dynamics*, Vol. 18, pp. 799-814.

[77] Papadimitriou C., Beck J.L., Katafygiotis L.S., (2001), “Updating robust reliability using structural test data”, *Probabilistic Engineering Mechanics*, Vol. 16, pp. 103-113.

[78] Papadimitriou C. and Katafygiotis L.S., (2004), “Bayesian Modeling and Updating” In: Engineering Design Reliability Handbook, E. Nikolaidis, D.M. Ghiocel and S. Singhal (Eds), CRC Press, New York.

[79] Peeters B. and De Roeck G., (1999), “Reference-based stochastic subspace identification for output-only modal analysis”, *Mechanical Systems and Signal Processing*, Vol. 13 (6), pp. 855-878.

[80] Peeters B., (2000), “System Identification and Damage Detection in Civil Engineering”, PhD thesis, Dept. of Civil Engineering, Katholieke Universiteit Leuven, Belgium.

[81] Peeters B. and De Roeck G., (2001), “One-year monitoring of the z24-bridge: environmental effects versus damage events”, *Earthquake Engineering and Structural Dynamics*, Vol. 30 (2), pp. 149-171.

[82] Peeters B., Van der Auweraer H., Guillaume P., Leuridan J., (2004), “The PolyMAX frequency-domain method: A new standard for modal parameter estimation?”, *Shock and Vibration*, Vol. 11 (2-4), pp. 395-409.

[83] Peeters B., Van der Auweraer H., (2005), “Recent developments in operational modal analysis”, *EURODYN 2005*, C. Soize & G.I Schueller (eds), Millpress, Rotterdam, pp. 149-154.

[84] Peeters B., Hendricx W., Debille J. (2009), “Modern solutions for ground vibration testing of large aircraft”, *Sound and Vibration*, Vol. 43 (1), pp. 8-15.

[85] Pitoiset X., Preumont A., (2000), “Spectral methods for multiaxial random fatigue analysis of metallic structures”, *International Journal of Fatigue*, Vol. 22, pp. 541–550.

[86] Preumont A. and Piefort V., (1994), “Predicting random high cycle fatigue life with finite elements”, *ASME Journal of Vibration and Acoustics*, Vol. 16, pp. 245–248.

[87] Roberts S., (2001), “Identification of the modal parameters affecting automotive ride characteristics”, *Proceedings of the 19th International Modal Analysis Conference (IMAC19),* pp. 270-274.

[88] Rychlik I., (1993), “On the ‘narrow-band’ approximation for expected fatigue damage”, *Probabilistic Engineering Mechanics*, Vol. 8, pp. 1–4.

[89] Safak E. (1995), “Detection and identification of soil-structure interaction in buildings from vibration recordings”, *Journal of Structural Engineering (ASCE)*, Vol. 121 (5), pp. 899-906.

[90] Sarkani S., Kihl D.P., Beach J.E., (1994), “Fatigue of welded joints under narrowband non-Gaussian loadings”, *Probabilistic Engineering Mechanics*, Vol. 9, pp. 179-190.

[91] Sohn H. and Law K.H., (1997), “Bayesian probabilistic approach for structural damage detection”, *Earthquake Engineering and Structural Dynamics*, Vol. 26, pp. 1259-1281.

[92] Siringoringo D.M. and Fujino Y., (2007), “Dynamic characteristics of a curved cable-stayed bridge identified from strong motion records”, *Engineering Structures*, Vol. 29, pp. 2001-2017.

[93] Smyth A.W., Pei J-S., Masri S.F., (2003), “System identification of the Vincent Thomas suspension bridge using earthquake records”, *Earthquake Engineering and Structural Dynamics*, Vol. 32, pp. 339–367.

[94] Souty C., (2008), “Modal identification of the structure of an aircraft with the LSCF method”, *International Conference on Noise and Vibration Engineering (ISMA2008),* Katholieke Universiteit Leuven, Leuven, Belgium, 15-17 September.

[95] Stengel R.F., (1986), Stochastic Optimal Control: Theory and Applications, John Wiley & Son.

[96] Tan R.Y. and Cheng W.M. (1993), “System identification of a non-classically damped linear system”, *Computers and Structures*, Vol. 46, pp. 67–75.

[97] Teughels A., De Roeck G., Suykens J.A.K., (2003), “Global optimization by coupled local minimizers and its application to FE model updating”, *Computers and Structures*, Vol. 81 (24-25), pp. 2337-2351.

[98] Teughels A. and De Roeck G., (2005), “Damage detection and parameter identification by finite element model updating”, *Archives of Computational Methods in Engineering*, Vol. 12 (2), pp. 123-164.

[99] Van Overschee P. and De Moor B., (1996), Subspace Identification for Linear Systems: Theory-Implementation-Applications, Kluwer Academic Publishers.

[100] Vanik M.W., Beck J.L., Au S.K., (2000), “Bayesian probabilistic approach to structural health monitoring”, *Journal of Engineering Mechanics (ASCE)*, Vol. 126, pp. 738-745.

[101] Verboven P., (2002), “Frequency domain system identification for modal analysis”, PhD Thesis, Department of Mechanical Engineering, Vrije Universiteit Brussel, Belgium.

[102] Wang X. and Sun J.Q., (2005), “Multi-stage regression fatigue analysis of non-Gaussian stress processes”, *Journal of Sound and Vibration*, Vol. 280, pp. 455-465.

[103] Welch P.D., (1967), “The use of fast Fourier transform for the estimation of power spectra: A method based on time averaging over short modified periodograms”, *IEEE Transactions on Audio and Electroacoustics*, Vol. 15, pp. 70-73.

[104] Werner S.D., Beck J.L., Levine M.B., (1987), “Seismic response evaluations of Meloland road overpass using 1979 Imperial Valley earthquake records”, *Earthquake Engineering and Structural Dynamics*, Vol. 15, pp. 249-274.

[105] Wilson J.C., (1986), “Analysis of the observed seismic response of a highway bridge”, *Earthquake Engineering and Structural Dynamics*, Vol. 14, pp. 339–354.

[106] Wirsching P.H. and Light M.C., (1980), “Fatigue under wide band random stress”, *Journal of Structural Engineering ASCE*, Vol. 106(7(, pp. 1593-160.

[107] You B.R. and Lee S.B., (1996), “A critical review on multiaxial fatigue assessments of metals”, *International Journal of Fatigue*, Vol. 18 (4), pp. 235–44.

[108] Yuen K.V. and Beck J.L., (2003), “Reliability-based robust control for uncertain dynamical systems using feedback of incomplete noisy response measurements”, *Earthquake Engineering and Structural Dynamics*, Vol. 32 (5), pp. 751-770.

[109] Yuen K.V., Beck J.L., Katafygiotis L.S., (2006), “Unified probabilistic approach for model updating and damage detection”, *Journal of Applied Mechanics – Transactions of the ASME*, Vol. 73 (4), pp. 555-564.

[110] Zitzler E. and Thiele L., (1999), “Multi-objective Evolutionary Algorithms: A Comparative Case Study and the Strength Pareto Approach”, *IEEE Transactions on Evolutionary Computation*, Vol. 3 (4), pp.257-271.